Selected Studies in Classical and Quantum Gravity

by

Ryo Saotome

A dissertation submitted in partial fulfillment
of the requirements for the degree of
Doctor of Philosophy
(Physics)
in the University of Michigan
2013

Doctoral Committee:

Professor Ratindranath Akhoury, Chair
Professor Charles R. Doering
Professor David Garfinkle, Oakland University
Professor Gordon L. Kane
Associate Professor Leopoldo A. Pando Zayas
Professor Bing Zhou

Acknowledgements

I would first like to thank my advisor Professor Akhoury for his generous guidance over my graduate career. This thesis would not have been possible without his constant mentoring and encouragement. I am truly lucky to have gained not just a great advisor but also a great friend.

I would also like to thank all of my collaborators, especially Professor Garfinkle and Professor Sterman, for their tutelage and support in the research projects that make up this thesis. I will always appreciate the fortune I had in being able to have enlightening discussions with such experts in the field.

I am also very grateful for all of the great friends and colleagues I met over the past five years. Their support was so extensive and varied that it would take me a second dissertation to properly express my gratitude, so in short: thank you for everything.

I would also like to thank Michelle for all of the support she has given me over my graduate studies. Without her pushing me to work when I needed to work and encouraging me to take a break when I needed a break, this thesis would not have been possible.

Lastly, I would like to thank my father, mother, and brother for all their help over the past five years and beyond. I especially appreciate my parents for sparking my fascination with science at a young age, and my brother for illuminating discussions on topics ranging from protein crystallization to the Boston Celtics' playoff chances whenever I needed a break from working on this thesis.

Table of Contents

List of Figures

Figure

List of Appendices

Appendix

Abstract

This thesis is composed of two parts, one corresponding to classical and the other to quantum gravitational phenomena. In the classical part, we focus on the behavior of various classical scalar fields in the presence of black holes. New fundamental results discussed include the first confirmation of the Belinskii, Khalatnikov, and Lifschitz (BKL) conjecture for an asymptotically flat spacetime, where we find that the dynamics of a canonical test scalar field near a black hole singularity are dominated by terms with time derivatives. We also perform a numerical simulation of the gravitational collapse of a non-canonical scalar field showing that signals can escape black holes in the k-essence dark energy model and find numerical confirmation that the accretion of various scalar fields onto a black hole from generic initial conditions is stationary.

In the second part, we focus on the long distance behavior of perturbative quantum gravity. New results discussed include a proof of the cancellation of collinear divergences to all orders in the amplitudes of the theory as well as a characterization of all infrared divergent diagrams. In particular, we find that the only diagrams that can have soft divergences are ladder and crossed ladder diagrams, and that the only collinearly divergent diagrams are those with only three point vertices and no internal jet loops.

Also presented is a construction of a double copy relation between gravity and gauge theory amplitudes similar to that conjectured by Bern, Carrasco, and Johansson for the case where there is no hard momentum exchange in the scattering, which we find implies a squaring relation between the classical shockwave solutions of the two theories as well. Finally, the first calculation of a gravitational scattering amplitude through the next-to-leading eikonal order is performed. We find that this correction to the scattering amplitude exponentiates, and that these power corrections probe smaller impact parameters compared to the leading eikonal case. This suggests that researching such corrections in a general setting may yield evidence of black hole formation from the quantum theory.

Chapter 1
Introduction

The birth of modern research into gravitational theory is often attributed to Galileo, who found in the 17th century that all objects are accelerated equally by gravity regardless of their mass. Although physicists have continued to actively research gravitational theory to the present day, it is safe to say that we are far from unravelling all the mysteries of gravity. This is in contrast to the study of electromagnetism, which today is generally thought to be more or less completely understood even though in the 17th century it was in a similar stage of infancy with the invention of the first electrostatic generator by von Guericke.

That is not to say there have not been major advancements in our understanding of gravity since the days of Galileo. Around 50 years later Newton, in his theory of universal gravitation, postulated that every point mass in the universe is attracted to every other point mass through an inverse square law. This theory was not improved upon for over 200 years until Einstein introduced his theory of general relativity, which provides a relativistically invariant description of gravitation where gravity results from the curvature of space-time.

Einstein's theory of general relativity resulted in (among many other things) two major questions which are still being actively researched today. The first arises when one attempts to use general relativity to understand the cosmology of the observable universe. This leads to the Λ-Cold Dark Matter (ΛCDM) model, which is a standard cosmological model predicting that over 70% of the energy of the observable universe comes from a vacuum energy associated with empty space. However, the experimental value of this vacuum energy density is some 120 orders of magnitude smaller than what we would expect if we believe, as many physicists do, that quantum corrections to general relativity come in at the Planck scale (a classic review of this problem can be found in [1]). This is known as the cosmological constant problem, and its resolution remains one of the largest open questions in gravitational physics today. Further exacerbating this already large issue with the cosmological constant is the fact that the vacuum energy density must be fine-tuned to be over a 100 orders of magnitude smaller than the initial matter energy density. However, in the present era the vacuum energy density is roughly the same order as the matter energy

density. This is usually referred to as the cosmic coincidence problem.

Another major question that naturally arises when one considers general relativity is the matter of its quantization. The most obvious approach would be to take the Einstein-Hilbert action and naively attempt to treat it as a quantum field theory. However, this theory is nonrenormalizable and will generate an infinite number of unsupressed operators as we consider energies close to the Planck scale. Due to this nonrenormalizability, formulating a fully adequate unification of quantum mechanics and general relativity has remained an unsolved problem for many years.

This thesis is a compilation of selected studies concerning one of these areas of gravitational physics. In the first half of the dissertation we investigate the completely classical issue of dark energy. Specifically, we research the scalar field models that cosmologists have introduced to avoid the aforementioned cosmic coincidence problem associated with the cosmological constant. The classical portion of this thesis addresses the robustness of such models around black holes.

The particular scalar field model we focus on is k-essence, which avoids fine-tuning problems by having, instead of a cosmological constant, a dynamical scalar field that has classical attractor solutions which mimics vacuum energy density in the present era [2]. This model necessitates the existence of a non-canonical scalar field of which not much is known, including whether or not they can even be dynamically evolved over local scales. One feature of k-essence which is particularly interesting and worrisome is the fact that it has been shown to necessarily propagate superluminally if it is to avoid the cosmological constant problem [3]. However, this superluminality has been shown to not cause any issues concerning causality [4].

Given these non-standard features of k-essence a stringent test of the robustness of this theory is needed. As these models are usually studied under the standard cosmological assumption of the homogeneity and isotropy of the universe, such a test over local scales becomes even more desirable. Thus, in the classical portion of this thesis we describe whether or not the dynamical evolution of these fields are possible in extremely localized situations such as black holes. Due to the possibility of superluminal propagation of these fields, an additional motivation for studying the behavior of these models is the possibility of two horizons being created during black hole formation. As the gravitational fields involved in such an evolution are extremely large, perturbation theory is not useful and we will have to perform numerical simulations.

In order to illustrate the difficulty of studying the dynamical evolution of these scalar field models we describe the simplest case of the gravitational collapse of a canonical test scalar field in chapter 2. Even in this case no analytic solution is possible and numerical

simulations are necessary. Aside from introducing the type of methods we use in analyzing these types of systems, we also provide evidence that the equation of motion of the scalar field around a black hole singularity is dominated by terms with time derivatives.

We move onto the more difficult issue of the gravitational collapse of the k-essence scalar field in chapter 3. We show for a wide range of parameters, including those that allow for superluminal motion, that these non-canonical fields can be simulated over local scales and successfully form black holes, which was the primary motivation for this study. Although we show these black holes have two horizons during the collapse process, in order to show that one can maintain two horizons indefinitely, the accretion of these fields onto black holes must be studied.

This accretion is the subject of chapter 4 where we test whether or not these non-canonical scalar fields settle down to a stationary solution during this process. We provide evidence that separate horizons can be maintained indefinitely given cosmological boundary conditions; this implies that signals can be sent out of black holes using superluminal k-essence fields. We also show for various non-canonical fields that the end state of this dynamical accretion process matches the analytic solutions in the literature calculated under the assumption of stationarity.

The second half of the dissertation is focused on matters related to the quantization of general relativity. Although string theory is a promising candidate to describe this quantization at short distances, in this thesis we study long distance physics which can be more suitably studied using techniques from quantum field theory. This is due to the fact that using string theory techniques alone to extract useful information concerning scattering processes dominated by long distance physics is extremely difficult. On the other hand, the technology behind calculating scattering amplitudes by summing Feynman diagrams is by now highly developed. Therefore, the particular theory we will work with is perturbative quantum gravity, which can be arrived at by separating the flat classical portion of the metric from the quantum contribution and utilizing the background field method (an elegant description of this can be found in [5]).

It should be noted that while nonrenormalizability is still an issue in perturbative quantum gravity, the new operators generated by the renormalization procedure are suppressed by powers of the Planck mass. As long as the distance scales involved in the scattering are much larger than the Planck length we can reliably use this theory. Thus, field theoretic methods are perfectly suitable for our purposes as there are an ample amount of interesting phenomena that occur at long distances in quantum gravity.

Perturbative quantum gravity is especially intriguing to study in the kinematic regime where the momenta of the internal gravitons involved in the studied process are much lower

than the external momenta. Such processes are said to be in the eikonal regime. This regime is of interest because studies of ultrahigh-energy gravitational scattering have provided evidence that for a large range of impact parameters, including those relevant for black hole formation, string effects are actually subdominant to field theoretic gravitational-loop contributions [6]. Thus, the majority of the quantum gravity portion of this thesis will be focused on processes in the eikonal regime.

Another reason that perturbative quantum gravity is interesting to study is the recent proposal by Bern, Carrasco and Johannson (BCJ) that there is a double copy relation between gravity and gauge theories [7]. They conjecture that the numerator factors of the gauge theory amplitude can always be arranged so that they obey the kinematic analogue of the Jacobi identities satisfied by the corresponding color factors. If this arrangement is made, then gravity amplitudes can easily be calculated via their gauge counterpart by simply replacing the gauge theory color factors by their associated numerator. If this conjecture is true then this would make calculating gravitational amplitudes enormously easier, as well as imply a deep relationship between the two theories. Because of this recent development, studying quantum gravity using field theoretic methods is as fascinating as it has ever been.

As infrared divergences are among the most interesting long distance features of a generic field theory, we start with categorizing all of the collinear and soft divergences in perturbative quantum gravity in chapter 5. We find that soft divergences only occur for ladder and crossed ladder type diagrams, and that collinear divergences only occur in jets with only three point vertices and no internal loops. By using the Ward identity, we provide the first complete proof of the cancellation of these collinear divergences in gravitational amplitudes. This cancellation is unique to gravity and is not present in gauge theories such as quantum chromodynamics (QCD) and massless quantum electrodynamics (QED).

The cancellation of collinear divergences in gravitational amplitudes can have extremely interesting consequences. One example of the utility of this cancellation is detailed in chapter 6, where we study the relationship between gravity and gauge theory amplitudes in the eikonal limit. In this study, motivated by the BCJ conjecture, we prove a double copy relation at all loop orders between the gravitational amplitude and the part of the gauge theory amplitude where collinear divergences are known to cancel amongst themselves. In order to both check the validity of this relation and show how it can be used, we deduce from our relationship a similar squaring relation between the associated classical shockwaves of the two theories. This is the first known relation between non-vacuum classical solutions of gravity and gauge theory, and is only seen in the particular gauge picked out by our method of calculation.

Finally, in chapter 7 we present the first calculations of the gravitational $2 \to 2$ scalar

scattering amplitude at next-to-eikonal order. The main motivation is to investigate whether or not the factorization between long and short distance physics that occurs at leading eikonal order persists at the next order in the eikonal expansion. A breakdown of this factorization and the accompanying breakdown of perturbation theory is thought to be indicative of black hole formation. Although we find that this factorization persists at next-to-eikonal order, we do find evidence that these power corrections probe smaller distance scales, suggesting that further exploration of such corrections may yield direct evidence of black hole formation.

An investigation of classicalization, a proposed method of ultraviolet completing quantum field theories via the production of extended classical objects similar to black holes, is presented in appendix A. Supportive material pertaining to the main text can be found in appendices B through G. Additional discussion by the author on the material in this thesis can be found in the publications [8, 9, 10, 11, 12, 13]. Further research performed by the author which is not found in this dissertation can be found in [14].

Chapter 2

Gravitational Collapse of a Test Scalar Field

2.1 Introduction

In this chapter we will begin our analysis of the classical behavior of gravity with an investigation of gravitational collapse using test scalar fields. This example will serve to illustrate the difficulty in numerically simulating systems with black holes, as well as provide an interesting result in and of itself.

Note that this gravitational collapse process results in black holes which contain singularities. The collapse process is not described by an analytical solution of the field equations, and the gravitational field is so strong that perturbation theory is not helpful either. This is the main reason that we require numerical simulations. But even when simulations are used, the full process of gravitational collapse is not usually examined: some examine the formation of black holes but not singularities [15] while others examine singularities but not black holes [16, 17] [1]. In the case where black holes are examined, the simulation sometimes ends when the black hole forms [15]. In other cases the simulation goes on, but the interior of the black hole is excised [19]. In the case where the singularity is examined, one usually imposes periodic boundary conditions, which means that what is studied is singularity formation in a closed cosmology.

Apart from serving as an introduction to our analysis of the collapse of a k-essence scalar field, the main objective of this chapter is to investigate the longstanding conjecture due to Belinskii, Khalatnikov, and Lifschitz (BKL) as to the general behavior of spacetime singularities [20]. Essentially the BKL conjecture states that as a generic singularity is approached in a comoving coordinate system, the field equations will be dominated by terms containing derivatives with respect to time, and all other terms can be neglected. The BKL

[1] There has been some recent progress in numerical simulations capable of examining the formation of both singularities and black holes in [18]

conjecture has been verified by numerical simulations [16, 17] for the case of singularity formation in a closed cosmology. Since BKL dynamics are local, it seems likely that the BKL conjecture is also true in the case of singularity formation inside a black hole (at least for part of the singularity, see [21] for a conjecture about another part of the singularity). However, one would like to verify the BKL conjecture by a treatment of the singularities inside black holes.

In order to do this we will utilize one of the earliest analytic studies of gravitational collapse, that of Oppenheimer and Snyder [22]. This model was capable of examining both the singularity and the black hole. In [22] the collapse process is modeled as a spherically symmetric spacetime containing two parts: the Schwarzschild metric on the outside and a Friedmann-Robertson-Walker (FRW) spacetime with non-relativistic matter (dust) on the inside. The Schwarzschild and FRW spacetimes have two different coordinate systems which must be matched along the boundary. This difficulty can be overcome [23] through a coordinate transformation which allows the full spacetime to be covered by a single coordinate system. However, a more serious difficulty is that pressureless dust is not a good model of how matter behaves in the extreme conditions of singularity formation. Thus, the properties of dust singularities tell us very little about the properties of generic singularities.

Ideally, one would like to check the BKL conjecture by treating the gravitational collapse of a more realistic matter model, like a scalar field, using a single coordinate system that follows the formation of the black hole and the singularity. As a preliminary step in that direction, we perform numerical simulations of the behavior of a test massive scalar field on the spacetime of [22] using the coordinates of [23]. The relevant equations and numerical methods are described in section 2.2, while results are presented and discussed in section 2.3.

2.2 Methods

In order to cover the entire spacetime using a single coordinate system, we will use the fact that a spherically symmetric spacetime can be put in the form [24, 25]

$$ds^2 = -(1-\psi^2)dt^2 + 2\psi dt dr + r^2(d\theta^2 + \sin^2\theta d\varphi^2) \tag{2.1}$$

Here, r is the usual area coordinate, while t is a time coordinate chosen so that $\nabla^a t \nabla_a t = -1$. We will now show how to put the Schwarzschild and FRW metrics in this form. The

Schwarzschild metric in the usual coordinates is

$$ds^2 = -\left(1 - \frac{2M}{r}\right) d\tilde{t}^2 + \left(1 - \frac{2M}{r}\right)^{-1} dr^2 + r^2(d\theta^2 + \sin^2\theta d\varphi^2) \tag{2.2}$$

We wish to express $\tilde{t}$ as a function of t and r so that the metric takes the form of (2.1). Some straightforward but tedious algebra shows that the expression

$$\tilde{t} = t - 2\left[\sqrt{2Mr} + M \ln\left(\frac{\sqrt{r} - \sqrt{2M}}{\sqrt{r} + \sqrt{2M}}\right)\right] \tag{2.3}$$

yields a metric of the form of (2.1) with

$$\psi = \sqrt{\frac{2M}{r}} \tag{2.4}$$

Let us now move on to the spatially flat dust FRW spacetime, which has the metric

$$ds^2 = -d\tilde{t}^2 + a^2(\tilde{t})(d\tilde{r}^2 + \tilde{r}^2[d\theta^2 + \sin^2\theta d\varphi^2]) \tag{2.5}$$

with the scale factor a given by

$$a = K\tilde{t}^{2/3} \tag{2.6}$$

where K is a constant. We wish to perform a coordinate transformation that gives this metric the form of (2.1). Comparing the angular parts of the metric, it is clear that we must have $r = a\tilde{r}$. It is then straightforward to show that with $\tilde{t} = t$ the metric of (2.5) takes the form of (2.1) with

$$\psi = -\frac{2r}{3t} \tag{2.7}$$

The collapse takes place at negative times and is complete at $t = 0$. The boundary between the interior FRW part of the spacetime and the exterior Schwarzschild part is given by $r = r_b(t)$, for some function $r_b(t)$. Since the metric, and therefore ψ must be continuous across the boundary, we have

$$r_b = \left(\tfrac{9}{2}Mt^2\right)^{1/3} \tag{2.8}$$

Thus the spacetime metric is given by (2.1), with ψ given by (2.4) for $r \geq r_b$ and ψ given by (2.7) for $r \leq r_b$.

We wish to simulate the Klein-Gordon equation on this spacetime assuming spherical symmetry for the scalar field. That is, we want a scalar field $\phi(r, t)$ that satisfies

$$\nabla_a \nabla^a \phi - m^2 \phi = 0 \tag{2.9}$$

For a metric of the form of (2.1) the Klein-Gordon equation for a spherically symmetric scalar field becomes

$$\begin{aligned}\partial_t\partial_t\phi &= 2\psi\partial_r\partial_t\phi + (\partial_t\psi)(\partial_r\phi) + (\partial_r\psi)(\partial_t\phi) + \frac{2\psi}{r}\partial_t\phi \\ &+ (1-\psi^2)\frac{1}{r^2}\partial_r(r^2\partial_r\phi) - 2\psi(\partial_r\psi)\partial_r\phi - m^2\phi \end{aligned} \tag{2.10}$$

For the numerical method used, we need to put this equation in first order form: we introduce the quantities P and S given by

$$P \equiv \partial_t\phi \tag{2.11}$$

$$S \equiv \partial_r\phi \tag{2.12}$$

From the definitions of P and S it immediately follows that

$$\partial_t\phi = P \tag{2.13}$$

$$\partial_t S = \partial_r P \tag{2.14}$$

while (2.10) becomes

$$\begin{aligned}\partial_t P &= 2\psi\partial_r P + (\partial_t\psi)S + (\partial_r\psi)P + \frac{2\psi}{r}P \\ &+ (1-\psi^2)\frac{1}{r^2}\partial_r(r^2 S) - 2\psi(\partial_r\psi)S - m^2\phi \end{aligned} \tag{2.15}$$

The equations to be evolved are equations (2.13-2.15). We evolve using finite differences, where each scalar $f(r)$ is represented by the quantities $f_i = f((i-1)\Delta r)$. Spatial derivatives are evaluated using standard centered differences, that is

$$\partial_r f \to \frac{f_{i+1} - f_{i-1}}{2\Delta r} \tag{2.16}$$

However, to maintain accuracy near the origin, the quantity $r^{-2}\partial_r(r^2 S)$ requires special treatment. We define S_+ and S_- by $S_+ = (S_{i+1} + S_i)/2$ and $S_- = (S_i + S_{i-1})/2$. Correspondingly we define $r_+ = r_i + (\Delta r/2)$ and $r_- = r_i - (\Delta r/2)$. Then we use the finite difference

$$\frac{1}{r^2}\partial_r(r^2 S) \to \frac{3}{r_+^3 - r_-^3}\left(r_+^2 S_+ - r_-^2 S_-\right) \tag{2.17}$$

The quantity ψ and its derivatives are evaluated analytically using the formulas in (2.4) and (2.7). Equations (2.13-2.15) are evolved using a three step iterated Crank-Nicholson method

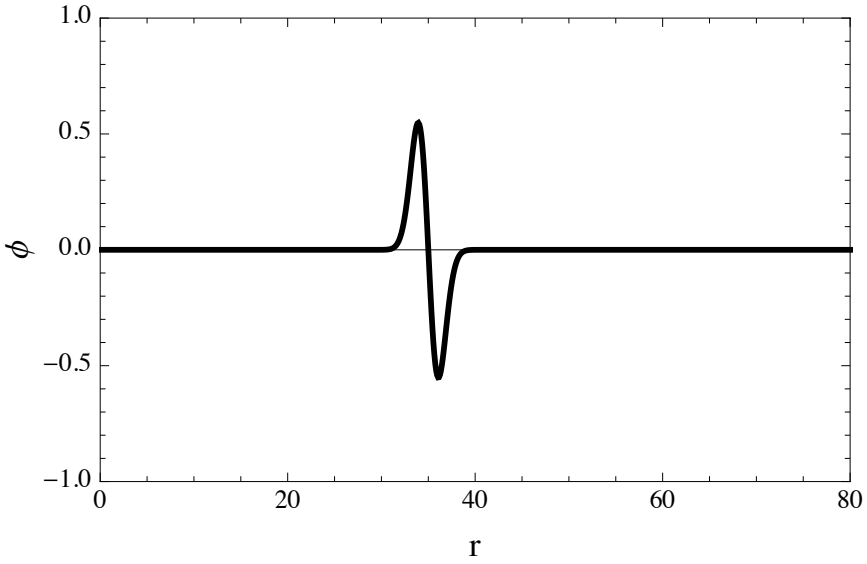

Figure 2.1 ϕ *vs* r at the initial time $t_0 = -20$

[26] with Kreiss-Oliger dissipation [27].

At the origin, (gridpoint $i = 1$) smoothness requires that S vanish and that ϕ and P have vanishing derivative with respect to r. We implement this condition as

$$\phi_1 = (4\phi_2 - \phi_3)/3 \tag{2.18}$$

$$S_1 = 0 \tag{2.19}$$

$$P_1 = (4P_2 - P_3)/3 \tag{2.20}$$

At the outer boundary, we impose the condition that ϕ, S and P all vanish.

2.3 Results and Discussion

In the simulations, let N be the number of gridpoints and $r_{\max}$ be the maximum value of r. We then have $\Delta r = r_{\max}/(N-1)$. $N = 800$ was used for the simulations resulting in figures 2.1-2.3. $N = 16000$ was used for the simulations resulting in figures 2.4-2.11. We choose initial data for the scalar field at a time t_0 to take the form $P = 0$ and

$$\phi = -2\frac{r - r_0}{\sigma^2} \exp\left(\frac{-(r - r_0)^2}{\sigma^2}\right) \tag{2.21}$$

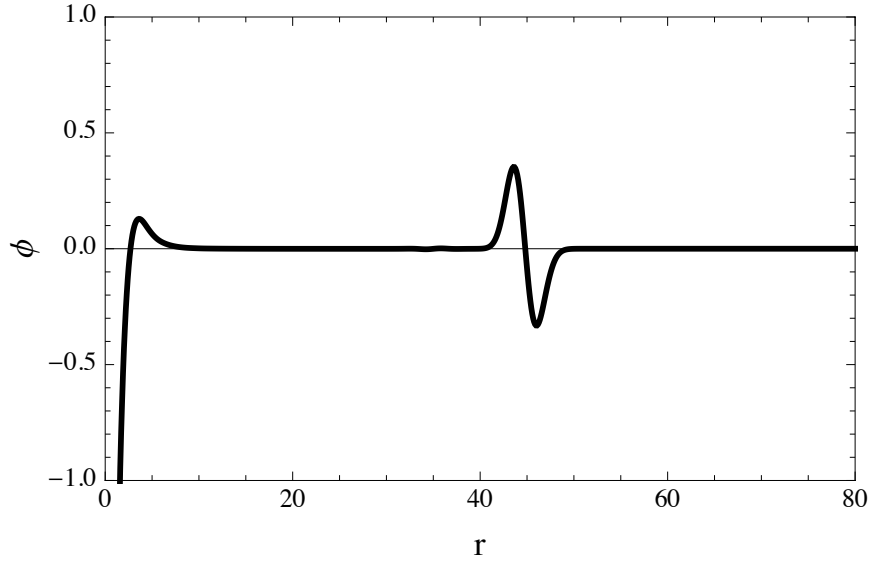

Figure 2.2 ϕ *vs* r for $m = 0$ at $t = -0.23$

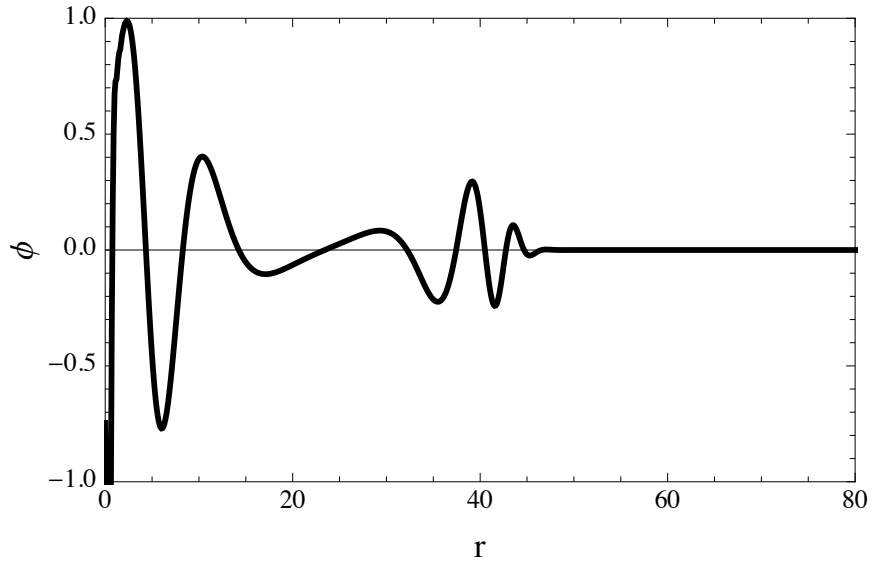

Figure 2.3 ϕ *vs* r for $m = 1$ at $t = -0.23$

with S given by the derivative of this expression. Here, r_0 and σ are constants. For all the results displayed, the parameters are $t_0 = -20$, $r_{\max} = 80$, $r_0 = 35$, $\sigma = 1.5$, and $M = 5$ where M is the mass of the Schwarzschild black hole. This initial configuration of the scalar field is shown in figure 2.1. We run the simulations to a time near the singularity. Figures 2.2 and 2.3 show the configuration of the scalar field near this final time. Both figures are for $t = -0.23$ with $m = 0$ for figure 2.2 and $m = 1$ for figure 2.3. The initial scalar field can be thought of as a linear combination of a left mover and a right mover. The right mover escapes from the black hole, while the left mover plunges towards it. Some part of the left mover scatters off of the black hole, while another part is captured and approaches the singularity.

We are particularly interested in finding the behavior of the scalar field as the singularity is approached. In our coordinate system, the singularity is approached as $t \to 0$ but only in the FRW portion of the spacetime. To examine the scalar field behavior near the singularity, we plot the scalar field at three different times near $t = 0$ and deduce a trend from those plots. The scalar field ϕ is plotted as a function of r in a small region near $r = 0$ for the times -0.02, -0.01 and -0.005 for the $m = 0$ case in figure 2.4 and for the $m = 1$ case in figure 2.5. It is clear that the trend is that as the singularity is approached, the scalar field gets a larger amplitude and a steeper profile. To see whether this behavior can be understood quantitatively, we turn to the BKL conjecture: the claim that as a generic singularity is approached in a comoving coordinate system, the field equations will be dominated by terms containing derivatives with respect to time, and all other terms can be neglected. To apply this conjecture, we consider the Klein-Gordon equation (2.9) in the untransformed FRW metric and coordinates given by (2.5) and (2.6). Keeping only terms containing time derivatives, we find

$$\tilde{t}^{-2}\partial_{\tilde{t}}(\tilde{t}^2\partial_{\tilde{t}}\phi) = 0. \tag{2.22}$$

The general solution of this equation is

$$\phi = \tilde{t}^{-1}A(\tilde{r}) + B(\tilde{r}) \tag{2.23}$$

for some functions $A(\tilde{r})$ and $B(\tilde{r})$. In particular, the BKL conjecture leads us to expect that as the singularity is approached, $\tilde{t}\phi$ should approach a function of $\tilde{r}$. Note, that expressed in terms of the t, r coordinates of our simulation, we have $\tilde{t} = t$ and $\tilde{r} = K^{-1}t^{-2/3}r$. Thus, we are led to expect that as the singularity is approached, if we plot $t\phi$ *vs* $t^{-2/3}r$ the plots should approach some limiting profile as $t \to 0$. To see whether that expectation is realized, such plots are given in figure 2.6 for $m = 0$ and 2.7 for $m = 1$. These figures are consistent with $t\phi$ approaching a limit as the singularity is approached. However, in order to be more

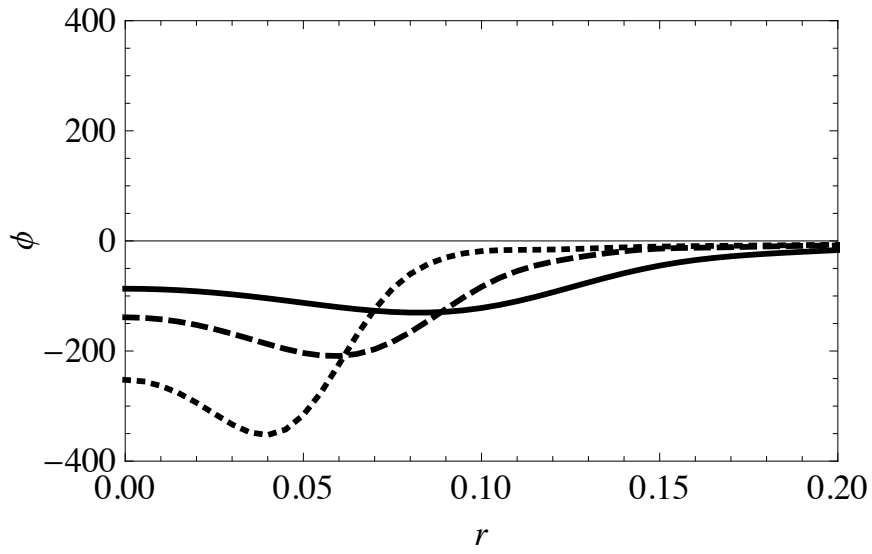

Figure 2.4 ϕ *vs* r for $m = 0$ at $t = -0.02$ (solid), -0.01 (dashed) and -0.005 (dotted)

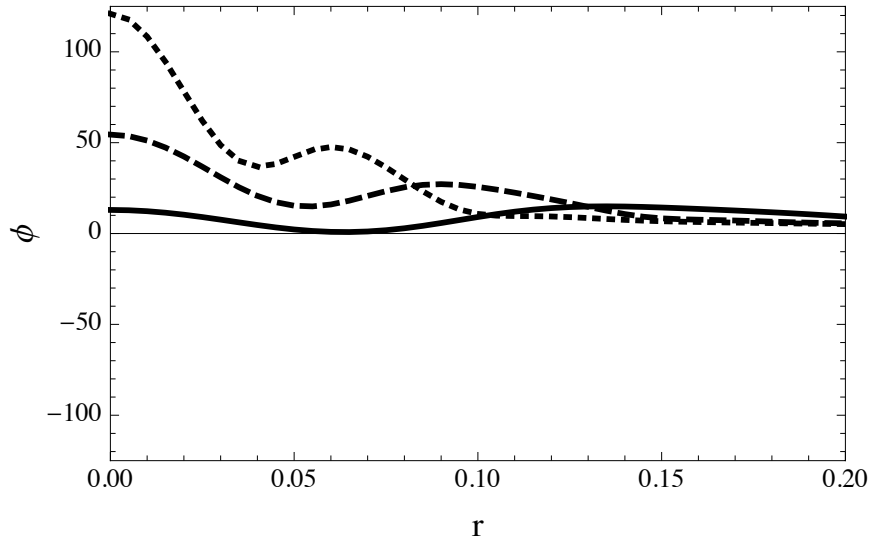

Figure 2.5 ϕ *vs* r for $m = 1$ at $t = -0.02$ (solid), -0.01 (dashed) and -0.005 (dotted)

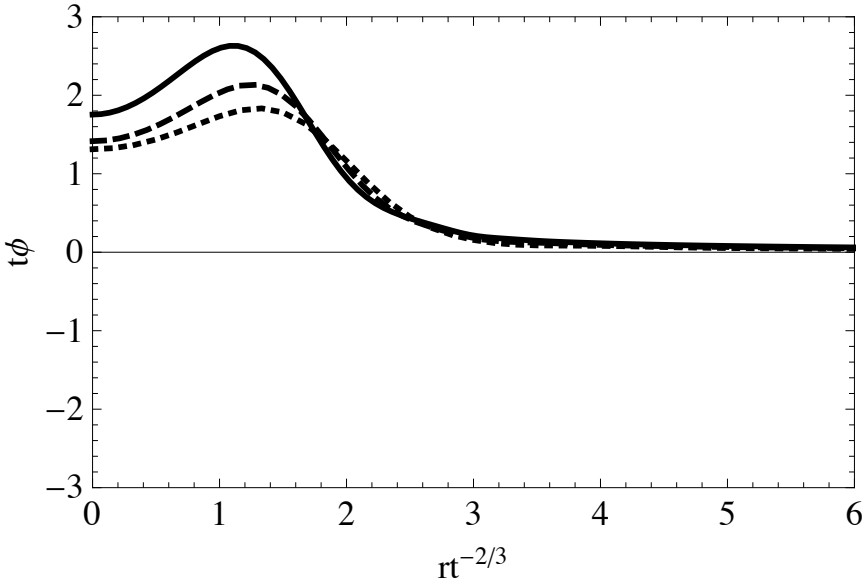

Figure 2.6 $t\phi$ *vs* $t^{-2/3}r$ for $m = 0$ at $t = -0.02$ (solid), -0.01 (dashed) and -0.005 (dotted)

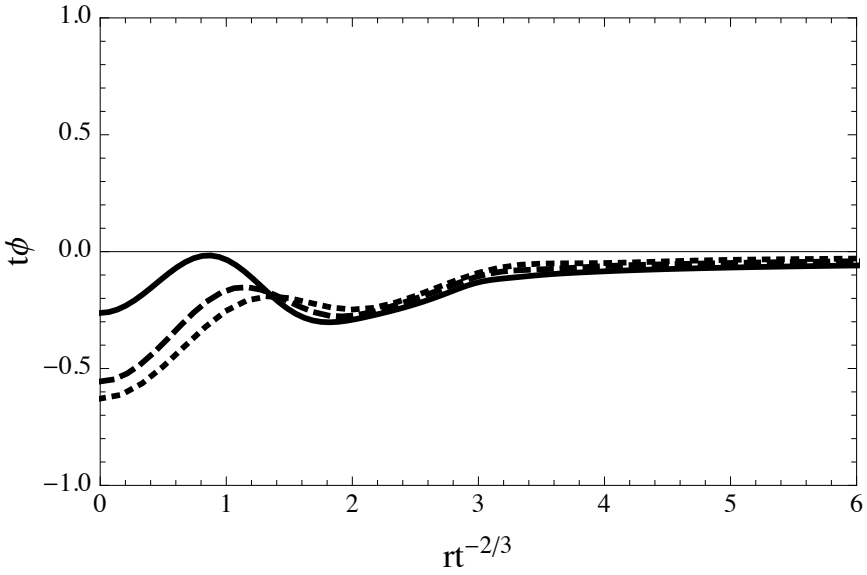

Figure 2.7 $t\phi$ *vs* $t^{-2/3}r$ for $m = 1$ at $t = -0.02$ (solid), -0.01 (dashed) and -0.005 (dotted)

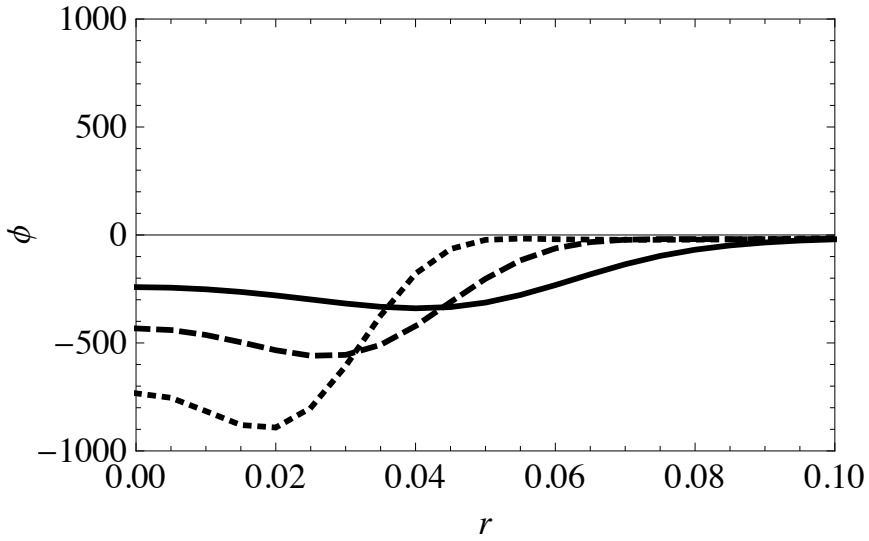

Figure 2.8 ϕ *vs* r for $m = 0$ at $t = -0.0055$ (solid), -0.0030 (dashed) and -0.0017 (dotted)

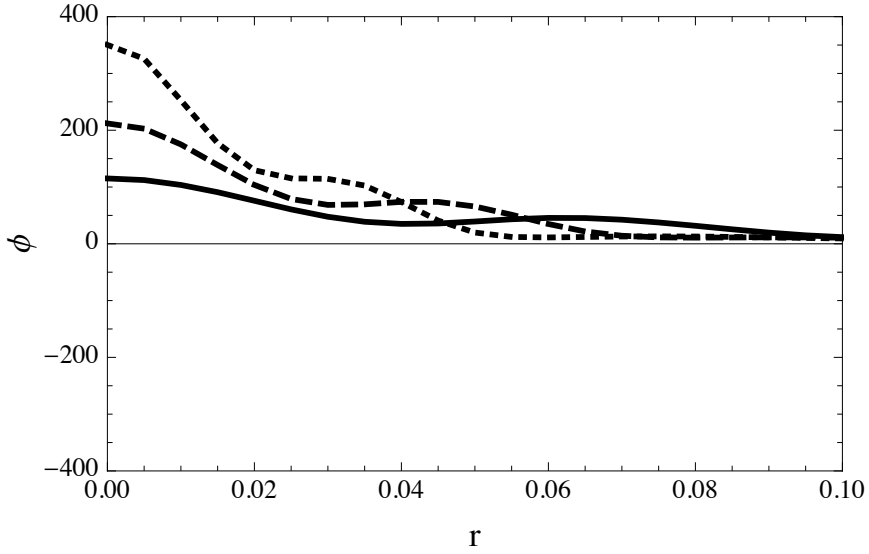

Figure 2.9 ϕ *vs* r for $m = 1$ at $t = -0.0055$ (solid), -0.0030 (dashed) and -0.0017 (dotted)

definite, we need to approach the singularity more closely. The results of simulations which show the scalar field at times closer to the singularity are shown in figures 2.8-2.11. Here figure 2.8 shows ϕ *vs* r for $m = 0$ and the times -0.0055, -0.0030, and -0.0017. Figure 2.9 shows ϕ *vs* r at the same times for the $m = 1$ case. The corresponding rescaled quantities, that is $t\phi$ *vs* $t^{-2/3}r$ are shown in figure 2.10 for $m = 0$ and in figure 2.11 for $m = 1$.

It is clear from figures 2.10 and 2.11 that $t\phi$ approaches a limit as the singularity is approached. Since this is just what one would expect from the BKL conjecture, our simulations

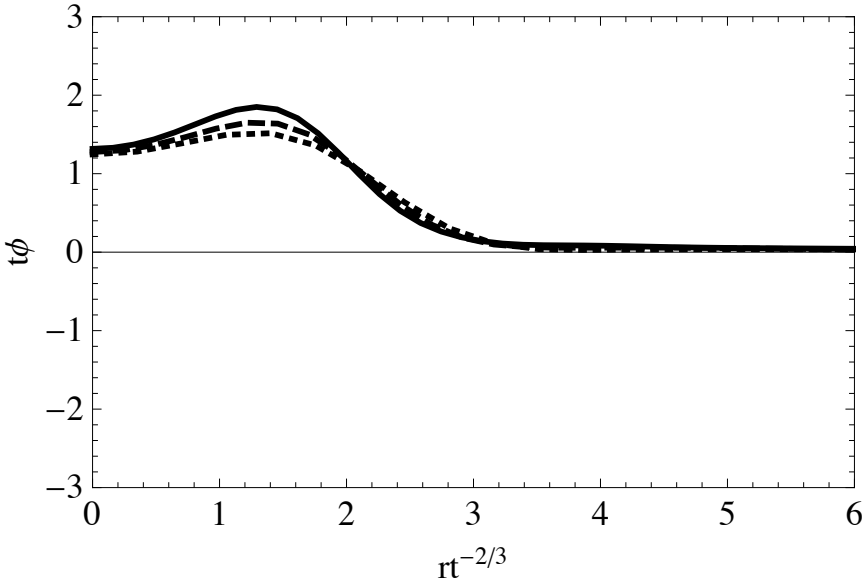

Figure 2.10 $t\phi$ *vs* $t^{-2/3}r$ for $m = 0$ at $t = -0.0055$ (solid), -0.0030 (dashed) and -0.0017 (dotted)

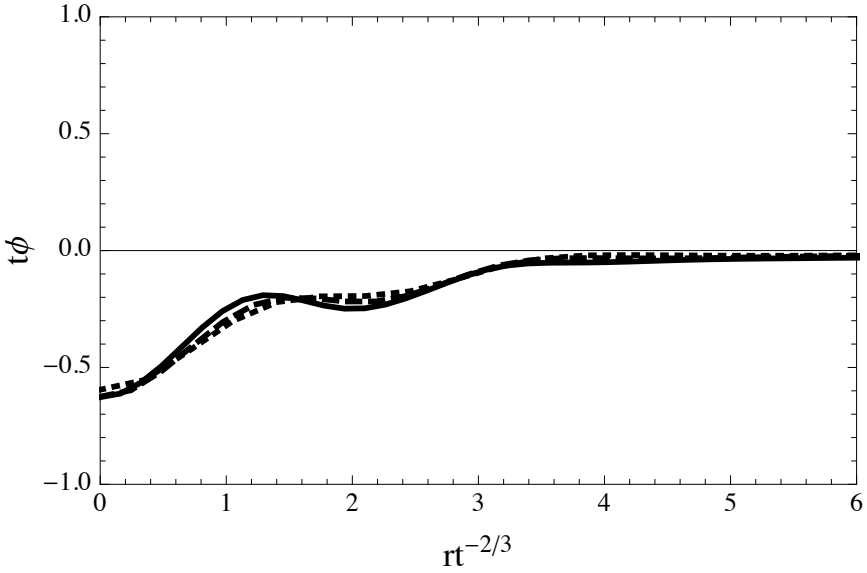

Figure 2.11 $t\phi$ *vs* $t^{-2/3}r$ for $m = 1$ at $t = -0.0055$ (solid), -0.0030 (dashed) and -0.0017 (dotted)

lend support to the notion that the BKL conjecture holds, not only in the extensively studied case of closed cosmologies, but also in the more physically interesting case of asymptotically flat spacetimes. To explore this issue further, it would be helpful to go beyond the case of a test scalar field on a background spacetime. In particular, one could treat the collapse of a self-gravitating scalar field using the method of [18] and see whether the singularity produced in the collapse satisfies the BKL conjecture.

Chapter 3

Gravitational Collapse of a k-essence Scalar Field

3.1 Introduction

Now that we have seen in the previous chapter how to perform numerical simulations of a test scalar field in a gravitationally collapsing spacetime, let us move on to the more challenging case of simulating the full gravitational collapse of a k-essence scalar field. As mentioned in chapter 1, dynamical scalar fields can mimic a cosmological constant in the present era, avoiding the need for fine tuning of around 120 orders in magnitude. k-essence [2, 28] is a particularly attractive model as it not only addreses the cosmological constant problem but also the coincidence problem: why does the accelerated expansion of the universe coincide with the onset of matter domination?

However, k-essence models necessitate the existence of a scalar field with non-standard kinetic terms that allows for the field to have negative pressure once the matter-dominated era begins. As the robustness of these models is not well understood, it is desirable to simulate the behavior of these scalar fields in extreme environments such as gravitational collapse. Compared to the previous simulation, the difficulty increases in two avenues since we will be simulating more complicated non-canonical scalar fields and because the fields will be undergoing a fully consistent gravitational collapse with back reaction taken into account.

It has been shown that if k-essence is to solve the coincidence problem, then fluctuations of the k-essence field must necessarily propagate superluminally at some point [3, 29]. However, it has been argued that this superluminality is physically acceptable since causality is not violated [4].

This possibility of superluminal propagation is another reason it is interesting to ask how a k-essence field would act during gravitational collapse. It has been found that the stationary solution describing k-essence scalar field accretion into a background Schwarzschild black

hole allows for the existence of two horizons, one corresponding to the fluctuations of the k-essence scalar field and the other being the normal light horizon [31]. This is interesting as the existence of two horizons also occurs in other theories that allow superluminal motion [32, 33], as well as for the case of general irrotational hydrodynamics [34]. It is possible that the stationary solution allowing for the existence of two horizons may be avoided kinematically given reasonable initial conditions. It is also possible that once back reactions of the scalar field on the metric are considered the two horizons may reduce to one. Another possibility is that gravitational collapse results not in the formation of a black hole but a naked singularity.

In order to see which of the above mentioned possibilities are realized during the gravitational collapse of a k-essence scalar field, one can perform numerical simulations of this process. Such simulations have often been done before for an ordinary scalar field [15, 35] and the methods used can be modified and generalized to treat k-essence. In this particular study, we will numerically simulate the self-consistent gravitational collapse of spherically symmetric scalar fields described by several different k-essence Lagrangians. The knowledge of what k-essence models allow for what type of horizons may help restrict the parameter space of acceptable k-essence models. Numerical simulations may also indicate whether or not there are any unique experimental signatures associated with the creation of a black hole from a k-essence scalar field.

The equations and numerical methods used are described in section 3.2 and in appendix B. Results are presented in section 3.3 and conclusions discussed in section 3.4.

3.2 Methods

The action for self gravitating k-essence is

$$I = \int \sqrt{g}\, d^4x \left(\frac{^{(4)}R}{2\kappa} + \mathcal{L}(X) \right) \tag{3.1}$$

Here $^{(4)}R$ is the spacetime scalar curvature, $\kappa = 8\pi G$ where G is Newton's gravitational constant, and $X = -\frac{1}{2}\nabla^a\phi\nabla_a\phi$ where ϕ is the k-essence scalar field. Varying the action with respect to the metric yields the Einstein field equation

$$G_{ab} = \kappa T_{ab} \tag{3.2}$$

where G_{ab} is the Einstein tensor, and the k-essence stress-energy tensor T_{ab} is given by

$$T_{ab} = \mathcal{L}_X \nabla_a \phi \nabla_b \phi + \mathcal{L} g_{ab} \tag{3.3}$$

Here, we introduce the shorthand $\mathcal{L}_X$ to mean $d\mathcal{L}/dX$ (and later we will also use $\mathcal{L}_{XX}$ to mean $d^2\mathcal{L}/dX^2$). Varying the action with respect to the k-essence scalar field ϕ yields the k-essence equation of motion

$$\tilde{g}^{ab} \nabla_a \nabla_b \phi = 0 \tag{3.4}$$

Here $\tilde{g}^{ab}$ is an effective inverse metric associated with the k-essence scalar field and is given by

$$\tilde{g}^{ab} = \mathcal{L}_X g^{ab} - \mathcal{L}_{XX} \nabla^a \phi \nabla^b \phi \tag{3.5}$$

We perform numerical simulations of equations (3.2) and (3.4) in the case of spherical symmetry. For an ordinary scalar field, such simulations are often performed using polar-radial coordinates [15]. Here the radial coordinate is chosen to be the usual area radius, while the time coordinate is chosen to be orthogonal to the radial coordinate. However, polar-radial coordinates only last until the first trapped surface forms. This would not be suitable for a simulation of k-essence gravitational collapse because k-essence travels faster than light and thus is not trapped by ordinary trapped surfaces but instead by the trapped surfaces of the effective metric of (3.5). Thus a k-essence black hole has not yet formed when the first trapped surface forms and a simulation using polar-radial coordinates stops. Instead, we use a different method with a set of coordinates that includes a region within the black hole horizon. This method uses maximal slicing, and a radial coordinate based on length rather than area, and is described in detail in appendix B.

Another complication of k-essence collapse has to do with the surfaces of constant time. In an evolution of the Einstein field equations, the surfaces of constant time must be spacelike. That is, we must have $g^{tt} < 0$. For an ordinary scalar field, this condition is also enough to render the evolution of the scalar field well posed. However, k-essence evolves in an effective metric whose light cones are different from those of the spacetime metric. In order that the surfaces of constant time are also Cauchy surfaces for the k-essence field, we must have $\tilde{g}^{tt} < 0$. In the simulations, it is sometimes the case that $\tilde{g}^{tt} \to 0$ without any singularity forming and sometimes even without the formation of any trapped surface. In this case we are forced to stop the simulation at that point without obtaining a clear answer as to the outcome of the collapse process. This also suggests the disturbing possibility that the light cones of the k-essence field could tip so much that no surface could be timelike for both the metric and the k-essence field. In that case, the theory itself would cease to be well

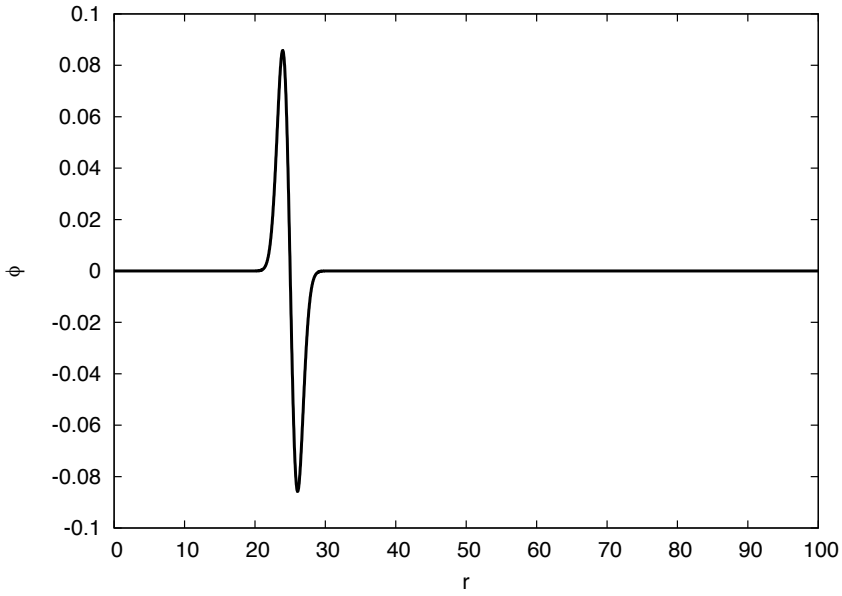

Figure 3.1 ϕ *vs* r at the initial time $t = 0$ for $A = 0.15$

defined.

In any case, our results are obtained by choosing a variety of k-essence Lagrangians $\mathcal{L}$ and a variety of initial data, and then evolving with the maximal slicing method, and noting the outome of the collapse process.

3.3 Results

We now present the results of the collapse simulations. Much like in the case of the previous chapter we choose the scalar field to initially have $\partial_t \phi = 0$ and the form:

$$\phi = -2A \frac{r - r_0}{\sigma^2} \exp(\frac{-(r - r_0)^2}{\sigma^2}) \tag{3.6}$$

where A, σ, and r_0 are constants. For all results and figures shown we used the values $\sigma = 1.5$, and $r_0 = 25$ (see figure 3.1 for which $A = 0.15$).

3.3.1 Sound Horizon Lagrangian

We first consider a k-essence model proposed in [30, 31] with a Lagrangian density given by:

$$\mathcal{L}(X) = \alpha^2 \left[\sqrt{1 + \frac{2X}{\alpha^2}} - 1 \right] - \Lambda \tag{3.7}$$

We chose $\Lambda = 0$ for all of our simulations. In [31] it was found that when there is a steady flux of scalar field described by this Lagrangian falling into a Schwarszschild black hole, there exists a stationary solution which can allow scalar field signals to escape from the light horizon. This is because the k-essence scalar field can propagate at speeds different from that of the speed of light. Thus there is a sound horizon associated with the scalar field which can differ from the traditional light horizon. When this sound horizon is located within the light horizon, signals can escape the black hole.

Before presenting the results, it is helpful to recall how this sort of initial data would evolve for an ordinary (non k-essence) massless free scalar field, both without and with gravity. For an ordinary non-gravitating scalar field, initial data of the type given in (3.6) separates into an outgoing pulse and an ingoing pulse. The ingoing pulse undergoes interference in a region near $r = 0$ and becomes an outgoing pulse, so that at sufficiently late times the scalar field consists of two outgoing pulses. For an ordinary gravitating scalar field, when the amplitude A is sufficiently small, the self-gravity of the field is weak, and the behavior is essentially that of a non-gravitating scalar field. However, when A is sufficiently large, as the ingoing pulse nears the center, it becomes trapped by its own self-gravity and forms a black hole.

For the model of (3.7) when α^2 is large compared to X, the Lagrangian approaches that of a massless free scalar field. Therefore we would expect that for large enough α we would get the same sort of behavior as for an ordinary (non k-essence) scalar field. To see whether this expectation is right, we performed simulations with $\alpha = 1.0$ and with $A = 0.05$ and $A = 0.15$. The result of the simulation with $A = 0.05$ is shown in figure 3.2. Here the scalar field ϕ is graphed as a function of r at time $t = 45$. In this amount of time the initially outgoing pulse has progressed to steadily larger r with approximately $1/r$ falloff in amplitude, while the initially ingoing pulse has undergone interference near the center and become an outgoing pulse which has moved away from the center undergoing its own approximately $1/r$ falloff in amplitude.

In contrast, figure 3.3 shows the result of the simulation with $A = 0.15$ (and $\alpha = 1.0$). Again the scalar field ϕ is graphed as a function of r at time $t = 45$. Once again, the outgoing pulse has progressed to steadily larger r with a corresponding falloff in amplitude.

However, now the ingoing pulse has not become outgoing and instead remains trapped near the center by its own self-gravity. Indeed we would expect the ingoing pulse to not merely "remain trapped" but rather to undergo complete gravitational collapse and form a singularity at the center of a black hole. The fact that it has not done so in this simulation is an artifact (and one of the main features) of the maximal slicing method. In maximal slicing, the lapse function N becomes small in regions that are strongly gravitating. This slows the evolution down in those regions and prevents the simulation from reaching the singularity (which would force the simulation to halt). Indeed such a "collapse of the lapse" is usually taken as an indication of black hole formation. This phenomenon is illustrated in figure 3.4 where the lapse for this simulation is plotted.

Nonetheless, we would like a more precise indication of black hole formation. In general relativity, such an indication is provided by the formation of a marginally outer trapped surface. Here a two dimensional surface has an outgoing null geodesic normal vector ℓ^a and the surface is marginally outer trapped if $\nabla_a \ell^a = 0$. This condition simplifies considerably in the case of spherical symmetry, where it becomes equivalent to $\ell^a \nabla_a R = 0$ where R is the area radius (*i.e.* $4\pi R^2$ is the area of the spheres of symmetry). That is, we want to know whether there is an outgoing vector ℓ^a such that $g_{ab}\ell^a\ell^b = 0$ and $\ell^a \nabla_a R = 0$. For the coordinate system we use (*i.e.* (B.1)) we find after some straight forward algebra that this condition becomes:

$$\frac{1}{2} R K^r_r + R' = 0 \tag{3.8}$$

Thus, to check for the presence of a marginally outer trapped surface (and thus the formation of a black hole) we only need to compute the left hand side of (3.8) and see whether it vanishes somewhere.

The condition of (3.8) works for the gravitational collapse of an ordinary scalar field. However, since k-essence can travel faster than light, we want to know not only whether an object forms that can trap light, but also whether an object forms that can trap k-essence. Since k-essence satisfies a wave equation using the effective inverse metric $\tilde{g}^{ab}$, it follows that the direction of propagation of k-essence is a vector that is null with respect to the effective metric $\tilde{g}^{-1}_{ab}$ which satisfies $\tilde{g}^{-1}_{ab}\tilde{g}^{bc} = \delta^c{}_a$. Straightforward calculation using (3.5) then shows that

$$\tilde{g}^{-1}_{ab} = \frac{1}{\mathcal{L}_X} g_{ab} + c_s^2 \frac{\mathcal{L}_{XX}}{\mathcal{L}_X^2} \nabla_a \phi \nabla_b \phi \tag{3.9}$$

where

$$c_s = \sqrt{\frac{\mathcal{L}_X}{\mathcal{L}_X + 2X\mathcal{L}_{XX}}} \tag{3.10}$$

is the speed of propagation of the k-essence waves for this model for the case where the

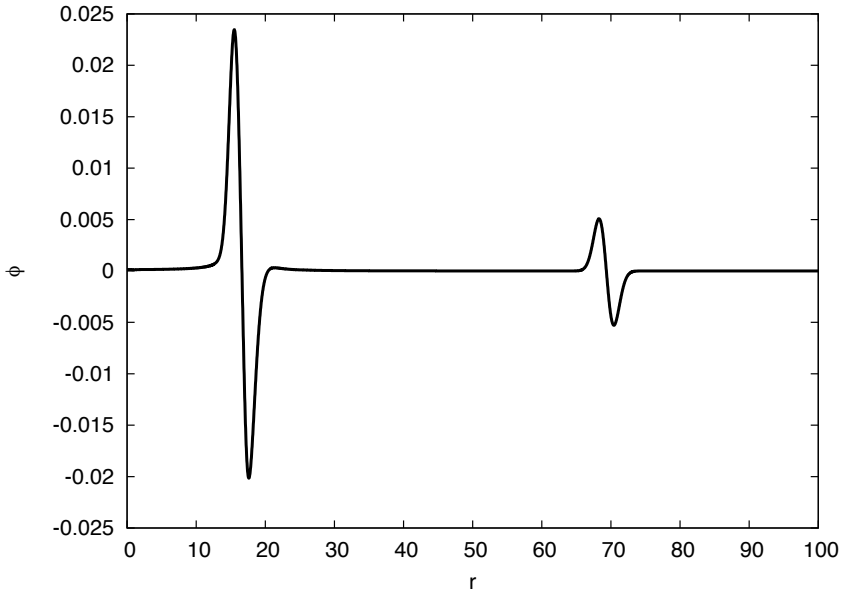

Figure 3.2 ϕ *vs* r at time $t = 45$ for $A = 0.05$ and $\alpha = 1.0$

k-essence field gradient is timelike. (we will also refer to c_s as the sound speed). Thus the condition for a sound horizon is just that for a light horizon, but with the effective metric replacing the metric. That is, the existence of an outgoing vector ℓ^a satisfying $\tilde{g}^{-1}_{ab}\ell^a\ell^b = 0$ and $\ell^a\nabla_a R = 0$. Some straightforward algebra using (B.1) then shows that this condition is

$$\begin{aligned} &\frac{1}{2}RK^r{}_r(\mathcal{L}_X + c_s^2\mathcal{L}_{XX}S^2) \\ &+R'(\sqrt{\mathcal{L}_X(\mathcal{L}_X - 2Xc_s^2\mathcal{L}_{XX})} - c_s^2\mathcal{L}_{XX}PS) = 0 \end{aligned} \tag{3.11}$$

In summary: the condition for a light horizon is the vanishing of the left hand side of (3.8) while for a sound horizon it is the vanishing of the left hand side of (3.11). We will refer to the left hand side of these equations with the symbol q in figures 3.5, 3.6, 3.7 and 3.8.

In figure 3.5 the left hand sides of (3.8) (light horizon, solid line) and (3.11) (sound horizon, dotted line) are plotted at a time shortly after the sound horizon first forms ($t = 38.8$). Note that each curve crosses zero more than once; however it is the outermost crossing for each curve that is the horizon. Also note that the sound horizon is inside the light horizon, as we would expect for k-essence that travels faster than light. A similar comparison done at $t = 45$ shows that both horizons have merged. In physical terms, the reason for this merger is that eventually all scalar field either falls into the black hole or escapes from it. Thus at sufficiently late times there is no scalar field on the horizon, which thus makes the k-essence effective metric equal to the spacetime metric in that region. Thus, the two horizons very

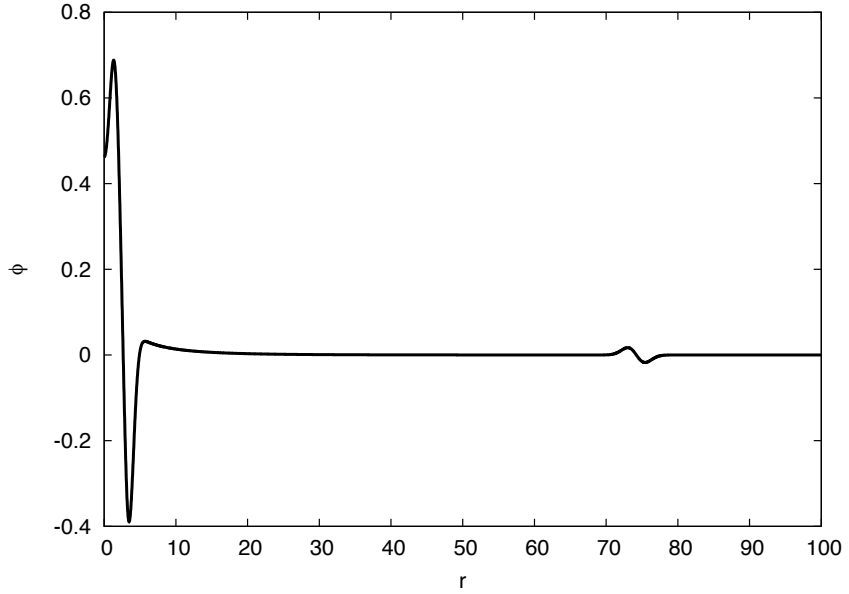

Figure 3.3 ϕ *vs* r at time $t = 45$ for $A = 0.15$ and $\alpha = 1.0$

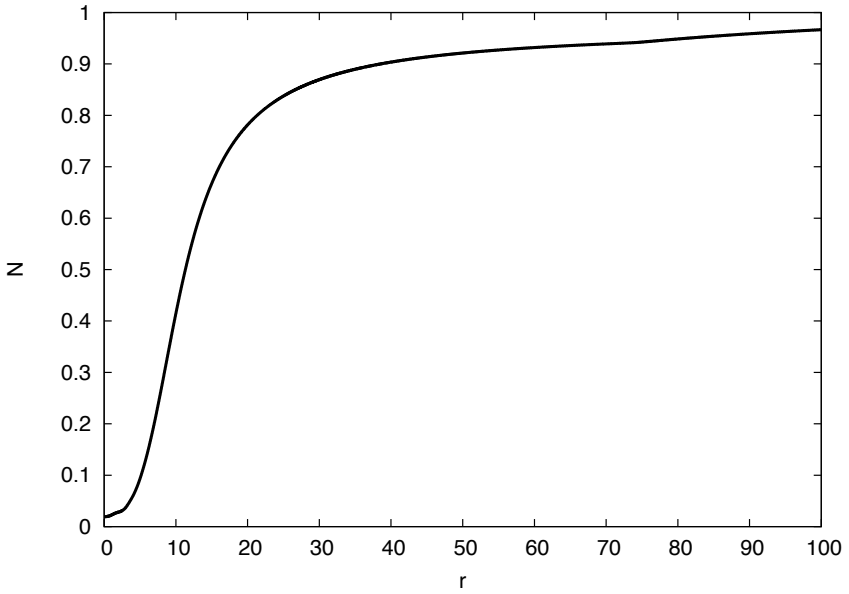

Figure 3.4 the lapse function N *vs* r at time $t = 45$ for $A = 0.15$ and $\alpha = 1.0$

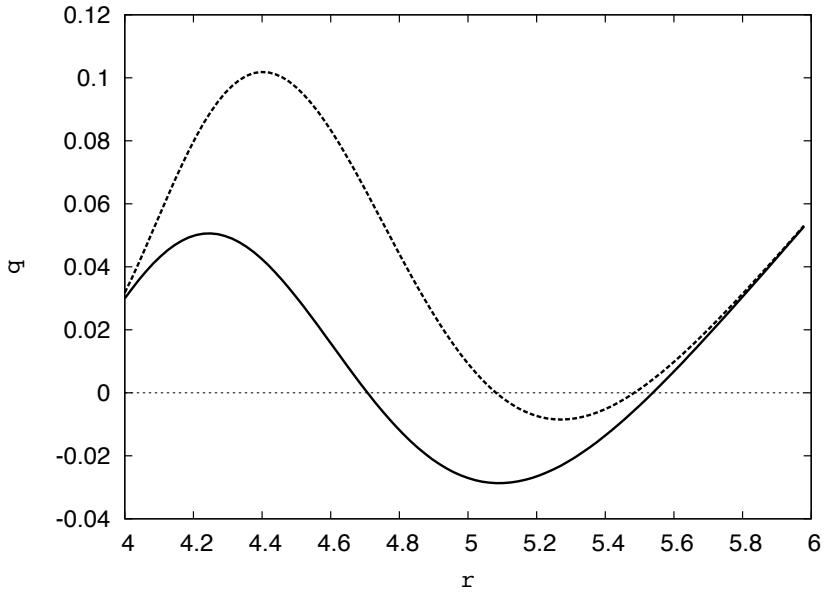

Figure 3.5 the conditions for light horizon (solid line) and sound horizon (dotted line) at time $t = 38.8$ for $A = 0.15$ and $\alpha = 1.0$ and $\mathcal{L}$ given by (3.7)

quickly coincide early in the collapse process. This would indicate that it is only possible to send signals from inside the black hole for a very short time window right after a scalar wave packet falls into the black hole. In contrast, the reason for the persistence of two distinct horizons in the stationary solution of [31] is that the separation is maintained by a constant flux of scalar field through the horizon.

Since the Lagrangian of (3.7) essentially coincides with that of a free scalar field for large α one might expect to find behavior more uniquely characteristic of k-essence by performing simulations with small α. However, such simulations quickly run into difficulties. In particular, a simulation with $A = 0.15$ and $\alpha = 0.5$ fails shortly after $t = 34$. At first sight this is somewhat puzzling, since at times shortly before the simulation fails, the scalar field shows no signs of the sort of rapid growth that would lead to singular behavior. However, this mystery was quickly resolved by an examination of (B.20). Note, that this equation involves division by the quantity $\mathcal{L}_X + \mathcal{L}_{XX}P^2$ and an examination of the simulation showed that this quantity was tending towards zero at a particular spatial point just as the simulation was about to fail. One can understand this phenomenon geometrically as follows: from (3.5), (B.1) and (B.10) it follows that

$$\tilde{g}^{tt} = -\frac{1}{N^2}(\mathcal{L}_X + \mathcal{L}_{XX}P^2) \tag{3.12}$$

So, it is evident that the program crashes when $\tilde{g}^{tt} = 0$. But this is precisely where the

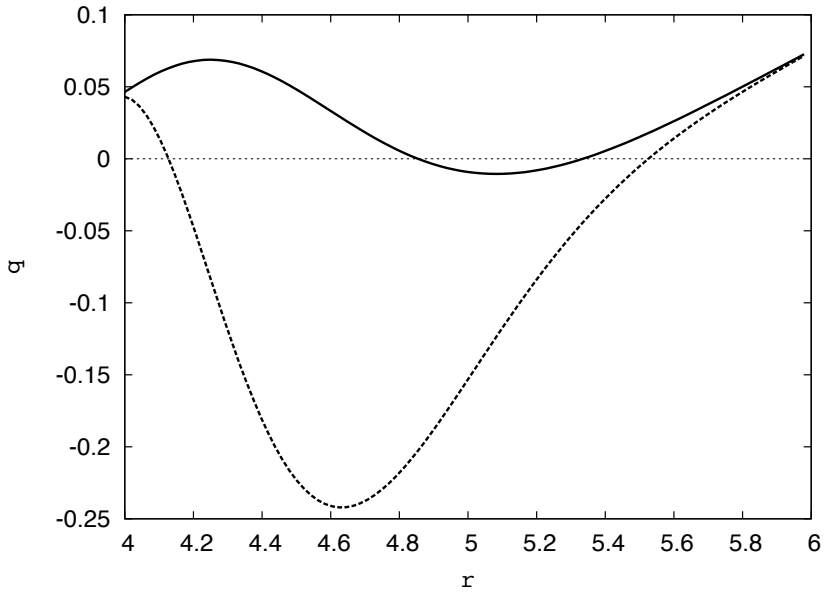

Figure 3.6 the conditions for light horizon (solid line) and sound horizon (dotted line) at time $t = 38.5$ for $A = 0.15$ and $\alpha = 0.5$ and $\mathcal{L}$ given by (3.13)

coordinate t fails to be timelike with respect to the k-essence effective metric, and therefore where the constant t surfaces fail to be Cauchy surfaces for the k-essence field equation. This sort of condition is familiar from general relativity, where the coordinates must be chosen so that $g^{tt} < 0$ in order that the constant t surfaces remain good Cauchy surfaces for the evolution of the spacetime metric. However, when one is evolving self-gravitating k-essence it is necessary that the constant t surfaces be timelike with respect to both the spacetime metric g^{ab} and the k-essence effective metric $\tilde{g}^{ab}$.

In order to avoid this problem, one is led to consider Lagrangians other than that of (3.7). In particular, one could simply change the sign of coefficient of α^2 in (3.7) to obtain

$$\mathcal{L}(X) = \alpha^2 \left[1 - \sqrt{1 - \frac{2X}{\alpha^2}} \right] \tag{3.13}$$

In figure (3.6) are plotted the results of a simulation using the Lagrangian of (3.13). Here $A = 0.15$ and $\alpha = 0.5$ and the plot is done at a time ($t = 38.5$) shortly after the formation of the light horizon. As in figure (3.5) what are plotted are the left hand sides of (3.8) (light horizon, solid line) and (3.11) (sound horizon, dotted line). As before, the horizons occur at the outermost point where each curve crosses zero. However, in this case the sound horizon is outside the light horizon, so there is no possibility of signals escaping from the black hole. Simulations using the Lagrangian of (3.13) do not seem to have the problem with $\tilde{g}^{tt}$

vanishing. Nonetheless, these simulations also fail at sufficiently small α. For example, a simulation with $A = 0.15$ and $\alpha = 0.1$ fails at around $t = 35$. Here the problem is not $\tilde{g}^{tt}$ which remains negative, but rather the vanishing of c_s. This is a familiar phenomenon from simulations of hydrodynamics. When the speed of propagation goes to zero, shock waves tend to form. One can still simulate such systems, but then special "shock capturing" numerical methods are needed rather than the simple finite differencing methods we use here.

We also performed simulations of the Lagrangian given in (3.7) in the absence of gravity. In this case, we found that for sufficiently small values of α the simulation still eventually fails due to $\tilde{g}^{tt}$ going to zero. This indicates that even the Minkowski time coordinate eventually ceases to be a valid global time coordinate for the emergent k-essence metric. As one might expect, no sound horizon was formed in this case.

On the other hand, it is possible to create a sound horizon in the absence of gravity if one simulates (3.13) with a sufficiently small α. As in the case where we did consider gravity, these simulations failed due to c_s going to zero as opposed to $\tilde{g}^{tt}$ going to zero.

3.3.2 Lagrangians Where t is a Valid Global Time Coordinate

Due to the problems encountered using the Lagrangians of (3.7) and (3.13) we are led to consider Lagrangians with non-standard kinetic terms that do not allow either $\tilde{g}^{tt}$ nor c_s to vanish. One such Lagrangian is:

$$\mathcal{L} = \frac{CX}{1+C} + \exp(\frac{X}{1+C}) - 1 \tag{3.14}$$

where C is a constant. Like the previous Lagrangians considered, this one has the desirable feature that it reduces to the free scalar field Lagrangian at small values of X. Note that as long as C is positive, both $\mathcal{L}_X$ and $\mathcal{L}_{XX}$ are positive so $\tilde{g}^{tt}$ will not go to zero. Another requirement is that the k-essence wave equation (3.4) be hyperbolic. The condition for hyperbolicity of (3.4) is that $\mathcal{L}_X + 2X\mathcal{L}_{XX} > 0$. (this condition is satisfied for the Lagrangians of (3.7) and (3.13)). For the Lagrangian of (3.14), $\mathcal{L}_X + 2X\mathcal{L}_{XX}$ has one global minimum with the value $\frac{C}{1+C} - \frac{2}{(1+C)e^{3/2}}$. Consequently, as long as we choose $C > 0.45$, the k-essence wave equation will be hyperbolic. The results of a simulation using this Lagrangian are plotted in figure (3.7). Here $A = 0.15$ and $C = 1$ and the plot is done at a time ($t = 38.5$) shortly after the formation of the light horizon. The plot shows the left hand sides of (3.8) (light horizon, solid line) and (3.11) (sound horizon, dotted line); and the horizons occur at the outermost point where each curve crosses zero. Here, the sound horizon is slightly

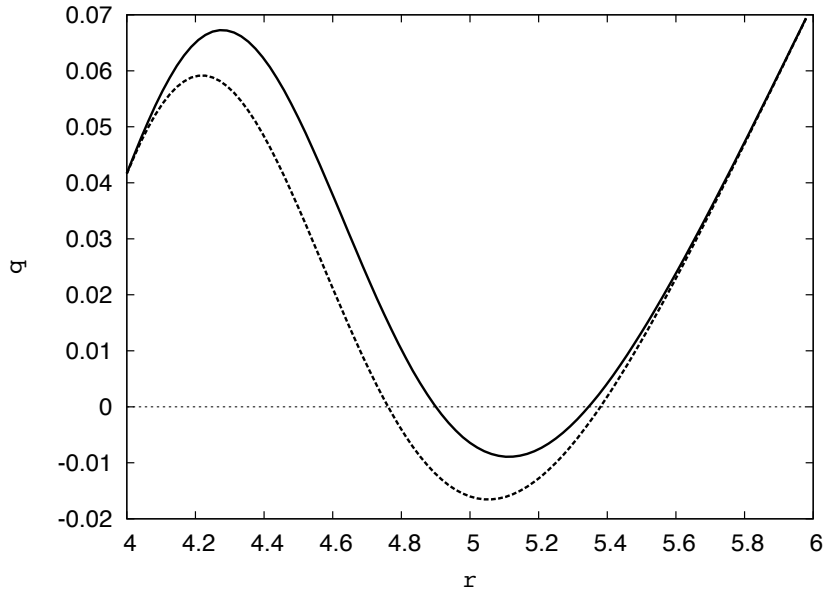

Figure 3.7 the conditions for light horizon (solid line) and sound horizon (dotted line) at time $t = 38.5$ for $A = 0.15$ and $C = 1.0$ and $\mathcal{L}$ given by (3.14)

outside the light horizon, so no signal can escape from the black hole.

Another Lagrangian that doesn't result in either $\tilde{g}^{tt}$ or c_s vanishing is

$$\begin{aligned} \mathcal{L} &= X + CX^2 \quad \text{for } X > 0 \\ \mathcal{L} &= X \qquad\quad \text{for } X < 0 \end{aligned} \tag{3.15}$$

It is clear that as long as C and X are positive, $\tilde{g}^{tt} < 0$ and $\mathcal{L}_X + 2X\mathcal{L}_{XX} > 0$. For negative X the Lagrangian is that of a free field so there are no issues in that regime. The results of a simulation using this Lagrangian are plotted in figure (3.8). Here $A = 0.15$ and $C = 1$ and the plot is done at a time ($t = 38.5$) shortly after the formation of the light horizon. The plot shows the left hand sides of (3.8) (light horizon, solid line) and (3.11) (sound horizon, dotted line); and the horizons occur at the outermost point where each curve crosses zero. Note that there is a discontinuity in the dotted line. This is due to the discontinuity at $X = 0$ of the quantity $\mathcal{L}_{XX}$. Here, the sound horizon is outside the light horizon, so no signal can escape from the black hole. Whether or not the sound horizon being outside the light horizon is a generic feature of k-essence models in which t remains a valid global time coordinate is yet to be answered.

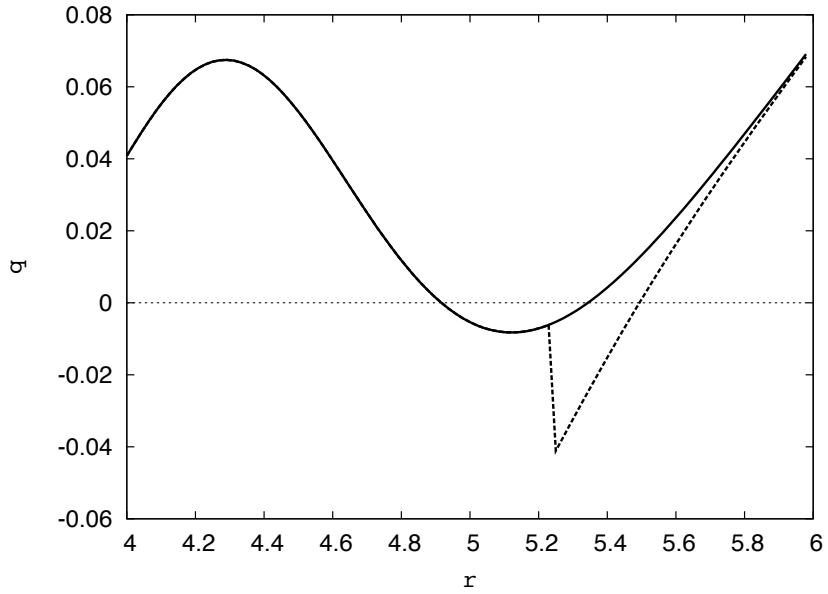

Figure 3.8 the conditions for light horizon (solid line) and sound horizon (dotted line) at time $t = 38.5$ for $A = 0.15$ and $C = 1.0$ and $\mathcal{L}$ given by (3.15)

3.3.3 Cosmological Lagrangians

Other models of interest are cosmological k-essence models which serve as dynamical attractors that cause the field to serve as a cosmological constant at the onset of the matter dominated era. In general these Lagrangians are of a factorizable form in ϕ and X, that is they take the form: $\mathcal{L} = A(\phi)B(X)$. Two such examples that can be found in the literature are [2, 28] :

$$\mathcal{L}(\phi, X) = \frac{1}{\phi^2}(-2.01 + 2\sqrt{1+X} + 3 \cdot 10^{-17}X^3 - 10^{-24}X^4) \tag{3.16}$$

and

$$\mathcal{L}(\phi, X) = \frac{1}{\phi^2}(-2.05 + 2\sqrt{1+f(X)}) \tag{3.17}$$

where

$$\begin{aligned} f(X) = X \quad &- \quad 10^{-8}X^2 + 10^{-12}X^3 - 10^{-16}X^4 \\ &+ \quad 10^{-20}X^5 - 10^{-24}X^6/2^6 \end{aligned} \tag{3.18}$$

Note during our simulations with these initial conditions, X does not get much larger than unity, so we can neglect terms that are higher order in X with small coefficients. Thus, for

our purposes, both these Lagrangians reduce to approximately:

$$\mathcal{L}(\phi, X) = \frac{2}{\phi^2}(-1 + \sqrt{1 + X}) \tag{3.19}$$

The energy density of this field is proportional to $\frac{2}{\phi^2}$. As we know the universe is approximately flat, we require that any fluctuation of this field be a perturbation on a large constant field. Thus, the factor of $\frac{2}{\phi^2}$ in the Lagrangian will amount to a small overall factor. As the energy density will be negligibly small with large ϕ, the gravitational effect will be small. Thus, both (3.16) and (3.17) should reduce to (3.7) in flat space with $\alpha = 1$ and a small overall rescaling factor multiplying the Lagrangian. This overall rescaling factor has no effect in the non-gravitational case. Simulations of (3.7) in flat space with $\alpha = 1$ result in no sound horizon but still suffer from having $\tilde{g}^{tt}$ go to zero.

3.4 Discussion

Our results show that the gravitational collapse of k-essence scalar fields can lead to black holes, just as it does for ordinary scalar fields. However, the nature of these black holes is different. Rather than a single horizon they have two: a light horizon and a sound horizon. The light horizon is what we ordinarily think of as the black hole horizon. The sound horizon (the place where the k-essence itself becomes trapped) can either be outside the light horizon (if the k-essence travels slower than light) or inside the light horizon (if the k-essence travels faster than light). Thus, k-essence can allow signals to escape from a black hole. In the cases we study, the black hole is formed by the collapse of a pulse of k-essence. Eventually all of this pulse either falls into the black hole or escapes from it. Once that has happened, the two horizons have merged into one, and it is no longer possible for signals to escape from the black hole. One should be able to maintain the two horizons, and the possibility of signals escaping from the black hole, by feeding a black hole a steady stream of k-essence scalar field. This will be the focus of chapter 4.

None of our simulations give any indication of the formation of a naked singularity. However, in certain cases our simulations fail not because of any singular behavior in the spacetime itself, but rather because our constant time surfaces fail to be Cauchy surfaces for the evolution of the k-essence scalar field. Since k-essence was originally proposed for cosmological models, one might wonder whether cosmological models might also be vulnerable to this sort of pathology. Here, it is helpful to remember that cosmology treats a situation that is homogeneous and therefore where all physical quantities depend only

on time. For k-essence this means in particular that the quantity X is always postive in cosmology. In our simulations of the k-essence model of (3.7) the constant time surfaces can fail to be Cauchy surfaces for k-essence only when X is negative. Thus, our gravitational collapse study brings to light certain properties of k-essence that would not be noticed in purely cosmological studies. We have also proposed two k-essence Lagrangians for which this Cauchy surface problem does not occur. It would be interesting to see if a Lagrangian of this sort could also be used for the usual purpose of k-essence: a natural cosmological explanation of dark energy.

For those cases where the constant time surfaces fail to be Cauchy surfaces for k-essence, a natural solution to try would simply be to pick a different time coordinate. However, for evolution of self-gravitating k-essence the constant time surfaces need to be Cauchy surfaces for *both* the gravitational field and the k-essence scalar field. It is not clear whether there is *any* time coordinate that will be able to do both jobs. If there is no time coordinate that can do both jobs, then that particular k-essence Lagrangian would be incompatible with gravity and would therefore not be a physically sensible theory. However, our study yields no such assertion of incompatibility because we have used only one time coordinate: that of maximal slicing. To resolve this issue, it is necessary to try other time coordinates to see whether they are compatible with both gravity and k-essence. For an example of subsequent work in different coordinates see [36].

Chapter 4

Accretion of k-essence Scalar Fields onto a Black Hole

4.1 Introduction

As we saw in the previous chapter, the gravitational collapse of k-essence fields proceeds through an intermediate stage of a black hole with two separate horizons, one being the traditional event horizon that corresponds to the speed of light, and the other being a sonic horizon which corresponds to the propagation speed of k-essence field perturbations. As these previous simulations required asymptotic flatness, only k-essence shells with finite width could be simulated.

Because we know that these k-essence fields can form black holes, an interesting question to answer is whether or not these fields eventually settle down and have simple behavior during accretion onto a Schwarzschild black hole. This is especially pressing because there have been numerous investigations of the evolution of black holes surrounded by various non-canonical scalar fields with the assumption that such end behavior occurs [4, 37, 38, 39, 40, 41, 42].

The simplest set-up for analytical studies of accretion is the steady state or Bondi accretion [43]. It was shown in [44] that for general k-essence fields exact stationary configurations are possible only for shift symmetric theories [1]. Since the Lagrangian has to be invariant under constant translations in field space, it is a function only of the derivatives of the scalar field. For such Lagrangians exact stationary solutions have been obtained [4, 37, 38, 39, 40] and steady state accretion analyzed. Indeed the existence of two separate horizons, the usual light horizon and a sound horizon which traps k-essence fluctuations, was to our best knowledge first discussed in [34] for general irrotational hydrodynamics. While this is very interesting, we would really like to know the outcome of a full dynamical

[1] For time-like gradients these shift-symmetric theories are equivalent to barotropic perfect fluids (see e.g. [34, 45, 46]).

evolution as the scalar field accretes on to the already existing black hole. In this case there will be a constant influx of scalar fields onto the black hole and it is far from clear that at late times a stationary or steady state configuration is reached. Because there is a constant influx of energy, a steady state is only one possibility. Alternatively, the evolution of the scalar field could result in a singularity, or the end state could be an oscillatory solution rather than a stationary one (as happens for variable stars). In particular, it was shown in [31] that for a superluminal Dirac-Born-Infeld (DBI)-type model and sound speeds higher than $2/\sqrt{3}$ at spatial infinity a steady state solution suffers from catastrophic gradient instabilities indicating that it is a repeller.

Stability of the steady state accretion is well studied, see e.g. [34] in the case of the time-like gradients when the shift-symmetric theory is equivalent to hydrodynamics. Since we are studying the full dynamical evolution of the scalar field, there can be regions where the gradient of the scalar field is space-like even though we start with a time-like gradient in our initial conditions. This has no effect on the final state of the scalar field, which we find is always stationary.

In order to resolve some of these issues, in this chapter we will simulate the accretion of a test k-essence field. In the case that the end behavior of this k-essence scalar field during the accretion process is stationary (if the field settles down at all), we will be able to compare our end result to the stationary analytic solutions found in the literature [4, 39]. This will require us to use cosmological boundary conditions, where at infinite radius we set the time derivative of the k-essence field to a constant. The two separate horizons can exist for a long enough time to confirm if signals can escape from the black hole when the sound horizon is inside the usual black hole horizon.

The chapter is organized as follows: In the next section we discuss the method used for the simulations and the results are presented in section 4.3. Certain technical details of the construction of the exact stationary solutions for the models considered are relegated to appendix C.

4.2 Methods

The action for a k-essence scalar field in a background curved spacetime is

$$I = \int \sqrt{g}\, d^4x\, \mathcal{L}(X)\,, \tag{4.1}$$

where $X = -\frac{1}{2} g^{\mu\nu} \nabla_\mu \phi \nabla_\nu \phi$ is the standard kinetic term for the scalar field ϕ and g is the absolute value of the determinant of the metric $g_{\mu\nu}$. The use of a fixed background means that we are neglecting the gravitational effects of the scalar field. Varying the action with respect to ϕ yields the equation of motion

$$\tilde{g}^{\mu\nu} \nabla_\mu \nabla_\nu \phi = 0 \ , \tag{4.2}$$

with $\tilde{g}^{\mu\nu}$ being an effective inverse (contravariant) metric associated with the k-essence acoustic geometry and is given by

$$\tilde{g}^{\mu\nu} = \mathcal{L}_X g^{\mu\nu} - \mathcal{L}_{XX} \nabla^\mu \phi \nabla^\nu \phi \ . \tag{4.3}$$

Here, we introduce the shorthand $\mathcal{L}_X$ to mean $d\mathcal{L}/dX$ and $\mathcal{L}_{XX}$ to mean $d^2\mathcal{L}/dX^2$.

We simulate the evolution of k-essence on a background Schwarzschild spacetime. In the usual coordinates, the Schwarzschild metric is given by

$$ds^2 = -f(r) dt^2 + f^{-1}(r) dr^2 + r^2 (d\theta^2 + \sin^2\theta d\varphi^2) \ , \tag{4.4}$$

where $f(r) = 1 - (2M/r)$. However, this coordinate system is not suitable for our simulation, since it becomes singular on the black hole horizon. The usual solution to this difficulty is to introduce Eddington-Finkelstein coordinates (v, r, θ, φ) where v is defined by

$$v = t + \int f^{-1} dr \ . \tag{4.5}$$

This coordinate system covers a region that includes the black hole interior; but it also is not suitable for our purposes since v is a null coordinate, and as with most numerical methods we require a time-like coordinate. Instead, we use the method of Marsa and Choptuik [47]. Introduce the coordinate T by

$$T = v - r \ . \tag{4.6}$$

Then the Schwarzschild metric takes the form

$$ds^2 = -\left(1 - \frac{2M}{r}\right) dT^2 + \left(1 + \frac{2M}{r}\right) dr^2 + \frac{4M}{r} dT dr + r^2 (d\theta^2 + \sin^2\theta d\varphi^2) \ . \tag{4.7}$$

In order to write the k-essence equation of motion in first order form, we introduce the

quantites P and S defined by

$$P = \partial_T \phi \,, \tag{4.8}$$

$$S = \partial_r \phi \,. \tag{4.9}$$

(4.8) provides an equation of motion for ϕ while from (4.9) it follows that

$$\partial_T S = \partial_r P \,, \tag{4.10}$$

which is an equation of motion for S. Finally, some straightforward but tedious algebra using (4.2) and (4.7) yields the equation of motion for P which takes the form

$$\partial_T P = \frac{\mathcal{L}_X A + \mathcal{L}_{XX} B}{C} \,, \tag{4.11}$$

where the quantities $A,\ B$ and C are given by

$$A = \frac{4M}{r}\partial_r P + \left(1 - \frac{2M}{r}\right)\partial_r S + \frac{2S + w}{r} \,, \tag{4.12}$$

$$B = (S + w)\left[2(P + w)\partial_r P - (S + w)\partial_r S - \frac{w^2}{4M}\right] \,, \tag{4.13}$$

$$C = \left(1 + \frac{2M}{r}\right)\mathcal{L}_X + (P + w)^2 \mathcal{L}_{XX} \,, \tag{4.14}$$

and the quantity w is given by

$$w = \frac{2M}{r}(P - S) \,. \tag{4.15}$$

We numerically evolve (4.8), (4.10), and (4.11) as follows: time derivatives are treated using the iterated Crank-Nicholson method. Spatial derivatives, except those on the boundary, are evaluated using standard centered differences; that is, for any quantity F we approximate $\partial_r F$ at grid point i by

$$\frac{F_{i+1} - F_{i-1}}{2dr} \,, \tag{4.16}$$

where dr is the spacing between adjacent grid points. At the boundary, spatial derivatives are evaluated using one-sided differences: that is at grid point 1 we approximate $\partial_r F$ by

$$\frac{F_2 - F_1}{dr} \,, \tag{4.17}$$

while at the final gridpoint (point N) we approximate $\partial_r F$ by

$$\frac{F_N - F_{N-1}}{dr} \, . \tag{4.18}$$

Physically appropriate boundary conditions must also be imposed on the k-essence field at each step of the time evolution. We are treating an overall constant flux of scalar field along with waves of scalar field that should be outgoing at the outer boundary. Therefore we impose the condition

$$P + S = c_p \, , \tag{4.19}$$

at the outer boundary, where c_p is a constant representing the rate of flux of scalar field. At the inner boundary, we use an excision method appropriate for k-essence. That is, we place the inner boundary sufficiently far inside the black hole that not only light but also k-essence modes are trapped and therefore ingoing at that point. Since all modes are ingoing at the inner boundary, no boundary condition is needed (or even allowed) there, and therefore we do not impose any boundary condition at the inner boundary.

4.3 Results

Unless stated otherwise, for all results and figures shown we chose the initial data at $T = 0$ such that $\phi = 0$, $S = 0$, and $P = 0.01$. The mass M of the black hole was chosen to be unity, so the corresponding standard Schwarzschild horizon is located at $r = 2$ for all shown simulations.

4.3.1 DBI-Type Action

We will first consider a k-essence scalar field with the DBI-like Lagrangian density:

$$\mathcal{L}(X) = \alpha \left[\sqrt{1 + \frac{2X}{\alpha}} - 1 \right] \, . \tag{4.20}$$

Note that the expression for the speed of sound (for time-like gradients) for this model is

$$c_{\rm s}^2 = 1 + \frac{2X}{\alpha} \, . \tag{4.21}$$

Thus, for negative α the propagation is subluminal and for positive α the propagation is superluminal. Moreover, for time-like gradients this field theory reproduces one of the

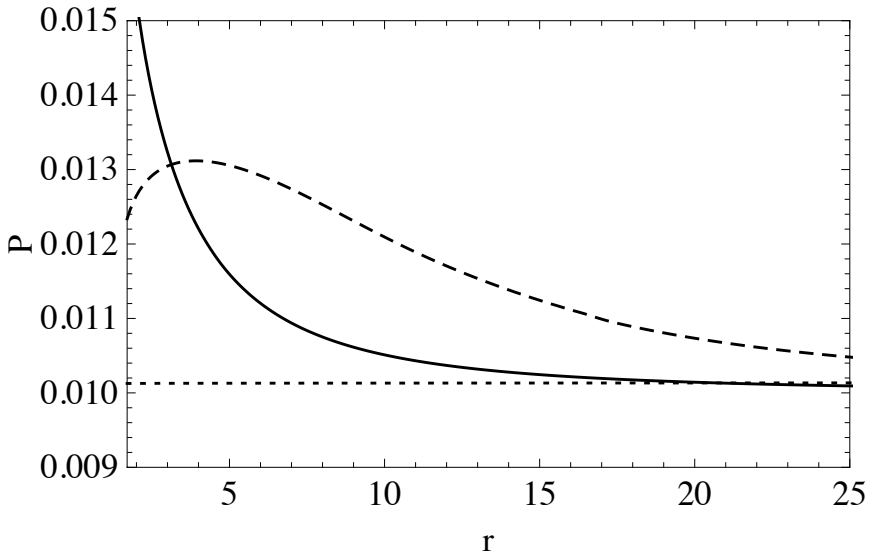

Figure 4.1 Profiles of P arrived at via simulation of the accretion of the field described by (4.20). The solid line corresponds to P at $T = 2.97524$, the dashed line corresponds to P at $T = 14.8762$, and the dotted line corresponds to P at $T = 148.771$. For this particular plot, we used $c_p = 0.01$, $\alpha = 0.0016$, and $M = 1$.

versions of a rather popular model among cosmologists, the so-called Chaplygin gas with the equation of state $p = -\alpha/\rho$, see [48]. This form of the kinetic term with positive α was proposed for the first time in [49]. The analytical solution for a steady state accretion in this model was found in [4, 37]. Upon simulating the accretion of this type of k-essence model into a Schwarzschild black hole, we found that for all positive α where the simulation ran successfully, the scalar field eventually settled down to a stationary solution. Simulated profiles for both P and S at various times are shown in figures 4.1 and 4.2.

For sufficiently small values of positive α (for our initial conditions this is approximately $\alpha = 0.001$), the simulation did not run successfully. This is because for these values of α, at some point in the simulation the quantity C given in (4.14) goes to zero. Since this quantity occurs as the denominator in (4.11), the evolution equation for P becomes singular. To understand what this means, note that C is proportional to $\tilde{g}^{TT} = \mathcal{L}_X g^{TT} - \mathcal{L}_{XX}\nabla^T\phi\nabla^T\phi$. Thus, in physical terms, our time coordinate T is no longer a valid global time coordinate in the emergent k-essence spacetime. This is because when $\tilde{g}^{TT} = 0$, we have:

$$\tilde{g}^{\mu\nu}\nabla_\mu T\nabla_\nu T = 0\ , \tag{4.22}$$

which indicates $\nabla_\mu T$ is not time-like in the emergent spacetime. This does not necessarily mean that there is no scalar function that can serve as a valid global time coordinate, which

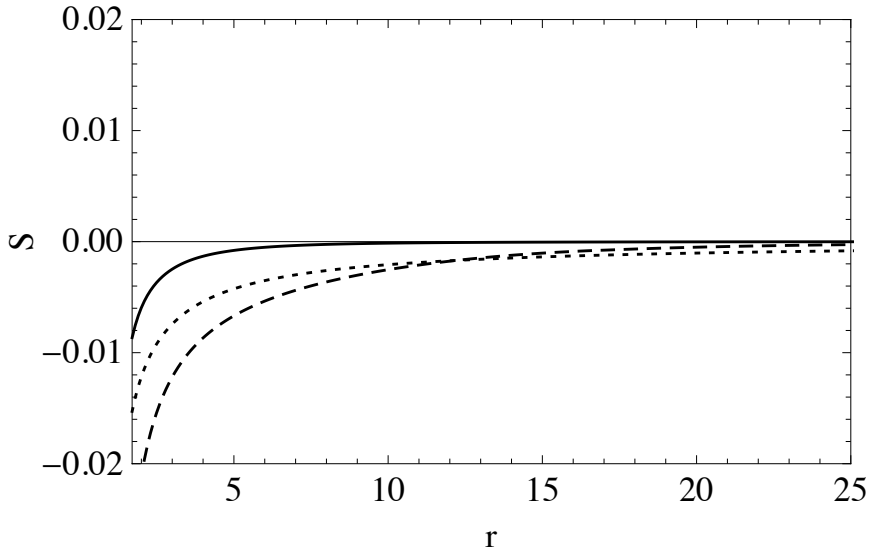

Figure 4.2 Profiles of S arrived at via simulation of the accretion of the field described by (4.20). The solid line corresponds to S at $T = 2.97524$, the dashed line corresponds to S at $T = 14.8762$, and the dotted line corresponds to S at $T = 148.771$. For this particular plot, we used $c_p = 0.01$, $\alpha = 0.0016$, and $M = 1$.

would indicate that the emergent spacetime is not stably causal [50].

We also simulated this k-essence model for negative values of α, since in this case we can ensure that $\tilde{g}^{TT} \neq 0$. Simulated profiles for both P and S for $\alpha = -0.0004$ at various times are shown in figures 4.3 and 4.4. In this subluminal case we also find that for all successfully run simulations the scalar field settles down to a stationary solution. For values of negative α sufficently close to zero (for our initial conditions this is approximately $\alpha = -0.00015$), the simulation did not run successfully due to the speed of sound approaching zero. This is indicative of a shockwave, which our code was not meant to handle.

For both positive and negative α, it was found that the scalar field would settle down to a stationary solution for a wide range of initial conditions as long as the same cosmological boundary condition ($P + S = c_p$) was maintained at infinite radius. An example of such inital data is:

$$P = \frac{c_p}{2}(\tanh(r - r_0) + 1) \,, \tag{4.23}$$

for various choices of c_p and r_0, with $\phi = 0$ and $S = 0$.

In order to confirm that the fields did indeed settle down to a stationary solution, we compared our results to the stationary solution found analytically in [4]. Expressed in our

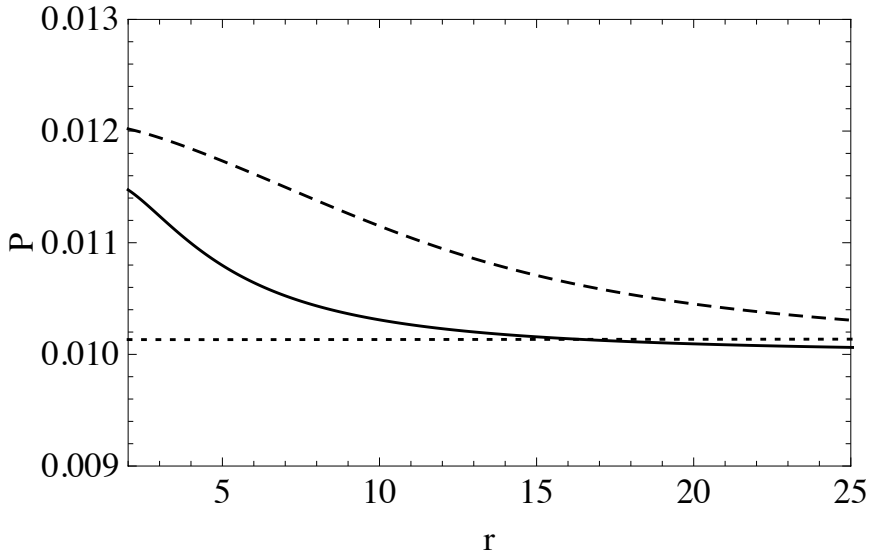

Figure 4.3 Profiles of P arrived at via simulation of the accretion of the field described by (4.20). The solid line corresponds to P at $T = 2.97074$, the dashed line corresponds to P at $T = 14.8537$, and the dotted line corresponds to P at $T = 148.536$. For this particular plot, we used $c_p = 0.01$, $\alpha = -0.0004$, and $M = 1$.

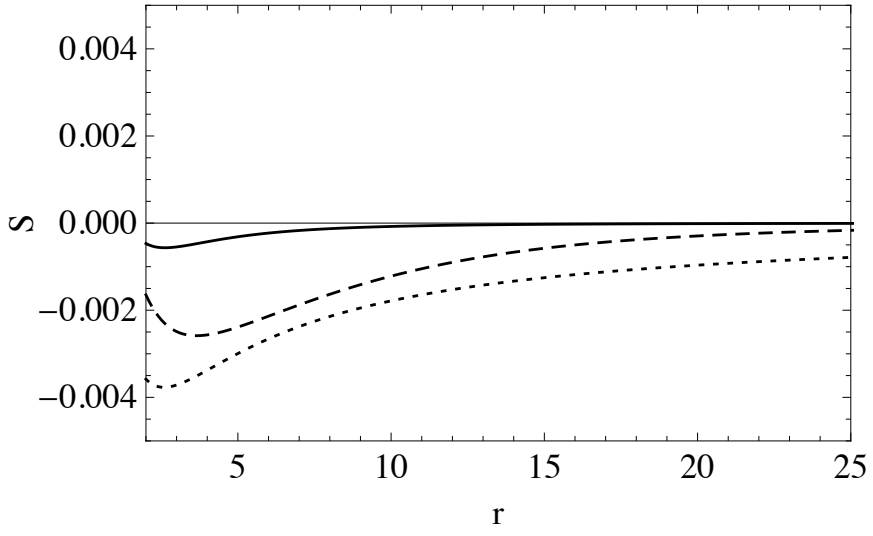

Figure 4.4 Profiles of S arrived at via simulation of the accretion of the field described by (4.20). The solid line corresponds to S at $T = 2.97074$, the dashed line corresponds to S at $T = 14.8537$, and the dotted line corresponds to S at $T = 148.536$. For this particular plot, we used $c_p = 0.01$, $\alpha = -0.0004$, and $M = 1$.

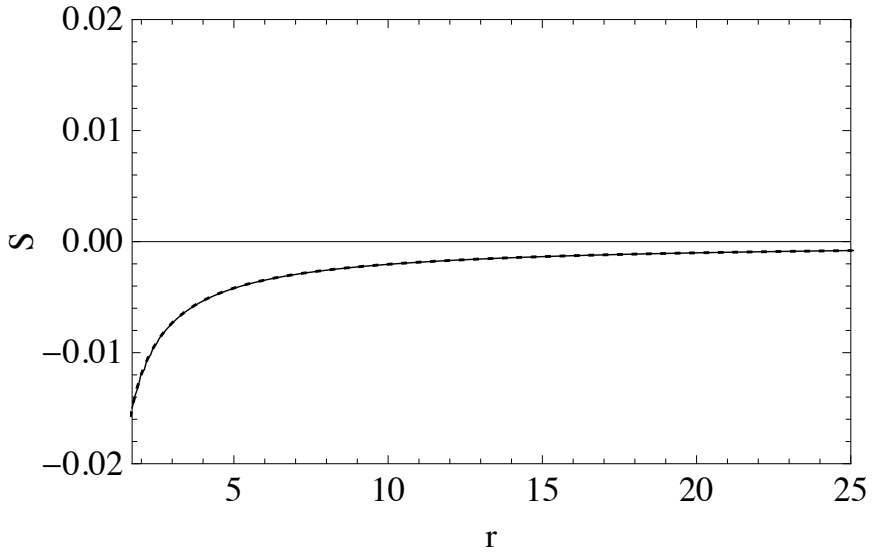

Figure 4.5 The solid line is the radial derivative of the stationary solution for ϕ eventually arrived at via simulation of the accretion of the field described by (4.20). The dotted line is the radial derivative of ϕ for the analytic stationary solution. For this particular plot, we used $c_p = 0.01$, $\alpha = 0.0016$, and $M = 1$. The sound horizon has settled down at $r = 1.88$. The radial derivative was chosen since the radial derivative of a stationary solution is time independent.

coordinates, the solution is (for a brief derivation see appendix C):

$$\phi(T, r) = c_p \left(T + r + \int F(r) dr \right) , \tag{4.24}$$

where

$$F(r) \equiv \frac{1}{f(r)} \left(\sqrt{\frac{c_\infty^2 + f(r) - 1}{f(r)\frac{r^4 c_\infty^8}{16M^4} + c_\infty^2 - 1}} - 1 \right) , \tag{4.25}$$

with $f(r) = 1 - (2M/r)$, and

$$c_\infty^2 \equiv c_s^2(r \to \infty) = 1 + \frac{c_p^2}{\alpha} . \tag{4.26}$$

Comparisons between the analytic stationary solution and the ones arrived at via simulation for both the positive and negative α cases are shown in figures 4.5 and 4.6.

We can define a sonic horizon as being the outermost radius at which null vectors with respect to the emergent k-essence metric become trapped. The null vectors l^μ are defined

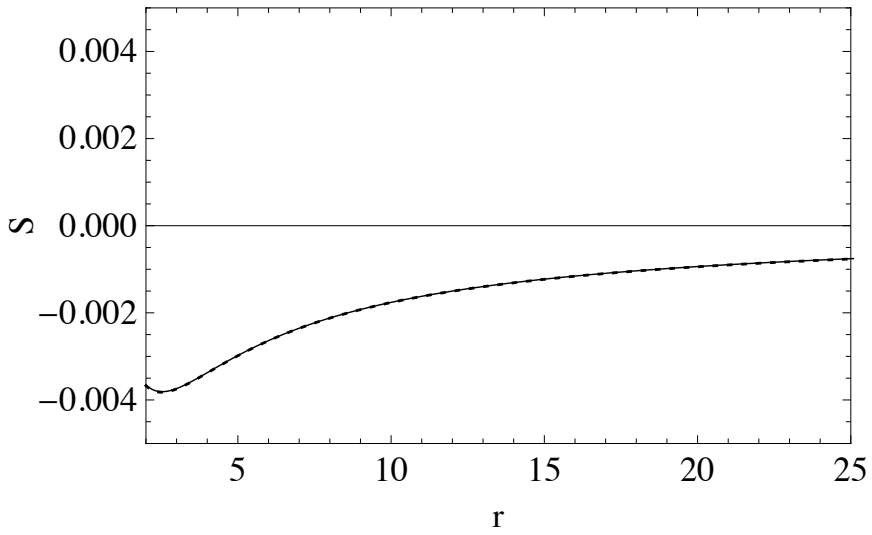

Figure 4.6 The solid line is the radial derivative of the stationary solution for ϕ eventually arrived at via simulation of the accretion of the field described by (4.20). The dotted line is the radial derivative of ϕ for the analytic stationary solution. For this particular plot, we used $c_p = 0.01$, $\alpha = -0.0004$, and $M = 1$. The sound horizon has settled down at $r = 2.67$. The radial derivative was chosen since the radial derivative of a stationary solution is time independent.

by:

$$\tilde{g}^{-1}_{\mu\nu} l^\mu l^\nu = 0 \,, \tag{4.27}$$

where $\tilde{g}^{-1}_{\mu\nu}$ is the inverse of $\tilde{g}^{\mu\nu}$. We can solve this quadratic equation for l^r/l^T, taking the positive root for outgoing null vectors. The sonic horizon is the outermost radius at which $l^r/l^T = 0$. For stationary solutions corresponding to scalar fields with the Lagrangian density of (4.20), the sonic horizon is located within the Schwarzschild radius for positive α and located outside the Schwarzschild radius for negative α. To see that this implies that one can send signals from within a black hole for the superluminal positive α models, we should plot a set of radial null geodesics with respect to the emergent k-essence metric. Because for radial null geodesics $dr/dT = l^r/l^T$, we can numerically integrate this quantity to find these geodesics, which are plotted in figure 4.7. As can be seen in figure 4.7, there exist null geodesics that start inside the Schwazschild radius at $T = 0$ (when as stated earlier, $P = c_p$ and $\phi = 0$ for all radii) and end up escaping as the field evolves towards the stationary solution. We want to emphasize that the null k-essence geodesics can escape a black hole not only in the stationary solution but also during the approach towards the stationary solution from more general initial conditions.

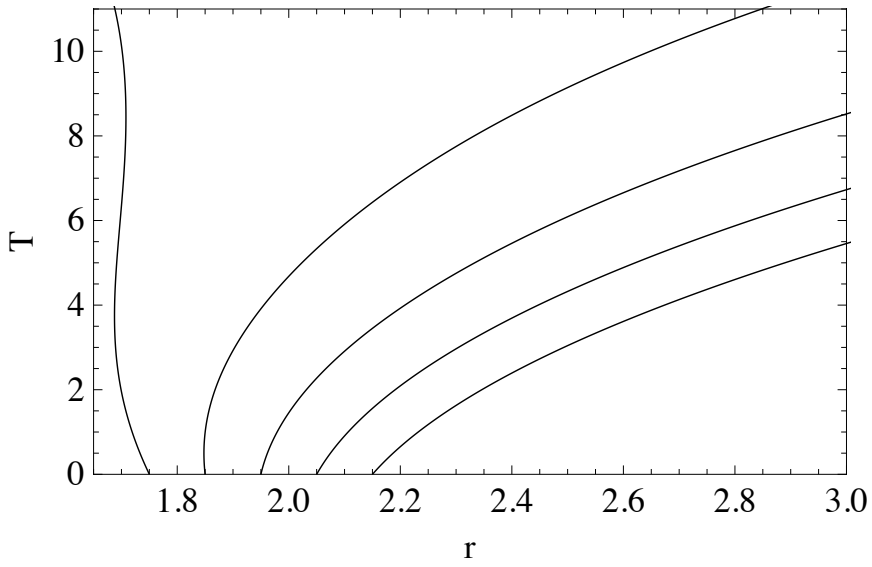

Figure 4.7 Outgoing radial null geodesics corresponding to the emergent k-essence metric. For this simulation, we chose the values $c_p = 0.01$, $\alpha = 0.0016$, and $M = 1$. We show five geodesics that start at $r = 1.75$, 1.85, 1.95, 2.05 and 2.15. The geodesic starting at 1.75 fails to escape the black hole; the other four all escape, with two of the escaping geodesics starting within the Schwarzschild radius at $r = 2$.

4.3.2 Ghost Condensate Action

Next we consider the ghost condensate models proposed in [51]. These provide a modification of gravity in the infrared regime with possible ramifications for the dark matter problem and inflation. This model is a k-essence like model, where X develops a non-zero vacuum expectation value. The ghost condensate field is not directly coupled to other fields, so the only scale in the ghost sector is a, the overall energy scale of the condensate. The simplest such model is described by [39, 40]:

$$\mathcal{L}(X) = \frac{1}{8a^4}(X - a^4)^2 \, . \tag{4.28}$$

The sound speed of the scalar field with this Lagrangian is given by:

$$c_s^2 = \frac{X - a^4}{3X - a^4} \, . \tag{4.29}$$

Thus, by making $|a|$ larger for a fixed value of $P(r \to \infty) = c_p$ (which as stated earlier, we set at 0.01), we can make the sound speed at infinite radius smaller. We found that for all simulations with sufficiently large sound speeds, the scalar field eventually settles down to a stationary solution. The code was not designed to simulate fields with sound speeds close to

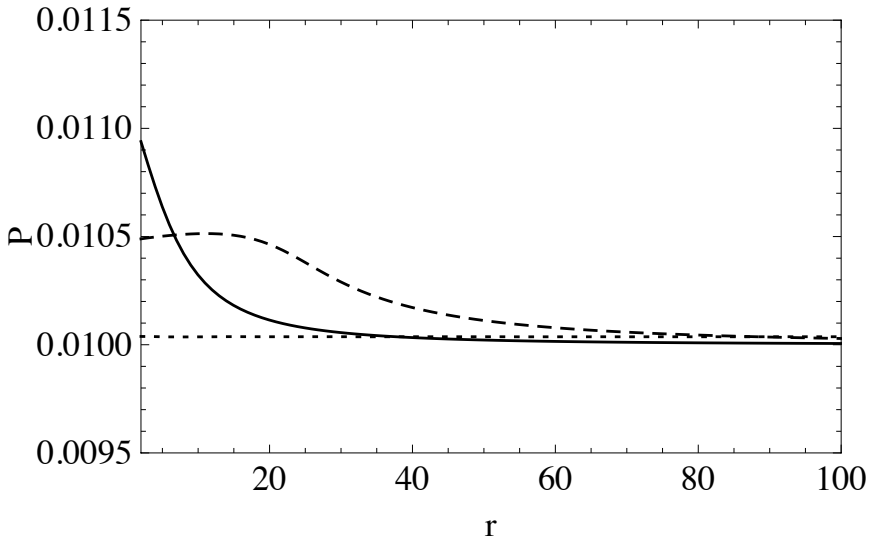

Figure 4.8 Profiles of P arrived at via simulation of the accretion of the field described by (4.28). The solid line corresponds to P at $T = 11.9406$, the dashed line corresponds to P at $T = 59.7061$, and the dotted line corresponds to P at $T = 597.357$. For this particular plot, we used $c_p = 0.01$, $a = 0.0638943$ (which corresponds to a sound speed at infinite radius having the value $c_\infty = \frac{1}{2}$), and $M = 1$.

zero. Simulated profiles for both P and S at various times are shown in figures 4.8 and 4.9. Note that although our initial conditions have a time-like gradient for the scalar field, during the course of the dynamical accretion the gradient became space-like at some regions. This can be seen from figures 4.1, 4.2, 4.8, and 4.9, where for the models given in (4.20) (for positive α) and (4.28), S is larger than P in some regions of spacetime.

We then compared the stationary solution we found from the simulation to the analytically derived stationary solution [39]. For this model, deriving the analytic solution involves solving a cubic equation (for details see appendix C). A comparison of the analytic solution (evaluated using Mathematica) and the simulated solution at late times is given in figure 4.10.

4.4 Discussion

Upon simulating the accretion of two very different types of non-canonical scalar fields onto a black hole, we find that both eventually settle down to a stationary solution. This is reassuring as it suggests that the numerous studies done on the stationary solutions of scalar field models with non-standard kinetic terms correspond to physically viable scenarios as opposed to special situations which cannot be reached dynamically from generic initial

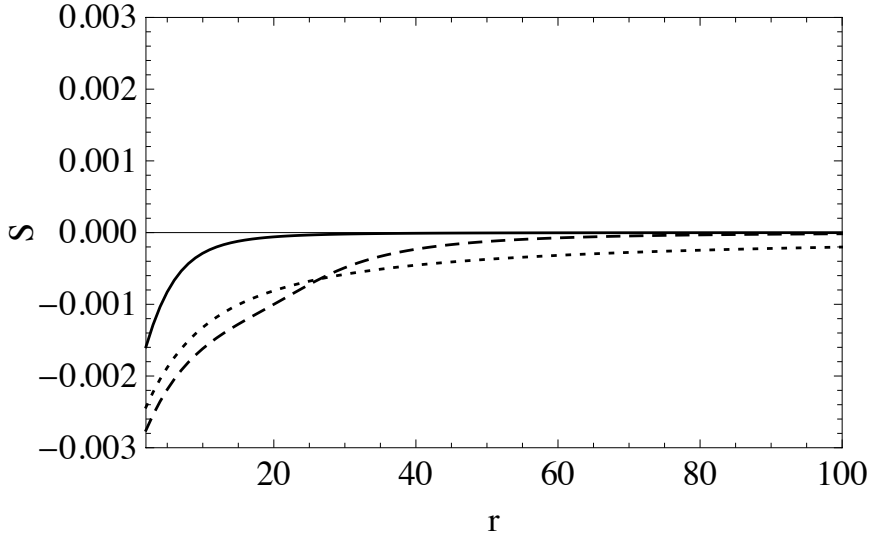

Figure 4.9 Profiles of S arrived at via simulation of the accretion of the field described by (4.28). The solid line corresponds to S at $T = 11.9406$, the dashed line corresponds to S at $T = 59.7061$, and the dotted line corresponds to S at $T = 597.357$. For this particular plot, we used $c_p = 0.01$, $a = 0.0638943$ (which corresponds to a sound speed at infinite radius having the value $c_\infty = \frac{1}{2}$), and $M = 1$.

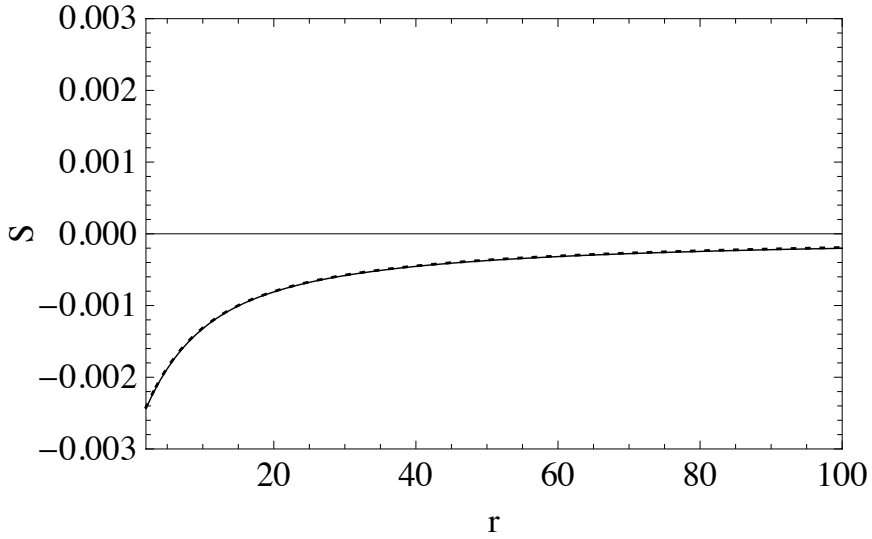

Figure 4.10 The solid line is the radial derivative of the stationary solution for ϕ eventually arrived at via simulation of the accretion of the field described by (4.28). The dotted line is the radial derivative of ϕ for the analytic stationary solution. For this particular plot, we used $c_p = 0.01$, $a = 0.0638943$ (which corresponds to a sound speed at infinite radius having the value $c_\infty = \frac{1}{2}$), and $M = 1$. The sound horizon has settled down at $r = 3.21$. The radial derivative was chosen since the radial derivative of a stationary solution is time independent.

conditions.

We find that for a k-essence scalar field with a DBI-type action, if the parameters are chosen such that the field can propagate superluminally, one can send signals from within a black hole as the field approaches this stationary solution. This was confirmed by numerically integrating outgoing null geodesics with respect to the emergent k-essence metric during simulations of this accretion process.

Simulations of a typical ghost condensate action revealed that the stationary solution reached is that derived analytically by Frolov in [39]. He showed that this particular solution has an extremely high accretion rate, which puts very strong constraints on the ghost condensate model. However, for the case where the sound speed is zero, the solution is ambiguous (see appendix C for further details). Mukohyama has argued in [40] that the sound speed should be extremely small on physical grounds, and for corresponding solutions in this limit the accretion rate is reasonable. As our numerical method is not meant to deal with extremely small sound speeds, it would be interesting to see this particular issue resolved with the use of another method.

Chapter 5

Collinear and Soft Divergences in Perturbative Quantum Gravity

5.1 Introduction

Now that we have investigated the robustness of a cosmological dark energy model in the presence of black holes, let us move on to examine the quantum mechanical side of general relativity. In particular, over the remaining chapters we will research the behavior of perturbative quantum gravity at energies well below the Planck scale, where the theory can be unambiguously defined. In this chapter we will start off with an investigation of the infrared divergences in quantum gravity, as these are among the most interesting low-energy features of a generic quantum field theory.

Infrared divergences in perturbative quantum gravity were examined long ago in [53], where the exponentiation of the singular contributions in ladder and the crossed ladder diagrams was verified by analogy to quantum electrodynamics. In the scattering of massless particles, or at very high energies, graviton ladder diagrams, like those in QED, also develop collinear singularities, or "mass divergences". In contrast to QED, however, collinear singularities turned out to cancel after the summation of all ladders, when treated in eikonal approximation. The cancellation of the remaining, non-collinear soft-graviton divergences between virtual and real ladder emission processes was also pointed out in [53], and subsequently confirmed in full quantum gravity at the one-loop level in [54].

The infrared behavior of quantum gravity has been revisited recently in [55, 56] in the context of exploiting analogies between gauge theories to gravity [57]. The study of perturbative quantum gravity amplitudes and cross sections also complements studies of nonperturbative quantum gravity at very high energies [58]. In this chapter we analyze amplitudes for fixed-angle scattering in quantum gravity. We will identify at arbitrary orders the classes of diagrams that give collinear or soft infrared divergences, and generalize the cancellation of the former to energetic lines, for which the eikonal approximation does not

apply in general.

We begin with a study of the collinear sector of quantum gravity, including its coupling to gauge theory matter, with the aim of complementing the work in [55] and [56], which concentrated primarily on soft gravitons. We consider amplitudes with all massless external lines, all at fixed angles relative to each other, both incoming and outgoing. We will show that for such "wide-angle" scattering, perturbative amplitudes are free of collinear singularities altogether to any fixed order, despite their presence on a diagram-by-diagram basis. This result generalizes the observation of [53] in the eikonal approximation. We go on to investigate soft graviton singularities, and conclude that they originate only from ladder exchange between finite-energy lines [55, 56]. To demonstrate these results, we will use the general infrared analysis developed for gauge theories in [59], [60, 61] and [62] and elaborated in [63]. To be specific, we consider the harmonic, or de Donder gauge for the quantization of quantum gravity, with perturbation theory rules, including ghosts [64, 65, 66, 67, 68] as summarized, for example, in [69, 70] and [71]. Happily, we will not need the detailed features of the rules, only their covariance and a counting of numbers of derivatives.

The method of [59] begins with the observation that a necessary condition for infrared enhancement, whether soft or collinear, is the presence of pinch singularities in subspaces (pinch surfaces) of virtual loop momentum integrals [72, 73, 74]. Each such pinch surface is conveniently characterized by a reduced diagram, consisting of the lines that are forced on-shell at the surface in question.

This analysis is particularly straightforward for wide-angle scattering. At leading power a single effective vertex in the reduced diagram mediates the hard scattering. Specifically, an analysis of the pinch surfaces for wide-angle scattering gives for the most general reduced diagram involving only massless lines (including gravitons) the form shown in Fig. 5.1, where for purposes of illustration, only four external legs are shown. The letters J and S denote respectively the jet and soft subdiagrams and H is a hard vertex [59, 60, 61]. At the pinch surface, all lines in each jet J_i are collinear to each other and to the external line p_i to which they attach, all lines in S carry zero momentum, and all lines in H are off-shell. In the following sections we study the nature of the various subdiagrams and find that a remarkably simple structure emerges, as suggested by the eikonal analysis of [53]. The infrared singular behavior of quantum gravity is simpler than that of massless quantum electrodynamics.

In section 5.2 we introduce a power-counting procedure to identify the types of reduced diagrams that yield collinear singularities in theories of pure gravity and of gravity coupled to other matter. The infrared divergences in the pure matter sector have been studied extensively in the literature so we only focus on the new divergences that arise as a result of

gravitational interactions. We find that the only types of diagrams that give mass divergences are those with no internal graviton jet loops, and which contain only three point vertices. We also show that mass divergences do not arise in diagrams with both standard model particles and gravitons when only the gravitons attach to an external leg.

Next, in section 5.3 we develop a power-counting procedure to find what types of reduced diagrams with virtual gravitons give soft divergences. We find that for the case of virtual soft graviton corrections to a hard vertex, only diagrams of the ladder type give rise to soft divergences, as previously observed in [55] and [56]. In addition, we observe that the representation of divergent soft graviton interactions in terms of Wilson lines, as explicitly conjectured in [55], follows readily from the cancellation of collinear singularities.

Section 5.4 is devoted to the proof that collinear singularities cancel when all collinear-divergent diagrams are combined, using a gravitational Ward identity. As an illustration of how the arguments of section 5.4 work, in appendix D we develop an extension of the analysis of [53], to show explicitly the cancellation of the graviton collinear singularities for kinematic regions where the eikonal approximation applies.

5.2 Jet Power Counting

In this section we will build upon a power counting procedure for infrared divergences developed in [59, 60, 61, 62]. Let us consider a graviton jet attached to a massless on-shell line with momentum p in an arbitrary diagram as in figure 5.2. The graviton jet reattaches to the rest of the diagram, labeled "rest" in the figure. For purposes of classification, gravitons that reattach to the same external leg from which they were emitted are considered as part of the jet, rather than attached to "rest". Such external leg corrections do not give rise to collinear singularities, as we will show later.

Let L_J be the number of loops, N_J the number of lines in jet J, and N_{num} the total power of what we will call "normal variables" in the numerator that arise from the vertices and propagators of the jet. Normal variables are chosen such that they vanish at the pinch singular point that causes the infrared divergence. Then, singularities of the integrand appear through their dependence on normal variables.

The loop momentum integrand corresponding to any Feynman diagram can be made a homogenous function of the normal variables by keeping only the lowest power in both the numerator and denominator factors. Counting powers of normal variables then enables us to determine the finiteness or potential for divergence of the pinch surface in question. This is measured by the degree of divergence, given by the number of normal variables,

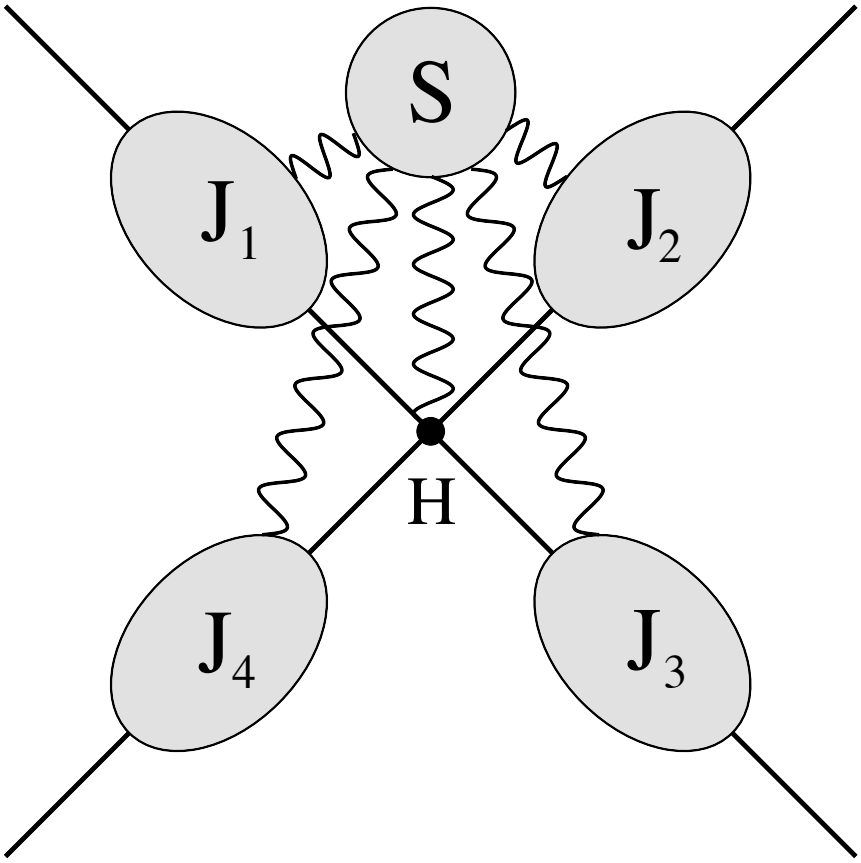

Figure 5.1 A general reduced diagram at the pinched singular point. J and S denote the jet and soft subdiagrams and H is a hard vertex. Here each line may represent any number of soft propagators connecting S to the remainder of the diagram, or the jets J_i to the hard part H.

minus the homogeneity (power in normal variables) of the product of denominators, plus the homogeneity for the numerators. For examples, see (5.3) and (5.15) below.

In order to identify the normal variables for collinear singularities, let us make a change of variables in each jet loop integral such that:

$$\int d^4l \sim \int dl_\perp^2 dl^+ dl^- \,, \tag{5.1}$$

where $l_\perp^2$ includes the two components of the loop momenta l that are transverse to p and $l^\pm$ is defined as $\frac{1}{\sqrt{2}}(l_0 \pm \vec{l}\cdot\hat{p})$, with $\hat{p}$ a unit 3-vector in the direction of the jet. This change of variables actually requires one to evaluate a Jacobian, but we omit this step as this factor will not contain any singularities. Note that for a collinear line we can rotate to a frame such that l^- and $l_\perp^2/l^+$ become small, so we choose these as the normal variables (for convenience, both with dimensions of mass). With this choice, each jet loop will contribute two normal

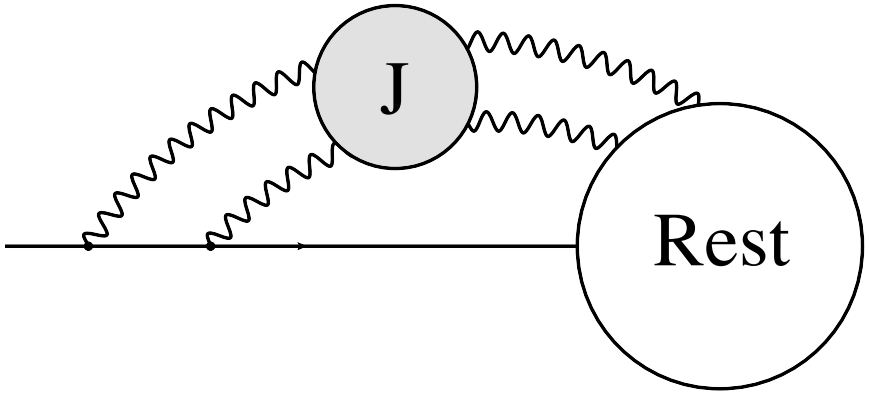

Figure 5.2 A diagram with a graviton jet attached to an external leg. We show the case where there are two gravitons being emitted from the external line and two gravitons attaching to "rest" but these can be any numbers. The analysis in section 5.2 shows that the number of gravitons emitted and attached do not need to be the same.

variables to the total collinear degree of divergence of the diagram. The consistency of this choice is discussed in [63] and [75]. A similar power counting plays a role in soft-collinear effective theory [76].

In the de Donder gauge, the graviton propagator is [70]

$$\frac{i}{2}[\eta^{\alpha\gamma}\eta^{\beta\delta} + \eta^{\beta\gamma}\eta^{\alpha\delta} - \eta^{\alpha\beta}\eta^{\gamma\delta}]\frac{1}{l^2 + i\epsilon}\,. \tag{5.2}$$

Since $l^2 = 2l^+l^- - l_\perp^2$, each graviton propagator will be linear in normal variables in the denominator. Thus, each graviton jet line will contribute -1 to the degree of divergence from the diagram. In summary, we can write the total collinear degree of divergence of diagrams of the type shown in figure 5.2 as

$$\gamma_{CO} = 2L_J - N_J + N_{num}\,. \tag{5.3}$$

A diagram can have a collinear singularity whenever $\gamma_{CO} \leq 0$, and $\gamma_{CO} = 0$ corresponds to a logarithmic divergence.

As each jet line connects two vertices, we can also use the relation,

$$2N_J = \sum_{i\geq 3} iV_i + N_G\,, \tag{5.4}$$

where V_i is the total number of i-point vertices in the diagram, not counting those that attach to "rest" (see figure 5.2) and N_G is the number of gravitons in the jet that attach to "rest". Here we treat "rest" as an $N_G + 1$-point vertex in the jet subdiagram, and we do not count

the external line of the jet in N_J.

We can write the minimum homogeneity of normal variables in the numerator as

$$N_{num} = \frac{1}{2}N_{mom} - \min[\frac{1}{2}N_{mom}, \sum_k \frac{k}{2}N_k] \,, \tag{5.5}$$

where N_{mom} is the total power of momentum vectors from the vertices in the jet subdiagram and N_k is the number of vertices with k powers of momentum that are contracted with non-collinear vectors from "rest". The factor of $\frac{1}{2}$ reflects that the scalar product of the momenta of any two jet lines is linear in the normal variables of the jet, and hence adds unity to the overall homogeneity of the numerator. We subtract $\sum_k \frac{k}{2}N_k$ from N_{num} because each graviton line attaches to "rest" at a vertex involving some integer, k, of powers of momenta, collectively denoted p'^μ, that are not collinear with p^μ. This is why we do not classify gravitons reattaching to the same leg they were emitted from as part of "rest", as in this case $p' = p$. The graviton propagator can then contract the momenta in the vertex in "rest" with momentum vectors from a vertex in the graviton jet. This will result in terms of order $(p \cdot p')^k$. These terms are zeroth order in normal variables. That is, at each such vertex, $k/2$ factors of momenta that are nearly proportional to p^μ can "escape" the jet, forming "large" invariants that do not vanish at the pinch surface. Thus, we must subtract $k/2$ from N_{num} for each of the N_k vertices from "rest". The last term in (5.5) is inserted simply to ensure that $N_{num} \geq 0$ in all cases.

For gravity we make the expansion $g_{\mu\nu} = \eta_{\mu\nu} + \kappa h_{\mu\nu}$ and take the quantum field to be $h_{\mu\nu}$. Gravitational vertices correspond to terms in the Lagrangian that are symbolically of the form $\kappa^{i+j-4}\partial^j h^i$. Let $V_{i,j}$ be the number of i-point vertices with j powers of momentum in the diagram (not including those in "rest"). This allows us to write N_{mom} as

$$N_{mom} = \sum_j j \sum_{i \geq 3} V_{i,j} \,. \tag{5.6}$$

For the case of pure gravity we can write the Einstein-Hilbert Lagrangian as [77]

$$\begin{aligned} \mathcal{L}_{EH} = \sqrt{-g}R = \frac{1}{2}(\hat{g}^{\alpha\kappa}\hat{g}_{\rho\sigma}\hat{g}^{\rho\sigma}_{,\alpha} + 2\hat{g}^{\alpha\kappa}_{,\alpha})_{,\kappa} \\ + \frac{1}{8}\hat{g}^{\alpha\kappa}_{,\rho}\hat{g}^{\lambda\beta}_{,\sigma}(2\hat{g}^{\rho\sigma}\hat{g}_{\lambda\alpha}\hat{g}_{\kappa\beta} - \hat{g}^{\rho\sigma}\hat{g}_{\alpha\kappa}\hat{g}_{\lambda\beta} - 4\eta^\sigma_\kappa\eta^\rho_\lambda\hat{g}_{\alpha\beta}) \,, \end{aligned} \tag{5.7}$$

where a comma denotes an ordinary partial derivative and $\hat{g}^{\alpha\beta} = \sqrt{g}g^{\alpha\beta}$. When written in this form, it is easy to see that $\mathcal{L}_{EH}$ only has terms with $j = 2$, so we take all i-point graviton vertices as having two powers of momentum. Of course from an effective field theory point

of view [71] there should be higher order terms in R but this will serve only to increase j in the vertices. Since it is clear from equations (5.3), (5.5), and (5.6) that increasing the number of derivatives, j will only increase γ_{CO}, considering only the linear term in R gives the most infrared divergent case.

The coupling of matter to gravity is given by $\kappa h_{\mu\nu} T^{\mu\nu}$, where $T^{\mu\nu}$ is the energy momentum tensor of the matter field. For bosons, the energy momentum tensor has at least two derivatives, so this situation is similar to the pure gravity case. For fermions, the energy momentum tensor is proportional to $\bar{\psi}\gamma^{\mu}(\overrightarrow{\partial}^{\nu} - \overleftarrow{\partial}^{\nu})\psi$. However, for power counting purposes, using the Gordon identity we may replace γ^{ν} by ∂^{ν}/m, where m is the fermion mass. (For massless fermions, the vanishing normalization of spinors leads to simply ∂^{ν}.)

If we combine the Euler identity (note that for the jet subdiagram we consider "rest" to be a vertex so the number of vertices in the jet subdiagram is $\sum_i V_i + 1$),

$$L_J = N_J - \sum_{i \geq 3} V_i \,, \tag{5.8}$$

with equations (5.3), (5.4), (5.5), and (5.6) we get the relation,

$$\gamma_{CO} = \sum_{i \geq 3} (\frac{i}{2} - 2) V_i + \frac{1}{2} N_G + \frac{1}{2} \sum_j j \sum_{i \geq 3} V_{i,j} - \min[\frac{1}{2} \sum_j j \sum_{i \geq 3} V_{i,j}, \sum_k \frac{k}{2} N_k] \,. \tag{5.9}$$

Let us consider the case where

$$\min[\frac{1}{2} \sum_j j \sum_{i \geq 3} V_{i,j}, \sum_k \frac{k}{2} N_k] = \sum_k \frac{k}{2} N_k \,, \tag{5.10}$$

as this is the more divergent case (since the other option is available solely to prevent N_{num} having an artificially negative contribution to γ_{CO}). In this case,

$$\gamma_{CO} = \sum_{i \geq 3} (\frac{i}{2} - 2) V_i + \frac{1}{2} N_G + \frac{1}{2} \sum_j j \sum_{i \geq 3} V_{i,j} - \sum_k \frac{k}{2} N_k \,. \tag{5.11}$$

We readily deduce the consequences of this result.

5.2.1 Ladder Diagrams

As a first example, let us consider the simplest case of ladder diagrams (figure 5.3). In this case, we only have 3-point vertices, which have two powers of momentum, and no internal jet loops. Thus $i = 3$, and $j = 2$. For the case of gravitational couplings $k = 2$, so

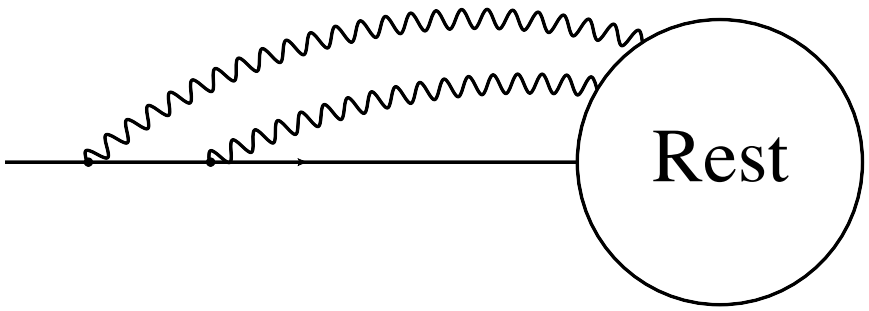

Figure 5.3 A typical ladder diagram.

$\sum_k \frac{k}{2} N_k = N_G$. Applying these conditions we have

$$\gamma_{CO} = -\frac{1}{2} V_3 + V_{3,2} - \frac{1}{2} N_G \,. \tag{5.12}$$

For ladder diagrams it is easy to see that $V_3 = V_{3,2} = N_G$, so we have $\gamma_{CO} = 0$, which corresponds to logarithmic divergence.

5.2.2 Diagrams with Only Three-Point Vertices

Once again we have $i = 3$, $j = 2$. So, $V_3 = V_{3,2}$ and again for gravitational couplings $\sum_k \frac{k}{2} N_k = N_G$. Therefore we (again) have

$$\gamma_{CO} = \frac{1}{2} (V_3 - N_G) \,. \tag{5.13}$$

Note in the case of diagrams with no internal jet loops as in figure 5.4, we have $V_3 = N_G$ and again we have a logarithmic collinear divergence. On the other hand, if we add any internal jet loops $V_3 > N_G$ and there is no collinear singularity. Adding a four-point (or higher) vertex will only increase the collinear degree of divergence and will prevent a mass divergence. Thus, the only diagrams that give mass divergences are those with no internal jet loops, and with only three-point vertices. These include the ladder diagrams discussed as the first example.

5.2.3 External Leg Corrections

As mentioned earlier, graviton lines that reattach to the same leg from which they were emitted are not considered as lines that attach onto "rest". This is because in this case the momenta at the two vertices the graviton line connects are collinear, so we get a numerator

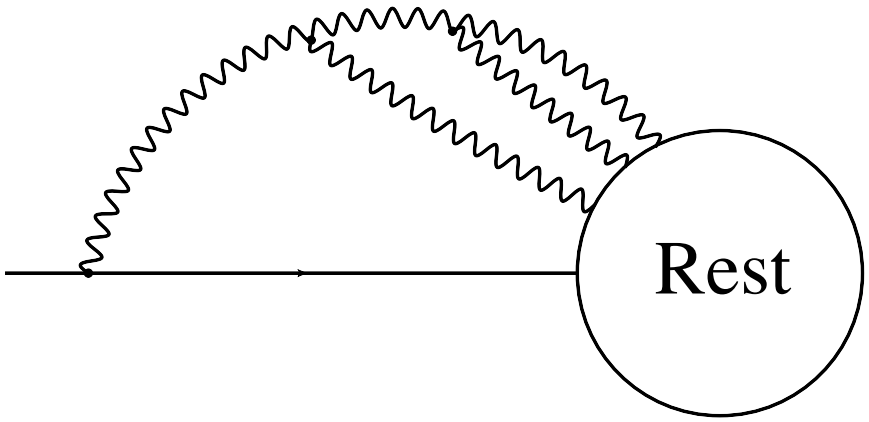

Figure 5.4 A diagram with no internal jet loops and only three point vertices.

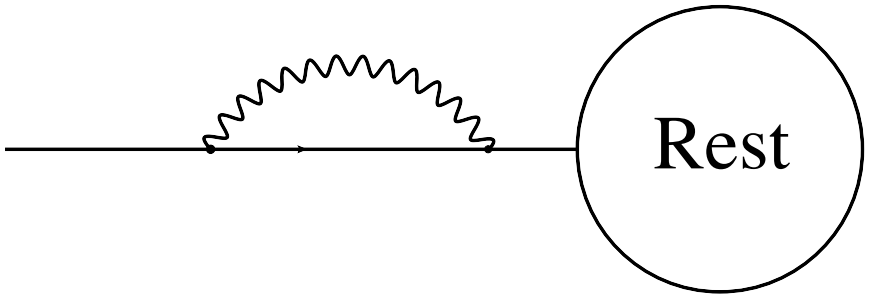

Figure 5.5 An example of an external leg correction. These do not result in collinear singularities.

factor that is quadratic in normal variables. Thus, these vertices do not contribute to the subtraction of N_k from momentum factors in the numerator in equation (5.5). Because of this, diagrams such as the one in figure 5.5 do not have collinear singularities. For figure 5.5 in particular, using (5.11) we see that $\gamma_{CO} = 1$. Gauge invariance ensures the cancellation of the single particle pole (which for power counting purposes corresponds to matching $+1$ from the normal variables of the numerator with -1 from the on-shell propagator.) We can see from equation (5.11) that adding further graviton lines cannot decrease the collinear degree of divergence wherever they are attached. Thus, self energy and other diagrams with graviton lines that reattach to the same leg from which they were emitted do not have collinear singularities.

5.2.4 Diagrams with Gravitons Turning into Standard Model Particles

Let us consider the case where a graviton emitted from one of the external line turns into standard model particles such as gluons. Such an example is given in figure 5.6. For this

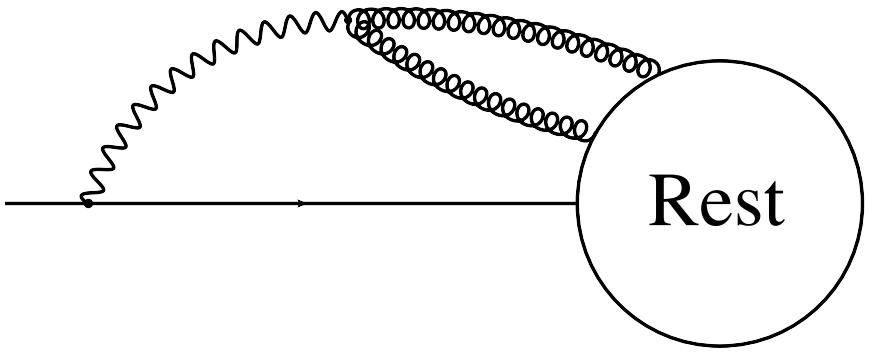

Figure 5.6 A graviton jet turning into two gluons.

particular case, (5.3) tells us that

$$\gamma_{CO} = 2(2) - 4(1) + N_{num} = N_{num}\,. \tag{5.14}$$

If the gluons were gravitons, according to (5.5) and (5.6), we would have $N_{num} = \frac{1}{2}(4)-2 = 0 = \gamma_{CO}$ and thus a logarithmic collinear singularity. This is because $k = 2$ for all vertices of "rest" to which gravitons attach. However, for the case of gluons we would have $k = 1$ for all vertices on "rest". This means that for the case of gluons, $N_{num} = \frac{1}{2}(4) - 1 = 1 = \gamma_{CO}$, so there is no collinear singularity. Note that since $\gamma_{CO} \geq 0$ for any diagram involving just gravitons, adding further graviton lines does not change the situation. Adding a higher point gluon-graviton vertex such as the one in figure 5.7 does not help, as in this case the the contribution to γ_{CO} from L_J and N_J will already be positive and N_{num} is at least zero. For instance, for the process shown in figure 5.7, $2L_J - N_J = 2$. Thus, it is impossible to have a collinear-divergent diagram with both standard model particles and gravitons where only the gravitons attach to the on-shell line. Precisely the same reasoning applies to the vector ghosts of quantum gravity [64, 65, 66], because, although their interactions with gravitons are not identical to those of photons or gluons, the numbers of derivatives at the vertex is the same.

In summary, we have found that collinear divergences may be found in diagrams: (1) with no internal jet loops, (2) with only three-point vertices among gravitons, and (3) that do not link gravitons to collinear standard model particles. We now turn to soft divergences.

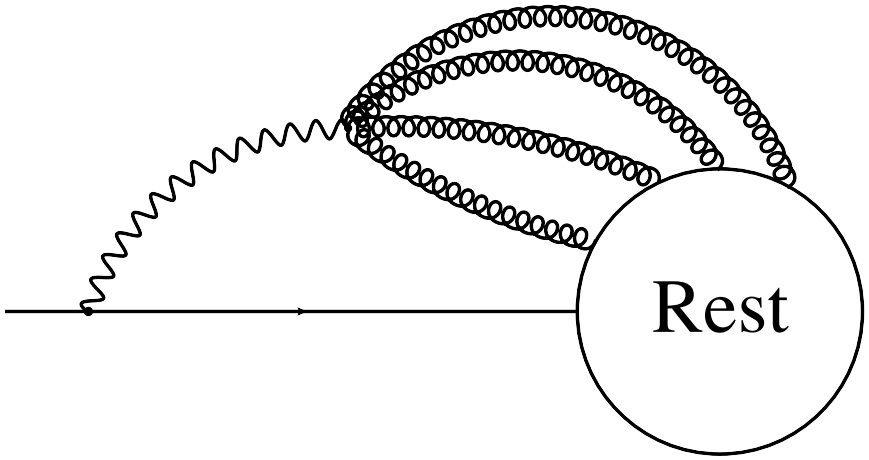

Figure 5.7 A graviton jet turning into four gluons.

5.3 Soft Power Counting

So far, we have concentrated on the "jet" subdiagrams of the arbitrary pinch surface represented in figure 5.1. We now describe the inclusion of interacting soft gravitons [55, 56], and show how our power counting arguments confirm the conclusion that to fixed order only ladder-like graphs show soft divergence, factorizable onto products of Wilson lines.

We can carry out power counting for soft divergences simultaneously with collinear divergences, by considering diagrams of the type shown in figure 5.8, which shows soft virtual graviton corrections to a hard vertex. All of the graviton lines in S are soft. Each solid line represents any set of collinear jet lines. In principle, the particles represented by the solid finite momentum lines can have any spin, as the dominant coupling of soft gravitons is to momentum flow, and independent of spin [53]. We now define, by analogy to (5.3) for the degree of collinear divergence, a degree of soft divergence,

$$\gamma_{soft} = 4L_S - 2N_S - N_E + N_{sn}\,, \tag{5.15}$$

where L_S is the number of loops in S, including loops that link S with the jets, N_S is the number of soft graviton lines, N_E is the number of virtual finite momentum lines in the diagram, and N_{sn} is the contribution of soft normal variables to the numerator (for clarification of these quantities, see the example given in figure 5.9). Specifically, we may take N_E to denote the *change* in the number of finite-momentum lines due to the attachment of soft gravitons to the jet. For simplicity, therefore, we choose the most singular case, in which all soft gravitons attach to the jets at vertices with only two finite-momentum lines.

For the soft subdiagram we can choose the normal variables to be all four components

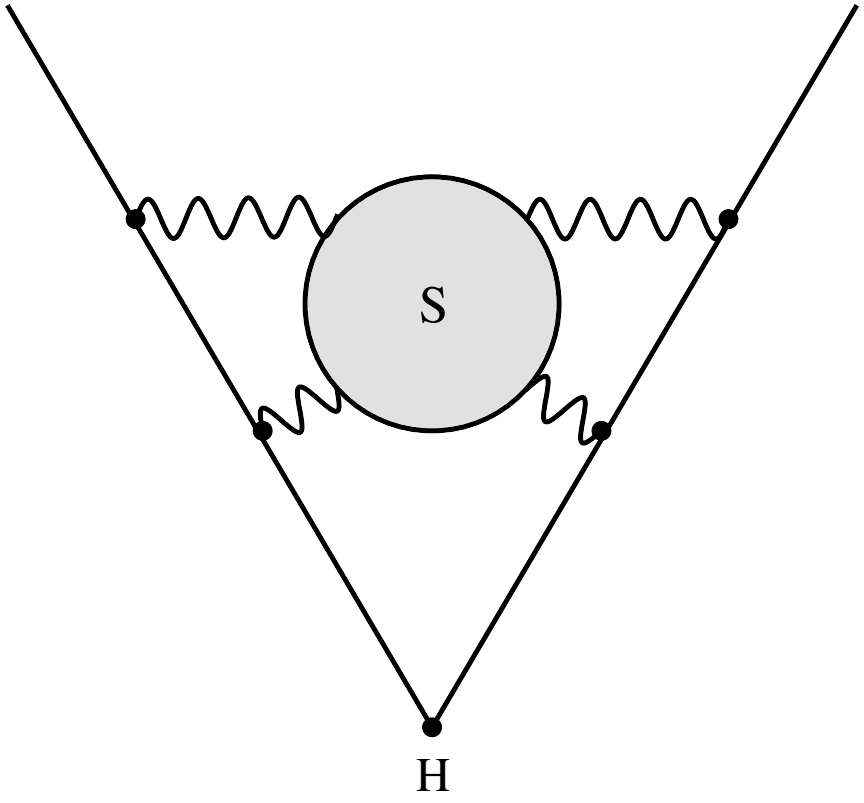

Figure 5.8 Arbitrary diagram with virtual soft graviton corrections to a hard vertex. The finite momentum lines are drawn with a solid line.

of the loop momenta, so that there is a factor of four times L_S in (5.15). With this choice, all soft graviton denominators are quadratic in normal variables, so there is a factor of minus two multiplying N_S. The denominators of the propagators corresponding to the (nearly on-shell) virtual finite momentum lines are, by contrast, linear in graviton momenta. Thus, N_E is associated with a factor of minus one. Notice that this requires the scales of normal variables for soft and collinear momenta to be the same. If, for example, the soft normal variables are larger than the collinear normal variables, the denominators of finite energy lines will be independent of the latter, which would eliminate collinear singularities.

The linearity of finite energy lines in soft normal variables, combined with the dominance of jet momenta in the coupling of soft gravitons to finite energy lines is equivalent to the eikonal approximation. We note that for wide angle scattering there are no additional pinches that would invalidate the eikonal approximation. We will return to this point below.

Using similar reasoning as with the case of collinear power counting we arrive at the

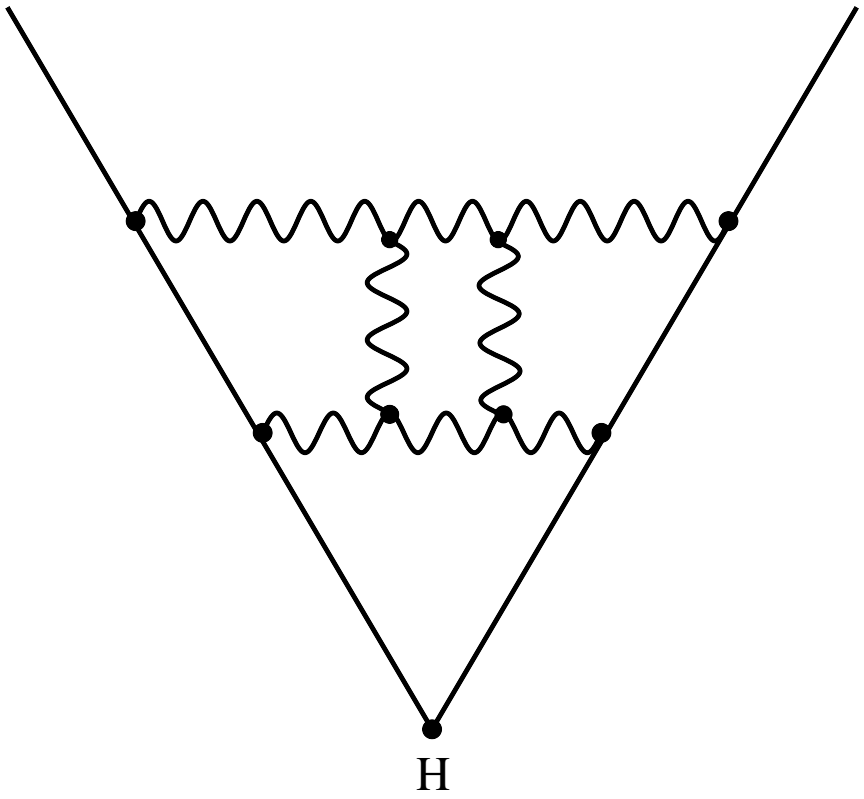

Figure 5.9 An example of the type of diagram that we discuss in section 5.3. In this diagram $L_S = 4$, $N_S = 8$, and N_E=4.

relations,

$$2N_S = \sum_{i\geq 3} iV_i + \sum_m mN_{hs}^{(m)} \,, \tag{5.16}$$

$$N_E = N_{hs} \,, \tag{5.17}$$

$$N_{sn} = \sum_j j \sum_{i\geq 3} V_{i,j} \,, \tag{5.18}$$

$$L_S = N_S + N_E - \sum_{i\geq 3} V_i - N_{hs} \,, \tag{5.19}$$

where again V_i is the number of i-point vertices in S and $V_{i,j}$ are the number i-point vertices in S with j powers of momentum. The term $N_{hs}^{(m)}$ is the number of vertices at which m soft lines attach to a finite momentum line, and $N_{hs} = \sum_m N_{hs}^{(m)}$. Note the vertices that count towards N_{hs} do not contribute to the homogeneity of normal variables from the numerator, N_{sn}, as their numerator momentum factors are given to leading power by the momenta of finite momentum lines, independent of soft normal variables. Combining equations (5.15),

(5.16), (5.17), (5.18), and (5.19), we get

$$\gamma_{soft} = \sum_{i\geq 3}(i-4)V_i + \sum_j j \sum_{i\geq 3} V_{i,j} + \sum_m m N_{hs}^{(m)} - N_{hs}\,. \tag{5.20}$$

Using this relation, we see that if there are no soft graviton vertices in S ($V_i = 0$, $V_{i,j} = 0$) and only vertices with one soft graviton attached to the finite momentum lines ($\sum_m m N_{hs}^{(m)} = N_{hs}^{(1)} = N_{hs}$) then $\gamma_{soft} = 0$, indicating a logarithmic soft divergence. An example of a diagram that gives a logarithmic divergence is shown in figure 5.10. On the other hand if there is even one soft vertex in S with $j \geq 2$ (as is the case for graviton vertices), or if there is even one vertex with more than one soft graviton coming off a finite momentum line (in which case $\sum_m m N_{hs}^{(m)} > N_{hs}$) then $\gamma_{soft} > 0$ and there is no soft divergence. Thus, in agreement with [55, 56] we have seen that the only diagrams that give rise to soft graviton divergences are ladder and crossed ladders with only three point vertices where the ladders attach to finite momentum lines.

The above conclusions apply whether or not the jet subdiagrams consist of single lines or contain loops. As we shall see in the next section, however, collinear singularities associated with nontrivial jet subdiagrams cancel, leaving only single finite-energy lines to couple to the soft gravitons. In this sense, the factorization of soft infrared gravitons conjectured in [55] is automatic, because as noted above, soft divergences are reproduced by considering only the linear dependence of finite-energy denominators on soft graviton momenta. In addition, as we have seen, infrared divergences are associated with the coupling of soft gravitons to a finite-energy graviton (or matter) line of momentum p through the vertex $\kappa p^\mu p^\nu$ only. Together, these features of soft graviton infrared divergences are precisely the perturbation theory rules of the Wilson lines described in [55], and this discussion serves as a proof of the conjecture there. The importance of the cancellation of collinear singularities was also noted in [56], and we now turn to a proof of this cancellation independent of the eikonal approximation for the collinear gravitons.

5.4 Cancellation of Collinear Singularities

In this section we give a general argument for the cancellation of gravitational collinear singularities using the basic gravitational Ward identity [80] that decouples unphysical graviton polarizations from physical processes. Our argument is independent of the eikonal approximation. A combinatoric proof of this cancellation along the lines of [53], in the special case of the eikonal approximation, is given in appendix D.

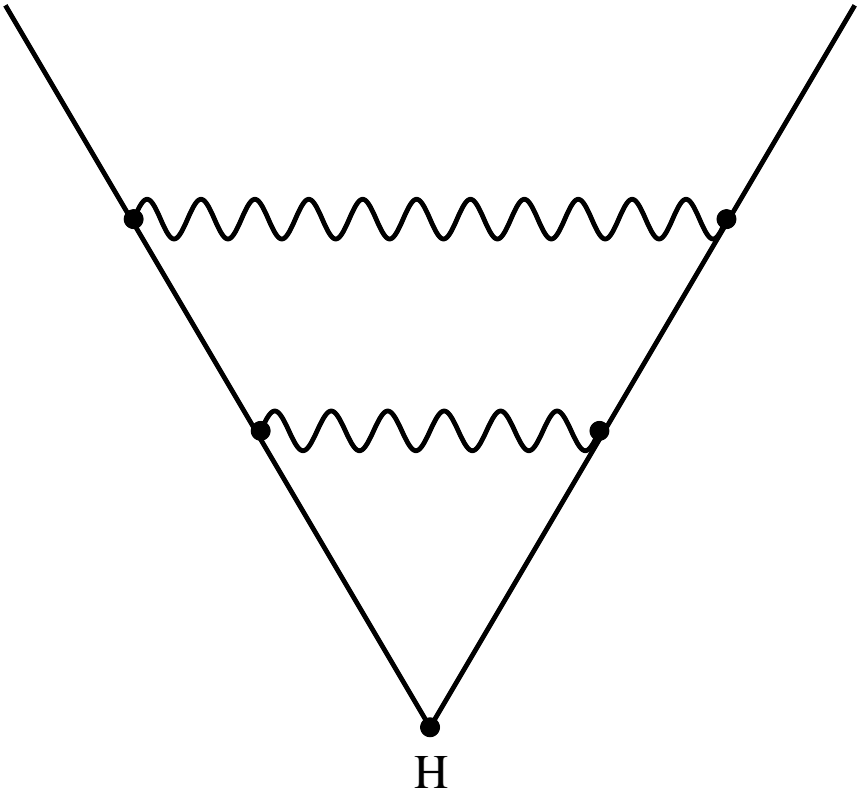

Figure 5.10 An example of a diagram with only three point couplings to hard lines that will lead to a soft divergence.

We have shown by power counting that collinear singularities require graviton jets that have no internal loops and only three point vertices. Let us consider the addition of such a jet to an arbitrary external line with momentum p^μ as in figure 5.2, where j gravitons with momentum l_i^μ and the now off-shell continuation of the original external line with momentum $p^\mu - \sum l_i^\mu$ attach to "rest". We can represent the matrix element corresponding to such a diagram as [78]

$$\begin{aligned} i\mathcal{M} = \int \frac{d^4 l_i}{(2\pi)^4} J(p^\mu - \sum_{i=1}^{j} l_i^{\mu_i}, \{l_i^{\mu_i}\})_{\{\mu_i \nu_i\}} \\ \times R(p^\mu - \sum_{i=1}^{j} l_i^{\mu}, \{l_i^{\mu_i}\})^{\{\mu_i \nu_i\}} , \end{aligned} \tag{5.21}$$

where R and J correspond to the "rest" and jet subdiagrams, respectively, and where $\{\mu_i \nu_i\}$ represent the $2j$ spacetime indices corresponding to the j collinear gravitons attached to "rest".

Since all the lines attaching to R from J have momenta collinear with the jet momentum

p^μ, we can isolate the leading power behavior near the collinear pinch surface, by making the replacement $l^\mu \to l_\alpha \bar{v}^\alpha v^\mu$, where we define the lightlike vectors $v^\mu = \delta^\mu_+$, and $\bar{v}^\mu = \delta^\mu_-$. Here we are working in the basis of normal variables where momentum vectors now have the components $l^\mu = (l^+, l^-, l_\perp)$ and $l^2 = 2l^+l^- - l_\perp^2$. After making this replacement and pulling out the factors of v^μ and $\bar{v}^\mu$, we can write the function J as

$$\begin{aligned} &J(p^\mu - \sum l_i^{\mu_i}, \{l_i^{\mu_i}\})_{\{\mu_i\nu_i\}} \\ \to &J(p^\alpha - \sum l_i^{\alpha_i}, \{l_i^{\alpha_i}\})_{\{\alpha_i\beta_i\}} \prod_i \bar{v}^{\alpha_i}\bar{v}^{\beta_i} v_{\mu_i} v_{\nu_i} \,. \end{aligned} \tag{5.22}$$

It is easy to see that to leading power in normal variables

$$\begin{aligned} &J(p^\alpha - \sum l_i^{\alpha_i}, \{l_i^{\alpha_i}\})_{\{\alpha_i\beta_i\}} \bar{v}^{\alpha_i}\bar{v}^{\beta_i} v_{\mu_i} v_{\nu_i} = \\ &\quad J(p^\alpha - \sum l_i^{\alpha_i}, \{l_i^{\alpha_i}\})_{\{\alpha_i\beta_i\}} \frac{n^{\alpha_i}}{n\cdot l_i}\frac{n^{\beta_i}}{n\cdot l_i} l_{i,\mu_i} l_{i,\nu_i} \,, \end{aligned} \tag{5.23}$$

for any vector n^α that is not collinear with l_i^μ by making the substitution $l^\mu \to l_\alpha \bar{v}^\alpha v^\mu$ on the right hand side of (5.23). Thus, we can write (5.21) as

$$\begin{aligned} i\mathcal{M} = \int \frac{d^4 l_i}{(2\pi)^4} &J(p^\alpha - \sum l_i^{\alpha_i}, \{l_i^{\alpha_i}\})_{\{\alpha_i\beta_i\}} \\ &\times \prod_i \frac{n^{\alpha_i}}{n\cdot l_i}\frac{n^{\beta_i}}{n\cdot l_i} l_{\mu_i} l_{\nu_i} \\ &\times R(p^\mu - \sum l_i^{\mu_i}, \{l_i^{\mu_i}\})^{\{\mu_i\nu_i\}} \,. \end{aligned} \tag{5.24}$$

This is known as the "collinear approximation" [78, 79]. We see from (5.24) that in the collinear approximation the j gravitons that attach to "rest" are longitudinally, or "scalar", polarized. This allows us to use the on-shell Ward identity for gravitons [80], which enforces the decoupling of such unphysical polarizations,

$$l_{\mu_j} l_{\nu_j} \mathcal{S}^{\cdots\mu_j\nu_j\cdots} = 0 \,. \tag{5.25}$$

where $\mathcal{S}^{\cdots\mu_j\nu_j\cdots}$ is an arbitrary S-matrix element with the polarization tensors factored out. For our particular case, we can apply the Ward identity to the subdiagram "rest", which includes an external line with momentum $p^\mu - \sum l_i^\mu$. In R, the latter may be considered on-shell with physical or scalar polarization, up to corrections that are higher order in normal variables. Diagramatically this can be expressed by figure 5.11, which corresponds a single longitudinally, or scalar, polarized graviton ($n = 1$) attached to "rest", which is drawn with

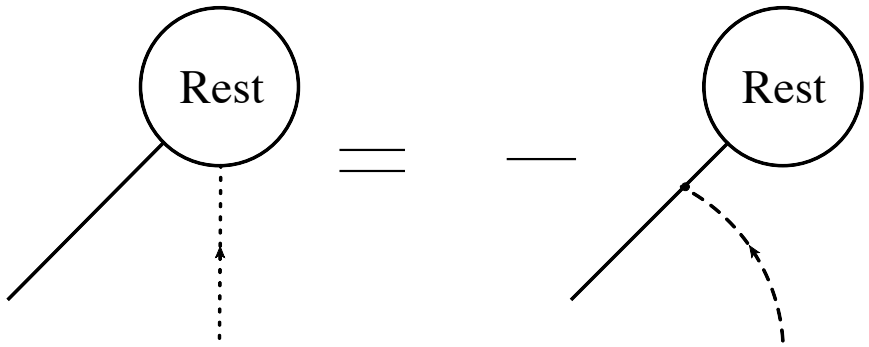

Figure 5.11 The Ward identity for the case $n = 1$

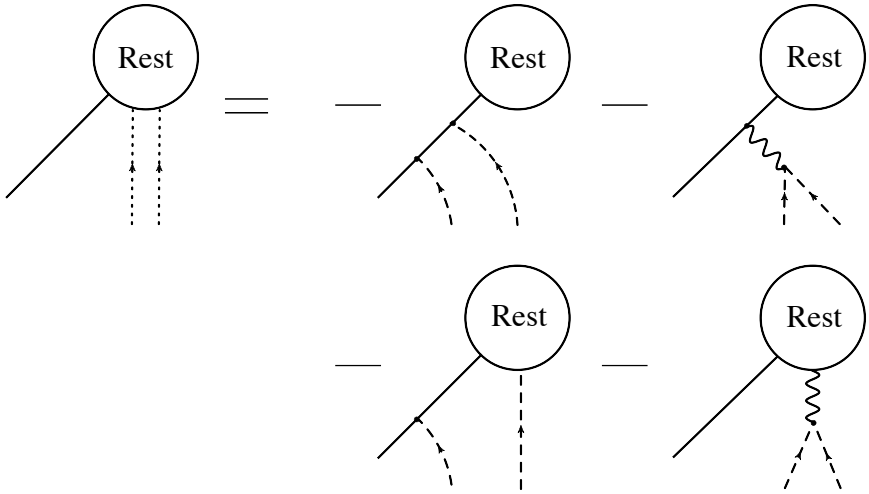

Figure 5.12 The Ward identity for the case $n = 2$. We do not explicitly show the diagrams where the longitudinal gravitons are interchanged.

a dotted line. The Ward identify (5.25) tells us that the sum of the diagrams shown on the left hand side of figure 5.11 and the attachment of the longitudinally polarized graviton on the external line shown on the right hand side is zero. The right hand side of figure 5.11 has the same collinear degree of divergence as a self energy correction, which we previously showed does not have a collinear singularity.

The application of the Ward identity to the case of two longitudinally polarized gravitons ($j = 2$) attached to "rest" is shown in figure 5.12. Note the first and third diagrams on the right hand side of figure 5.12 contain a self energy-like correction, so these are not collinearly divergent. The second and fourth diagrams result in an internal jet loop, and we know diagrams containing such loops are also not collinear-divergent. So there are no collinear singularities for this case either. Thus, the use of the Ward identities on (5.24) allows us to rule out any collinear singularity in the sum of diagrams contributing to it.

For gauge theories, by contrast, collinear singularities remain in the corresponding set of diagrams when the Ward identities are applied [78]. The application of this reasoning to collinear gauge particles results in the factorization, rather than cancellation, of collinear singularities.

It is clear that adding any number of longitudinally polarized gravitons and applying the Ward identity in the manner above will always result in either additional self energy-like corrections or internal jet loops, which as we have seen preclude collinear singularities. Thus, while diagrams where an external leg emits a graviton jet with no internal loops and only three point vertices may be divergent on a diagram by diagram basis, when we consider the attachment of such a jet with the rest of the diagram, the Ward identity insures that collinear singularities cancel. It is instructive to verify the cancellation for the case where collinear gravitons are relatively soft, so that we may apply the eikonal approximation. This is shown in appendix D.

5.5 Discussion

In this chapter we have introduced a power-counting procedure in order to see what types of reduced diagrams yield collinear and soft divergences in perturbative quantum gravity. For the fixed-angle elastic scattering amplitudes that we have considered, we find that the only types of reduced diagrams that give soft divergences are those of the ladder and crossed ladder type, where the soft gravitons interact only with finite momentum lines and not with each other [55, 56]. These diagrams give rise to logarithmic soft divergences, which do not cancel when all diagrams of a given order are summed for an amplitude with fixed external lines.

For the case of collinear singularities, we see that the only types of diagrams that give mass divergences are those with no internal jet loops and only three-point vertices. These include the ladder and crossed ladder diagrams [53]. When all possible diagrams of this class are summed the Ward identity insures that the collinear singularities cancel. This is in contrast to the case of massless QCD or other massless gauge theories, where collinear singularities factorize rather than cancel.

The absence of collinear singularities has its basis in classical physics, where gravitational radiation is more suppressed in the collinear direction than electromagnetic radiation. Indeed, the leading multipole contributing to electromagnetic radiation is dipole while for gravitational radiation it is quadrupole. This can be seen conveniently in the rates of the lowest order modes of radiation in the two theories [81]. For electromagnetic radiation

sourced by an electric dipole with dipole moment p oscillating with frequency ω, the energy rate is

$$\frac{d^2E}{d\Omega dt} = \omega^2(\frac{\omega^2 p^2}{8\pi c^3})\sin^2\theta\,. \tag{5.26}$$

For gravitational radiation sourced by a mass M with trajectory $\mathbf{R}(t) = \mathbf{R}_0 \sin\omega t$ the energy rate is

$$\frac{d^2E}{d\Omega dt} = \frac{G\omega^6 M^4 R_0^4}{4\pi c^3}\sin^4\theta, \tag{5.27}$$

which clearly shows the additional suppression in the forward direction. As we will see in chapter 6, this absence of collinear singularities in gravity can have interesting consequences for gauge theories as well.

The discussion in this chapter has dealt with wide-angle scattering only. These methods may be useful as well, however, in studies of higher order corrections for the Regge limit in quantum gravity [82, 83, 84], and of higher-order cancellations between virtual and real radiation.

Chapter 6

Relationship Between Gravity and Gauge Scattering in the High Energy Limit

6.1 Introduction

In the previous chapter we saw that infrared divergences in perturbative quantum gravity have interesting and simple structure. Another facet of this theory that has been an object of great interest is the relationship between gravity and gauge theory amplitudes [7, 85]. This relationship is thought to endure to all loop orders and would imply a much deeper relationship between gravity and gauge theories than is apparent at the Lagrangian level. It is this connection we wish to explore further in this chapter in the context of a simplified approximation scheme, the eikonal approximation, relevant for high energy large s and small t scattering. It has been known for some time [86] that there is a relationship between the amplitudes in the eikonal scheme to the scattering of a quantum particle in a classical shockwave background. In an attempt to extend the double copy relation beyond the domain of scattering amplitudes, we also explore the relationship between the relevant shockwave solutions in gravity and gauge theories. Our results support the double copy conjecture on both fronts.

High-energy graviton-graviton scattering in the eikonal approximation has attracted interest because of the potential relevance of the large s small t regime to black hole production [6, 86, 87, 88, 89, 90, 91, 92]. Furthermore, this approximation scheme has been used to investigate gravitational infrared divergences, which have been shown to have an elegant and simple structure [11, 53, 93]. For the purposes of this chapter, a key result of these investigations, which holds beyond the eikonal approximation, is that for scattering amplitudes in perturbative quantum gravity, the collinear divergences completely cancel to all loop orders. This will be used to identify the class of gauge theory diagrams that partici-

pate in the double copy relation with the gravity amplitudes in the eikonal approximation. Within this class of diagrams, the collinear divergences cancel amongst themselves. As we will discuss later, there are many other gauge theory diagrams with different group structure that are present in the eikonal approximation. For the double copy conjecture to work, the collinear divergences must cancel between these separately. This has not been explicitly verified in this chapter, and would be an interesting subject for future research.

In light of these new developments, as mentioned above, we have investigated whether or not it is possible to elucidate a double copy relationship between gravity and gauge theory amplitudes in the eikonal approximation. Some progress along these lines has been made in [94], where the insertion of infrared gravitons and gluons into a tree level diagram with hard momentum exchange was investigated. The results of this investigation upheld the double copy conjecture in the infrared approximation to all loop orders. However, in this chapter we will be considering high energy scattering at large s and small t where there is no hard momentum transfer at all. This situation is drastically different for a number of reasons. First, the large s and $|u|$ limit is such that the number of diagrams contributing at leading order in $1/s$ is reduced greatly. Secondly, in this approximation the numerator factors do not contain any factors of the loop momenta, as these are suppressed compared to the external momenta. Thus the numerator factors are uniquely fixed in terms of the external momenta in both the gauge theory and the gravity side. In a certain sense this makes the analysis easier. On the other hand, the arguments of [7, 85] do not directly apply to such a situation. Fortunately, the fact that collinear divergences in gravity cancel allows us to identify which gauge theory diagrams participate in the double copy relation.

Another aspect of the relationship between eikonalized gravity and gauge theory amplitudes that we have explored in this chapter concerns classical shockwave solutions [95, 96, 97]. We detail a new method to directly derive both gravity and gauge shockwaves using eikonalized field-theoretic methods, and show that due to the direct nature of this derivation these shockwaves reflect the double copy relation as well. This double copy relation is only clearly seen in a certain gauge, which seems to be a generic property of such relations. We would like to emphasize that this is one of the few instances where a double copy relation has been studied for classical solutions to the two theories in question and that in order to make this analysis we necessarily had to restrict ourselves to the eikonal regime where there is no hard momentum transfer.

A pedagogical review of eikonal graviton-graviton scattering is given in section 6.2.1. Analogous gluon-gluon scattering results and the restrictions necessary to get a double copy relation are described in section 6.2.2. The resultant eikonal double copy relation is described in section 6.2.3. In sections 6.3.1 and 6.3.2 we derive respectively the gravity and

QCD shockwaves before describing their relationship in section 6.3.3. In the final section we review our results.

6.2 Eikonal Scattering

In this section we present results on high-energy graviton-graviton and gluon-gluon scattering in the eikonal limit, with incoming momentum (p, q) and outgoing momentum (p', q'). As mentioned previously, we will work in the kinematic limit of large s and small t and keep only the leading contributions. Thus, up to corrections of order $1/s$, only the t channel exchange diagrams contribute. Also in keeping with the eikonal approximation, we will neglect all the loop momenta in the numerator factors, and replace the denominators of all propagators by the rule:

$$(P + K)^2 - m^2 + i\epsilon \to 2P \cdot K + i\epsilon, \tag{6.1}$$

where, P is an external momentum and K denotes any combination of internal loop momenta. We will begin with a review of graviton-graviton scattering before moving on to the case of gluon-gluon scattering.

6.2.1 Gravity

Let use start with a review of the gravity case in order to establish our conventions and because we will be using these results in later sections. We will be working in the de Donder gauge and the frame where $\Delta = p' - p$ is such that $\Delta^0 = \Delta^z = 0$, in coordinates where $\mathbf{p}$ is in the positive z-direction and $\mathbf{q}$ is in the negative z-direction. This is the center of momentum frame in the kinematic regime where we can ignore the transferred momentum compared to the incoming and outgoing momenta.

Tree Level

Let us first work with the simplest case where only a single graviton is exchanged (figure 6.1). In this case, the matrix element corresponding to this diagram is:

$$\mathcal{M}_1 = (-\frac{i\kappa}{2})^2 \frac{i}{2} \frac{L_{\mu\nu\alpha\beta}}{\Delta^2 + i\epsilon} \tau^{\alpha\beta\gamma\delta\sigma\eta}(p) \tau^{\mu\nu\omega\epsilon\rho\lambda}(q) \epsilon_{\gamma\delta}(p) \epsilon_{\rho\lambda}(q) \epsilon^*_{\sigma\eta}(p) \epsilon^*_{\omega\epsilon}(q) \tag{6.2}$$

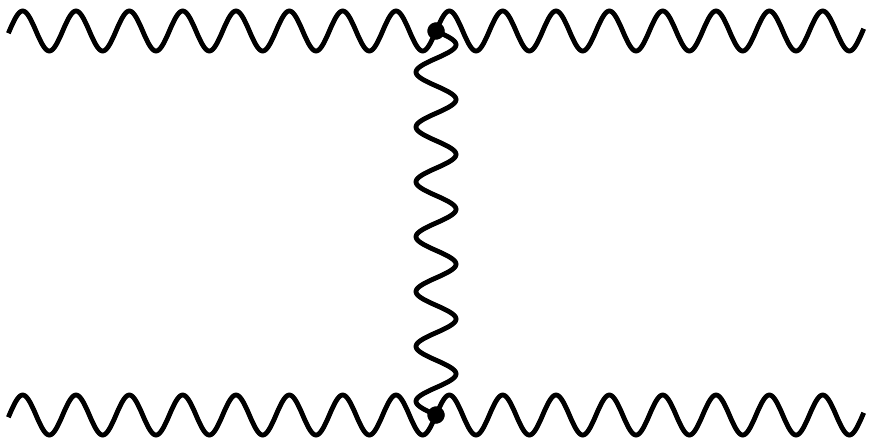

Figure 6.1 A scattering process with a single graviton/gluon exchanged.

where:

$$L_{\mu\nu\alpha\beta} = \eta_{\mu\alpha}\eta_{\nu\beta} + \eta_{\mu\beta}\eta_{\nu\alpha} - \eta_{\mu\nu}\eta_{\alpha\beta} \tag{6.3}$$

is the numerator of the de Donder gauge graviton propagator and

$$\tau^{\mu\nu\omega\epsilon\rho\lambda}(q) \approx q^{\mu}q^{\nu}L^{\omega\epsilon\rho\lambda} \tag{6.4}$$

is the three graviton vertex in the eikonal limit. Thus, we have for the one graviton exchange amplitude:

$$\mathcal{M}_1 = (-\frac{i\kappa}{2})^2 \frac{is^2}{\Delta^2 + i\epsilon}. \tag{6.5}$$

One-Loop

Let us now consider the scattering process where two gravitons are exchanged. At this order there are two diagrams, the box and the crossed box (figures 6.2 and 6.3). In this case, the matrix element becomes:

$$\begin{aligned}\mathcal{M}_2 = (-\frac{i\kappa}{2})^4 \frac{1}{16} L_{\gamma'\delta'\sigma'\eta'} L_{\rho'\lambda'\omega'\epsilon'} \tau^{\alpha_2\beta_2\sigma'\eta'\sigma\eta}(p) \tau^{\alpha_1\beta_1\gamma\delta\gamma'\delta'}(p) \tau^{\mu_1\nu_1\rho'\lambda'\rho\lambda}(q) \tau^{\mu_2\nu_2\omega\epsilon\omega'\epsilon'}(q) \\ \times \int \frac{d^4k_1 d^4k_2}{(2\pi)^4} \delta(k_1 + k_2 + \Delta) \frac{1}{k_1^2 + i\epsilon} \frac{1}{k_2^2 + i\epsilon} \frac{1}{-2p \cdot k_1 + i\epsilon} \\ \times [\frac{L_{\alpha_1\beta_1\mu_1\nu_1} L_{\alpha_2\beta_2\mu_2\nu_2}}{2q \cdot k_1 + i\epsilon} + \frac{L_{\alpha_1\beta_1\mu_2\nu_2} L_{\alpha_2\beta_2\mu_1\nu_1}}{2q \cdot k_2 + i\epsilon}] \epsilon_{\gamma\delta}(p) \epsilon_{\rho\lambda}(q) \epsilon^*_{\sigma\eta}(p) \epsilon^*_{\omega\epsilon}(q)\end{aligned} \tag{6.6}$$

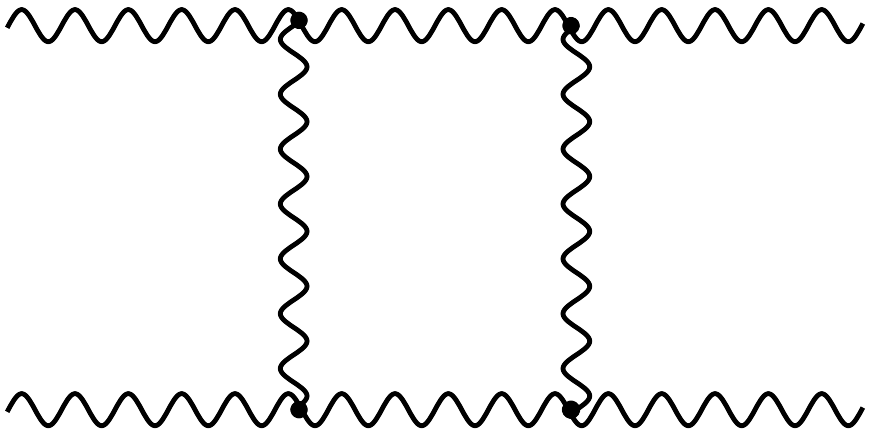

Figure 6.2 The box diagram.

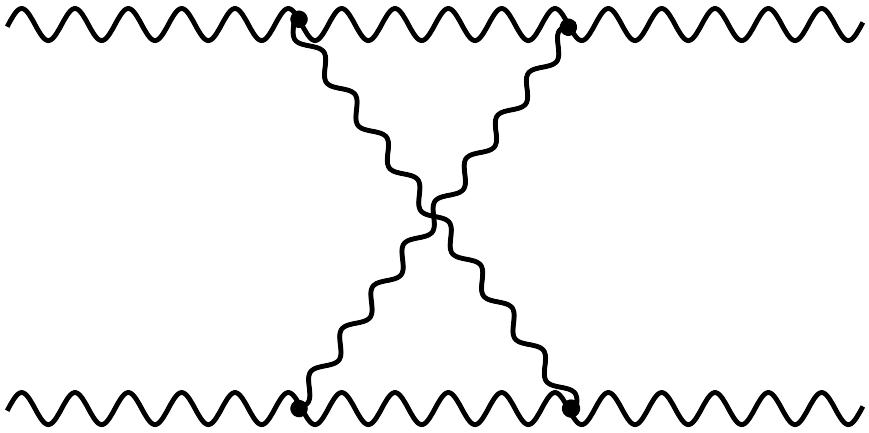

Figure 6.3 The crossed box diagram.

where the sum on the third line is the sum over the two diagrams. It is apparent that even at the one-loop level there are a huge amount of internal space-time indices. The situation greatly simplifies when one uses the identities:

$$\begin{aligned}
\tau^{\alpha_1\beta_1\gamma\delta\gamma'\delta'}(p)\tau^{\mu_1\nu_1\rho'\lambda'\rho\lambda}(q)L_{\alpha_1\beta_1\mu_1\nu_1} &= \frac{s^2}{2}L^{\gamma\delta\gamma'\delta'}L'^{\lambda'\rho\lambda} \\
L^{\gamma\delta\gamma'\delta'}L_{\gamma'\delta'\sigma'\eta'}L^{\sigma'\eta'\sigma\eta} &= 4L^{\gamma\delta\sigma\eta} \\
L^{\gamma\delta\sigma\eta}\epsilon_{\gamma\delta}(p)\epsilon^*_{\sigma\eta}(p) &= 2.
\end{aligned} \tag{6.7}$$

That is, each "rung" of the ladder gives a factor $\frac{s^2}{2}$, each propagator on the two "legs" of the ladder gives a factor of 4, and there is an overall factor of 4 coming from the contractions of the polarization tensors. So, with our normalizations, the contraction of all the space-time indices in a ladder or crossed ladder diagram gives a factor of $\frac{1}{4}(8s^2)^n$, where n is the number of gravitons exchanged.

Thus we have that:

$$\mathcal{M}_2 = (-\frac{i\kappa}{2})^4 s^4 \int \frac{d^4k_1 d^4k_2}{(2\pi)^4}\delta(k_1+k_2+\Delta)\frac{1}{k_1^2+i\epsilon} \times \frac{1}{k_2^2+i\epsilon}\frac{1}{-2p\cdot k_1+i\epsilon}[\frac{1}{2q\cdot k_1+i\epsilon}+\frac{1}{2q\cdot k_2+i\epsilon}]. \tag{6.8}$$

$n-1$ Loop

Let us now consider the case where n gravitons are exchanged within the diagram. In this case after applying the identities in (6.7) we have:

$$\mathcal{M}_n = -(-\frac{i\kappa}{2})^{2n}(-is^2)^n \int \frac{\prod_i^n d^4k_i}{(2\pi)^{4n-4}}\delta(\sum_i^n k_i+\Delta) \times \prod_i^n \frac{1}{k_i^2+i\epsilon}\prod_i^{n-1}\frac{1}{-2p\cdot K_i+i\epsilon}\sum_{\text{perms}}[\prod_i^{n-1}\frac{1}{2q\cdot K_i+i\epsilon}] \tag{6.9}$$

where $K_i \equiv \sum_j^i k_j$ and the sum over permutations in the last line generates all of the distinct ladder and crossed ladder diagrams at this loop order.

Exponentiation

We will now proceed to show that the expression for the $n-1$ loop scattering amplitude (6.9) implies that the eikonal amplitude exponentiates. We will find it useful to evaluate this integral in light-cone coordinates. We then have:

$$\mathcal{M}_n = 2s(-\frac{i\kappa}{2})^{2n}(\frac{is}{2})^n \int \frac{\prod_i^n dk_{i+}dk_{i-}d^2k_{i\perp}}{(2\pi)^{4n-4}}\delta(\sum_i^n k_{i+})\delta(\sum_i^n k_{i-})\delta(\sum_i^n k_{i\perp}+\Delta_\perp) \times \prod_i^n \frac{1}{k_i^2+i\epsilon}\prod_i^{n-1}\frac{1}{K_{i-}-i\epsilon}\sum_{\text{perms}}[\prod_i^{n-1}\frac{1}{K_{i+}+i\epsilon}]. \tag{6.10}$$

We will find it very useful to use the identity (a proof is outlined in appendix E for completeness):

$$\delta(\omega_1+...+\omega_n)\sum_{\text{Perms of }\omega_i}\frac{1}{\omega_1+i\epsilon}...\frac{1}{\omega_1+...+\omega_{n-1}+i\epsilon} = (-2\pi i)^{n-1}\delta(\omega_1)...\delta(\omega_n) \tag{6.11}$$

over the k_{i+} coordinates to arrive at:

$$\mathcal{M}_n = 2is(-\frac{i\kappa}{2})^{2n}(-\frac{s}{2})^n \times \int \frac{\prod_i^n dk_{i-}d^2k_{i\perp}}{(2\pi)^{3n-3}}\delta(\sum_i^n k_{i-})\delta(\sum_i^n k_{i\perp}+\Delta_\perp)\prod_i^n \frac{1}{k_{i\perp}^2}\prod_i^{n-1}\frac{1}{K_{i-}-i\epsilon}. \tag{6.12}$$

We can then symmetrize the integrand in the k_{i-} coordinates and again use (6.11) to arrive at:

$$\mathcal{M}_n = -\frac{2s}{n!}(-\frac{i\kappa}{2})^{2n}(\frac{is}{2})^n \int \frac{\prod_i^n d^2k_{i\perp}}{(2\pi)^{2n-2}}\delta(\sum_i^n k_{i\perp}+\Delta_\perp)\prod_i^n \frac{1}{k_{i\perp}^2}. \tag{6.13}$$

If we then Fourier transform the amplitude into impact parameter space we arrive at:

$$\begin{aligned}\mathcal{N}_n &= \frac{1}{(2\pi)^2}\int d^2\Delta_\perp \mathcal{M}_n e^{-ib_\perp\cdot\Delta_\perp} \\ &= -\frac{2s}{n!}[\frac{-i\kappa^2 s}{8}\int \frac{d^2k_\perp}{(2\pi)^2}\frac{1}{k_\perp^2}e^{ib_\perp\cdot k_\perp}]^n.\end{aligned} \tag{6.14}$$

So we see that when we sum over all n we have for our full Fourier transformed amplitude:

$$\mathcal{N} = -2s[e^{i\chi}-1] \tag{6.15}$$

where:

$$\chi = -\frac{\kappa^2 s}{8}\int \frac{d^2k_\perp}{(2\pi)^2}\frac{1}{k_\perp^2}e^{ib_\perp\cdot k_\perp}. \tag{6.16}$$

This reproduces the well known result that the amplitude exponentiates in impact parameter space.

6.2.2 QCD

In this section we identify the set of gauge theory amplitudes at each loop order that can participate in a double copy relation with the gravity amplitudes derived in the previous section in the eikonal approximation. To be specific, we seek a double copy relation which relates the gravity amplitudes to two gauge theory amplitudes, both of which are in the eikonal approximation. As mentioned previously, an important constraint is that on the gauge theory side, all the collinear divergences have to cancel. This constraint becomes relevant because

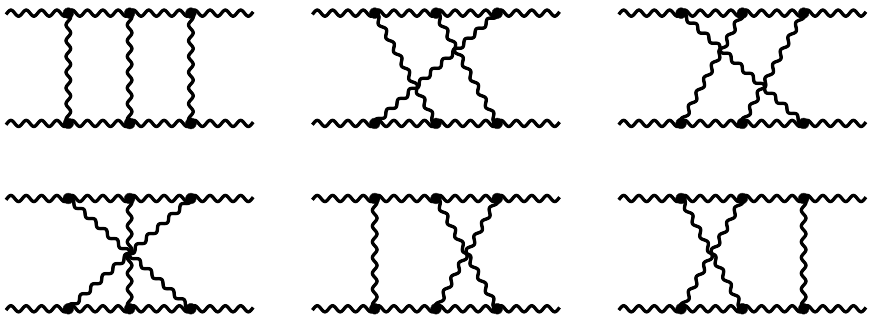

Figure 6.4 The set of two-loop ladder diagrams relevant for the double copy relation in the eikonal approximation. For the same color factors the collinear divergences between these cancel.

for gauge theories there are more diagrams in the leading eikonal approximation than those discussed in the previous section for the gravity case.

While it is well known that only ladder and crossed ladder diagrams contribute to the graviton scattering amplitude at leading eikonal order, this is not the case for nonabelian gauge theories such as QCD. The eikonal approximation in QCD has been extensively studied in the context of the Reggeization phenomenon. [98] depicts all the diagrams to the third loop order and summarizes the result of investigations in this area. For an interesting attempt to investigate high-energy QCD scattering using less standard methods, see [99], who model the scattering process as a simplified two dimensional effective field theory.

One of the big differences between QCD and gravity at the one loop order stems from the fact that the corresponding box and crossed box diagrams (figures 6.2 and 6.3) come with different color factors. Each of the corresponding Feynman integrals contributes a $\ln s$ term coming from a collinear divergence and for gravity these $\ln s$ terms cancel between the two diagrams. However, this cancellation is prevented in QCD because of the different color factors for the two diagrams.

For example, at the one loop level the box graph has a color factor of $(T^aT^b)_{ij}(T^aT^b)_{kl}$, whereas the the crossed box gives $(T^aT^b)_{ij}(T^bT^a)_{kl}$. Here, T^a are the matrices in the adjoint representation and (ij) and (kl) denote the color indices of the external gluons. We may rewrite the color factor of the crossed box as $(T^aT^b)_{ij}(T^bT^a)_{kl} = (T^aT^b)_{ij}(T^aT^b)_{kl} + \frac{3}{2}(T^a)_{ij}(T^a)_{kl}$. Thus the sum of the two diagrams now has a piece proportional to the same color factor $(T^aT^b)_{ij}(T^aT^b)_{kl}$ and a piece which has the same color factor as the tree level diagram. The piece proportional to $(T^aT^b)_{ij}(T^aT^b)_{kl}$ is just like the contribution in gravity for which the $\ln s$ terms cancel, and the term proportional to $\frac{3}{2}(T^a)_{ij}(T^a)_{kl}$ contains a $\ln s$ term which together with similar pieces from higher orders containing higher powers of $\ln s$ terms then Reggeizes the one gluon exchange amplitude [98, 100]. The key point now is that it is only the first type of contribution which is relevant

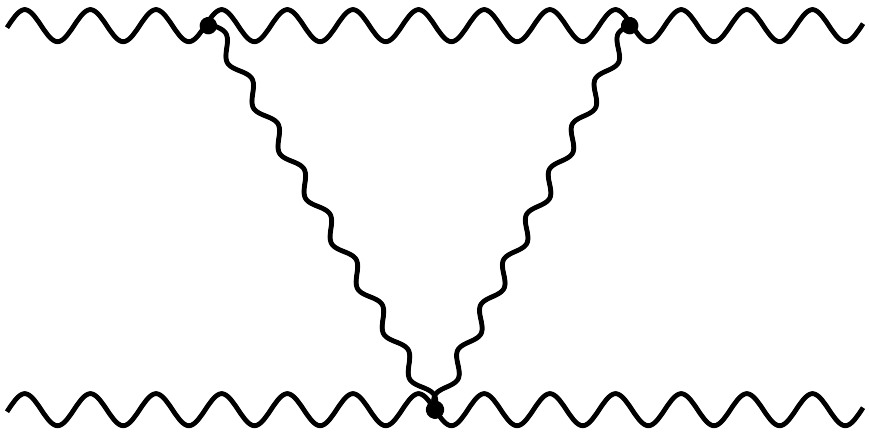

Figure 6.5 The seagull diagram.

for the double copy relation. This is because the leading numerator factors in the eikonal approximation have no dependence on loop momenta, so these logarithms will persist even once the double copy conjecture is applied. However, as collinear singularities are known to be absent in gravitational amplitudes, we will need to systematically restrict our attention to a subset of the QCD amplitudes that has no such logarithms. When the double copy relation is applied to the full gauge theory the cancellation of those $\ln s$ terms which are responsible for gluon Reggeization proceeds through terms other than those given by the leading eikonal approximation and the exact mechanism for this is beyond the scope of this chapter. (The fact that all the collinear divergences do cancel in the gauge theory side once the exact double copy relations are applied has been explicitly checked at fixed order for some theories in [101]). As we discuss later in this section, this argument can be easily extended to higher loop orders and the net result is the following: In order to eliminate the $\ln s$ contributions which arise from collinear divergences, we restrict our attention only to those diagrams in the scattering amplitude that are same ones as considered for the case of gravitational eikonal scattering and have the common color structure of an uncrossed ladder diagram (for instance, the color factors associated with figure 6.2 and the first diagram of figure 6.4 at orders g^4 and g^6, respectively). The fact that the $\ln s$ dependence in such terms cancel through sixth-order in the coupling constant was seen in [98, 100]. We show this cancellation endures to all orders in the following sections.

Before we proceed to a systematic discussion of the class of diagrams of interest to us for checking the double copy relation in the eikonal approximation, we would like to comment on the contributions of the seagull and the triangle type diagrams shown in figure 6.5 and figure 6.6 respectively.

Let us begin with diagrams with seagull type interactions (for example figure 6.5). We

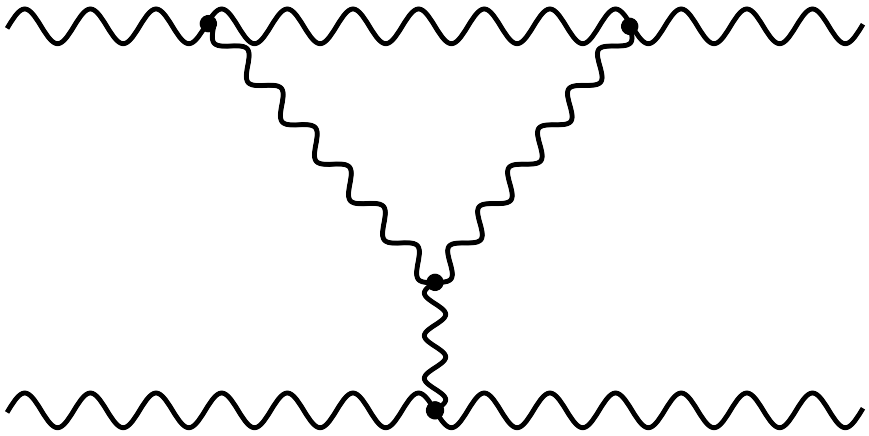

Figure 6.6 The triangle diagram.

will show that these are subleading in the eikonal approximation even for the case of gauge theories. In order to see this, note that the Feynman integral for this diagram is:

$$I_{\text{sea}} = \int \frac{dk_{1+}dk_{2+}dk_{1-}dk_{2-}d^2k_{1\perp}d^2k_{2\perp}}{(2\pi)^4}\delta(k_{1+}+k_{2+})\delta(k_{1-}+k_{2-}) \\ \times \delta^2(k_{1\perp}+k_{2\perp}+\Delta_\perp)\frac{1}{k_{1+}k_{2+}q_-}\frac{1}{k_{1-}-\frac{k_{1\perp}^2}{k_{1+}}+\frac{i\epsilon}{k_{1+}}}\frac{1}{k_{2-}-\frac{k_{2\perp}^2}{k_{2+}}+\frac{i\epsilon}{k_{2+}}}\frac{1}{k_{1+}+i\epsilon} \quad (6.17)$$

We have assumed there are two vertices attaching onto the bottom leg but switching to the case where two vertices attach to the upper leg is trivial. Using the delta function over k_{2-} we have:

$$I_{\text{sea}} = -\int \frac{dk_{1+}dk_{2+}dk_{1-}d^2k_{1\perp}d^2k_{2\perp}}{(2\pi)^4}\delta(k_{1+}+k_{2+}) \\ \times \delta^2(k_{1\perp}+k_{2\perp}+\Delta_\perp)\frac{1}{k_{1+}k_{2+}q_-}\frac{1}{k_{1-}-\frac{k_{1\perp}^2}{k_{1+}}+\frac{i\epsilon}{k_{1+}}}\frac{1}{k_{1-}+\frac{k_{2\perp}^2}{k_{2+}}-\frac{i\epsilon}{k_{2+}}}\frac{1}{k_{1+}+i\epsilon} \quad (6.18)$$

Now let us consider the integration over k_{1-}. Due to the delta function $\delta(k_{1+}+k_{2+})$ we see that both poles in k_{1-} must lie on the same side of the real axis. Now, it is well known (for a pedagogical discussion see [63]) that infrared sensitive effects only arise from pinch singular points. Because of this, it is easy to see that the above does not contain any infrared effects. Thus a Feynman integral with eikonalized propagators will not have any leading-order contributions for diagrams with a seagull interaction.

Note that we can extend the above reasoning for the case of diagrams with a three point interaction at one loop order as in figure 6.6. This is because the only difference between the Feynman integral of the seagull diagram (figure 6.5) and the triangle diagram (figure

6.6) are numerator factors of k_{i+}, which do not alter the presented argument.

Keeping these things in mind, in this section we give the expressions for the matrix elements of diagrams contributing to high-energy gluon-gluon scattering at leading eikonal order. As discussed earlier, we only retain terms with the color structure corresponding to uncrossed ladder diagrams and keep only the lowest order coefficient of each color factor. We explicitly show what we mean by this below.

Tree Level

We will start by stating the tree level result. This is straightforward at leading eikonal order since any of the polarization vectors contracted with its own momenta gives zero, which kills all of the factors in the three-gluon vertex at leading eikonal order except for one from each vertex.:

$$\begin{aligned}\mathcal{A}_1 &= i\frac{g^2}{\Delta^2}g^{\alpha\beta}g^{\rho\sigma}(p+p')\cdot(q+q')f_{acb}f_{ade}\epsilon_\alpha(p)\epsilon_\rho(q)\epsilon^*_\beta(p')\epsilon^*_\sigma(q') \\ &\approx i\frac{2g^2 s}{\Delta^2}F_1 \end{aligned} \tag{6.19}$$

where we have written the color factor as $F_1 = (T^a)_{ij}(T^a)_{kl}$.

One-Loop

Let us now move on to the one-loop level. Much like in the graviton scattering case, at leading eikonal order the kinematic factors in the vertices have a very simple structure.

This is due to the fact that the eikonalized three-gluon vertex gives a factor of $2iT^a g_{\alpha\beta}p_\mu$ on the top leg and a factor of $2iT^a g_{\alpha\beta}q_\mu$ on the bottom leg. This is because all other vertex factors are proportional to momenta that will contract with either itself or their corresponding polarization vector. As the factors of $g^{\alpha\beta}$ in the vertices contract to give a factor of $\epsilon\cdot\epsilon^* = 1$, we are left with a factor of $-2s$ for each "rung" of the ladder, multiplied by a diagram dependent color factor. Thus at one-loop we have for the matrix element:

$$\begin{aligned}\mathcal{A}_2 = 4s^2 g^4 \int \frac{d^4k_1 d^4k_2}{(2\pi)^4}\delta(k_1+k_2+\Delta)\frac{1}{k_1^2+i\epsilon} \\ \times \frac{1}{k_2^2+i\epsilon}\frac{1}{-2p\cdot k_1+i\epsilon}\left[\frac{F_2}{2q\cdot k_1+i\epsilon}+\frac{F_2'}{2q\cdot k_2+i\epsilon}\right]\end{aligned} \tag{6.20}$$

where the sum in the second line represents the box and crossed box diagrams and

$F_2 = (T^a T^b)_{ij}(T^a T^b)_{kl}$ and $F_2' = (T^a T^b)_{ij}(T^b T^a)_{kl}$ are their respective color factors. Recall that we can use the group theory relation:

$$F_2' = F_2 + \frac{3}{2}F_1 \tag{6.21}$$

To arrive at:

$$\begin{aligned}\mathcal{A}_2 = 4s^2 g^4 F_2 \int \frac{d^4k_1 d^4k_2}{(2\pi)^4}\delta(k_1+k_2+\Delta)\frac{1}{k_1^2+i\epsilon} \\ \times \frac{1}{k_2^2+i\epsilon}\frac{1}{-2p\cdot k_1+i\epsilon}[\frac{1}{2q\cdot k_1+i\epsilon}+\frac{1}{2q\cdot k_2+i\epsilon}] + \mathcal{O}(g^4)F_1\end{aligned} \tag{6.22}$$

where we have ignored the term proportional to F_1 since it has an uncanceled collinear divergence. Note that a convenient bookkeeping device is to keep only the term that is lowest order in the coupling constant for each relevant color factor. In this case, the contribution to F_1 from (6.22) is higher order than the contribution from (6.19).

At the two-loop level we will consider only the set of diagrams in figure 6.4. Our prescription is to then commute the color factors so that in the end we only retain a contribution with a color factor of the first diagram in figure 6.4.

$n-1$ Loop

We now state the expression for the matrix element at the $n-1$ loop level. Knowing that we get a factor of $-2s$ times a color factor for each "rung" of the ladder makes this task very straightforward. We have:

$$\begin{aligned}\mathcal{A}_n = -g^{2n}(-2is)^n \int \frac{\prod_i^n d^4k_i}{(2\pi)^{4n-4}}\delta(\sum_i^n k_i+\Delta) \\ \times \prod_i^n \frac{1}{k_i^2+i\epsilon}\prod_i^{n-1}\frac{1}{-2p\cdot K_i+i\epsilon}\sum_{\text{perms}}[\prod_i^{n-1}\frac{c_{\text{perm}}}{2q\cdot K_i+i\epsilon}]\end{aligned} \tag{6.23}$$

where the sum over permutations that generate all the distinct ladder and crossed ladder diagrams at this order now include the distinct color factor for each of these diagrams, which we write as c_{perm}. Note that as we did in the 1-loop case, we can commute the terms in each distinct color factor so that they all are reduced to $F_n = (T^{a_1}T^{a_2}....T^{a_n})_{ij}(T^{a_1}T^{a_2}....T^{a_n})_{kl}$, the color factor corresponding to the $n-1$ loop uncrossed ladder diagram, plus terms that have color factors corresponding to lower loop diagrams but are ignored due to having higher power dependence on the coupling constant. These latter terms have collinear divergences

and are therefore of no interest to us. Thus we can write:

$$\mathcal{A}_n = -g^{2n} F_n (-2is)^n \int \frac{\prod_i^n d^4k_i}{(2\pi)^{4n-4}} \delta(\sum_i^n k_i + \Delta) \times \prod_i^n \frac{1}{k_i^2 + i\epsilon} \prod_i^{n-1} \frac{1}{-2p \cdot K_i + i\epsilon} \sum_{\text{perms}} [\prod_i^{n-1} \frac{1}{2q \cdot K_i + i\epsilon}] + \mathcal{O}(g^{2n}) F_{i \leq n-1} \tag{6.24}$$

Note that it is clear that the above expression will not have any collinear divergences since we can proceed as we did in section 6.2.1 and integrate over the $+$ and $-$ components of all the loop momenta, leaving only transverse components.

6.2.3 Double Copy Relation

We have seen in the last section that by retaining only the lowest order coefficient of color structures corresponding to uncrossed ladder diagrams, we can eliminate all collinear logarithms in the QCD eikonal scattering amplitude. Now that we have identified the correct subset of the amplitude to consider, a double copy relation is seen immediately, as:

$$\frac{(-i)^{n-1}}{g^{2n}} \mathcal{A}_n = -i\tilde{F}_n s^n \int \frac{\prod_i^n d^4k_i}{(2\pi)^{4n-4}} \delta(\sum_i^n k_i + \Delta) \prod_i^n \frac{1}{k_i^2 + i\epsilon} \times \prod_i^{n-1} \frac{1}{-2p \cdot K_i + i\epsilon} \sum_{\text{perms}} [\prod_i^{n-1} \frac{1}{2q \cdot K_i + i\epsilon}] \tag{6.25}$$

where we have rescaled $F_n \to \frac{\tilde{F}_n}{(-2)^n}$ as prescribed by [85]. We then see from (6.9) that:

$$\frac{(-i)^n}{(\kappa/2)^{2n}} \mathcal{M}_n = -s^{2n} \int \frac{\prod_i^n d^4k_i}{(2\pi)^{4n-4}} \delta(\sum_i^n k_i + \Delta) \prod_i^n \frac{1}{k_i^2 + i\epsilon} \times \prod_i^{n-1} \frac{1}{-2p \cdot K_i + i\epsilon} \sum_{\text{perms}} [\prod_i^{n-1} \frac{1}{2q \cdot K_i + i\epsilon}] \tag{6.26}$$

so we see that if we replace the color factor $\tilde{F}_n$ with the numerator factor $-is^n$ the gravitational result is recovered.

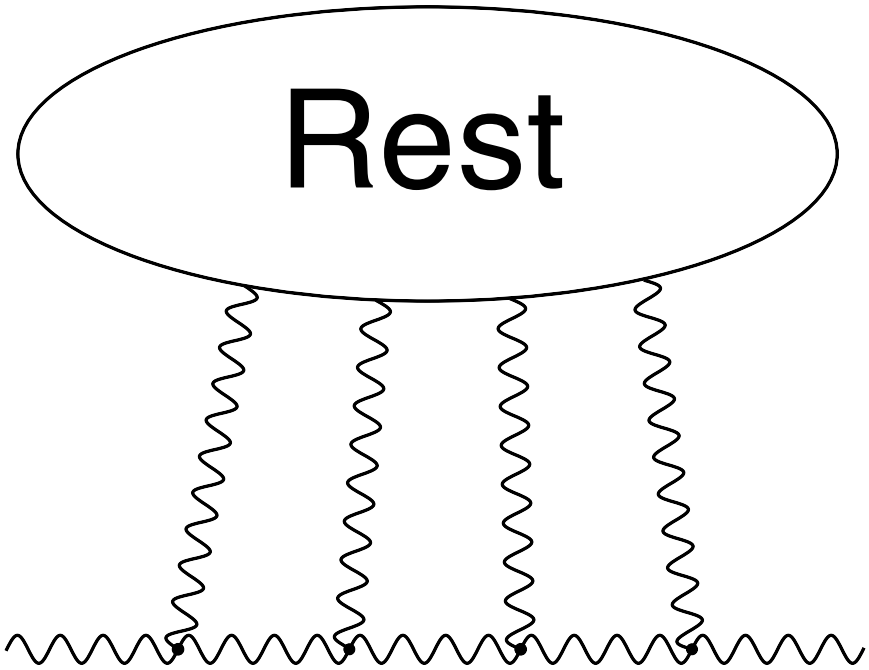

Figure 6.7 A high energy graviton/gluon interacting with the rest of the diagram through eikonalized graviton/gluon exchange. We show the case with $n = 4$ gravitons/gluons for purposes of illustration.

6.3 Connection to Shockwaves

In this section we will explore the possibility of replacing a fast moving particle in interaction with the rest of an arbitrary Feynman diagram by an external potential. In particular, we will present a field theoretic calculation that directly illustrates the connection between the eikonal approximation and shockwaves. This is done by comparing the expressions for the interaction of an arbitrary diagram through eikonalized graviton or gluon exchange with a relativistic graviton/gluon line (figure 6.7) to that of its interaction with external tensor/vector field sources (figure 6.8).

6.3.1 Aichelberg-Sexl Metric

We first start with the gravitational case, for which the shockwave is described by the Aichelberg-Sexl metric. Let us consider an arbitrary diagram R interacting with a relativistic graviton line by exchanging n eikonalized gravitons. In this case using similar methods to

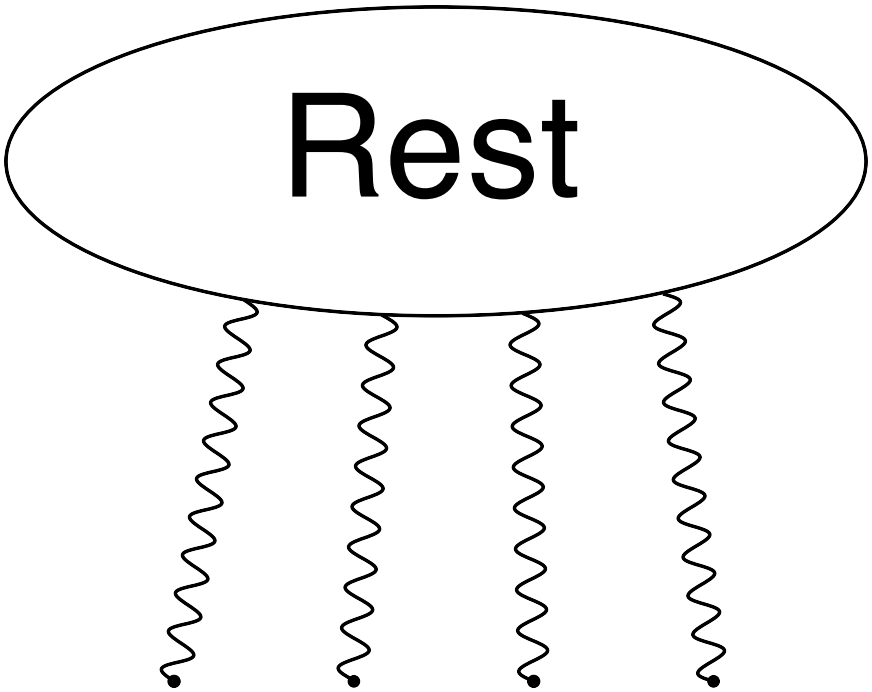

Figure 6.8 Interaction of the rest of the diagram with an external tensor/vector field. We show the case with $n = 4$ gravitons/gluons for purposes of illustration.

those used in section 6.2.1 we see that the matrix element corresponding to this process is:

$$\mathcal{M}_n^{(A)} = -i(i\kappa)^n \int \frac{\prod_i^n d^4k_i}{(2\pi)^{4n-4}} \delta^4(\sum_i^n k_i + \Delta) \prod_i^n q_{\mu_i} q_{\nu_i}$$
$$\times \prod_i^n \frac{1}{k_i^2 + i\epsilon} \sum_{\text{perms}} [\prod_i^{n-1} \frac{1}{2q \cdot K_i + i\epsilon}] R^{\{\mu_i,\nu_i\}}(\{p_i\}, \{k_i\}) \tag{6.27}$$

where $R^{\{\mu_i,\nu_i\}}(\{p_i\}, \{k_i\})$ denotes the expressions for the rest of the diagram. The p_i are the momenta going into and out of rest, k_i are the momenta attaching the hard line to rest, (q, q') are the incoming and outgoing momenta of the hard line, and we are still defining $\Delta = p' - p = q - q'$, where p is the net momentum going into R and p' is the net momentum going out. We can now simplify our result using (6.11):

$$\mathcal{M}_n^{(A)} = \kappa^n 2q_0 \int \frac{\prod_i^n d^4k_i}{(2\pi)^{3n-3}} \delta^3(\sum_i^n \mathbf{k_i} + \mathbf{\Delta}) \prod_i^n q_{\mu_i} q_{\nu_i}$$
$$\times \prod_i^n \frac{\delta(2q \cdot k_i)}{k_i^2 + i\epsilon} R^{\{\mu_i,\nu_i\}}(\{p_i\}, \{k_i\}) \tag{6.28}$$

Let us now compare this result to the case where this same arbitrary diagram is interacting n times with an external tensor field:

$$h_{\mu\nu} = \int \frac{d^4k}{(2\pi)^4} e^{i(k\cdot x)} C_{\mu\nu}(k) \tag{6.29}$$

The net result is:

$$\begin{aligned}\mathcal{M}_n^{(B)} = &\int \frac{\prod_i^n d^4k_i}{(2\pi)^{4n-4}} \delta^4(\sum_i^n k_i + \Delta) \\ &\times C_{\mu_1\nu_1}(k_1)...C_{\mu_n\nu_n}(k_n) R^{\{\mu_i,\nu_i\}}(\{p_i\},\{k_i\}),\end{aligned} \tag{6.30}$$

Let us choose:

$$C_{\mu\nu}(k) = 2\kappa\pi q_\mu q_\nu \delta(2q\cdot k)\frac{1}{k^2 + i\epsilon} \tag{6.31}$$

Note that:

$$\begin{aligned}&\delta^4(p' - p + k_1 + ... + k_n)\delta(2q\cdot k_1)...\delta(2q\cdot k_n) \\ &= \delta(p'^0 - p^0 + k_1^0 + ... + k_n^0)\delta^3(\mathbf{p'} - \mathbf{p} + \mathbf{k_1} + ... + \mathbf{k_n})\delta(2q\cdot k_1)...\delta(2q\cdot k_n) \\ &= \delta(p'^0 - p^0 + \mathbf{v_q}\cdot(\mathbf{p} - \mathbf{p'}))\delta^3(\mathbf{q} - \mathbf{q'} + \mathbf{k_1} + ... + \mathbf{k_n})\delta(2q\cdot k_1)...\delta(2q\cdot k_n) \\ &= 2q_0\delta(2q\cdot(p - p'))\delta^3(\mathbf{q} - \mathbf{q'} + \mathbf{k_1} + ... + \mathbf{k_n})\delta(2q\cdot k_1)...\delta(2q\cdot k_n)\end{aligned} \tag{6.32}$$

where $\mathbf{v_q} \equiv \frac{\mathbf{q}}{q_0}$ and we have used the fact that there are delta functions that impose the condition $k_i^0 = \mathbf{v_q}\cdot\mathbf{k_i}$ and that $\mathbf{p} - \mathbf{p'} = \mathbf{q'} - \mathbf{q} = \sum \mathbf{k_i}$. Now, $\delta(p'^0 - p^0 + k_1^0 + ... + k_n^0) = 2q_0\delta(2q\cdot(p - p'))$ can be pulled out of the $\mathbf{k}$ integrations and we get:

$$\mathcal{M}_n^{(B)} = 2\pi\delta(2q\cdot(p - p'))\mathcal{M}_n^{(A)} \tag{6.33}$$

so we see that the effect of the high energy line is the same as that of the external field (6.29) with $C_{\mu\nu}(k)$ given by (6.31). Note that this field can be written as:

$$\begin{aligned}h_{\mu\nu} &= \kappa q_\mu q_\nu \int \frac{d^4k}{(2\pi)^3} e^{i(k\cdot x)}\delta(2q\cdot k)\frac{1}{k^2 + i\epsilon} \\ &= \frac{\kappa}{2q_0} q_\mu q_\nu \int \frac{d^3\mathbf{k}}{(2\pi)^3} e^{-i\mathbf{k}\cdot(\mathbf{r} - \mathbf{v_q}t)}\frac{1}{(\mathbf{v_q}\cdot\mathbf{k})^2 - \mathbf{k}^2}\end{aligned} \tag{6.34}$$

If we take $\mathbf{q}$ in the z direction, we have:

$$h_{\mu\nu} = -\frac{\kappa}{2} q_0 u_\mu u_\nu \int \frac{d^2\mathbf{k}_\perp dk_3}{(2\pi)^3} e^{-i\mathbf{k}_\perp \cdot \mathbf{r}_\perp} e^{-ik_3(z-v_q t)} \frac{1}{\mathbf{k}_\perp^2 + k_3^2(1-v_q^2)} \tag{6.35}$$

Let us take the limit as $v_q \to 1$ (q_0 is held fixed), in which case the external field becomes:

$$h_{\mu\nu} = -\frac{\kappa}{2} q_0 u_\mu u_\nu \delta(z-t) \int \frac{d^2\mathbf{k}_\perp}{(2\pi)^2} e^{-i\mathbf{k}_\perp \cdot \mathbf{r}_\perp} \frac{1}{\mathbf{k}_\perp^2} \tag{6.36}$$

where u is the 4-velocity corresponding to q. The equation of motion for the de Donder gauge we are using is:

$$\Box(h_{\alpha\beta} - \frac{1}{2}\eta_{\alpha\beta} h) = -\frac{\kappa}{2} T_{\alpha\beta} \tag{6.37}$$

Note in the limit $v_q \to 1$, $h = 0$. We then have using $h_{\alpha\beta}$ from (6.36):

$$\begin{aligned} \Box h_{\alpha\beta} &= (\partial_{t+z}\partial_{t-z} - \partial_{r_\perp}^2) h_{\alpha\beta} \\ &= -\frac{\kappa}{2} q_0 u_\alpha u_\beta \delta(z-t)\delta(y)\delta(x) \end{aligned} \tag{6.38}$$

Thus the energy momentum tensor corresponding to our external field is:

$$T_{\alpha\beta} = q_0 u_\alpha u_\beta \delta(z-t)\delta(y)\delta(x) \tag{6.39}$$

Which is precisely the energy momentum tensor of a massless particle, which will give the Aichelburg-Sexl metric once the Einstein equation is solved for.

We can also directly apply a gauge transformation to (6.36) to show that it is indeed the Aichelberg-Sexl metric. The key fact to note here is that:

$$\partial_x \int \frac{d^2\mathbf{k}_\perp}{(2\pi)^2} e^{-i\mathbf{k}_\perp \cdot \mathbf{r}_\perp} \frac{1}{\mathbf{k}_\perp^2} = \partial_x \frac{-1}{4\pi} \ln(r_\perp^2) = -\frac{1}{2\pi} \frac{x}{x^2+y^2} \tag{6.40}$$

Because of this, when we make the gauge transformation:

$$h'_{\mu\nu} = h_{\mu\nu} + \partial_\mu \eta_\nu + \partial_\nu \eta_\mu \tag{6.41}$$

with:

$$\eta_- = \frac{\kappa}{4} q_0 \Theta(z-t) [\int \frac{d^2\mathbf{k}_\perp}{(2\pi)^2} e^{-i\mathbf{k}_\perp \cdot \mathbf{r}_\perp} \frac{1}{\mathbf{k}_\perp^2} + \frac{1}{4\pi} \ln(r_\perp^2)] \tag{6.42}$$

and all other components of η_μ being zero, we have $\partial_x \eta = \partial_y \eta = 0$. Thus, by choosing this gauge parameter we ensure that we only change the h_{--} component with this gauge transformation, which is the only non-zero component.

After this gauge transformation we arrive at:

$$\kappa h'_{\mu\nu} = 4Gq_0 u_\mu u_\nu \delta(z-t)\ln(r_\perp^2) \tag{6.43}$$

which is precisely the standard expression for the Aichelberg-Sexl metric (for example, see equation 1 of [96]).

The expression for the Riemann tensor corresponding to this metric, which is gauge invariant at the linearized level, is given in equation 3.12 of [95]. This Riemann tensor is seen to have terms proportional to $\delta(y)\delta(x)$, which is just a reflection of the fact that our solutions have a source as given by (6.39). Note that it is valid for us to consider linearized gravity as in the eikonal limit the spin of the hard line does not matter, so in principle we could have used a high-energy scalar instead of a high-energy graviton in this derivation.

6.3.2 Gauge Shockwave

Here we discuss how one can arrive at a gauge shockwave using methods analogous to those used to arrive at the Aichelberg-Sexl metric.

Let us first consider an arbitrary diagram exchanging n gluons with a high energy gluon line. Using similar methods to section 6.2.2 we find that the matrix element corresponding to this process is:

$$\begin{aligned}\mathcal{A}_n^{(A)} = -i(2g)^n \int \frac{\prod_i^n d^4k_i}{(2\pi)^{4n-4}} \delta^4(\sum_i^n k_i + \Delta) \\ \times \prod_i^n q_{\mu_i} \prod_i^n \frac{1}{k_i^2 + i\epsilon} \sum_{\text{perms}} [\prod_j^{n-1} \frac{d_n^{\{a_i\}}}{2q\cdot K_j + i\epsilon}] R^{\{\mu_i\}}_{\{a_i\}}(\{p_i\},\{k_i\})\end{aligned} \tag{6.44}$$

Note that each permutation that generates a new diagram will have a different color factor $d_n^{\{a_i\}}$ which will be contracted with the rest of the diagram. However, we can again commute the color matrices so that they all reduce to a common color factor plus a suppressed term that has a color factor of a lower order diagram and would contain potential collinear divergences. Again, we ignore terms of this latter type to arrive at:

$$\mathcal{A}_n^{(A)} = -i(2g)^n D_n^{\{a_i\}} \int \frac{\prod_i^n d^4k_i}{(2\pi)^{4n-4}} \delta^4(\sum_i^n k_i + \Delta)$$
$$\times \prod_i^n q_{\mu_i} \prod_i^n \frac{1}{k_i^2 + i\epsilon} \sum_{\text{perms}} [\prod_i^{n-1} \frac{1}{2q \cdot K_i + i\epsilon}] R_{\{a_i\}}^{\{\mu_i\}}(\{p_i\}, \{k_i\}) \tag{6.45}$$

where $D_n^{\{a_i\}}$ is the color factor that corresponds to the diagrams where n gluons are exchanged with the rest of the diagram in an uncrossed fashion. Typically it will be of the form, $D_n^{\{a_i\}} = (T^{a_1} T^{a_2} .... T^{a_n})_{ij}$. Note that there is a similar chain of the product of the T^a included inside $R_{\{a_i\}}^{\{\mu_i\}}(\{p_i\}, \{k_i\})$.

Then, after using (6.11) we have:

$$\mathcal{A}_n^{(A)} = (-2ig)^n 2q_0 D_n^{\{a_i\}} \int \frac{\prod_i^n d^4k_i}{(2\pi)^{3n-3}} \delta^3(\sum_i^n \mathbf{k_i} + \mathbf{\Delta})$$
$$\times \prod_i^n q_{\mu_i} \prod_i^n \frac{\delta(2q \cdot k_i)}{k_i^2 + i\epsilon} R_{\{a_i\}}^{\{\mu_i\}}(\{p_i\}, \{k_i\}) \tag{6.46}$$

Let us now compare this expression to that obtained by letting this arbitrary diagram interact n times with an external vector field:

$$A_\mu^{(a)} = \int \frac{d^4k}{(2\pi)^4} e^{i(k \cdot x)} B_\mu^{(a)}(k) \tag{6.47}$$

In this case, we find that the resulting amplitude is:

$$\mathcal{A}_n^{(B)} = \int \frac{\prod_i^n d^4k_i}{(2\pi)^{4n-4}} \delta^4(\sum_i^n k_i + \Delta) B_{\mu_1}^{(a_1)}(k_1) ... B_{\mu_n}^{(a_n)}(k_n) R_{\{a_i\}}^{\{\mu_i\}}(\{p_i\}, \{k_i\}) \tag{6.48}$$

Note that if we make the identification:

$$B_\mu^{(a)}(k) = -4ig\pi q_\mu D_1^{(a)} \delta(2q \cdot k) \frac{1}{k^2 + i\epsilon} \tag{6.49}$$

we see that:

$$\mathcal{A}_n^{(B)} = (-2ig)^n 4\pi q_0 \delta(2q \cdot (p - p')) \int \frac{\prod_i^n d^4k_i}{(2\pi)^{3n-3}} \delta^3(\sum_i^n \mathbf{k_i} + \mathbf{\Delta})$$
$$\times \prod_i^n D_1^{(a_i)} \prod_i^n q_{\mu_i} \prod_i^n \frac{\delta(2q \cdot k_i)}{k_i^2 + i\epsilon} R_{\{a_i\}}^{\{\mu_i\}}(\{p_i\}, \{k_i\}) \tag{6.50}$$

Note that as $\prod_i^n D_1^{(a_i)} = D_n^{\{a_i\}}$, we have:

$$\mathcal{A}_n^{(B)} = 2\pi\delta(2q\cdot(p-p'))\mathcal{A}_n^{(A)} \tag{6.51}$$

as desired. Going through the exact same procedure as the gravitational case, we then find that:

$$A_\mu^{(a)}(k) = -igu_\mu D_1^{(a)}\delta(z-t)\int \frac{d^2\mathbf{k}_\perp}{(2\pi)^2}e^{-i\mathbf{k}_\perp\cdot\mathbf{r}_\perp}\frac{1}{\mathbf{k}_\perp^2} \tag{6.52}$$

If we insert this vector field into the Yang-Mills equation:

$$D^\mu F_{\mu\nu}^{(a)} = j_\nu^{(a)} \tag{6.53}$$

we find that the corresponding current is:

$$j_\mu^{(a)} = -igu_\mu D_1^{(a)}\delta(z-t)\delta(x)\delta(y) \tag{6.54}$$

Note this is exactly the source that gives rise to a QED shockwave, with the identification of $igD_1^{(a)}$ being the electromagnetic charge.

As we did for the gravitational case we can also instead show the equivalence using a gauge transformation:

$$A'_\mu = A_\mu + \partial_\mu\Omega \tag{6.55}$$

with:

$$\Omega = igD_1^{(a)}\Theta(t-z)\int \frac{d^2\mathbf{k}_\perp}{(2\pi)^2}e^{-i\mathbf{k}_\perp\cdot\mathbf{r}_\perp}\frac{1}{\mathbf{k}_\perp^2} \tag{6.56}$$

we have:

$$\begin{aligned} &A_0 = A_z = 0; \\ &A_\perp = -\frac{igD_1^{(a)}}{4\pi}\Theta(t-z)\nabla\ln(r_\perp^2) \end{aligned} \tag{6.57}$$

which is exactly the QED result with the identification of $igD_1^{(a)}$ being the electromagnetic charge. So we have seen that deriving a shockwave in the eikonal limit causes it to take an abelian form, even for the case of nonabelian gauge theories such as QCD.

We would like to point out here that the field strength corresponding to our gauge shockwave takes the form:

$$F_{\mu\nu} = D_1^{(a)} F_{\mu\nu}^{\text{abelian}} \tag{6.58}$$

where $F_{xt}^{\text{abelian}} = F_{zx}^{\text{abelian}} = \frac{ig}{2\pi}\delta(z-t)\frac{x}{x^2+y^2}$, $F_{yt}^{\text{abelian}} = F_{zy}^{\text{abelian}} = \frac{ig}{2\pi}\delta(z-t)\frac{y}{x^2+y^2}$, and the other non-zero components can be arrived at by symmetries.

6.3.3 Relationship Between the Two Shockwaves

It is interesting to note that the double copy relation similar to that which we showed in section 6.2.3 can also be seen in the two shockwaves (6.36) and (6.52). For the full scattering amplitude we looked at the gravitational quantity $\frac{(-i)^n}{(\kappa/2)^{2n}}\mathcal{M}_n$. The analogous quantity to look at for the gravitational shockwave is:

$$\frac{1}{\kappa}h_{\mu\nu} = -q_\mu q_\nu \frac{\delta(z-t)}{2q_0}\int \frac{d^2\mathbf{k}_\perp}{(2\pi)^2} e^{-i\mathbf{k}_\perp\cdot\mathbf{r}_\perp}\frac{1}{\mathbf{k}_\perp^2} \tag{6.59}$$

since we have accounted for factors corresponding to graviton couplings and numerator factors of the propagators that reside in "rest". Note that we have identified $\frac{\delta(z-t)}{2q_0}$ as being a propagator as this piece was derived solely from non-numerator contributions.

On the gauge theory side, the quantity we looked at for the full scattering amplitude was $\frac{(-i)^{n-1}}{g^{2n}}\mathcal{A}_n$. The analogous quantity to look at for the shockwave is:

$$\frac{1}{g}A_\mu = iq_\mu \tilde{D}_1^{(a)}\frac{\delta(z-t)}{2q_0}\int \frac{d^2\mathbf{k}_\perp}{(2\pi)^2} e^{-i\mathbf{k}_\perp\cdot\mathbf{r}_\perp}\frac{1}{\mathbf{k}_\perp^2} \tag{6.60}$$

where we have accounted for a factor of g that corresponds to gluon couplings that reside in "rest". We have also rescaled the color factor to $\tilde{D}_1^{(a)} = -\frac{1}{2}D_1^{(a)}$ (instead of scaling by $-\frac{i}{\sqrt{2}}$) since there are two factors of $D_1^{(a)}$ that need to be accounted for in the $n=1$ case that the single external gauge field corresponds to (one factor in the gauge field and another factor residing in the attachment onto "rest"). We then easily see that if we make the replacement $\tilde{D}_1^{(a)} \to iq_\mu$ in the gauge shockwave we clearly recover the gravitational result.

Another example of a double copy relation between classical solutions has been pointed out in Exercise IXC1.1 of [102], where it is noted that the gravitational vacuum plane wave solution is related to a gauge field plane wave by the relations:

$$g_{\mu\nu} = \eta_{\mu\nu} + \frac{1}{g^2}\text{tr}(A_\mu A_\nu)$$
$$R_{\mu\nu\rho\sigma} = \frac{1}{g^2}\text{tr}(F_{\mu\nu}F_{\rho\sigma}) \tag{6.61}$$

A major difference between (6.61) and our classical double copy relation is that (6.61) applies to vacuum solutions, while our relation applies for classical solutions with delta function type sources seen in (6.39) and (6.54). Indeed, our solutions are similar to those in [102] apart from the delta function sources. However, these sources are all important in our analysis of large s small t scattering, and causes the double copy relation between the two different types of solutions to be very different. For instance, we see that there is no double copy relation between the gauge shockwave field strength (6.58) and the Riemann tensor given in equation 3.12 of [95] due to delta function terms in the Riemann tensor.

In concluding this section we would like to point out that this double copy relation is only obvious when the fields are in the gauges (6.36) and (6.52). For example, when the fields are in the gauges (6.43) and (6.57) the double copy relation is greatly obscured.

6.4 Discussion

We have shown that there exists a double copy relation between eikonalized gravity and gauge theory amplitudes, as long as we consider only the lowest order contribution to the color factors corresponding to completely uncrossed ladder diagrams. This restriction is necessary as the inclusion of other contributions to the amplitude will result in collinearly divergences which are known to cancel in gravitational amplitudes. This is a feature particular to the eikonal approximation, as in this limit the numerator factors have no dependence on the loop momenta which does not allow one to change the integrals found in gauge theories once the double copy conjecture is applied.

An interesting consequence of this double copy relation between the eikonalized amplitudes is that the corresponding shockwave solutions have a double copy relation as well. While both the gauge and gravity shockwaves had been calculated previously using completely classical methods, our method directly shows the relationship between eikonal amplitudes and shockwaves. Furthermore, the double copy relation between the two shockwaves had not previously been seen. This is because this double copy relation is only apparent in a particular choice of gauge, which was naturally selected by our method of calculation.

One aspect of this analysis we would like to comment on is that we did not need to consider gravity coupled to a dilaton or an anti-symmetric tensor in order to arrive at a double copy relation in this kinematic regime at leading eikonal order. Such a coupling is necessary for a double copy relation in the unrestricted kinematic region as discussed in [7, 85]. However, it is to be expected that we would not need to consider these couplings as in the soft regime scalars decouple due to power counting arguments. This reasoning is also why ghosts do not need to be considered in the soft limit [65]. Arguments for the decoupling of scalars and anti-symmetric tensors also apply at the tree level, as is well known.

Chapter 7

High Energy Scattering in Perturbative Quantum Gravity at Next-to-Leading Order

7.1 Introduction

In the previous two chapters, we showed through some concrete examples the simplicity that perturbative quantum gravity possesses in the infrared regime. Because of this simplicity, in this chapter we will conclude our investigations of quantum gravity by looking for observables for which long distance effects are particularly important. A fundamentally infrared dominated physical quantity of note in perturbative quantum gravity is the eikonal phase that has been calculated for small-angle high-energy scattering processes. An eloquent overview of the eikonal regime for this type of scattering is given in a set of lectures by Giddings [92].

This type of process has been shown to be largely independent of short distance physics. Giddings, Gross and Maharana [6] argued that the scattering of strings may be replaced by graviton contributions alone with short distance physics playing no significant role. Thus non-local string effects are actually subdominant to higher loop gravitational processes for a large range of impact parameters. The eikonal approximation provides the leading contribution which can be shown to exponentiate in the impact parameter space. This exponentiation can be used to show that large impact parameters dominate the scattering in this regime.

Although the leading eikonal contribution to gravitational small-angle high-energy scattering processes has garnered much attention, the next-to-eikonal contribution to small-angle high-energy gravitational scattering has to our knowledge never before been calculated. For the case of non-abelian gauge theories, there has been interesting progress on this topic [103, 104]. In [56] the effective vertices at the next-to-eikonal level for gravity are given. However, they have not been applied to any process and in particular their exponentiation

has not been explicitly demonstrated, though the subtleties involved are discussed. The next-to-leading contribution is of particular interest since it is fundamentally quite different from the eikonal contribution. For instance the spin of the external particles involved is of no consequence for the latter but is for the former.

The power corrections to the eikonal approximation that we will consider in this chapter give a leading $\frac{1}{E_\phi}$ (E_ϕ is the energy of the incoming fast particle) correction to the high-energy small-angle scattering. These corrections can provide some insight into whether the factorization of short and long distance physics will endure at the level of power corrections to such processes. We expect that the failure of this factorization due to the power corrections will be a feature of black hole formation since the hard scattering point will be cloaked by the horizon when a black hole is formed. It will therefore be impossible to separate initial from final state interactions. The leading eikonal approximation does not by itself have much to say about black hole formation. Thus one of the primary motivations for this work is to look for hints of black hole formation in perturbation theory by investigating the power corrections to the leading eikonal approximation. At the technical level, in a certain kinematic regime, we have been able to explicitly extend the well known exponentiation that occurs at leading eikonal order to the next-to-eikonal order also. It has been shown in [92] that the leading eikonal approximation is justified for studying high energy small angle scattering since the impact parameter as determined from the saddlepoint of the loop integrations is larger than the typical gravitational radius $2GE$ by a factor of s/t. In a slightly different kinematic regime, to be discussed later, we show that this enhancement factor is missing for the subleading contributions coming from the corrections to the eikonal phase.

In section 7.2.1 we will review the calculation for the leading eikonal phase to establish our conventions. We proceed to calculating the next-to-eikonal phase in section 7.2.2. This is done by expanding the scalar propagator to next-to-eikonal order as well as allowing seagull type vertices in the diagram. We find that part of this contribution exponentiates, and calculate the correction to the saddlepoint at this order.

We conclude with a discussion of our results. Certain technical details are relegated to appendices F and G.

7.2 Relativistic Scattering

It was first noticed by 't Hooft [86] that the scattering of ultrarelativistic particles could be reliably studied by considering graviton exchanges in perturbative quantum gravity. In the

rest frame of one of the particles, the gravitational field of the rapidly moving particle is that of a gravitational shock wave, which can be described by the Aichelburg-Sexl metric [95]. The particle at rest is a quantum particle whose dynamics can be described by the solutions of Klein-Gordon equation in the Aichelburg-Sexl background. This was 't Hooft's approach [86] and the results can also be obtained by summing a class of Feynman diagrams in the eikonal approximation [58, 105]. In this section we will demonstrate how this latter approach can be extended to the next-to-eikonal level.

We will investigate the small-angle gravitational scattering of an ultra-relativistic light scalar particle of energy E_ϕ off of a very heavy scalar particle. The mass of the heavy particle, M_σ, is bigger than E_ϕ and both are much larger than the transferred momentum. This approximation is only made for the purposes of simplifying the calculations needed to determine the next-to-eikonal corrections. We first show the exponentiation of the amplitude in the leading eikonal approximation in the above mentioned kinematic regime. Then we consider the next-to-leading eikonal corrections where we will look for hints in perturbation theory of the absorption of the high energy particle by the heavy particle. In order to make our kinematics explicit, throughout this section, we will be working in the large center of mass energy and small angle scattering regime, so we will take the incoming and outgoing momentum p and p' of the light scalar particle ϕ to be much larger than the momentum transferred between the two scalars $\Delta = p' - p$. We will take q and q' to be the incoming and outgoing momenta of the heavy scalar σ. We will also work in the frame where $\Delta^0 = 0$ and in the de Donder gauge.

7.2.1 Eikonal Phase

Let us first consider this process in the eikonal limit to establish our conventions and set up our departure from previous calculations. In this limit it is well known that only the ladder and crossed-ladder type diagrams contribute. It will be instructive to consider the cases where one and two gravitons are being exchanged between the scalars before moving to the general n-graviton case.

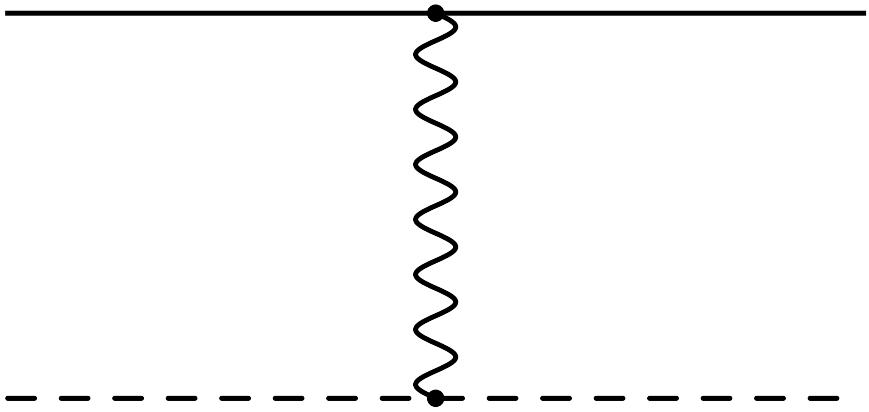

Figure 7.1 A scattering process with a single graviton exchanged. The heavy scalar is the solid line and the light scalar is the dotted line.

One Graviton Exchange

Let us first work with the simplest case where only a single graviton is exchanged (figure 7.1). The matrix element corresponding to this diagram is:

$$i\mathcal{M}_1^0 = (-\frac{i\kappa}{2})^2 \frac{i}{2} \frac{L_{\mu\nu\alpha\beta}}{\Delta^2 + i\epsilon} \tau^{\alpha\beta}(p, p', M_\phi)\tau^{\mu\nu}(q, q', M_\sigma) \tag{7.1}$$

where:

$$L_{\mu\nu\alpha\beta} = \eta_{\mu\alpha}\eta_{\nu\beta} + \eta_{\mu\beta}\eta_{\nu\alpha} - \eta_{\mu\nu}\eta_{\alpha\beta} \tag{7.2}$$

is the numerator of the de Donder gauge graviton propagator,

$$\tau^{\mu\nu}(q, q', M_\sigma) = q^\mu q'^\nu + q^\nu q'^\mu - \eta^{\mu\nu}((q \cdot q') - M_\sigma^2) \tag{7.3}$$

is the scalar-scalar-graviton vertex, and $\kappa^2 = 32\pi G$.

We will use the fact that in the large M_σ limit:

$$L_{\mu\nu\alpha\beta}\tau^{\mu\nu}(q, q', M_\sigma) = 2M_\sigma^2(2\delta_{0\alpha}\delta_{0\beta} - \eta_{\alpha\beta}) \tag{7.4}$$

Note that the right hand side of (7.4) is independent of the momentum flowing through the vertex so we will always be free to use this identity for any vertex on a heavy line.

In the ultra-relativistic limit $M_\phi = 0$ and $p^0 = |\mathbf{p}| \equiv E_\phi$ so:

$$(2\delta_{0\alpha}\delta_{0\beta} - \eta_{\alpha\beta})\tau^{\alpha\beta}(p, p', M_\phi) = 4E_\phi^2 \tag{7.5}$$

Note we used the fact that in the $\Delta^0 = 0$ frame $p^0 = p'^0$. This identity is valid whenever the $p^0 = p'^0$ condition holds.

Using (7.4) and (7.5), we have:

$$i\mathcal{M}_1^0 = (-\frac{i\kappa}{2})^2 \frac{i}{2}(2M_\sigma^2)(4E_\phi^2)\frac{1}{\Delta^2 + i\epsilon} \tag{7.6}$$

Two Graviton Exchange

Let us now consider the scattering process where two gravitons are exchanged. In this case the matrix element becomes:

$$\begin{aligned} i\mathcal{M}_2^0 = (-\frac{i\kappa}{2})^4(\frac{i}{2})^2(i)^2(2\pi)^{-4}(2M_\sigma^2)^2 \int d^4k_1 d^4k_2 \delta^4(k_1 + k_2 + \Delta) \\ \times \tau^{\alpha_1\beta_1}(p, p - k_1, M_\phi)\tau^{\alpha_2\beta_2}(p - k_1, p', M_\phi) \\ \times \frac{2\delta_{0\alpha_1}\delta_{0\beta_1} - \eta_{\alpha_1\beta_1}}{k_1^2 + i\epsilon}\frac{2\delta_{0\alpha_2}\delta_{0\beta_2} - \eta_{\alpha_2\beta_2}}{k_2^2 + i\epsilon}\frac{1}{(p - k_1)^2 + i\epsilon} \\ \times [\frac{1}{(q + k_1)^2 - M_\sigma^2 + i\epsilon} + \frac{1}{(q + k_2)^2 - M_\sigma^2 + i\epsilon}] \end{aligned} \tag{7.7}$$

where we have made use of (7.4). Note that the sum in the last line of (7.7) corresponds to summing over the ladder (figure 7.2) and crossed ladder (figure 7.3) diagrams. In the large M_σ limit and the $\Delta^0 = 0$ frame, we have:

$$\begin{aligned} \delta(k_1^0 + k_2^0 + \Delta^0)[\frac{1}{(q + k_1)^2 - M_\sigma^2 + i\epsilon} + \frac{1}{(q + k_2)^2 - M_\sigma^2 + i\epsilon}] \\ = (2M_\sigma)^{-1}\delta(k_1^0 + k_2^0)[\frac{1}{k_1^0 + i\epsilon} + \frac{1}{k_2^0 + i\epsilon}] \end{aligned} \tag{7.8}$$

This can be simplified by use of the identity (see appendix E):

$$\begin{aligned} \delta(\omega_1 + ... + \omega_n) \sum_{\text{Perms of } \omega_i} \frac{1}{\omega_1 + i\epsilon}...\frac{1}{\omega_1 + ... + \omega_{n-1} + i\epsilon} \\ = (-2\pi i)^{n-1}\delta(\omega_1)...\delta(\omega_n) \end{aligned} \tag{7.9}$$

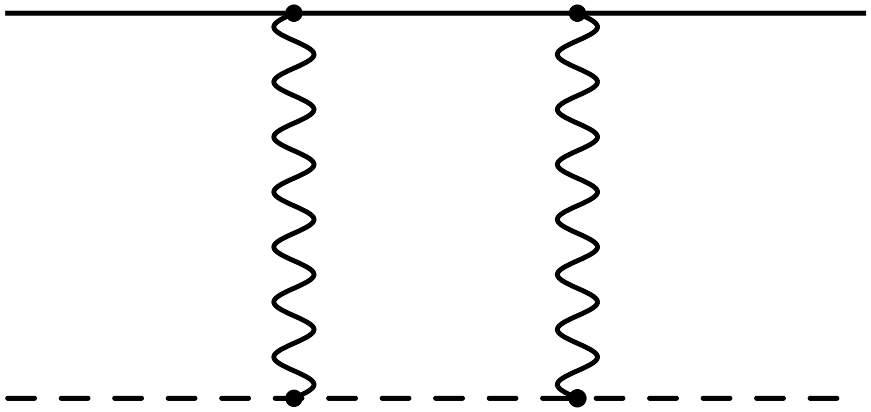

Figure 7.2 A two-graviton ladder diagram. The heavy scalar is the solid line and the light scalar is the dotted line.

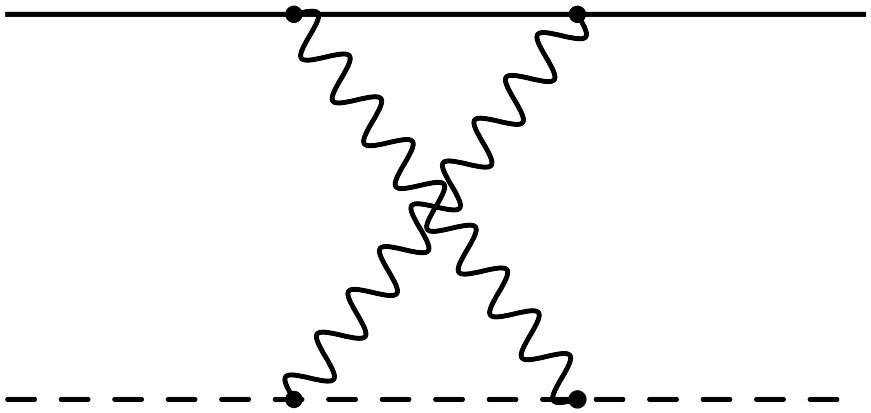

Figure 7.3 A two-graviton crossed ladder diagram. The heavy scalar is the solid line and the light scalar is the dotted line.

for $\omega_i = k_i^0$, $n = 2$. After applying (7.9) we have:

$$\begin{aligned} i\mathcal{M}_2^0 = (-\frac{i\kappa}{2})^4(\frac{i}{2})^2(i)^2(2\pi)^{-4}M_\sigma(-2\pi i)\int d^4k_1 d^4k_2 \delta(k_1^0)\delta(k_2^0)\delta^3(\mathbf{k_1}+\mathbf{k_2}+\mathbf{\Delta}) \\ \times \tau^{\alpha_1\beta_1}(p, p-k_1, M_\phi)\tau^{\alpha_2\beta_2}(p-k_1, p', M_\phi) \\ \times \frac{2\delta_{0\alpha_1}\delta_{0\beta_1}-\eta_{\alpha_1\beta_1}}{k_1^2+i\epsilon}\frac{2\delta_{0\alpha_2}\delta_{0\beta_2}-\eta_{\alpha_2\beta_2}}{k_2^2+i\epsilon}\frac{1}{(p-k_1)^2+i\epsilon} \end{aligned} \tag{7.10}$$

Note that the delta functions over k_1^0 and k_2^0 guarantee that $p^0 = (p^0 - k_1^0) = p'^0$ so we are

free to use (7.5). After applying this identity we have:

$$i\mathcal{M}_2^0 = (-\frac{i\kappa}{2})^4(\frac{i}{2})^2(i)^2(2\pi)^{-4}M_\sigma(-2\pi i)(4E_\phi^2)^2\int d^4k_1 d^4k_2\delta(k_1^0)\delta(k_2^0)\delta^3(\mathbf{k_1}+\mathbf{k_2}+\mathbf{\Delta}) \times \frac{1}{k_1^2+i\epsilon}\frac{1}{k_2^2+i\epsilon}\frac{1}{(p-k_1)^2+i\epsilon} \tag{7.11}$$

n-Graviton Exchange

Let us now consider the form of the matrix element when n-gravitons are being exchanged. In this case, the matrix element is:

$$\begin{aligned} i\mathcal{M}_n^0 = (-\frac{i\kappa}{2})^{2n}(\frac{i}{2})^n(i)^{2n-2}(2\pi)^{4-4n}(2M_\sigma^2)^n\int d^4k_1...d^4k_n\delta^4(k_1+...+k_n+\Delta) \\ \times\prod_{i=1}^{n}[\tau_i^{\alpha_i\beta_i}(p-K_{i-1},p-K_i,M_\phi)\frac{2\delta_{0\alpha_i}\delta_{0\beta_i}-\eta_{\alpha_i\beta_i}}{k_i^2+i\epsilon}]\prod_{i=1}^{n-1}\frac{1}{(p-K_i)^2+i\epsilon} \\ \times\sum_{\text{perms of }k_i}[\frac{1}{(q+k_1)^2-M_\sigma^2+i\epsilon}...\frac{1}{(q+k_1+...+k_{n-1})^2-M_\sigma^2+i\epsilon}] \end{aligned} \tag{7.12}$$

where k_i are the graviton momenta and $K_i \equiv \sum_j^i k_j$. The $\tau_i^{\alpha_i\beta_i}(p-K_{i-1},p-K_i,M_\phi)$ are the n scalar-scalar-graviton vertices on the light scalar line. We have made use of (7.4). As we saw in the two graviton case, the summation over all permutations of the ordering of the graviton momenta onto the heavy line generates all of the possible diagrams.

Just like in the two graviton case, we can simplify (7.12) by applying (7.9) and (7.5) in succession. The result is:

$$\begin{aligned} i\mathcal{M}_n^0 &= (-\frac{i\kappa}{2})^{2n}(\frac{i}{2})^n(i)^{2n-2}(2\pi)^{4-4n}2M_\sigma^{n+1}(-2\pi i)^{n-1}(4E_\phi^2)^n \\ &\times\int d^4k_1...d^4k_n\delta(k_1^0)...\delta(k_n^0)\delta^3(\mathbf{k_1}+...+\mathbf{k_n}+\mathbf{\Delta})\prod_{i=1}^{n}\frac{1}{k_i^2+i\epsilon}\prod_{i=1}^{n-1}\frac{1}{(p-K_i)^2+i\epsilon} \\ &= -2i(2\pi)^3M_\sigma(-\frac{\kappa^2M_\sigma E_\phi^2}{2(2\pi)^3})^n\int d^3\mathbf{k_1}...d^3\mathbf{k_n}\delta^3(\mathbf{k_1}+...+\mathbf{k_n}+\mathbf{\Delta}) \\ &\times\prod_{i=1}^{n}\frac{1}{\mathbf{k_i^2}}\prod_{i=1}^{n-1}\frac{1}{2\mathbf{p}\cdot\mathbf{K_i}-\mathbf{K_i^2}+i\epsilon} \end{aligned} \tag{7.13}$$

The remaining scalar propagators can be expanded as:

$$\frac{1}{2\mathbf{p}\cdot\mathbf{K_i}-\mathbf{K_i^2}+i\epsilon}\approx\frac{1}{2E_\phi}(\frac{1}{K_i^z+i\epsilon}+\frac{\mathbf{K_i^2}}{2E_\phi}\frac{1}{(K_i^z+i\epsilon)^2}) \tag{7.14}$$

where we have taken $\mathbf{p}$ to be in the z direction. For the leading eikonal phase we will only need to keep the first term in the expansion. It will be useful to symmetrize across the n graviton momenta so that we have:

$$\begin{aligned}i\mathcal{M}_n^0=-4i(2\pi)^3E_\phi M_\sigma\frac{1}{n!}(-\frac{\kappa^2M_\sigma E_\phi}{4(2\pi)^3})^n\int d^3\mathbf{k_1}...d^3\mathbf{k_n}\delta^3(\mathbf{k_1}+...+\mathbf{k_n}+\mathbf{\Delta})\\ \times\prod_{i=1}^n\frac{1}{\mathbf{k_i^2}}\sum_{\text{perms of }k_i^z}[\frac{1}{k_1^z+i\epsilon}...\frac{1}{k_1^z+...+k_{n-1}^z+i\epsilon}]\end{aligned} \tag{7.15}$$

Note that in the frame $\Delta^0=0$, $p^0=p'^0\equiv E_\phi=|\mathbf{p}|$, which we have taken to be in the z-direction. Thus we have that $\Delta^z=0$. So we can again apply (7.9) this time for the k_z components to get:

$$\begin{aligned}i\mathcal{M}_n^0=4(2\pi)^2E_\phi M_\sigma\frac{1}{n!}(i\frac{\kappa^2M_\sigma E_\phi}{4(2\pi)^2})^n\int d^3\mathbf{k_1}...d^3\mathbf{k_n}\\ \times\delta(k_1^z)...\delta(k_n^z)\delta^2(\mathbf{k_1^\perp}+...+\mathbf{k_n^\perp}+\mathbf{\Delta^\perp})\prod_{i=1}^n\frac{1}{\mathbf{k_i^2}}\end{aligned} \tag{7.16}$$

Now let us Fourier transform into impact parameter space (**b**) by operating with $\int\frac{d^3\mathbf{\Delta}}{(2\pi)^3}e^{i\mathbf{b}\cdot\mathbf{\Delta}}$. We then have:

$$i\widetilde{\mathcal{M}}_n^0=4(E_\phi M_\sigma)\frac{1}{n!}(i\frac{\kappa^2M_\sigma E_\phi}{4(2\pi)^2})^n\int d^2\mathbf{k_1^\perp}...d^2\mathbf{k_n^\perp}\prod_{i=1}^n[\frac{1}{(\mathbf{k_i^\perp})^\mathbf{2}}e^{-i\mathbf{b}^\perp\cdot\mathbf{k_i^\perp}}] \tag{7.17}$$

So after summing over all n we have:

$$i\widetilde{\mathcal{M}}^0=2(s-M_\sigma^2)(e^{i\chi_0}-1) \tag{7.18}$$

where:

$$\begin{aligned}\chi_0&=\frac{\kappa^2M_\sigma E_\phi}{4(2\pi)^2}\int d^2\mathbf{k}^\perp\frac{1}{(\mathbf{k}^\perp)^\mathbf{2}}e^{-i\mathbf{b}^\perp\cdot\mathbf{k}^\perp}\\ &=4GM_\sigma E_\phi[\frac{1}{d-4}-\log b^\perp+\text{terms independent of }b^\perp]\end{aligned} \tag{7.19}$$

where we have evaluated the integral in d-dimensions and omitted finite terms independent

of b as detailed in appendix G. Note we can find the saddle point by Fourier transforming back into momentum space. In this case we find that the saddle point is located at:

$$b^{\perp} \sim \frac{4GM_{\sigma}E_{\phi}}{\Delta^{\perp}} = 2R_s\frac{E_{\phi}}{\Delta^{\perp}}, \tag{7.20}$$

where, R_s is the Schwarzschild radius of the heavy particle and $\Delta^{\perp\,2} = t$. Thus in the ultrarelativistic regime of small momentum transfer, this process is dominated by impact parameters much larger than the Schwarzschild radius of the target particle.

7.2.2 Next-to-Eikonal Phase

There are many types of corrections that have been studied to the set of diagrams discussed in the previous section [87, 88, 89, 90, 91, 92]. We will be only considering the following three types of related corrections of the same order in $\Delta^{\perp}/E_{\phi}$. First, we include those coming from the next term to the scalar propagator in the eikonal approximation. In other words, for each scalar in turn, we will keep at most one insertion of the second term in the propagator expansion of equation (7.14). The other two corrections are shown in (figure 7.4) and (figure 7.5) which are also inserted only once. We call this the next-to-eikonal approximation. We will show that part of this contribution will also exponentiate in impact parameter space and we can determine the leading corrections to the eikonal phase (χ_0) of the previous section. This particular set of corrections to ultrarelativistic gravitational scattering in the eikonal approximation has not been obtained before and as discussed in the introduction, is of interest in black hole formation in particle collisions.

Let us now calculate the next-to-eikonal term. As stated above, in order to calculate this phase, we will have to retain the next order term in (7.14) and also consider seagull (figure 7.4) and triangle type (figure 7.5) interactions which were previously ignored. As we shall discuss, it turns out that only the seagull interaction is necessary. The one graviton exchange process will not have a correction at this order since there are no scalar propagators. Let us consider the two graviton exchange.

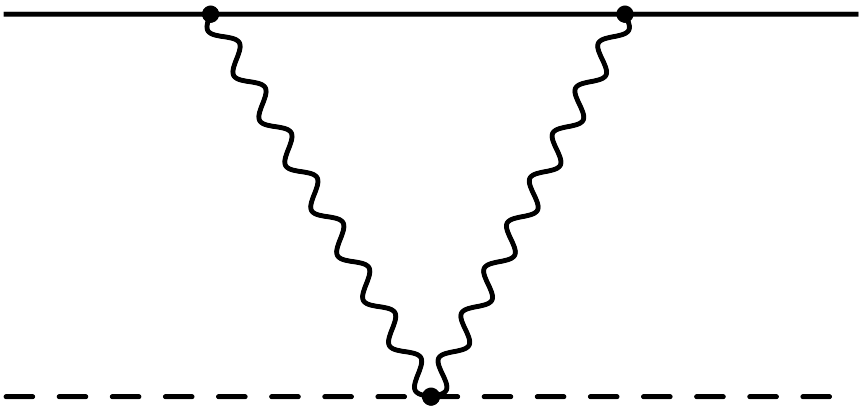

Figure 7.4 A diagram with a seagull interaction. The heavy scalar is the solid line and the light scalar is the dotted line.

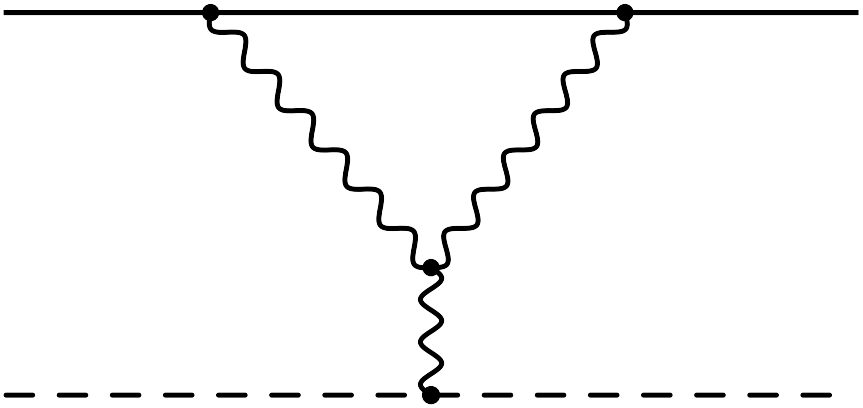

Figure 7.5 A diagram with a triangle interaction. The heavy scalar is the solid line and the light scalar is the dotted line.

Two Graviton Exchange

Let us first consider the contribution that arises when we retain the next order term in (7.14). In this case we can see from (7.13) that we have:

$$i\mathcal{M}_2^{1a} = -2i(2\pi)^3 M_\sigma (-\frac{\kappa^2 M_\sigma E_\phi^2}{2(2\pi)^3})^2 (2E_\phi)^{-2} \times \int d^3\mathbf{k_1} d^3\mathbf{k_2} \delta^3(\mathbf{k_1} + \mathbf{k_2} + \mathbf{\Delta}) \frac{1}{\mathbf{k_1^2}} \frac{1}{\mathbf{k_2^2}} \frac{\mathbf{k_1^2}}{(k_1^z + i\epsilon)^2} \tag{7.21}$$

If we symmetrize across all the graviton momenta we have:

$$i\mathcal{M}_2^{1a} = -2i(2\pi)^3 M_\sigma(-\frac{\kappa^2 M_\sigma E_\phi^2}{2(2\pi)^3})^2(2E_\phi)^{-2}\frac{1}{2}\int d^3\mathbf{k_1}d^3\mathbf{k_2}\delta^3(\mathbf{k_1}+\mathbf{k_2}+\mathbf{\Delta}) \\ \times \frac{1}{\mathbf{k_1^2}}\frac{1}{\mathbf{k_2^2}}[\frac{\mathbf{k_1^2}}{(k_1^z+i\epsilon)^2}+\frac{\mathbf{k_2^2}}{(k_2^z+i\epsilon)^2}] \tag{7.22}$$

Note that this expression is suppressed by a power of E_ϕ compared to the eikonal order piece. Let us now consider the expression that we get when we consider the seagull interaction. In this case we have:

$$i\mathcal{M}_2^{1b} = (-\frac{i\kappa}{2})^2(i\kappa^2)(\frac{i}{2})^2(i)(2\pi)^{-4}(2M_\sigma^2)^2(\frac{1}{2}) \\ \times \int d^4k_1 d^4k_2 \delta^4(k_1+k_2+\Delta)\tau^{\alpha_1\beta_1\alpha_2\beta_2}(p,p')\frac{2\delta_{0\alpha_1}\delta_{0\beta_1}-\eta_{\alpha_1\beta_1}}{k_1^2+i\epsilon} \\ \times \frac{2\delta_{0\alpha_2}\delta_{0\beta_2}-\eta_{\alpha_2\beta_2}}{k_2^2+i\epsilon}[\frac{1}{(q+k_1)^2-M_\sigma^2+i\epsilon}+\frac{1}{(q+k_2)^2-M_\sigma^2+i\epsilon}] \tag{7.23}$$

where we have symmetrized across the graviton momenta and used (7.4). $\tau^{\alpha_1\beta_1\alpha_2\beta_2}(p,p')$ is the scalar-scalar-graviton-graviton vertex. Note we can now use (7.8) and (7.9) to simplify this expression so that:

$$i\mathcal{M}_2^{1b} = (-\frac{i\kappa}{2})^2(i\kappa^2)(\frac{i}{2})^2(i)(2\pi)^{-4}(2M_\sigma^2)^2(\frac{1}{2})(2M_\sigma)^{-1}(-2\pi i)\int d^4k_1 d^4k_2 \delta(k_1^0)\delta(k_2^0) \\ \times \delta^4(k_1+k_2+\Delta)\tau^{\alpha_1\beta_1\alpha_2\beta_2}(p,p')\frac{2\delta_{0\alpha_1}\delta_{0\beta_1}-\eta_{\alpha_1\beta_1}}{k_1^2+i\epsilon}\frac{2\delta_{0\alpha_2}\delta_{0\beta_2}-\eta_{\alpha_2\beta_2}}{k_2^2+i\epsilon} \tag{7.24}$$

We can now use the identity:

$$(2\delta_{0\alpha_1}\delta_{0\beta_1}-\eta_{\alpha_1\beta_1})(2\delta_{0\alpha_2}\delta_{0\beta_2}-\eta_{\alpha_2\beta_2})\tau^{\alpha_1\beta_1\alpha_2\beta_2}(p,p') \\ = (4p^0p'^0 - p\cdot p') \approx 4E_\phi^2 \tag{7.25}$$

where we have used that fact that $p\cdot p'$ is subleading in E_ϕ compared to $p^0p'^0$ in the ultra-relativistic limit. At this point, we would like to point out that an almost identical analysis goes through for the case of the triangle diagram, except that instead of (7.25) one has:

$$(2\delta_{0\alpha_1}\delta_{0\beta_1}-\eta_{\alpha_1\beta_1})(2\delta_{0\alpha_2}\delta_{0\beta_2}-\eta_{\alpha_2\beta_2})L_{\mu\nu\eta\lambda}\tau^{\mu\nu}(p,p')\tau^{\alpha_1\beta_1\alpha_2\beta_2\eta\lambda}(k_1,k_2)/\Delta^2 \\ = -16(p\cdot p') + \text{terms not of infrared origin} \tag{7.26}$$

where $\tau^{\alpha_1\beta_1\alpha_2\beta_2\eta\lambda}(k_1,k_2)$ is the three graviton vertex. The terms not explicitly included above are not infrared sensitive. They include ultraviolet divergences related to the vertex

renormalization which we assume are taken care of by the counterterms to this order. Further, as we noted earlier, $p \cdot p'$ is subleading in E_ϕ compared to $p^0 p'^0$. Thus we can safely ignore the triangle interaction compared to the seagull interaction in the following analysis. In the small momentum transfer regime this suppression of non-linear effects for the long distance physics can also be seen from the analysis of chapter 5. First we note that in the small momentum transfer limit, the graviton line connected to the light line in (figure 7.5) must carry soft momentum. From the power counting analysis of chapter 5, for this diagram to give a contribution that is not suppressed, the other two graviton lines to which this soft line connects must be hard. Thus the loop integral in (figure 7.5) is ultraviolet dominated and will contribute to vertex renormalization as mentioned earlier. This suppression of non-linear effects is also seen in the context of classical black hole production in [106]. Once we apply (7.25) we have:

$$i\mathcal{M}_2^{1b} = (-\frac{i\kappa}{2})^2(i\kappa^2)(\frac{i}{2})^2(i)(2\pi)^{-4}(2M_\sigma^2)^2(\frac{1}{2})(2M_\sigma)^{-1}(-2\pi i)(4E_\phi^2)\int d^3\mathbf{k_1} d^3\mathbf{k_2} \\ \times \delta^3(\mathbf{k_1}+\mathbf{k_2}+\mathbf{\Delta})\frac{1}{\mathbf{k_1^2}}\frac{1}{\mathbf{k_2^2}} \tag{7.27}$$

It is now clear that (7.27) has the same power in E_ϕ as (7.22).

Finally we note that the diagrams which are mirror reflections of those in (figure 7.4) and (figure 7.5) (i.e., those with the two distinct matter-graviton vertices on the light line) are suppressed in the limit of a heavy sigma particle. This simplifies the combinatorics of the next section and was our primary reason for considering this particular kinematic limit.

n-Graviton Exchange

Let us now see what structure arises when we consider the n-graviton case. Let us first start by considering the propagator expansion piece. From (7.13) and (7.14) we see that:

$$i\mathcal{M}_n^{1a} = -2i(2\pi)^3 M_\sigma(-\frac{\kappa^2 M_\sigma E_\phi^2}{2(2\pi)^3})^n(2E_\phi)^{-n} \\ \times \int d^3\mathbf{k_1}...d^3\mathbf{k_n}\delta^3(\mathbf{k_1}+...+\mathbf{k_n}+\mathbf{\Delta})\prod_{i=1}^{n}\frac{1}{\mathbf{k_i^2}}\prod_{i=1}^{n-1}\frac{1}{K_i^z+i\epsilon}\sum_i^{n-1}\frac{\mathbf{K_i^2}}{K_i^z+i\epsilon} \tag{7.28}$$

where the sum at the end corresponds to replacing each of the $n-1$ scalar propagators with the second order term from (7.14) one time. Note the expression is not symmetric in the

graviton momenta so let us symmetrize. In this case we will have:

$$i\mathcal{M}_n^{1a} = -\frac{2i}{n!}(2\pi)^3 M_\sigma(-\frac{\kappa^2 M_\sigma E_\phi^2}{2(2\pi)^3})^n(2E_\phi)^{-n} \\ \times \int d^3\mathbf{k_1}...d^3\mathbf{k_n}\delta^3(\mathbf{k_1}+...+\mathbf{k_n}+\mathbf{\Delta})\prod_{i=1}^{n}\frac{1}{\mathbf{k_i^2}}\sum_{\text{Perms over } k_i}[\prod_{i=1}^{n-1}\frac{1}{K_i^z+i\epsilon}\sum_{i}^{n-1}\frac{\mathbf{K_i^2}}{K_i^z+i\epsilon}] \tag{7.29}$$

We will reduce this expression to a simplified form once we have arrived at the corresponding amplitude where a single seagull vertex on the light scalar line is allowed. For now, we would like to point out that the terms corresponding to the last term in (7.29) will be of two types: those that have $\mathbf{k_i^2}$ in the numerator and those that have $\mathbf{k_i}\cdot\mathbf{k_j}$ in the numerator.

Let us now move on to consider the next-to-eikonal contribution arising from allowing a single seagull vertex on the light scalar line. In this case the general matrix element for an n-graviton exchange process is:

$$i\mathcal{M}_n^{1b} = \frac{(2\pi)^4}{E_\phi^2}(\frac{i\kappa^2 M_\sigma^2 E_\phi^2}{(2\pi)^4})^n\frac{1}{2}\int d^4k_1..d^4k_n\delta^4(k_1+..+k_n+\Delta) \\ \times\prod_{i=1}^{n}\frac{1}{k_i^2}\prod_{i=1}^{n-1}\frac{1}{(p-K_i)^2+i\epsilon}(\sum_{i=1}^{n-1}(p-K_i)^2) \\ \times\sum_{\text{perms of } k_i}[\frac{1}{(q+k_1)^2-M_\sigma^2+i\epsilon}...\frac{1}{(q+k_1+...+k_{n-1})^2-M_\sigma^2+i\epsilon}] \tag{7.30}$$

The products and sum in the third line generate all possible places where the seagull vertex can be placed on the light scalar line and the permutations in the third line generate all of the possible diagrams for each placement of this vertex. Note there is an over counting due to the fact that exchanging the order of the seagull legs does not result in a distinct diagram, so we divide by 2. If we now apply (7.9) in the ultrarelativistic limit as we did for the eikonal contribution we arrive at:

$$i\mathcal{M}_n^{1b} = 8iM_\sigma(2\pi)^3(\frac{-\kappa^2 M_\sigma E_\phi}{4(2\pi)^3})^n\frac{1}{2} \\ \times\int d^3\mathbf{k_1}..d^3\mathbf{k_n}\delta^3(\mathbf{k_1}+..+\mathbf{k_n}+\mathbf{\Delta})\prod_{i=1}^{n}\frac{1}{\mathbf{k_i^2}}\prod_{i=1}^{n-1}\frac{1}{K_i^z+i\epsilon}(\sum_{i=1}^{n-1}K_i^z) \tag{7.31}$$

After symmetrizing and using a simple manipulation of the last term we have:

$$i\mathcal{M}_n^{1b} = 4iM_\sigma(2\pi)^3(\frac{-\kappa^2 M_\sigma E_\phi}{4(2\pi)^3})^n\frac{1}{n!}\int d^3\mathbf{k_1}..d^3\mathbf{k_n}\delta^3(\mathbf{k_1}+..+\mathbf{k_n}+\mathbf{\Delta})$$
$$\times\prod_{i=1}^{n}\frac{1}{\mathbf{k_i^2}}\sum_{\text{perms of } k_i}\prod_{i=1}^{n-1}\frac{1}{K_i^z+i\epsilon}(\sum_{i=1}^{n-1}\frac{(K_i^z)^2}{K_i^z+i\epsilon}) \tag{7.32}$$

Note this is an almost identical expression to (7.29), which allows for the use of an almost identical process to simplifying this expression. We can simplify (7.29) and (7.32) by Fourier transforming and going through a tedious exersize in combinatorics, which is described in detail in appendix F (the relevant expressions are given explicitly in (F.17), (F.19)). After this process we arrive at the total next-to-eikonal amplitude in impact parameter space:

$$i\widetilde{\mathcal{M}}_n^1 = -\frac{2i}{(n-1)!}\frac{M_\sigma}{(2\pi)^2}(i\frac{\kappa^2 M_\sigma E_\phi}{4(2\pi)^2})^n[\int\frac{d^2\mathbf{k}^\perp}{(k^\perp)^2}e^{-i\mathbf{b}^\perp\cdot\mathbf{k}^\perp}]^{n-1}\int\frac{d^3\mathbf{k}}{\mathbf{k^2}}e^{-i\mathbf{k}\cdot\mathbf{b}}\frac{(\mathbf{k}^\perp)^2-(k^z)^2}{(k^z+i\epsilon)^2}$$
$$-\frac{2}{(n-2)!}\frac{M_\sigma}{(2\pi)^3}(i\frac{\kappa^2 M_\sigma E_\phi}{4(2\pi)^2})^n[\int\frac{d^2\mathbf{k}^\perp}{(k^\perp)^2}e^{-i\mathbf{b}^\perp\cdot\mathbf{k}^\perp}]^{n-2}$$
$$\times\int\frac{d^3\mathbf{k}_\alpha}{\mathbf{k}_\alpha^2}\frac{d^3\mathbf{k}_\beta}{\mathbf{k}_\beta^2}e^{-i(\mathbf{k}_\alpha+\mathbf{k}_\beta)\cdot\mathbf{b}}(\frac{1}{k_\alpha^z+i\epsilon}\frac{1}{k_\beta^z+i\epsilon}\frac{\mathbf{k}_\alpha^\perp\cdot\mathbf{k}_\beta^\perp-k_\alpha^z k_\beta^z}{k_\alpha^z+k_\beta^z+i\epsilon}) \tag{7.33}$$

As elaborated in appendix F, this can be reduced to (for details on the evaluation of these integrals please see appendix G):

$$i\widetilde{\mathcal{M}}_n^1 = 2(s-M_\sigma^2)[\frac{(i\chi_0)^{n-1}}{(n-1)!}\chi_1+\frac{(i\chi_0)^{n-2}}{(n-2)!}i\chi_2] \tag{7.34}$$

where:

$$\chi_1 = \frac{\kappa^2 M_\sigma}{8(2\pi)^4}\int\frac{d^3\mathbf{k}}{\mathbf{k^2}}e^{-i\mathbf{k}\cdot\mathbf{b}}\frac{(\mathbf{k}^\perp)^2-(k^z)^2}{(k^z+i\epsilon)^2}$$
$$= -\frac{\kappa^2 M_\sigma}{8(2\pi)^2}[\frac{1}{|\mathbf{b}|}+\Theta(z)z(2\pi)\delta^2(\mathbf{b}^\perp)]$$
$$= -\frac{R_s}{2\pi}[\frac{1}{|\mathbf{b}|}+\Theta(z)z(2\pi)\delta^2(\mathbf{b}^\perp)] \tag{7.35}$$

and:

$$\chi_2 = -i\frac{\kappa^4 M_\sigma^2 E_\phi}{32(2\pi)^7}\int \frac{d^3\mathbf{k}_\alpha}{\mathbf{k}_\alpha^2}\frac{d^3\mathbf{k}_\beta}{\mathbf{k}_\beta^2}e^{-i(\mathbf{k}_\alpha+\mathbf{k}_\beta)\cdot\mathbf{b}}\left(\frac{1}{k_\alpha^z+i\epsilon}\frac{1}{k_\beta^z+i\epsilon}\frac{\mathbf{k}_\alpha^\perp\cdot\mathbf{k}_\beta^\perp - k_\alpha^z k_\beta^z}{k_\alpha^z+k_\beta^z+i\epsilon}\right)$$
$$= \frac{\kappa^4 M_\sigma^2 E_\phi}{128(2\pi)^3}\frac{1}{b^\perp}[\pi-2] + \mathcal{O}(\frac{z}{b^\perp}) \tag{7.36}$$

where we have ignored a term higher order in $\frac{z}{b^\perp}$ in χ_2.

Note that χ_1 is suppressed by a power of E_ϕ compared to χ_0 but χ_2 is not. This is resolved by that fact that χ_2 is suppressed by a factor of κ^2 compared to χ_0, so to match order by order in κ, each term that has a factor χ_2 must have one less power of χ_0 than each term with χ_1 at that same order in κ. This causes a suppression by a factor of E_ϕ, which can readily be seen in (7.34).

It is interesting to see that when we sum over all n $i\widetilde{\mathcal{M}}^0 + i\widetilde{\mathcal{M}}^1$ exponentiates in the following manner:

$$i\widetilde{\mathcal{M}}^{0+1} = 2(s-M_\sigma^2)(1+\chi_1)[e^{i(\chi_0+\chi_2)}-1] \tag{7.37}$$

To confirm this exponentiation gives a satisfactory expression for $i\widetilde{\mathcal{M}}_n^{0+1}$, all one needs to do is Taylor expand and group the terms order by order in κ^2 and throw away any terms that are suppressed by more than one factor of E_ϕ at that order in κ.

Let us next discuss the implications of the correction χ_1 to the multiplicative factor derived in (7.37). This contribution clearly decreases the amplitude. However, we expect unitarity is still maintained because the phase space boundaries also change at this order.

We now can calculate the correction to the saddlepoint (7.20) due to χ_2. For this purpose we transform back to momentum space and define:

$$\text{Phase} = i(\chi_0+\chi_2 - b^\perp\Delta^\perp - z\Delta^z). \tag{7.38}$$

The condition $\frac{\partial}{\partial b^\perp}$Phase$= 0$ determines the new saddlepoint. This condition gives:

$$\Delta^\perp(b^\perp)^2 + 4GM_\sigma E_\phi b^\perp + G^2M_\sigma^2E_\phi(1-\frac{2}{\pi}) = 0 \tag{7.39}$$

Thus, we have that:

$$b^\perp \sim \frac{2R_sE_\phi}{\Delta^\perp} - \frac{R_s}{8}(1-\frac{2}{\pi}) \tag{7.40}$$

The first term on the right hand side of (7.40) is the leading order saddlepoint for the

impact parameter and the second term is the correction due to the next to leading eikonal phase we have just calculated. While the leading order term shows that the impact parameter differs from the Schwarzschild radius of the heavy particle by a large factor of $E_\phi/\Delta^\perp$, no such enhancement is present for the correction. Thus as discussed earlier, the leading order result suggests that the scattering process is dominated by large values of the impact parameter. However, the power correction to the leading eikonal result shifts it to slightly smaller values. This is all we can deduce in the context of perturbation theory. However, our conclusion does support the possibility that power corrections probe smaller values of the impact parameter and therefore provide more information about the process of black hole formation than the leading order result.

7.3 Discussion

In this chapter we have calculated the next-to-eikonal contribution to the gravitational scattering amplitude by expanding the propagator to next-to-eikonal order and allowing seagull type vertices, all of which are power corrections suppressed by a power of $1/E_\phi$ with respect to the leading eikonal term. We found that this part of this contribution exponentiates. The next-to-eikonal phase also causes the impact parameter to decrease in magnitude compared to the purely eikonal case.

Our primary motivation for this study and one which is borne out by the results, is that the study of power corrections to the leading eikonal result provides useful information about black hole production in high energy gravitational scattering. Once a black hole is formed, there should be no factorization of short and long distance physics because there is no accessible reference hard scattering point to make this separation manifest. This is because the hard scattering point is shielded by the horizon. The formation process is in itself a non-perturbative phenomenon. However, we expect that some indication of the breakdown of factorization will present itself at some order in the higher order power corrections, providing a signal for this breakdown in perturbation theory. As happens in the case of gauge theories for similar processes, we expect that once factorization and hence perturbation theory break down, all power corrections will become equally important. We did not explicitly find this breakdown of factorization at next-to-eikonal order. Nevertheless, we did find a tendency for power corrections to probe smaller impact parameters. Thus it would be interesting to precisely look for these effects in a general setting. Such an approach for gauge theories was discussed in [107, 108]. The corresponding analysis for perturbative quantum gravity would be an extremely interesting subject of future research.

Chapter 8
Conclusion

In this thesis we have presented selected studies concerning both classical and quantum issues in theoretical gravitational physics. On the classical side of gravity, we focused on the matter of dark energy, specifically the k-essence model. Although this model necessarily has non-canonical scalar fields with strange behavior such as superluminality, we found that it is possible to successfully simulate its behavior around black holes and during gravitational collapse for a large range of parameters, greatly increasing confidence in the robustness of the theory and similar non-canonical field theories. However, the question of whether or not a global time coordinate can always be defined for these theories remains an open question. We also demonstrated that these non-canonical field theories settle down to a stationary solution during accretion with cosmological boundary conditions, which is an assumption that has gone into many previous analytic studies of the subject.

On the quantum side of gravity, we circumvented problems associated with the nonrenormalizability of the theory by focusing on investigations of perturbative quantum gravity at energies smaller than the Planck scale. As among the most interesting long distance properties of a generic field theory are infrared divergences, we performed an extensive study of these divergences. In particular, we found that collinear divergences cancel in all gravitational amplitudes at all orders. We were also able to derive a double copy relation similar to that of [7] in the case where there is no hard momentum transfer and showed that this implies a similar relation between the corresponding shockwave solutions of both theories. Finally, we calculated the next-to-eikonal amplitude for the gravitational scattering of two scalars, finding that this second order correction tended to decrease the dominant length scale involved in this process. This gives hope that studying these power corrections in a more general setting will yield direct evidence of black hole production from the quantum theory.

The two main issues concerning gravity addressed in this thesis, namely the true nature of dark energy and quantum gravity, have been lacking an adequate explanation for many years. Although the progress presented in this dissertation is only a minuscule step towards

understanding these grandiose issues, the fact that new interesting fundamental features of gravitational physics can still be found so long after physicists first started researching the subject gives hope that we will some day fully understand the theory.

Appendices

Appendix A

Examining Classicalization Without Spherical Symmetry

A.1 Introduction

In this appendix we study a novel proposal to the UV-completion of a class of non-renormalizable theories [109]. In this approach, called *classicalization*, high-energy scattering amplitudes are conjectured to be unitarized by the production of extended classical objects, dubbed *classicalons*. Although classicalization has no direct connection to gravitational physics, these classicalons play an analogous role to black holes in graviton-graviton scattering, where the effective gravitational coupling blows up for center-of-mass energies large than the Planck scale. However, as will be seen in this appendix, unlike in the case of black holes, classicalons do not serve to unitarize high energy scattering when we examine the system out of spherical symmetry. Thus this appendix will serve as an example of how quantum gravity is fundamentally different from other quantum theories.

Although the existence and properties of classicalons have not been studied at all, it has been somehow suspected that they might form below the length scale called the *classicalization radius* [110, 112]. The classicalization radius is defined as the classical radius down to which high-energy shells of fields propagate essentially freely, without experiencing a significant correction from interaction. We can at least consider the condition

$$(\text{classicalization radius}) \gg (\text{cutoff length}) \tag{A.1}$$

as a necessary condition for the formation of classicalons.

If classicalization really works then we would have to change our view of non-renormalizable field theories and Wilsonian UV completion, in which a weakly coupled quantum field theory above the cutoff scale of an effective field theory is reconstructed by integrating in some new degrees of freedom. In the classicalization approach, a non-

renormalizable field theory would unitarize itself by its own resources, above the scale that would otherwise be the UV cutoff of the theory.

Hence it is important to investigate the validity of the classicalization proposal. However, so far, the studies of the classicalization approach have been rather limited. One of the limitations is that all considerations in the literature assume perfect spherical symmetry. The purpose of this appendix is to study the classicalization proposal beyond spherical symmetry. Unfortunately, we shall see that the above mentioned necessary condition (A.1) does not hold if spherical symmetry is significantly relaxed. Thus, considerations in this appendix point towards the conclusion that classicalization does not serve as UV-completion for the class of non-renormalizable theories.

The rest of the appendix is organized as follows. In section A.2 we shall briefly review the classicalization proposal. We shall also argue that classicalization does not serve as a way to UV complete the other classes of the field theories considered in the literature, except for the Goldstone-type field theory. For this reason, we shall investigate the Goldstone-type field theory in starting with section A.3. In section A.3 we consider a small non-spherical deformation and show that the classicalization radius tends to decrease in a region where a shell made of the field is slightly flattened. In section A.4, in order to describe a sufficiently large flattened region, we consider the high-energy collision of planar shells and show that the system never classicalizes before reaching sub-cutoff lengths. This no-go result is further strengthened by the analysis of a small non-planar deformation in section A.5. In section A.6 we show that the shape of scattered planar wave is UV sensitive. Section A.7 is devoted to a summary of the main results of this appendix.

Throughout this appendix we shall adopt the mostly plus sign $(-+++)$ for the metric.

A.2 A Brief Review of the Classicalization Proposal

In the literature, the classicalization proposal has been studied for a scalar field without shift symmetry, a scalar field with shift symmetry (Goldstone-type field), and the graviton in general relativity. In this appendix we shall investigate the robustness of the classicalization proposal for the theory of Goldstone bosons. Before going into further detail, let us explain why we will not consider the other two cases.

The example of the scalar field without shift symmetry has a Lagrangian of the form

$$\mathcal{L} = -\frac{1}{2} g^{\mu\nu} \partial_\mu \phi \partial_\nu \phi - \frac{\phi}{2M_*} g^{\mu\nu} \partial_\mu \phi \partial_\nu \phi + \cdots . \tag{A.2}$$

In [109], the second term on the right hand side was considered as a possible source of classicalization. However, one can redefine the field ϕ so that the sum of the first and the second terms becomes a canonical kinetic term of the new field $\phi_c = (2/3)(1+\phi/M_*)^{3/2}$. Thus, the system is equivalent to a noninteracting canonical scalar field. The field redefinition does not work for $\phi < -M_*$, but in this regime $\bar{\phi}_c = |\phi_c|$ has a wrong sign kinetic term and unitarity is violated. Therefore, the first two terms in this Lagrangian do not serve as a good example of classicalization.

The graviton in Einstein gravity has been considered as a possible candidate that exhibits the classicalization phenomenon [112, 113]. However, it is well known that in general relativity, one can form a black hole with arbitrarily small mass [15]. Moreover, there are known counterexamples to the cosmic censorship conjecture in general relativity [116, 117, 118]. Therefore, in general relativity one can in principle probe arbitrarily short distances unless new physics above the cutoff scale somehow prevents one from doing so. [1] Therefore, classicalization is unlikely to work in general setups in general relativity.

In this appendix we shall consider the Goldstone-type field, i.e. a scalar field with shift symmetry, since this is the only remaining situation that has been studied in the literature so far.

Classicalization of the Goldstone-type field was investigated in the Euclidean path integral formulation in [114]. However, the background solution is singular and the corresponding Euclidean action is infinite. Therefore, it seems rather difficult to extract any physically meaningful insights from the result of [114]. For this reason, in this analysis we will not adopt the path integral formulation.

The Goldstone-type field that has been studied in the context of classicalization has a Lagrangian of the form

$$\mathcal{L} = -\frac{1}{2} g^{\mu\nu}\partial_\mu\phi\partial_\nu\phi + \frac{L_*^4}{4}\left[g^{\mu\nu}\partial_\mu\phi\partial_\nu\phi\right]^2 . \tag{A.3}$$

Following references [110, 112], we investigate the classical dynamics of a spherical shell made of this scalar field in a Minkowski spacetime. Namely, we assume that the backreaction of the scalar field on the background geometry is negligible and we seek a solution $\phi(t,r)$ to the equation of motion

$$\Box_4\phi = L_*^4\partial^\mu\left[(\partial\phi)^2\partial_\mu\phi\right] \tag{A.4}$$

[1] Note that since fine tuning is necessary to create a classical state that will result in such an arbitrarily small black hole, one can make the argument that some quantum fluctuations will prevent such a state from being prepared. However, as we discuss in the conclusions, the argument that we will make in this analysis regarding the model of Goldstone bosons is not dependent on any fine-tuning and is robust.

in a Minkowski spacetime

$$ds^2 = -dt^2 + dr^2 + r^2(d\theta^2 + \sin^2(\theta)d\bar{\theta}^2). \tag{A.5}$$

Our neglect of the backreaction effects is justified in the decoupling limit $M_{pl}L_* \gg 1$.

What we are interested in is the classical radius r_* down to which high-energy spherical shells propagate essentially freely, without experiencing a significant correction from the interaction term. This radius is dubbed the *classicalization radius*. In order to determine r_* for this system, references [110, 112] solved the equation of motion iteratively by expanding ϕ as

$$\phi = \phi_0 + \phi_1 + \cdots, \tag{A.6}$$

and assuming that ϕ_0 satisfies the equation of motion with $L_* = 0$. We shall soon see what the expansion parameter is.

Under the assumed spherical symmetry, a general solution to the zeroth order equation $\Box_4\phi_0 = 0$ is

$$\phi_0 = \frac{1}{r}\left[F_0(t+r) - F_0(t-r)\right], \tag{A.7}$$

where we have imposed the regularity of ϕ_0 at $r = 0$. In order for this solution to represent a shell with thickness a, the form of the function $F_0(t)$ is set to

$$F_0(t) = Af(t/a), \tag{A.8}$$

where $f(\tau)$ is a function whose amplitude and derivatives are of $O(1)$ in the vicinity of the shell configuration, so that the total energy and the occupation number of the configuration are $\sim A^2/a$ and $\sim A^2$, respectively. According to [110, 112], we are interested in configurations with a small occupation number. Thus we suppose that

$$A = O(1). \tag{A.9}$$

We are interested in the behavior of the system before the thin shell peaked at $t + r \sim 0$ reaches the center. Hence we can safely drop $-F_0(t-r)$. We thus have

$$\phi_0 = \frac{A}{r}f(\tau_+), \quad \tau_+ = \frac{t+r}{a}. \tag{A.10}$$

Since ϕ_0 is small at large r but becomes large at small r, the nonlinear interaction is negligible at large r but becomes significant at small r. The classicalization radius r_* for this system is thus defined as a radius at which the amplitude of ϕ_1 catches up with that of ϕ_0.

One can easily guess r_* from (A.10). Since

$$g^{\mu\nu}\partial_\mu\phi\partial_\nu\phi = -\frac{A^2}{ar^3}\left[f'(\tau_+)f(\tau_+) + O(a/r)\right], \tag{A.11}$$

the second term in the Lagrangian (A.3) becomes as important as the first term when

$$\frac{L_*^4}{ar^3} \sim 1. \tag{A.12}$$

Thus, it is expected that the classicalization radius r_* is

$$r_* \sim (L_*^4/a)^{1/3}. \tag{A.13}$$

To confirm this expectation, let us seek the first order solution ϕ_1, which is the retarded solution to

$$\Box_4\phi_1 = L_*^4\partial^\mu\left[(\partial\phi_0)^2\partial_\mu\phi_0\right]. \tag{A.14}$$

Since the right hand side is calculated as

$$\bar{s}_0(\tau_+, r) = \frac{A^3L_*^4}{2a^2r^5}\left\{\left[f''(\tau_+)(f(\tau_+))^2 \ \ +4(f'(\tau_+))^2f(\tau_+)\right] + O(a/r)\right\}, \tag{A.15}$$

we obtain

$$\begin{aligned}\phi_1 &= \frac{a}{2r}\int_r^\infty dr'r'\int_{-\infty}^{\tau_+} d\tau_1\bar{s}_0(\tau_1, r') \\ &= -\frac{A^3L_*^4}{12ar^4}\int_{-\infty}^{\tau_+} d\tau_1\left\{\left[f''(\tau_1)(f(\tau_1))^2 \ \ +4(f'(\tau_1))^2f(\tau_1)\right] + O(a/r)\right\}.\end{aligned} \tag{A.16}$$

Since the integral is of $O(1)$ in the vicinity of the shell, the amplitude of ϕ_1 catches up with that of ϕ_0 at $r \sim r_*$, where r_* is given by (A.13).

A.3 Non-Spherical Deformation

In this section we consider a non-spherical deformation of the shell and see that if a part of the shell is flatter (or more curved), r_* is slightly reduced (or increased) in that part.

A.3.1 Zeroth Order Solution

For the zeroth order part, we adopt the ansatz

$$\phi_0 = \phi_{00}(t,r) + \phi_{02}(t,r)P_2(\cos\theta). \tag{A.17}$$

Then the zeroth order equation leads to the solution

$$\begin{aligned}
\phi_{00} &= \frac{1}{r}\left[F_0(t+r) + G_0(t-r)\right], \\
\phi_{02} &= r\left(\partial_r \frac{1}{r}\right)^2 \left[F_2(t+r) + G_2(t-r)\right].
\end{aligned} \tag{A.18}$$

Imposing regularity at $r = 0$ leads to the condition $F_0(t) + G_0(t) = F_2(t) + G_2(t) = 0$ for $^\forall t$. Thus, the zeroth order solution is

$$\begin{aligned}
\phi_0 &= \frac{1}{r}\left[F_0(t+r) - F_0(t-r)\right] \\
&+ r\left(\partial_r \frac{1}{r}\right)^2 \left[F_2(t+r) - F_2(t-r)\right] P_2(\cos\theta).
\end{aligned} \tag{A.19}$$

Let us suppose that

$$F_0(t) = Af(t/a), \quad F_2(t) = Aar_2 \int_{-\infty}^{t/a} d\tau_1 f(\tau_1), \tag{A.20}$$

where r_2 is a constant. For $r \gg a$, this solution is reduced to

$$\begin{aligned}
\phi_0 &\simeq \frac{A}{r}\left\{\left[f(\tau_+) - f(\tau_-)\right] + \left[f'(\tau_+) - f'(\tau_-)\right]\frac{r_2}{a}P_2(\cos\theta)\right\} \\
&= \frac{A}{r}\left[f(\tilde{\tau}_+) - f(\tilde{\tau}_-)\right] + O(r_2^2/a^2),
\end{aligned} \tag{A.21}$$

where

$$\tau_\pm \equiv \frac{t \pm r}{a}, \quad \tilde{\tau}_\pm = \tau_\pm + \frac{r_2}{a}P_2(\cos\theta). \tag{A.22}$$

If $f(\tau)$ represents a wave packet peaked at $\tau = 0$ then $f(\tilde{\tau}_\pm)$ is peaked at $r \simeq \mp[t + r_2 P(\cos\theta)]$.

The non-spherical deformation ϕ_{02} includes $O(a/r)$ and $O(a^2/r^2)$ corrections. The $O(a/r)$ correction to (A.21) slightly changes the height of the peak. Indeed, by including

the $O(a/r)$ correction, (A.21) is modified as

$$\begin{aligned}\phi_0 &= \frac{A}{r}\left\{f(\tilde{\tau}_+)\left[1-\frac{3r_2}{r}P_2(\cos\theta)\right]-f(\tilde{\tau}_+)\left[1+\frac{3r_2}{r}P_2(\cos\theta)\right]\right. \\ &\left.+O(a^2/r^2)+O(r_2^2/a^2)\right\}, \end{aligned} \tag{A.23}$$

Although we shall not write it explicitly here, the $O(a^2/r^2)$ correction represents the tail induced by the motion of the deformed shell.

A.3.2 Retarded Solution to Inhomogeneous Equation

It is easy to show that

$$\phi_1(t_+,t_-)=\frac{\psi_{10}}{r}+r\left(\partial_r\frac{1}{r}\right)^2\psi_{12}P_2(\cos\theta) \tag{A.24}$$

with

$$\psi_{1n}=-\frac{1}{4}\int_{-\infty}^{t_+}dt'_+\int_{-\infty}^{t_-}dt'_-f_n(t'_+,t'_-)\quad(n=0,2) \tag{A.25}$$

satisfies the inhomogeneous equation

$$\Box_4\phi_1=\frac{f_0(t_+,t_-)}{r}+r\left(\partial_r\frac{1}{r}\right)^2 f_2(t_+,t_-)P_2(\cos\theta) \tag{A.26}$$

and the retarded boundary condition. Note $t_\pm\equiv t\pm r$.

There is freedom to add $B_2(t)r^3+C_2(t)r$ to $f_2(t_+,t_-)$ but $B_2(t)$ and $C_2(t)$ can be fixed by demanding that $f_2(t_+,t_-)$ remains finite at $r\to\infty$ for $^\forall t$. Thus, when the inhomogeneous equation is of the form

$$\Box_4\phi_1=s_0(t,r)+s_2(t,r)P_2(\cos\theta), \tag{A.27}$$

we have

$$\begin{aligned} f_0(t_+,t_-) &= rs_0(t,r), \\ f_2(t_+,t_-) &= r\int_r^\infty dr_1 r_1\int_{r_1}^\infty dr_2\frac{s_2(t,r_2)}{r_2}, \end{aligned} \tag{A.28}$$

where t and r on the right hand side should be understood as $(t_++t_-)/2$ and $(t_+-t_-)/2$ respectively.

A.3.3 First Order Solution up to $O(r_2/a)$ with $O(a/r)$ Correction

We are interested in the behavior of the system before the thin shell peaked at $t + r \sim 0$ reaches the center. Hence, we can safely drop $-F_0(t-r)$ and $-F_2(t-r)$ in (A.19). We thus have

$$\begin{aligned}\phi_0 &= \frac{A}{r}\left\{f(\tau_+)\left[1-\frac{3r_2}{r}P_2(\cos\theta)\right] + f'(\tau_+)\frac{r_2}{a}P_2(\cos\theta) + O(a^2/r^2)\right\} \\ &= \frac{A}{r}\left\{f(\tilde{\tau}_+)\left[1-\frac{3r_2}{r}P_2(\cos\theta)\right] + O(a^2/r^2) + O(r_2^2/a^2)\right\}, \end{aligned} \tag{A.29}$$

where τ_+ and $\tilde{\tau}_+$ are defined in (A.22). Consequently, up to $O(r_2/a)$ the equation for ϕ_1 is of the form (A.27) with

$$\begin{aligned}\bar{s}_0 &= \frac{A^3L_*^4}{2a^2r^5}\left\{\left[f''(\tau_+)(f(\tau_+))^2 + 4(f'(\tau_+))^2 f(\tau_+)\right] - \frac{3l}{r}f'(\tau_+)(f(\tau_+))^2 + O(a^2/r^2)\right\}, \\ \bar{s}_2 &= \frac{r_2}{a}\left\{\frac{\partial \bar{s}_0}{\partial \tau_+} - \frac{15A^3L_*^4}{2ar^6}\left[f''(\tau_+)(f(\tau_+))^2 + 4(f'(\tau_+))^2 f(\tau_+)\right]\right. \\ &\quad \left. + \frac{A^3L_*^4}{a^2r^5}\times O(a^2/r^2)\right\}. \end{aligned} \tag{A.30}$$

where $\bar{s}_n \equiv s_n(t = a\tau_+ - r, r)$ $(n = 0, 2)$ is s_n written as a function of (τ_+, r). Note that in the coordinates $(\tau_+, r, \theta, \bar{\theta})$, the Minkowski metric (A.5) is written as

$$ds^2 = -a^2 d\tau_+^2 + 2a d\tau_+ dr + r^2(d\theta^2 + \sin^2\theta d\bar{\theta}^2), \tag{A.31}$$

and

$$g^{\mu\nu}\partial_\mu\partial_\nu = \frac{1}{a}\partial_+\partial_r + \frac{1}{4}\partial_r^2 + \frac{1}{r^2}\partial_\theta^2 + \frac{1}{r^2\sin^2\theta}\partial_{\bar{\theta}}^2. \tag{A.32}$$

From $\bar{s}_2$, f_2 is obtained by solving

$$\begin{aligned}\bar{s}_2 &= r\left[\left(\frac{\partial}{\partial r} + \frac{1}{a}\frac{\partial}{\partial \tau_+}\right)\frac{1}{r}\right]^2 \bar{f}_2 \\ &= \frac{1}{a^2 r}\left[\frac{\partial^2}{\partial \tau_+^2} - \frac{3a}{r}\frac{\partial}{\partial \tau_+} + O(a^2/r^2)\right]\bar{f}_2. \end{aligned} \tag{A.33}$$

Here and in the following, $\bar{f}_n \equiv f_n(t_+ = a\tau_+, t_- = a\tau_+ - 2r)$ $(n = 0, 2)$ is f_n written as a function of (τ_+, r). Thus, we obtain

$$\begin{aligned}\bar{f}_2(\tau_+, r) &= a^2 r\left[\int_{-\infty}^{\tau_+} d\tau_1 \int_{-\infty}^{\tau_1} d\tau_2 \bar{s}_2(\tau_2, r) + \frac{3a}{r}\int_{-\infty}^{\tau_+} d\tau_1 \int_{-\infty}^{\tau_1} d\tau_2 \int_{-\infty}^{\tau_2} d\tau_3 \bar{s}_2(\tau_3, r)\right. \\ &\quad \left. + O(a^2/r^2)\right]. \end{aligned} \tag{A.34}$$

We of course have

$$\bar{f}_0(\tau_+, r) = r\bar{s}_0(r, \tau_+). \tag{A.35}$$

Now by changing the integration variables from (t'_+, t'_-) to $(\tau'_+ = t'_+/a, r' = (t'_+ - t'_-)/2)$, the formula (A.25) is written as

$$\bar{\psi}_{1n}(\tau_+, r) = -\frac{a}{2}\int_r^\infty dr' \int_{-\infty}^{\tau_+} d\tau'_+ \bar{f}_n(\tau'_+, r') \quad (n = 0, 2), \tag{A.36}$$

where $\bar{\psi}_{1n} \equiv \psi_{1n}(t_+ = a\tau_+, t_- = a\tau_+ - 2r)$ is ψ_{1n} written as a function of (τ_+, r). Concretely,

$$\begin{aligned}
\bar{\psi}_{10}(\tau_+, r) &= -\frac{a}{2}\int_r^\infty dr' r' \int_{-\infty}^{\tau_+} d\tau_1 \bar{s}_0(\tau_1, r'), \\
\bar{\psi}_{12}(\tau_+, r) &= -\frac{a^3}{2}\int_r^\infty dr' r' \\
&\quad \times \left[\int_{-\infty}^{\tau_+} d\tau_1 \int_{-\infty}^{\tau_1} d\tau_2 \int_{-\infty}^{\tau_2} d\tau_3 \bar{s}_2(\tau_3, r') \right. \\
&\quad + \frac{3a}{r'} \int_{-\infty}^{\tau_+} d\tau_1 \int_{-\infty}^{\tau_1} d\tau_2 \int_{-\infty}^{\tau_2} d\tau_3 \\
&\quad \left. \times \int_{-\infty}^{\tau_3} d\tau_4 \bar{s}_2(\tau_4, r') + O(a^2/r'^2) \right].
\end{aligned} \tag{A.37}$$

Therefore, up to $O(r_2/a)$, the formula (A.24) gives

$$\phi_1 \simeq \bar{\phi}_{10}(\tau_+, r) + \bar{\phi}_{12}(\tau_+, r) P_2(\cos\theta), \tag{A.38}$$

where

$$\begin{aligned}
\bar{\phi}_{10} &= -\frac{a}{2r}\int_r^\infty dr' r' \int_{-\infty}^{\tau_+} d\tau_1 \bar{s}_0(\tau_1, r'), \\
\bar{\phi}_{12} &= -\frac{a}{2r}\left[\int_r^\infty dr' r' \int_{-\infty}^{\tau_+} d\tau_1 \bar{s}_2(\tau_1, r') - \frac{3a}{r}\int_r^\infty dr' \int_{r'}^\infty dr'' \int_{-\infty}^{\tau_+} d\tau_1 \int_{-\infty}^{\tau_1} d\tau_2 \bar{s}_2(\tau_2, r') \right. \\
&\quad \left. + O(a^2/r^2) \right].
\end{aligned} \tag{A.39}$$

Here, we have integrated by parts in order to obtain the expression for $\bar{\phi}_{12}$. Finally, by using the explicit expressions (A.30), it is shown that

$$\begin{aligned}
\bar{\phi}_{10} &= -\frac{A^3 L_*^4}{12ar^4}\left\{ g(\tau_+) - \frac{3a}{4r}(f(\tau_+))^3 + O(a^2/r^2) \right\}, \\
\bar{\phi}_{12} &= -\frac{A^3 L_*^4}{12ar^4}\frac{r_2}{a}\left\{ g'(\tau_+) - \frac{9a}{4r} f'(\tau_+)(f(\tau_+))^2 - \frac{12a}{r} g(\tau_+) \right\},
\end{aligned} \tag{A.40}$$

where

$$g(\tau_+) \equiv \int_{-\infty}^{\tau_+} d\tau_1 \left[f''(\tau_1)(f(\tau_1))^2 + 4(f'(\tau_1))^2 f(\tau_1) \right]. \tag{A.41}$$

In summary,

$$\begin{aligned} \phi_1 &= -\frac{A^3 L_*^4}{12ar^4} \left\{ g(\tilde{\tau}_+) \left[1 - \frac{12r_2}{r} P_2(\cos\theta) \right] - \frac{3a}{4r} (f(\tilde{\tau}_+))^3 \right. \\ &\quad \left. + O(a^2/r^2) + O(r_2^2/a^2) \right\}. \end{aligned} \tag{A.42}$$

Hence, we obtain

$$\begin{aligned} \frac{\phi_1}{\phi_0} &= -\frac{A^2 L_*^4}{12ar^3} \left\{ \frac{g(\tilde{\tau}_+)}{f(\tilde{\tau}_+)} \left[1 - \frac{9r_2}{r} P_2(\cos\theta) \right] - \frac{3a}{4r} (f(\tilde{\tau}_+))^2 \right. \\ &\quad \left. + O(a^2/r^2) + O(r_2^2/a^2) \right\}. \end{aligned} \tag{A.43}$$

As noted earlier, the classicalization radius r_* is the value of r at which the amplitude of ϕ_1 catches up with that of ϕ_0. Thus, this result clearly shows that r_* is slightly reduced (or increased) if $r_2 P_2(\cos\theta)$ is positive (or negative), i.e. if the shell is flatter (or more curved) in some region. This is exactly what we have expected.

In the next section, in order to describe a sufficiently large flattened region, we consider a planarly symmetric case.

A.4 Planarly Symmetric Case

In 4-dimensional flat spacetime

$$ds_4^2 = -dt^2 + dx^2 + dy^2 + dz^2, \tag{A.44}$$

we consider a planarly symmetric ansatz $\phi = \phi(t, x)$. By integrating out the two spatial dimensions parallel to the plane of symmetry, y and z, we obtain a scalar field $\varphi = \sqrt{\mathcal{A}_2}\phi$ in 2-dimension, where $\mathcal{A}_2$ is the area of the plane.

In a two dimensional flat spacetime

$$ds_2^2 = -dt^2 + dx^2 = -dt_+ dt_-, \quad t_\pm \equiv t \pm x, \tag{A.45}$$

the retarded solution to

$$\Box_2 \varphi_1 = f(t_+, t_-) \tag{A.46}$$

is given by

$$\varphi_1 = -\frac{1}{4}\int_{-\infty}^{t_+} dt'_+ \int_{-\infty}^{t_-} dt'_- f(t'_+, t'_-). \tag{A.47}$$

The equation of motion

$$\Box_4 \phi = L_*^4 \partial^\mu \left[(\partial\phi)^2 \partial_\mu \phi\right] \tag{A.48}$$

in 4-dimensions is reduced to

$$\Box_2 \varphi = \frac{L_*^4}{\mathcal{A}_2} \partial^\mu \left[(\partial\varphi)^2 \partial_\mu \varphi\right] \tag{A.49}$$

in 2-dimensions. Let us solve this equation iteratively by expanding φ as

$$\varphi = \varphi_0 + \varphi_1 + \cdots, \tag{A.50}$$

and assuming that φ_0 satisfies the equation of motion with $L_* = 0$, i.e., $\Box_2 \varphi = 0$. Thus,

$$\varphi_0 = \varphi_+(t_+) + \varphi_-(t_-). \tag{A.51}$$

We shall soon see what the expansion parameter is.

The first order equation is

$$\Box_2 \varphi_1 = \frac{8L_*^4}{\mathcal{A}_2} \left[\varphi''_+(t_+)(\varphi'_-(t_-))^2 + \varphi_-(t_-)''(\varphi'_+(t_+))^2\right]. \tag{A.52}$$

Thus the retarded solution is

$$\varphi_1 = -\frac{2L_*^4}{\mathcal{A}_2} \int_{-\infty}^{t_+} dt'_+ \int_{-\infty}^{t_-} dt'_- \left[\varphi''_+(t'_+)(\varphi'_-(t'_-))^2 + \varphi_-(t'_-)''(\varphi'_+(t'_+))^2\right]. \tag{A.53}$$

Let us suppose that

$$\varphi_+(t) = \varphi_-(t) = A\, f(t/a). \tag{A.54}$$

Roughly speaking, the total energy and the occupation number of the configuration are $\sim A^2/a$ and $\sim A^2$. Then we obtain

$$\frac{\varphi_1}{A} = -\frac{2L_*^4 A^2}{\mathcal{A}_2\, a^2} \int_{-\infty}^{t_+/a} d\tau_1 \int_{-\infty}^{t_-/a} d\tau_2 \left[f''(\tau_1)(f'(\tau_2))^2 + f''(\tau_2)(f'(\tau_1))^2\right]. \tag{A.55}$$

We now see that the expansion parameter is

$$\epsilon \equiv \frac{2L_*^4 A^2}{\mathcal{A}_2\, a^2}. \tag{A.56}$$

The iterative solution is a good approximation if $\epsilon \ll 1$.

As an example, let us consider a Gaussian wave packet

$$f(\tau) = e^{-\tau^2}. \tag{A.57}$$

Figures A.1 and A.2 show φ_0/A and $\varphi_1/(-A\epsilon)$, respectively, as functions of $\tau_\pm \equiv t_\pm/a$. This clearly shows that φ_1 stays small compared to φ_0 as far as $\epsilon \ll 1$ and that the interaction length is $\sim a$. In this case the system never classicalizes. For $\epsilon \sim 1$, the amplitude of φ_1 becomes as large as that of φ_0 but the interaction length is still $\sim a$. Thus, for high-energy scattering with $a \ll L_*$, there is no sign of classicalization before reaching the sub-cutoff length.

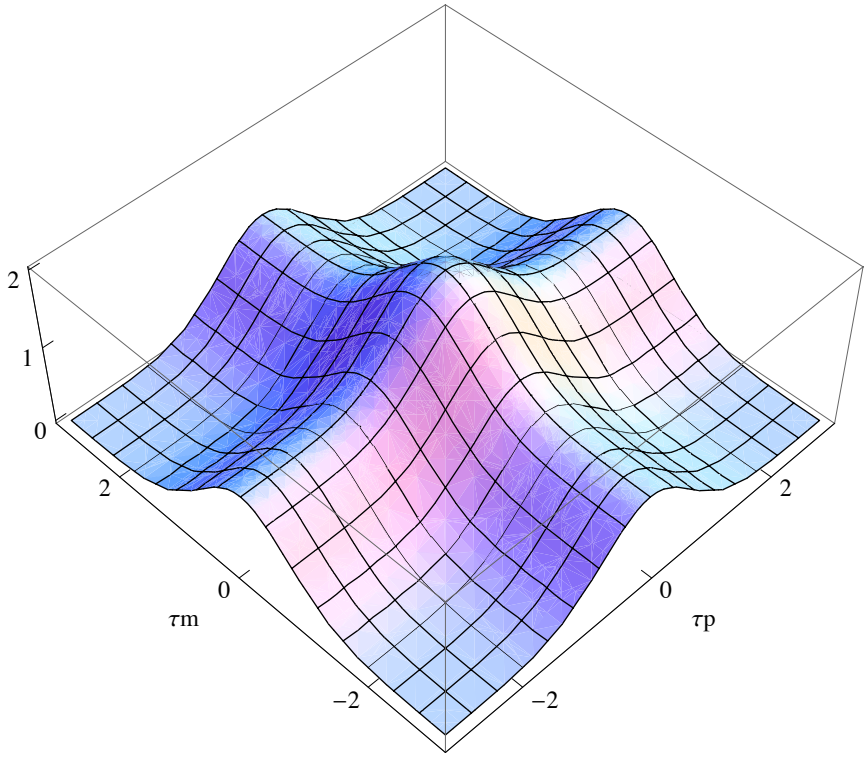

Figure A.1 The plot of φ_0/A as a function of $\tau_\pm \equiv t_\pm/a$ for $f(\tau) = e^{-\tau^2}$.

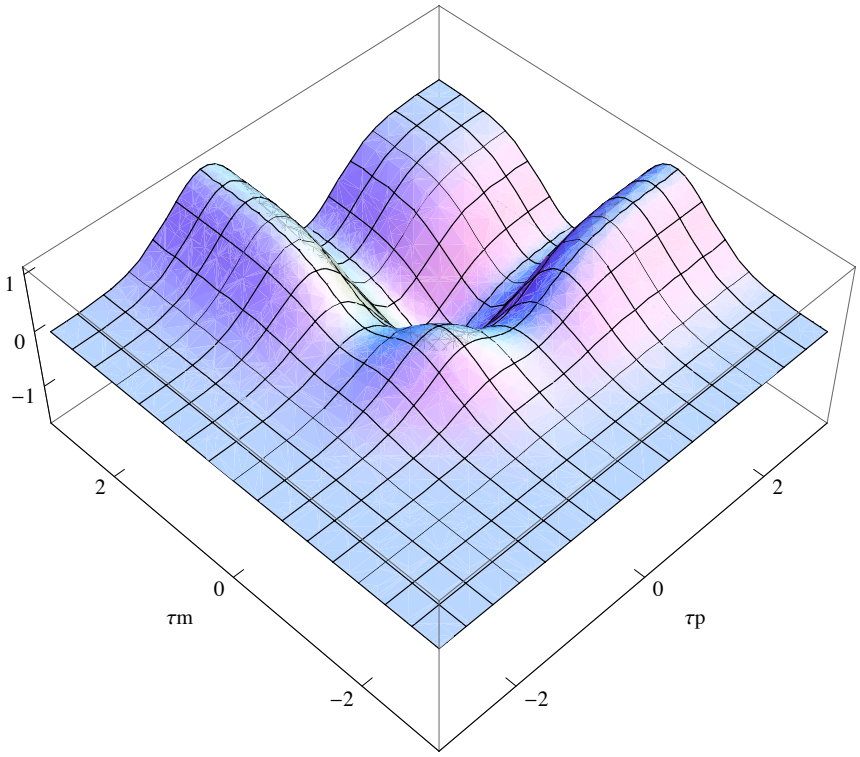

Figure A.2 The plot of $\varphi_1/(-A\epsilon)$ as a function of $\tau_\pm \equiv t_\pm/a$ for $f(\tau) = e^{-\tau^2}$.

A.5 Deviation from Perfect Planar Symmetry

In this section we will consider deviations from the perfect planar symmetry discussed above. Our purpose in doing so is to see if the fluctuations will introduce a classicalization radius. Since classicalization was shown for spherical symmetry, our expectation is to observe a tendency away from the results of the strictly planar symmetric case.

We want to probe in a 4-dimensional spacetime, the behavior of the field:

$$\phi(t,x,y,z) = \phi_0(t,x,y,z) + \phi_1(t,x,y,z) + \dots \,, \tag{A.58}$$

where ϕ_0 satisfies $\Box_4\phi_0 = 0$. In terms of the rescaled fields φ of the previous section, let us make the ansatz:

$$\phi_0(t,x,y,z) = \frac{1}{\sqrt{\mathcal{A}_2}}\varphi_{00}(t,x) + \frac{1}{\sqrt{\mathcal{A}_2}}\varphi_{01}(t,x)\mathrm{Re}(e^{i(k_y y + k_z z)}). \tag{A.59}$$

In this case, in order for $\Box_4\phi_0 = 0$ to be satisfied, we must have:

$$\begin{aligned} \Box_2\varphi_{00} &= 0 \\ (\Box_2 - m^2)\varphi_{01} &= 0, \end{aligned} \tag{A.60}$$

where $m^2 = k_y^2 + k_z^2$. Let us expand φ_{01} in orders of m^2a^2 so that:

$$\varphi_{01} = \varphi_{01}^{(0)} + \varphi_{01}^{(1)} + \dots \,. \tag{A.61}$$

Matching powers of m^2a^2 we see that if $\varphi_{01}^{(0)}$ satisfies $\Box_2\varphi_{01}^{(0)} = 0$, then the equation that is to be satisfied by $\varphi_{01}^{(1)}$ is:

$$a^2\Box_2\varphi_{01}^{(1)} = m^2a^2\varphi_{01}^{(0)}. \tag{A.62}$$

Anticipating that the leading modification, as in section A.3, due to the deformation will be a shift in the peak position of the wavepacket, we will make the ansatz up to terms of order r/a:

$$\begin{aligned} \varphi_{00} &= Af(\tau_+) + Af(\tau_-) \\ \varphi_{01}^{(0)} &= -\frac{Ar_1}{a}[f'(\tau_+) + f'(\tau_-)], \end{aligned} \tag{A.63}$$

where $\tau_\pm \equiv \frac{t_\pm}{a} \equiv \frac{t\pm x}{a}$.

We begin our analysis to determine if there is a change in the classicalization radius, r_* by calculating the deformed ϕ_1 to order r_1/a. Then we have for ϕ_0 in this approximation:

$$\begin{aligned} \phi_0(\tau_+, \tau_-, y, z) &\approx \frac{A}{\sqrt{\mathcal{A}_2}}[f(\bar{\tau}_+) + f(\bar{\tau}_-)] \\ &\equiv \frac{A}{\sqrt{\mathcal{A}_2}} f(\bar{\tau}_+, \bar{\tau}_-), \end{aligned} \tag{A.64}$$

where $\bar{\tau}_\pm = \frac{t_\pm - r_1\cos(k_\perp\cdot x_\perp)}{a}$. Note that $f(\bar{\tau}_+)$ is a wave peaked at $x = -t + r_1\cos(k_\perp\cdot x_\perp)$ and $f(\bar{\tau}_-)$ is a wave peaked at $x = t - r_1\cos(k_\perp\cdot x_\perp)$. A cartoon of ϕ_0 at a time slice $t < 0$ is shown in figure A.3. We are interested in the region where the two plane waves are bent away from each other, which corresponds to a deformation that brings us from the perfect planar case closer to that of the spherical case. For our ansatz, this corresponds to the region where $r_1\cos(k_\perp\cdot x_\perp)$ is positive. We expect that r_* will tend to increase in this region as we increase r_1.

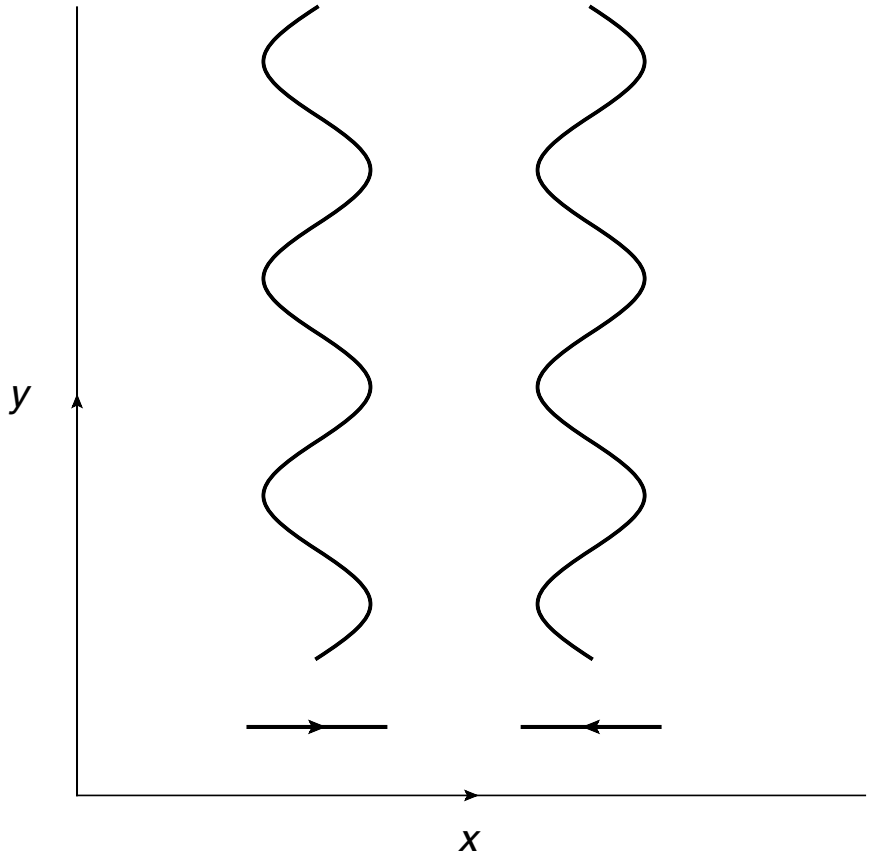

Figure A.3 A sketch showing the peak of ϕ_0 in the x-y plane for some time $t < 0$.

We now need to find ϕ_1 using the equation of motion:

$$\Box_4 \phi = L_*^4 \partial^\mu (\partial_\mu \phi (\partial_\nu \phi)^2), \tag{A.65}$$

for which the first order correction is:

$$\Box_4 \phi_1 = L_*^4 \partial^\mu (\partial_\mu \phi_0 (\partial_\nu \phi_0)^2). \tag{A.66}$$

One such contribution to this order, ϕ_{10}, is obtained by substituting $\frac{1}{\sqrt{\mathcal{A}_2}}\varphi_{00}$ for ϕ_0 above.:

$$\Box_4 \phi_{10} = \frac{8 L_*^4 A^3}{a^4 \mathcal{A}_2^{3/2}} b(\tau_+, \tau_-), \tag{A.67}$$

where we have defined $b(\tau_+, \tau_-) = f''(\tau_+) f'(\tau_-)^2 + f''(\tau_-) f'(\tau_+)^2$ for later convenience. It is not hard to show that the solution to the above differential equations in the limit $m^2 a^2 \to 0$

is:

$$\phi_{10} = -\frac{2L_*^4 A^3}{a^2 \mathcal{A}_2^{3/2}}[g(\tau_+, \tau_-) + \mathcal{O}(m^2 a^2)], \tag{A.68}$$

where the function $g(\tau_+, \tau_-)$ is given by:

$$g(\tau_+, \tau_-) = \int_{-\infty}^{\tau_+} d\tau'_+ \int_{-\infty}^{\tau_-} d\tau'_- b(\tau'_+, \tau'_-). \tag{A.69}$$

This solution is just the one presented in the previous section. In the following, just as in the case for ϕ_0, we will find the contribution to ϕ_1 up to order $\frac{r_1}{a}$. We will denote this contribution $\phi_{11}^{(0)}$.

$\phi_{11}^{(0)}$ can be found by considering the right hand side of (A.66) with linear contributions from $\frac{1}{\sqrt{\mathcal{A}_2}}\varphi_{01}^{(0)} \cos(k_\perp \cdot x_\perp)$ and quadratic contributions from $\frac{1}{\sqrt{\mathcal{A}_2}}\varphi_{00}$. In this case:

$$\Box_4 \phi_{11}^{(0)} = -\frac{8L_*^4 A^3 r_1}{a^5 \mathcal{A}_2^{3/2}} \cos(k_\perp \cdot x_\perp)[\partial_{\tau+} b(\tau_+, \tau_-) + \partial_{\tau-} b(\tau_+, \tau_-)]. \tag{A.70}$$

The solution to the above differential equation in the limit $m^2 a^2 \to 0$ is easily obtained:

$$\phi_{11}^{(0)} = \frac{2L_*^4 A^3 r_1}{a^3 \mathcal{A}_2^{3/2}} \cos(k_\perp \cdot x_\perp)[\partial_{\tau+} g(\tau_+, \tau_-) + \partial_{\tau-} g(\tau_+, \tau_-) + \mathcal{O}(m^2 a^2)]. \tag{A.71}$$

Adding up both contributions, we get that:

$$\phi_1 = -\frac{2L_*^4 A^3}{a^2 \mathcal{A}_2^{3/2}} g(\bar{\tau}_+, \bar{\tau}_-). \tag{A.72}$$

From this we get:

$$\frac{\phi_1}{\phi_0} = -\frac{2L_*^4 A^2}{a^2 \mathcal{A}_2}[\frac{g(\bar{\tau}_+, \bar{\tau}_-)}{f(\bar{\tau}_+, \bar{\tau}_-)} + \mathcal{O}(\frac{r_1^2}{a^2}) + \mathcal{O}(m^2 a^2)]. \tag{A.73}$$

Thus, we conclude that we need to consider the $\mathcal{O}(m^2 a^2 \frac{r_1}{a})$ corrections in order to see effects on r_*.

The only order $(m^2 a^2 \frac{r_1}{a})$ correction to ϕ_0 will be to φ_{01} since our expression for φ_{00} satisfies its free field equation of motion exactly. In order for (A.62) to be satisfied, we must

have:

$$\begin{aligned}\varphi_{01}^{(1)} &= \frac{Ar_1m^2a}{4}[(\tau_- - \tau_0)\int_{\tau_0}^{\tau_+} d\tau'_+ f'(\tau'_+) + (\tau_+ - \tau_0)\int_{\tau_0}^{\tau_-} d\tau'_- f'(\tau'_-)] \\ &= \frac{Ar_1m^2a}{4}[(\tau_- - \tau_0)(f(\tau_+) - f(\tau_0)) + (\tau_+ - \tau_0)(f(\tau_-) - f(\tau_0))] \\ &\equiv \frac{Ar_1m^2a}{4}w(\tau_+, \tau_-), \end{aligned} \tag{A.74}$$

where τ_0 is an IR cutoff introduced to ensure that the massive wave modes do not spread out too far before coming together. We have also defined the function w for later convenience. Our expression for ϕ_0 is now:

$$\phi_0 = \frac{A}{\sqrt{\mathcal{A}_2}}[f(\bar{\tau}_+, \bar{\tau}_-) - \frac{r_1m^2a}{4}\cos(k_\perp \cdot x_\perp)w(\tau_+, \tau_-) + \mathcal{O}(\frac{r_1^2}{a^2}) + \mathcal{O}(m^4a^4)]. \tag{A.75}$$

We now need to consider the order $m^2a^2(\frac{r_1}{a})$ corrections to ϕ_1. There are actually only three such contributions. One will come from the fact that our solution for ϕ_{11} (A.71) to the differential equation (A.70) neglected terms of order $m^2a^2(\frac{r_1}{a})$ (we will denote this contribution $\phi_{11}^{(1b)}$). Another contribution will be found by considering the right hand side of (A.66) to linear order in $\varphi_{01}^{(1)}$ (we will denote this contribution $\phi_{11}^{(1a)}$). The last contribution will come from that fact we now need to consider a term of order $m^2a^2(\frac{r_1}{a})$ that comes from the linear contribution of $\varphi_{01}^{(0)}$ in the right hand side of (A.66) (we will denote this contribution $\phi_{11}^{(1c)}$). All other corrections are of order $\frac{r_1^2}{a^2}$ or m^4a^4. In order to get $\phi_{11}^{(1b)}$ all we have to do is note that if we make the ansatz:

$$\begin{aligned}\phi_{11}^{(0)} &= \frac{2L_*^4A^3r_1}{a^3\mathcal{A}_2^{3/2}}\cos(k_\perp \cdot x_\perp)\int_{-\infty}^{\tau_+} d\tau'_+ \int_{-\infty}^{\tau_-} d\tau'_- h_b(\tau'_+, \tau'_-) - \frac{L_*^4A^3r_1m^2}{2a\mathcal{A}_2^{3/2}}\cos(k_\perp \cdot x_\perp) \\ &\times \int_{\tau_0}^{\tau_+} d\tau'_+ \int_{-\infty}^{\tau'_+} d\tau''_+ \int_{\tau_0}^{\tau_-} d\tau'_- \int_{-\infty}^{\tau'_-} d\tau''_- h_b(\tau''_+, \tau''_-) + \mathcal{O}(\frac{r_1^2}{a^2}) + \mathcal{O}(m^4a^4), \end{aligned} \tag{A.76}$$

where

$$h_b(\tau_+, \tau_-) = \partial_{\tau+}b(\tau_+, \tau_-) + \partial_{\tau-}b(\tau_+, \tau_-), \tag{A.77}$$

then (A.70) is satisfied to order $m^2a^2(\frac{r_1}{a})$. Thus:

$$\phi_{11}^{(1b)} = -\frac{L_*^4A^3r_1m^2}{2a\mathcal{A}_2^{3/2}}\cos(k_\perp \cdot x_\perp)\int_{\tau_0}^{\tau_+} d\tau'_+ \int_{-\infty}^{\tau'_+} d\tau''_+ \int_{\tau_0}^{\tau_-} d\tau'_- \int_{-\infty}^{\tau'_-} d\tau''_- h_b(\tau''_+, \tau''_-). \tag{A.78}$$

In order to find $\phi_{11}^{(1a)}$ we need to solve (A.66) with linear order contributions from $\varphi_{01}^{(1)}$ on the right hand side. In this case, the equation becomes:

$$\begin{aligned}\Box_4\phi_{11}^{(1a)} &= \frac{2L_*^4A^3r_1m^2}{a^3\mathcal{A}_2^{3/2}}\cos(k_\perp\cdot x_\perp)[(\tau_+-\tau_0)f'(\tau_+)^2f''(\tau_-)+(\tau_--\tau_0)f'(\tau_-)^2f''(\tau_+)\\ &+2f'(\tau_-)f''(\tau_+)((\tau_+-\tau_0)f'(\tau_-)+f(\tau_+)-f(\tau_0))\\ &+2f'(\tau_+)f''(\tau_-)((\tau_--\tau_0)f'(\tau_+)+f(\tau_-)-f(\tau_0))]\\ &\equiv \frac{2L_*^4A^3r_1m^2}{a^3\mathcal{A}_2^{3/2}}\cos(k_\perp\cdot x_\perp)h_a(\tau_+,\tau_-).\end{aligned} \tag{A.79}$$

The solution up to the order we seek is:

$$\phi_{11}^{(1a)} = -\frac{L_*^4A^3r_1m^2}{2a\mathcal{A}_2^{3/2}}\cos(k_\perp\cdot x_\perp)\int_{\tau_0}^{\tau_+}d\tau'_+\int_{\tau_0}^{\tau_-}d\tau'_-h_a(\tau'_+,\tau'_-). \tag{A.80}$$

The final correction of this order comes from the order $m^2a^2(\frac{r_1}{a})$ term that arises from linear contributions from $\varphi_{01}^{(0)}$ on the right hand side of (A.66):

$$\begin{aligned}\Box_4\phi_{11}^{(1c)} &= \frac{2L_*^4A^3r_1m^2}{a^3\mathcal{A}_2^{3/2}}\cos(k_\perp\cdot x_\perp)[2(f'(\tau_+)+f'(\tau_-))]f'(\tau_+)f'(\tau_-)\\ &\equiv \frac{2L_*^4A^3r_1m^2}{a^3\mathcal{A}_2^{3/2}}\cos(k_\perp\cdot x_\perp)h_c(\tau_+,\tau_-).\end{aligned} \tag{A.81}$$

So we have that the order $m^2a^2(\frac{r_1}{a})$ correction to ϕ_1 is:

$$\begin{aligned}\phi_{11}^{(1)} &= \phi_{11}^{(1a)}+\phi_{11}^{(1b)}+\phi_{11}^{(1c)}\\ &= -\frac{L_*^4A^3r_1m^2}{2a\mathcal{A}_2^{3/2}}\cos(k_\perp\cdot x_\perp)\\ &[\int_{\tau_0}^{\tau_+}d\tau'_+\int_{-\infty}^{\tau'_+}d\tau''_+\int_{\tau_0}^{\tau_-}d\tau'_-\int_{-\infty}^{\tau'_-}d\tau''_-h_b(\tau''_+,\tau''_-)\\ &+\int_{\tau_0}^{\tau_+}d\tau'_+\int_{\tau_0}^{\tau_-}d\tau'_-(h_a(\tau'_+,\tau'_-)+h_c(\tau'_+,\tau'_-))]\\ &\equiv -\frac{L_*^4A^3r_1m^2}{2a\mathcal{A}_2^{3/2}}\cos(k_\perp\cdot x_\perp)q(\tau_+,\tau_-).\end{aligned} \tag{A.82}$$

So, after adding in this contribution, we have:

$$\phi_1 = -\frac{2L_*^4 A^3}{a^2 \mathcal{A}_2^{3/2}} g(\bar{\tau}_+, \bar{\tau}_-)[1 + \frac{m^2 r_1 a}{4} \cos{(k_\perp \cdot x_\perp)} \frac{q(\tau_+, \tau_-)}{g(\bar{\tau}_+, \bar{\tau}_-)} + \mathcal{O}(\frac{r_1^2}{a^2}) + \mathcal{O}(m^4 a^4)]. \tag{A.83}$$

We thus get that:

$$\begin{aligned} \frac{\phi_1}{\phi_0} = &-\frac{2L_*^4 A^2}{a^2 \mathcal{A}_2} \frac{g(\bar{\tau}_+, \bar{\tau}_-)}{f(\bar{\tau}_+, \bar{\tau}_-)}[1 + \frac{m^2 r_1 a}{4} \cos{(k_\perp \cdot x_\perp)}(-\frac{w(\tau_+, \tau_-)}{f(\bar{\tau}_+, \bar{\tau}_-)} + \frac{q(\tau_+, \tau_-)}{g(\bar{\tau}_+, \bar{\tau}_-)}) \\ &+ \mathcal{O}(\frac{r_1^2}{a^2}) + \mathcal{O}(m^4 a^4)]. \end{aligned} \tag{A.84}$$

What we are interested in is the sign of the quantity: $(-\frac{w(\tau_+, \tau_-)}{f(\bar{\tau}_+, \bar{\tau}_-)} + \frac{q(\tau_+, \tau_-)}{g(\bar{\tau}_+, \bar{\tau}_-)})$. It is clear that $f(\bar{\tau}_+, \bar{\tau}_-)$ is always positive for $f(t) = e^{-t^2}$. Writing $g(\bar{\tau}_+, \bar{\tau}_-)$ explicitly for this ansatz for $f(t)$, we have:

$$\begin{aligned} g(\bar{\tau}_+, \bar{\tau}_-) = &\frac{1}{2} e^{2(\bar{\tau}_+^2 + \bar{\tau}_-)^2} [4 e^{\bar{\tau}_-^2} \bar{\tau}_- \bar{\tau}_+ + 4 e^{\bar{\tau}_+^2} \bar{\tau}_- \bar{\tau}_+ \\ &+ \sqrt{2\pi} e^{2\bar{\tau}_-^2 + \bar{\tau}_+^2} \bar{\tau}_+ (-2 + \text{erfc}(\sqrt{2}\bar{\tau}_-) \\ &+ \sqrt{2\pi} e^{2\bar{\tau}_+^2 + \bar{\tau}_-^2} \bar{\tau}_- (-2 + \text{erfc}(\sqrt{2}\bar{\tau}_+)]. \end{aligned} \tag{A.85}$$

It can be seen that $g(\bar{\tau}_+, \bar{\tau}_-) > 0$ for $\bar{\tau}_+, \bar{\tau}_- < 0$, which is the region we are interested in. Since:

$$\begin{aligned} &-\frac{w(\tau_+, \tau_-)}{f(\bar{\tau}_+, \bar{\tau}_-)} + \frac{q(\tau_+, \tau_-)}{g(\bar{\tau}_+, \bar{\tau}_-)} \\ &= \frac{1}{f(\bar{\tau}_+, \bar{\tau}_-) g(\bar{\tau}_+, \bar{\tau}_-)} [-w(\tau_+, \tau_-) g(\tau_+, \tau_-) + q(\tau_+, \tau_-) f(\tau_+, \tau_-) + \mathcal{O}(\frac{r_1}{a})]. \end{aligned} \tag{A.86}$$

We are interested in the sign of the quantity:

$$\sigma(\tau_+, \tau_-) = -w(\tau_+, \tau_-) g(\tau_+, \tau_-) + q(\tau_+, \tau_-) f(\tau_+, \tau_-). \tag{A.87}$$

Let us plot $\sigma(\tau_+ = v, 0)$ in order to find the sign. We see in figure A.4 that $\sigma(\tau_+ = v, 0)$ remains positive until $v \gg -1$. As we saw previously, the interaction length for the perfect planar case is of order a (which corresponds to the region where $v \sim -1$), so we see that increasing r_1 tends to increase r_* in the region where $r_1 \cos{(k_\perp \cdot x_\perp)}$ is positive. This is what we expected.

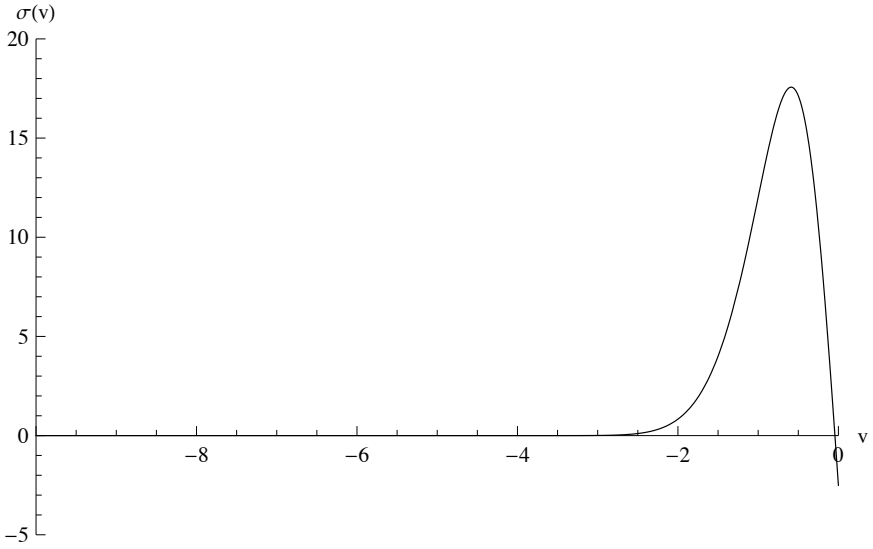

Figure A.4 $\sigma(\tau_+ = v, 0)$ as a function of v. $\tau_0 = -10$ was chosen, but any τ_0 much smaller than the τ_-, τ_+ where the interaction takes place defines an appropriate boundary condition.

A.6 UV Sensitivity

We have so far explored a model with the Lagrangian:

$$\mathcal{L} = X + L_*^4 X^2, \tag{A.88}$$

where $X = -\frac{1}{2}\partial^\mu\phi\partial_\mu\phi$ is the standard kinetic term. Let us generalize this so as to include the possibility of a higher order non-linear term:

$$\mathcal{L} = X + L_*^{4n-4} X^n. \tag{A.89}$$

For the planarly symmetric case, we have for the first order EOM:

$$\Box_2\varphi_1 = -nL_*^{4n-4}\partial^\mu\left[\varphi_0\partial_\mu(X_0^{n-1})\right], \tag{A.90}$$

where $X_0 = -\frac{1}{2\mathcal{A}_2}\partial^\mu\varphi_0\partial_\mu\varphi_0$. If we choose:

$$\varphi_0 = Af(\tau_+) + Af(\tau_-). \tag{A.91}$$

Then:

$$X_0 = \frac{2A^2}{\mathcal{A}_2 l^2} f'(\tau_+) f'(\tau_-). \tag{A.92}$$

In this case, (A.90) simplifies to:

$$\begin{aligned}\Box_2 \varphi_1 =& n(n-1) 2^n A^{2n-1} \mathcal{A}_2^{-n+1} L_*^{4n-4} l^{-2n} \\ & [f'(\tau_+)^n f'(\tau_-)^{n-2} f''(\tau_-) + f'(\tau_-)^n f'(\tau_+)^{n-2} f''(\tau_+)].\end{aligned} \tag{A.93}$$

The retarded solution to the above equation is:

$$\varphi_1 = -A\epsilon \int_{-\infty}^{\tau+} d\tau'_+ \int_{-\infty}^{\tau-} d\tau'_- [f'(\tau'_+)^n f'(\tau'_-)^{n-2} f''(\tau'_-) + f'(\tau'_-)^n f'(\tau'_+)^{n-2} f''(\tau'_+)]. \tag{A.94}$$

where

$$\epsilon = n(n-1) 2^{n-2} A^{2n-2} \mathcal{A}_2^{-n+1} L_*^{4n-4} l^{2-2n}. \tag{A.95}$$

It can be seen by comparing figure A.2 ($\varphi_1/(-A\epsilon)$ for the $n = 2$ case) to figure A.5 ($\varphi_1/(-A\epsilon)$ for the $n = 3$ case) that the overall profile of ϕ_1 for odd and even values of n can be quite different. It should also be noted that we find relatively modest dependence of the profiles of two even (or two odd) ϕ_1 on n.

In order to compare the behavior of φ_1 for various values of n, let us plot the quantity:

$$\xi(v) = \frac{\varphi_1(\tau_+ = v, \tau_- = 0)}{\text{Max}_v[\varphi_1(\tau_+ = v, \tau_- = 0)]}. \tag{A.96}$$

The function $\xi(v)$ is the normalized peak amplitude of the right moving plane wave $f(\tau_-)$. We normalize by $\text{Max}_v[\varphi_1(\tau_+ = v, \tau_- = 0)]$, the maximum value of $\varphi_1(\tau_+ = v, \tau_- = 0)$ in the region $-\infty < v \leq 0$, so that the peak value of $\xi(v)$ is 1 regardless of what n we choose. Note that since we set $\tau_- = 0$, $v = \frac{2t}{a} = \frac{2x}{a}$. Thus, the right moving plane wave evolves from $v = -\infty$ to $v = 0$, where it will meet the left moving plane wave.

We see in figure A.6 that $\xi(v)$ reaches its peak value at the value of $v = \frac{\sqrt{2}}{2}$ for all plots shown. Thus, the interaction length is $\sim a$ regardless of what value we choose for n. It is also apparent that as we increase n, there is a tendency for $\xi(v)$ to become more sharply peaked, so ϕ_1 will become significant at somewhat smaller values of x as we increase n. Hence we can conclude that increasing n will not cause classicalization to occur for planarly symmetric waves. Moreover, the shape of the scattered wave is UV sensitive.

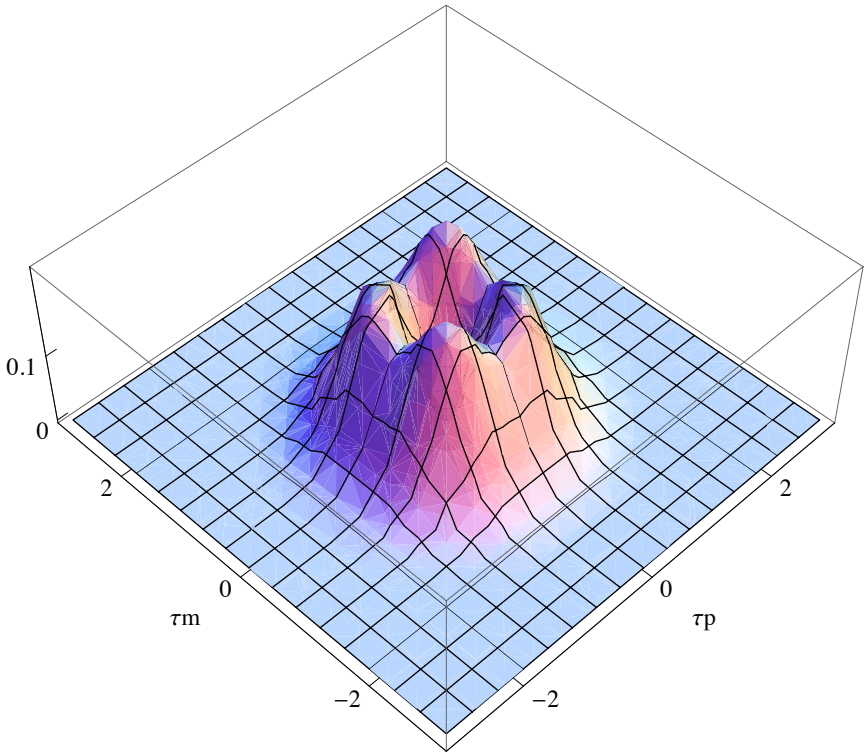

Figure A.5 The plot of $\varphi_1/(-A\epsilon)$ as a function of $\tau_\pm \equiv t_\pm/a$ for $f(\tau) = e^{-\tau^2}$, $n = 3$.

A.7 Discussion

The following quotations by the creators of the classicalization proposal summarize the basic idea behind the theory: "A universal physical meaning of r_*-radius can be defined as of a shortest distance down to which, in a given scattering process, particles propagate freely, without experiencing a significant interaction." [110]

"The condition for classicalization is the growth of r_* with energy, in such a way, that above some critical energy it exceeds all the relevant quantum length scales in the system. When this is the case, system classicalizes." [111]

"The analogy between r_* and the gravitational Schwarzschild radius is clear. We can define a classical Schwarzschild radius for an arbitrary quantum particle, but a particle for which the Schwarzschild radius is deep within its Compton wavelength cannot be regarded as a classical state. Similarly, the classical r_*-radius can be defined for an arbitrary wave-packet, but only ones with $r_* \gg L_*$ classicalize." [110]

We have seen in our analysis that the classicalization radius r_* tends to decrease in a region where a shell made of the field is flattened and that in the planar limit, the system never classicalizes before reaching sub-cutoff lengths. Thus, although we can define an r_*

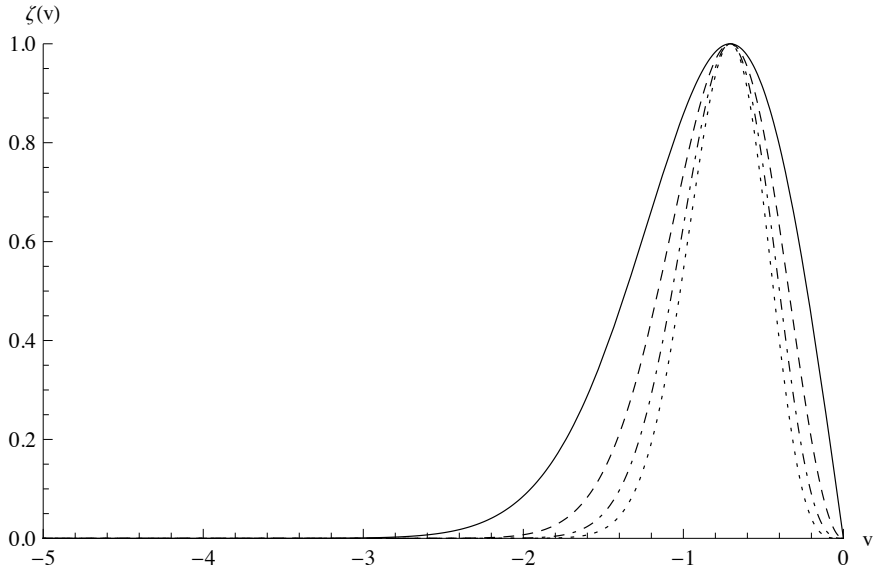

Figure A.6 The plot of $\xi(v)$ for $n = 2$ (solid line), $n = 3$ (dashed line), $n = 4$ (dot-dashed line), $n = 5$ (dotted line).

for arbitrary initial configurations of the wave packet, we have shown that the condition $r_* \gg L_*$ is not satisfied in general. The fact that r_* does not generally exceed all the relevant quantum length scales in the system (i.e. L_*) points towards the conclusion that classicalization, as described by the quotations above, does not serve as UV-completion for the class of non-renormalizable field theories. This claim is further bolstered by the fact that shape of the scattered wave is UV sensitive.

Lastly, we would like to make a comment that our result is not dependent on any fine-tuning, which makes it clear that quantum fluctuations will not change our no-go result. The following physical argument should make it clear that our result is rather robust in this regard. The Goldstone-type field considered in the literature of classicalization has the action of the form

$$I_\phi = \int dx^4 \sqrt{-g} P(X), \quad X \equiv -g^{\mu\nu}\partial_\mu\phi\partial_\nu\phi. \tag{A.97}$$

The corresponding stress-energy tensor is

$$T_{\mu\nu} = 2P'(X)\partial_\mu\phi\partial_\nu\phi + P(X)g_{\mu\nu}, \tag{A.98}$$

satisfying the conservation equation $\nabla^\mu T_{\mu\nu} = 0$. In particular, the pressure along directions perpendicular to the gradient $\partial_\mu\phi$ is $P(X)$. [2] Thus, for a shell made of the scalar field, the

[2]This is true regardless of X being time-like or space-like. From (A.98) it is clear that for the time-like

pressure tangent to the shell is $P(X)$. For a spherically symmetric shell, the resultant force due to the tangential pressure will be a repulsive radial force. Thus, as the spherical shell shrinks and the amplitude of X in the vicinity of the shell increases, the tangential pressure and the resultant radial force become large. At some point, the radial force becomes strong enough to significantly deviate the evolution of the shell from that of the linear theory. This is the reason why the classicalization radius can be significantly greater than the cutoff length of the theory under perfect spherical symmetry. On the other hand, when spherical symmetry is significantly relaxed, the resultant force due to the tangential pressure will not generate a significant repulsive force. Indeed, in a sufficiently large flattened region, the configuration is well approximated by a planar shell and there is no net radial force. Thus, the system never classicalizes in this case. All of these arguments are explicitly verified in the preceding sections of this appendix. Note that we do not need to fine-tune the initial conditions in order to invalidate the classicalization: the net radial force is small as long as the deviation from spherical symmetry is large enough. Since we do not need to fine-tune the initial conditions, our no-go result is rather robust.

case, the energy is $2XP'(X) - P(X)$ and the pressure $P(X)$ is isotropic. For the space-like case the energy is $-P(X)$ and the pressure is anisotropic. The pressure in the direction of the gradient is $2XP'(X) + P(X)$, but the pressure perpendicular to the gradient is still $P(X)$. Thus for both cases the pressure is still $P(X)$ in directions perpendicular to the gradient.

Appendix B
Maximal Slicing

Here we present the details of the maximal slicing method. The metric is chosen to take the form

$$ds^2 = -N^2 dt^2 + (dr + \beta^r dt)^2 + R^2(d\theta^2 + \sin^2\theta d\varphi^2) \tag{B.1}$$

which is the form for a spherically symmetric metric where the radial coordinate r is length in the radial direction in a constant time slice. Note that the usual area radius R is not one of the coordinates and is instead a function of the coordinates t and r. Thus the spatial metric γ_{ab} has components

$$\begin{aligned} \gamma_{rr} &= 1 \\ \gamma_{\theta\theta} &= R^2 \\ \gamma_{\varphi\varphi} &= R^2 \sin^2\theta \end{aligned} \tag{B.2}$$

The extrinsic curvature, K_{ab} is defined by

$$K_{ab} = -\gamma_a{}^c \nabla_c n_b \tag{B.3}$$

where n^a is the unit normal to the surfaces of constant time t. However, due to spherical symmetry and maximal slicing, there is only one independent component of the extrinsic curvature. Specifically we have

$$K^\theta{}_\theta = K^\varphi{}_\varphi = -\tfrac{1}{2} K^r{}_r \tag{B.4}$$

Equation (B.3) is equivalent to

$$\partial_t \gamma_{ij} = -2NK_{ij} + D_i\beta_j + D_j\beta_i \tag{B.5}$$

where D_i is the covariant derivative of the spatial metric γ_{ij}. The rr component of equation (B.5) yields

$$\partial_r \beta^r = N K^r{}_r \tag{B.6}$$

whose solution is

$$\beta^r = \int_0^r N K^r{}_r \, dr \tag{B.7}$$

The $\theta\theta$ component of (B.5) yields

$$\partial_t R = \beta^r \partial_r R + \frac{N}{2} R K^r{}_r \tag{B.8}$$

We now use the momentum constraint of the Einstein field equation to determine the extrinsic curvature. For maximal slicing ($K = 0$) this constraint is

$$D_a K^{ab} = -\kappa \gamma^{bc} n^d T_{cd} \tag{B.9}$$

Define the quantities P and S by

$$P = n^a \nabla_a \phi, \quad S = \partial_r \phi \tag{B.10}$$

Then the quantity X is given by

$$X = \tfrac{1}{2}(P^2 - S^2) \tag{B.11}$$

while (B.9) becomes

$$R^{-3} \partial_r (R^3 K^r{}_r) = -\kappa \mathcal{L}_X P S \tag{B.12}$$

The solution of (B.12) is

$$K^r{}_r = -\kappa R^{-3} \int_0^r R^3 \mathcal{L}_X P S \, dr \tag{B.13}$$

Note that there is also a Hamiltonian constraint associated with the Einstein field equation. In the case of maximal slicing, this constraint is

$${}^{(3)}R - K_{ab} K^{ab} = 2\kappa T_{ab} n^a n^b \tag{B.14}$$

where ${}^{(3)}R$ is the spatial scalar curvature. This equation yields

$$\begin{aligned}\partial_r\partial_r R &= \frac{1-(\partial_r R)^2}{2R} \\ &- \tfrac{1}{4}R\left[\tfrac{3}{2}(K^r{}_r)^2 + 2\kappa(\mathcal{L}_X P^2 - \mathcal{L})\right] \end{aligned} \tag{B.15}$$

We now determine the lapse N. It follows from the maximal slicing condition that

$$D_a D^a N = N\left[K_{ab}K^{ab} + \frac{\kappa}{2}T_{ab}(n^a n^b + \gamma^{ab})\right] \tag{B.16}$$

which yields

$$\begin{aligned}\partial_r\partial_r N &+\frac{2}{R}(\partial_r R)(\partial_r N) \\ &= N\left[\tfrac{3}{2}(K^r{}_r)^2 + \kappa\left(\tfrac{1}{2}\mathcal{L}_X(P^2+S^2) + \mathcal{L}\right)\right] \end{aligned} \tag{B.17}$$

We now consider the evolution of the k-essence scalar field. From the definitions of P and S it follows that

$$\partial_t\phi = NP + \beta^r S \tag{B.18}$$

$$\partial_t S = N(\partial_r P + K^r{}_r S) + P\partial_r N + \beta^r\partial_r S \tag{B.19}$$

The k-essence equation of motion, equation (4.2) becomes after some straightforward but tedious algebra

$$\begin{aligned}\partial_t P &= \beta^r\partial_r P + S\partial_r N \\ &+ \frac{N\mathcal{L}_{XX}}{\mathcal{L}_X + P^2\mathcal{L}_{XX}}\left(K^r{}_r P S^2 + 2PS\partial_r P - S^2\partial_r S\right) \\ &+ \frac{N\mathcal{L}_X}{\mathcal{L}_X + P^2\mathcal{L}_{XX}}R^{-2}\partial_r(R^2 S) \end{aligned} \tag{B.20}$$

The initial data are chosen as follows: P and ϕ are chosen freely, with S set equal to $\partial_r\phi$. Then X is determined using (B.11) and then used to find $\mathcal{L}$ and $\mathcal{L}_X$ Then (B.13) is integrated to find $K^r{}_r$. Then (B.15) is integrated for R using the fact that at the origin $R = 0$ and $\partial_r R = 1$. Then at each time step, the evolution proceeds as follows: first X is determined using (B.11) and then used to find $\mathcal{L}, \mathcal{L}_X$ and $\mathcal{L}_{XX}$. Then (B.13) is integrated to find $K^r{}_r$. And then (B.17) is solved for the lapse N (using a tridiagonal method and the fact that $\partial_r N = 0$ at the origin and $N \to 1$ at infinity). Then (B.7) is integrated to find the shift β^r. Finally, the quantities R, ϕ, S and P are evolved to the next time step using (B.8), (B.18), (B.19) and (B.20) respectively. The evolution is done using the iterated Crank-Nicholson

method, and all spatial derivatives are found using standard centered differences.

Appendix C

Analytic Stationary Solution

Here we present some details concerning the derivation of the stationary solution used in figures 4.5, 4.6, and 4.10 that were found by Babichev et. al. [4] and Frolov [39]. We generalize their solutions to our formalism and present further details relevant to the results presented earlier in chapter 4. In this appendix we use standard Schwarzschild coordinates ($ds^2 = -f(r)dt^2 + f^{-1}(r)dr^2 + r^2 d\Omega^2$). These coordinates are related those that we use in the main text by equations (4.5) and (4.6).

For a Lagrangian $\mathcal{L}(X)$ that is purely a function of the kinetic variable X, the equation of motion can be written as:

$$\nabla_\mu(\mathcal{L}_X \nabla^\mu \phi) = 0 \,, \tag{C.1}$$

We use the stationary ansatz[1]:

$$\phi = c_p \left(t + r* + \int F(r) dr \right) \,, \tag{C.2}$$

where $r* = \int f^{-1}(r) dr$. Note that under this ansatz, in the Schwarzschild metric we have:

$$\nabla_\mu \phi = c_p (\nabla_\mu t + f^{-1} W \nabla_\mu r) \,, \tag{C.3}$$

where we have defined: $W \equiv 1 + fF$.
We also see that:

$$\nabla^\mu \phi = c_p (-f^{-1} \delta^\mu_t + W \delta^\mu_r) \,. \tag{C.4}$$

So with this ansatz (applying the general formula for divergence) we find that the equation

[1] In [44] we have shown that this form of the solution directly follows from the requirement of stationarity, c.f. with the so-called delayed field approximation from [52]

of motion becomes:

$$\frac{1}{r^2}\partial_r(r^2\mathcal{L}_X c_p W) = 0 \ . \tag{C.5}$$

This gives us the following equation for W:

$$c_1 = r^2\mathcal{L}_X W \ , \tag{C.6}$$

where c_1 is a constant. Note from $\nabla_\mu\phi$ and $\nabla^\mu\phi$ we have that:

$$X = \frac{1}{2}c_p^2 f^{-1}(1 - W^2) \ . \tag{C.7}$$

For the Lagrangian given in (4.20), we have that
$\mathcal{L}_X = (1 + \frac{2X}{\alpha})^{-1/2}$, so our equation for W becomes:

$$W^2 = \frac{f + c_\infty^2 - 1}{\frac{r^4 f}{c_1^2} + c_\infty^2 - 1} \ . \tag{C.8}$$

In order to ensure that the solution is non-singular on and outside the sound horizon, we choose $c_1 = \frac{4M^2}{c_\infty^4}$ [4]. This uniquely defines W and thus F, giving us the closed form for our stationary solution which is plotted in figures (4.5) and (4.6).

For the ghost condensate Lagrangian given in (4.28), $\mathcal{L}_X = \frac{1}{4}(\frac{X}{a^4} - 1)$, so the equation for W is:

$$r^2(\frac{c_p^2}{2a^4}(1 - W^2) - f)W - 4c_1 f = 0 \ . \tag{C.9}$$

Before we go further, consider the horizon at $r = 2M$. Because $f[2M] = 0$, we know that the equation for $W[2M]$ becomes:

$$(1 - W[2M]^2)W[2M] = 0 \ . \tag{C.10}$$

Thus both $W[2M] = \pm 1$ and $W[2M] = 0$ are possible solutions. Note that since $W = 1 + fF$, if $W[2M] = 1$, then $F[2M]$ is nonsingular. If $W[2M] = 0$ or $W[2M] = -1$, $F[2M]$ is singular and nonphysical.

Upon solving the full cubic equation using Mathematica (as can be expected, these cubic roots are neither brief nor illuminating and are omitted), we chose the solution for W that has $W[2M] = 1$. Normally, as was in the previous case, we would choose the value of c_1 that makes $W[r \to \infty] = 0$, as this prevents $\phi \sim r$ at large radii. However, we find that in

the limit $r \to \infty$, W is independent of c_1. Furthermore, the cubic root that corresponds to $W[2M] = 1$ goes to a non-zero constant as $r \to \infty$. However, there is another cubic root which has $W[r \to \infty] = 0$. We can stitch these two separate roots together provided there exists some radius at which the roots become degenerate and coincide with each other.

This occurs for critical values of W and r where the full differential of the cubic equation (C.9) vanishes. These are the values for W and r where both coefficients vanish in the equation:

$$\frac{dC(W,r)}{dW}dW + \frac{dC(W,r)}{dr}dr = 0 \,, \tag{C.11}$$

where $C(W,r) = 0$ gives the cubic equation defined in (C.9). The constant c_1 can then be chosen so that these critical values of W and r are solutions to the cubic equation. We can then stitch together the two solutions (one with proper limiting behavior at the horizon and the other with proper limiting behavior at infinite radius) at this critical radius. The resulting solution is well behaved, and is plotted in figure (4.10).

One exceptional case where this procedure is ambiguous is when we have $c_\infty = 0$ or equivalently, $c_p^2 = 2a^4$. In this case as $r \to \infty$, all three cubic roots have $W[2M] = 0$. Thus, there is no longer an obvious condition on c_1.

Appendix D

Cancellation of Collinear Singularities in the Eikonal Approximation

In this appendix, we review how the cancellation of collinear singularities is realized in the eikonal approximation, as discussed by Weinberg in [53]. We present this argument for completeness, and also because it confirms the use of the Ward identity illustrated by figures 5.11 and 5.12. In particular, we emphasize that although we derive the factorization (and hence cancellation) of collinear gravitons from the hard scattering by using the Ward identity of (5.25), at no point does the hard scattering, whether in the eikonal approximation or not, include all the diagrams of an S-matrix element (see figure 5.12).

We start by rewriting equation (5.24), using the left-hand side of equation (5.23),

$$\begin{aligned} i\mathcal{M} &= \int \frac{d^4 l_i}{(2\pi)^4} J_m(p_m^\alpha - \sum l_i^{\alpha_i}, \{l_i^{\alpha_i}\})_{\{\alpha_i\beta_i\}} \\ &\quad \times \prod_{i=1}^{j} \bar{v}_m^{\alpha_i} \bar{v}_m^{\beta_i} v_{m\mu_i} v_{m\nu_i} \\ &\quad \times R^{(\mathrm{eik})}(p_m^\mu - \sum l_i^{\mu_i}, \{l_i^{\mu_i}\}, \{p_n\})^{\{\mu_i\nu_i\}} , \end{aligned} \tag{D.1}$$

where we now consider explicitly all of the E external legs in the full diagram. The indices i refer to gluons l_i attaching J_m to R, $i = 1 \ldots j$. The external leg connected to the jet we consider has momentum p_m (the nearly on-shell portion of this line is not included in R) and the remaining $E - 1$ non-collinear external legs have momentum p_n, $n \neq m$ (these non-collinear legs are included explicitly in R).

In this discussion, we follow reference [53] by taking for the function R, representing the remainder of the diagram, a product of eikonal lines, linked at a point-like vertex $H(\{p_n\})$, and treat all connections of collinear gravitons to R in the eikonal approximation, summing over all diagrams.

Let us denote by $P(\{N_n\})$ any *unordered* partition of the j external gravition lines

of J_m into a set of bins with N_n gravitons attached to line p_n. At fixed momenta l_i, each ordering corresponds to a distinct diagram, and we must still sum over all orderings of graviton connections to each line p_n, $n \neq m$. In these terms we write the contraction of the function R with vectors v in (D.1) as

$$R^{(\mathrm{eik})}(p_m^\mu - \sum l_i^{\mu_i}, \{l_i^{\mu_i}\}, \{p_n\})^{\{\mu_i \nu_i\}} \prod_i v_{m\mu_i} v_{m\nu_i} \quad = \\ \sum_{P(\{N_n\})} \mathcal{E}_{\mathrm{num}}(\{N_n\})\, \mathcal{E}_{\mathrm{den}}(\{N_n\})\, H(\{p_n\}, (\{N_n\}))\ . \tag{D.2}$$

In this expression, the eikonal numerator factors are given by

$$\mathcal{E}_{\mathrm{num}}(\{N_n\}) = \prod_{n \neq m}^{E-1} ((p_n \cdot v_m)^2)^{N_n}\,, \tag{D.3}$$

since each graviton attached to a non-collinear external line contributes a numerator factor of $(p_n \cdot v_m)^2$.

Similarly, $\mathcal{E}_{\mathrm{den}}$ summarizes all eikonal denominators, including the sum over orderings of graviton lines (labeled with the index i) from the jet J_m to each of the other incoming massless lines, p_n for a given choice of $P\,(\{N_n\})$. That is, for each partition P, we sum over all permutations $\pi(N_n)$ of the connections of these lines to each of the p_n. To the sum of these connections we may apply for each external line p_n the well-known identity for eikonal denominators, giving

$$\begin{aligned} \mathcal{E}_{\mathrm{den}}(\{N_n\}) &= \prod_{n \neq m} \sum_{\pi(N_n)} \prod_{a=1}^{N_n} \left(\sum_{i=1}^{a} p_n \cdot q^{(n)}_{\pi_{N_n}(i)} \right)^{-1} \\ &= \prod_{n \neq m} \prod_{i=1}^{N_n} (p_n \cdot q_i^{(n)})^{-1}\,, \end{aligned} \tag{D.4}$$

where $q_i^{(n)}$ denotes the momentum of the ith graviton attached to the nth non-collinear external line. The subscript π_{N_n} denotes that it is the momenta $q_i^{(n)}$ that we are permuting over. This identity shows that the momentum dependence associated with denominators factors into simple products for each external graviton of $R^{(\mathrm{eik})}$.

Before combining equations (D.3) and (D.4) for the eikonal numerator and denominator

factors, respectively we define

$$q_i^{(n)} = \alpha_i v_m \,, \tag{D.5}$$

which holds in the leading collinear region. Each momentum $q_i^{(n)}$ and hence each α_i, is independent of to which p_n the collinear graviton attaches. In these terms, we have

$$\mathcal{E}_{\rm den}(\{N_n\}) \;\; = \;\; \prod_{\text{all } i} \prod_{n \neq m} \frac{1}{\alpha_i} \; (p_n \cdot v_m)^{-N_n} \;\; , \tag{D.6}$$

so that the energy-dependence of the collinear gravitons is collected into a universal factor that is independent of the partition P. Substituting the numerator and denominator forms (D.3) and (D.6) into (D.2) for $R^{(\rm eik)}$, we find

$$\begin{aligned} R^{(\rm eik)}(p_m^\mu - \sum l_i^\mu, \{l_i^\mu\}, \{p_n\})^{\{\mu_i \nu_i\}} \prod_i v_{m\mu_i} v_{m\nu_i} \;\; = \\ H(\{p_n\}, (\{N_n\})) \left(\prod_{\text{all } i} \frac{1}{\alpha_i} \right) \\ \times \sum_{P(\{N_n\})} \left(\prod_{n \neq m}^{E-1} (p_n \cdot v_m)^{N_n} \right) \,. \end{aligned} \tag{D.7}$$

In this form we see explicitly that the factor $R^{(\rm eik)}$ depends only on the numbers N_n of each unordered assignment of the collinear gluons l_i to the external lines p_n. For fixed $\{N_n\}$, the result is the same for every choice of unordered partition $P\,(\{N_n\})$.

We may make this independence explicit by replacing the sum over unordered assignments by a sum over all N_n that add up to j, multiplying each term in the sum by the appropriate combinatoric weight. We thus have the sum

$$\begin{aligned} R^{(\rm eik)} \;\; \propto \;\; & \sum_{\{N_n / \sum N_n = j\}} \frac{j!}{N_1! N_2! \ldots \overline{N_m!} \ldots N_E!} \\ & \times \left(\prod_{n \neq m}^{E} (p_n \cdot v_m)^{N_n} \right) \,, \end{aligned} \tag{D.8}$$

where $\overline{N_m!}$ indicates that this factor is omitted in the product. If we use the multinomial

theorem, this directly simplifies to

$$\begin{aligned} R^{(\mathrm{eik})} &\propto \left(\sum_{n\neq m}(p_n\cdot v_m)\right)^j \\ &= \quad (\,-p_m\cdot v_m\,)^j \\ &= \quad 0\,, \end{aligned} \tag{D.9}$$

where in the second line we have used momentum conservation, and in the third the assumed masslessness of p_m, which implies $p_m \cdot v_m = 0$.

Appendix E

A Proof of an Identity Used in the Text

In this appendix, for completeness, we present a proof of the identity (6.11) used in the main text. This identity is a very useful one for applications of the eikonal approximation [98].

$$\delta(\omega_1 + ... + \omega_n) \sum_{\text{Perms of } \omega_i} \frac{1}{\omega_1 + i\epsilon} ... \frac{1}{\omega_1 + ... + \omega_{n-1} + i\epsilon}$$
$$= (-2\pi i)^{n-1} \delta(\omega_1) ... \delta(\omega_n) \tag{E.1}$$

We will use the representations:

$$\delta(\omega_1 + \omega_2 + ... + \omega_n) = \frac{1}{2\pi} \int dt_n \prod_{j=1}^{n} e^{-i\omega_j t_n}$$
$$\frac{1}{\omega + i\epsilon} = -i \int d\tau \theta(\tau) e^{i(\omega + i\epsilon)\tau} \tag{E.2}$$

To rewrite the left hand side of (E.1) as:

$$\delta(\omega_1 + ... + \omega_n) \sum_{\text{Perms of } \omega_i} \frac{1}{\omega_1 + i\epsilon} ... \frac{1}{\omega_1 + ... + \omega_{n-1} + i\epsilon}$$
$$= (-i)^{n-1} \frac{1}{2\pi} \sum_{\text{Perms over } i} \int dt_n [\prod_{j=1}^{n-1} d\tau_j \theta(\tau_j) \exp(i \sum_{k=1}^{j} (\omega_{i_k} + i\epsilon)\tau_j)][\prod_{j=1}^{n} e^{-i\omega_j t_n}] \tag{E.3}$$

Now let us make the coordinate transformation $\tau_i = t_{i+1} - t_i$. The Jacobian of this transformation is 1, so we find:

$$\begin{aligned}
&\delta(\omega_1 + ... + \omega_n) \sum_{\text{Perms of } \omega_i} \frac{1}{\omega_1 + i\epsilon} ... \frac{1}{\omega_1 + ... + \omega_{n-1} + i\epsilon} \\
&= (-i)^{n-1} \frac{1}{2\pi} \sum_{\text{Perms of } \omega_i} \int dt_n ... dt_1 \theta(t_n - t_{n-1}) ... \theta(t_2 - t_1) \\
&\times e^{i\omega_{i_1}(\tau_1 + \tau_2 + ... + \tau_{n-1} - t_n)} e^{i\omega_{i_2}(\tau_2 + \tau_3 + ... + \tau_{n-1} - t_n)} ... e^{i\omega_{i_{n-1}}(\tau_{n-1} - t_n)} e^{i\omega_{i_n}(-t_n)} \\
&= (-i)^{n-1} \frac{1}{2\pi} \sum_{\text{Perms of } \omega_i} \int dt_n ... dt_1 \theta(t_n - t_{n-1}) ... \theta(t_2 - t_1) \exp(-i \sum_{j=1}^{n} \omega_{i_j} t_j) \\
&= (-i)^{n-1} \frac{1}{2\pi} \int dt_n ... dt_1 \exp(-i \sum_{j=1}^{n} \omega_{i_j} t_j) \\
&= (-2\pi i)^{n-1} \delta(\omega_1) ... \delta(\omega_n) \qquad \text{(E.4)}
\end{aligned}$$

So we see that (E.1) does indeed hold true.

Appendix F

Next-to-Eikonal Coefficients

In this appendix we describe in detail how to calculate the coefficients for all the terms in the next-to-eikonal contribution to the relativistic small angle gravitational scattering amplitude, which are integral to the calculations in chapter 7. We will separate these terms into two classes: those that go as $\mathbf{k_m}^2$ and $(k^z)^2$, and those that go as $\mathbf{k}_\alpha \cdot \mathbf{k}_\beta$ and $k_\alpha^z k_\beta^z$.

F.1 $\mathbf{k_m}^2$ and $(k^z)^2$ coefficients

Let us first start off with the contribution to the next-to-eikonal amplitude from the $\mathbf{k_m}^2$ and k_z^2 coefficients. Note that if we can simplify the terms that go as $\mathbf{k_m^2}$ in the numerator of (7.29) by making the manipulation:

$$\begin{aligned}
&\sum_{\text{Perms over } k_i} [\prod_{i=1}^{n-1} \frac{1}{K_i^z + i\epsilon} \sum_{i=1}^{n-1} \frac{\mathbf{K_i^2}}{K_i^z + i\epsilon}] \\
\Rightarrow &\sum_{\text{Perms over } k_i} [\sum_{m=1}^{n-1} -\mathbf{k_m^2} \frac{\partial}{\partial k_m^z} \prod_{i=1}^{n-1} \frac{1}{K_i^z + i\epsilon}] \\
= &\sum_{\text{Perms over } k_i} [\sum_{m=1}^{n} -\mathbf{k_m^2} \frac{\partial}{\partial k_m^z} \prod_{i=1}^{n-1} \frac{1}{K_i^z + i\epsilon}] \\
= &\sum_{m=1}^{n} -\mathbf{k_m^2} \frac{\partial}{\partial k_m^z} [\sum_{\text{Perms over } k_i} \prod_{i=1}^{n-1} \frac{1}{K_i^z + i\epsilon}]
\end{aligned} \tag{F.1}$$

where we have only retained terms that go as $\mathbf{k_m^2}$ in the second line. In the third line we have used the fact that the derivative of the momentum not included in the $n-1$ momenta in the product will give zero. In the last line we exchanged the ordering of the sums since we have written the first sum in a symmetric way. Similar reasoning applies for the case of extracting the $(k^z)^2$ contributions from (7.32).

Thus we see that the sum of the contributions of the $\mathbf{k_m}^2$ and $(k^z)^2$ terms from (7.29) and (7.32) is:

$$i\mathcal{M}^1_{n,\,k_i^2} = -\frac{2i}{n!}(2\pi)^3 M_\sigma(-\frac{\kappa^2 M_\sigma E_\phi^2}{2(2\pi)^3})^n(2E_\phi)^{-n}\int d^3\mathbf{k_1}...d^3\mathbf{k_n}\delta^3(\mathbf{k_1}+...+\mathbf{k_n}+\mathbf{\Delta}) \\ \times\prod_{i=1}^{n}\frac{1}{\mathbf{k_i^2}}\sum_{m=1}^{n}-[(\mathbf{k_m^\perp})^2-(k_m^z)^2]\frac{\partial}{\partial k_m^z}\sum_{\text{Perms over } k_i}\prod_{i=1}^{n-1}\frac{1}{K_i^z+i\epsilon} \tag{F.2}$$

Let us now Fourier transform by applying $\int \frac{d^3\mathbf{\Delta}}{(2\pi)^3}e^{i\mathbf{b}\cdot\mathbf{\Delta}}$:

$$i\mathcal{M}^1_{n,\,k_i^2} = -\frac{2i}{n!}M_\sigma(-\frac{\kappa^2 M_\sigma E_\phi}{4(2\pi)^3})^n\int d^3\mathbf{k_1}...d^3\mathbf{k_n}e^{-i(\mathbf{k_1}+...+\mathbf{k_n})\cdot\mathbf{b}} \\ \times\prod_{i=1}^{n}\frac{1}{\mathbf{k_i^2}}\sum_{m=1}^{n}-[(\mathbf{k_m^\perp})^2-(k_m^z)^2]\frac{\partial}{\partial k_m^z}\sum_{\text{Perms over } k_i}\prod_{i=1}^{n-1}\frac{1}{K_i^z+i\epsilon} \tag{F.3}$$

We can choose $m = n-1$ since the expression is symmetric in the momenta. Thus, we have:

$$i\mathcal{M}^1_{n,\,k_i^2} = \frac{2i}{(n-1)!}M_\sigma(-\frac{\kappa^2 M_\sigma E_\phi}{4(2\pi)^3})^n\int d^3\mathbf{k_1}...d^3\mathbf{k_n}e^{-i(\mathbf{k_1}+...+\mathbf{k_n})\cdot\mathbf{b}} \\ \times\prod_{i=1}^{n}\frac{1}{\mathbf{k_i^2}}[(\mathbf{k_{n-1}^\perp})^2-(k_{n-1}^z)^2]\frac{\partial}{\partial k_{n-1}^z}\sum_{\text{Perms with } k_{n-1}}\prod_{i=1}^{n-1}\frac{1}{K_i^z+i\epsilon} \tag{F.4}$$

Note now the permutations only include the permutations with k_{n-1} since the ones without k_{n-1} vanish due to the derivative. We can now choose the missing momentum in these permutations to always be k_n since the expression is symmetric in all the momenta besides k_{n-1}, and k_{n-1} is never missing from the permutations. Thus we have:

$$i\mathcal{M}^1_{n,\,k_i^2} = \frac{2i}{(n-2)!}M_\sigma(-\frac{\kappa^2 M_\sigma E_\phi}{4(2\pi)^3})^n\int d^3\mathbf{k_1}...d^3\mathbf{k_n}e^{-i(\mathbf{k_1}+...+\mathbf{k_n})\cdot\mathbf{b}} \\ \times\prod_{i=1}^{n}\frac{1}{\mathbf{k_i^2}}[(\mathbf{k_{n-1}^\perp})^2-(k_{n-1}^z)^2]\frac{\partial}{\partial k_{n-1}^z}\sum_{\text{Perms without } k_n}\prod_{i=1}^{n-1}\frac{1}{K_i^z+i\epsilon} \tag{F.5}$$

We can now use the eikonal identity:

$$\sum_{\text{perms}}\prod_{i=1}^{n}\frac{1}{K_i+i\epsilon} = \prod_{i}^{n}\frac{1}{k_i+i\epsilon} \tag{F.6}$$

over the permutations in (F.5) since we now have permutations such that the same momentum is always missing. Thus we have:

$$i\mathcal{M}^1_{n,\,k_i^2} = -\frac{2i}{(n-2)!}M_\sigma(-\frac{\kappa^2 M_\sigma E_\phi}{4(2\pi)^3})^n \int d^3\mathbf{k_1}...d^3\mathbf{k_n}e^{-i(\mathbf{k_1}+...+\mathbf{k_n})\cdot\mathbf{b}} \\ \times \prod_{i=1}^{n}\frac{1}{\mathbf{k_i^2}}[(\mathbf{k_{n-1}^\perp})^2 - (k^z_{n-1})^2]\prod_{i=1}^{n-2}\frac{1}{k_i^z+i\epsilon}\frac{1}{(k^z_{n-1}+i\epsilon)^2} \tag{F.7}$$

F.2 $\mathbf{k}_\alpha \cdot \mathbf{k}_\beta$ and $k^z_\alpha k^z_\beta$ coefficients

Let us now move on to the $\mathbf{k}_\alpha \cdot \mathbf{k}_\beta$ and $k^z_\alpha k^z_\beta$ coefficients. Note that we can simplify the terms that go as $\mathbf{k}_\alpha \cdot \mathbf{k}_\beta$ in (7.29) by making the manipulation:

$$\sum_{\text{Perms over } k_i}[\prod_{i=1}^{n-1}\frac{1}{K_i^z+i\epsilon}\sum_{i=1}^{n-1}\frac{\mathbf{K_i^2}}{K_i^z+i\epsilon}] \\ \Rightarrow \sum_{\text{possible }\alpha,\,\beta}\ \sum_{\text{missing momentum}}\ \prod_{i\neq\,\alpha,\,\beta}^{n-1}\frac{1}{k_i^z+i\epsilon}(\frac{1}{k_\alpha^z+i\epsilon}\frac{1}{k_\beta^z+i\epsilon}\frac{2\mathbf{k}_\alpha\cdot\mathbf{k}_\beta}{k_\alpha^z+k_\beta^z+i\epsilon}) \\ = n(n-1)\sum_{\text{missing momentum}}\ \prod_{i\neq\,\alpha,\,\beta}^{n-1}\frac{1}{k_i^z+i\epsilon}(\frac{1}{k_\alpha^z+i\epsilon}\frac{1}{k_\beta^z+i\epsilon}\frac{\mathbf{k}_\alpha\cdot\mathbf{k}_\beta}{k_\alpha^z+k_\beta^z+i\epsilon}) \\ = n(n-1)\sum_{\text{Perms over } k_i(i\neq\alpha,\beta)}\ \prod_{i\neq\,\alpha,\,\beta}^{n-1}\frac{1}{K_i^z+i\epsilon}(\frac{1}{k_\alpha^z+i\epsilon}\frac{1}{k_\beta^z+i\epsilon}\frac{\mathbf{k}_\alpha\cdot\mathbf{k}_\beta}{k_\alpha^z+k_\beta^z+i\epsilon}) \tag{F.8}$$

In the second line we have only retained terms that go as $\mathbf{k}_\alpha \cdot \mathbf{k}_\beta$ in the numerator. The validity of the transformation in the second line can easily be seen by working through the $n = 3$ and $n = 4$ cases, which we omit here for brevity. In the third line we have used the fact that each choice of α, β will give the same contribution due to the fact that the rest of (7.29) is symmetric in the graviton momenta, giving a factor of $\frac{n(n-1)}{2}$. In the fourth line we have used the eikonal identity (F.6). We arrive at a nearly identical expression for the $k^z_\alpha k^z_\beta$ terms by making the same manipulation in (7.32).

Thus we see that the total contribution of the $\mathbf{k}_\alpha \cdot \mathbf{k}_\beta$ and $k^z_\alpha k^z_\beta$ terms from (7.29) and

(7.32) is:

$$
\begin{aligned}
i\mathcal{M}^1_{n\,k_\alpha\cdot k_\beta} &= -\frac{2i}{(n-2)!}(2\pi)^3 M_\sigma(-\frac{\kappa^2 M_\sigma E_\phi}{4(2\pi)^3})^n \\
&\times \int d^3\mathbf{k_1}...d^3\mathbf{k_n}\delta^3(\mathbf{k_1}+...+\mathbf{k_n}+\mathbf{\Delta})\prod_{i=1}^{n}\frac{1}{\mathbf{k_i^2}} \\
&\times \sum_{\text{Perms over } k_i (i\neq\alpha,\beta)} \prod_{i\neq\,\alpha,\,\beta}^{n-1} \frac{1}{K_i^z+i\epsilon}(\frac{1}{k_\alpha^z+i\epsilon}\frac{1}{k_\beta^z+i\epsilon}\frac{\mathbf{k}_\alpha^\perp\cdot\mathbf{k}_\beta^\perp-k_\alpha^z k_\beta^z}{k_\alpha^z+k_\beta^z+i\epsilon})
\end{aligned}
\tag{F.9}
$$

Fourier transforming at this stage, we have:

$$
\begin{aligned}
i\mathcal{M}^1_{n\,k_\alpha\cdot k_\beta} &= -\frac{2i}{(n-2)!}M_\sigma(-\frac{\kappa^2 M_\sigma E_\phi}{4(2\pi)^3})^n \int d^3\mathbf{k_1}...d^3\mathbf{k_n}e^{-i(\mathbf{k_1}+...+\mathbf{k_n})\cdot\mathbf{b}}\prod_{i=1}^{n}\frac{1}{\mathbf{k_i^2}} \\
&\times \sum_{\text{Perms over } k_i (i\neq n,n-1)} \prod_{i}^{n-3} \frac{1}{K_i^z+i\epsilon}(\frac{1}{k_n^z+i\epsilon}\frac{1}{k_{n-1}^z+i\epsilon}\frac{\mathbf{k}_n^\perp\cdot\mathbf{k}_{\mathbf{n-1}}^\perp-k_n^z k_{n-1}^z}{k_n^z+k_{n-1}^z+i\epsilon})
\end{aligned}
\tag{F.10}
$$

where we have chosen $\alpha,\beta = n, n-1$. Using the same argument as in the previous subsection, we can symmetrize such that k_{n-2} is the missing momentum. In this case we can use the eikonal identity (F.6) so that:

$$
\begin{aligned}
i\mathcal{M}^1_{n\,k_\alpha\cdot k_\beta} &= -\frac{2i}{(n-3)!}M_\sigma(-\frac{\kappa^2 M_\sigma E_\phi}{4(2\pi)^3})^n \int d^3\mathbf{k_1}...d^3\mathbf{k_n}e^{-i(\mathbf{k_1}+...+\mathbf{k_n})\cdot\mathbf{b}} \\
&\times \prod_{i=1}^{n}\frac{1}{\mathbf{k_i^2}}\prod_{i}^{n-3}\frac{1}{k_i^z+i\epsilon}(\frac{1}{k_n^z+i\epsilon}\frac{1}{k_{n-1}^z+i\epsilon}\frac{\mathbf{k}_n^\perp\cdot\mathbf{k}_{\mathbf{n-1}}^\perp-k_n^z k_{n-1}^z}{k_n^z+k_{n-1}^z+i\epsilon})
\end{aligned}
\tag{F.11}
$$

F.3 Simplifying Identity

Note that the expressions corresponding to both the coefficients have the similar factor:

$$
\int d^3\mathbf{k_1}...d^3\mathbf{k_m}e^{-i(\mathbf{k_1}+...+\mathbf{k_m})\cdot\mathbf{b}}\prod_{i=1}^{m}\frac{1}{\mathbf{k_i^2}}\prod_{i=1}^{m-1}\frac{1}{k_i^z+i\epsilon} \tag{F.12}
$$

where $m = n-1$ for (F.7) and $m = n-2$ for (F.11). Let us see if we can change this expression to something more useful.

We can first use the eikonal identity to write:

$$\int d^3\mathbf{k_1}...d^3\mathbf{k_m}e^{-i(\mathbf{k_1}+...+\mathbf{k_m})\cdot\mathbf{b}}\prod_{i=1}^{m}\frac{1}{\mathbf{k_i^2}}\prod_{i=1}^{m-1}\frac{1}{k_i^z+i\epsilon}$$
$$=\int d^3\mathbf{k_1}...d^3\mathbf{k_m}e^{-i(\mathbf{k_1}+...+\mathbf{k_m})\cdot\mathbf{b}}\prod_{i=1}^{m}\frac{1}{\mathbf{k_i^2}}\sum_{\text{Perms without } k_m}\prod_{i=1}^{n-1}\frac{1}{K_i^z+i\epsilon} \tag{F.13}$$

We can now use the argument we made in the previous section in reverse to symmetrize the permutations such that they are over all the momenta:

$$\int d^3\mathbf{k_1}...d^3\mathbf{k_m}e^{-i(\mathbf{k_1}+...+\mathbf{k_m})\cdot\mathbf{b}}\prod_{i=1}^{m}\frac{1}{\mathbf{k_i^2}}\prod_{i=1}^{m-1}\frac{1}{k_i^z+i\epsilon}$$
$$=\frac{1}{m}\int d^3\mathbf{k_1}...d^3\mathbf{k_m}e^{-i(\mathbf{k_1}+...+\mathbf{k_m})\cdot\mathbf{b}}\prod_{i=1}^{m}\frac{1}{\mathbf{k_i^2}}\sum_{\text{Perms}}\prod_{i=1}^{n-1}\frac{1}{K_i^z+i\epsilon} \tag{F.14}$$

Let us write the exponential in a familiar way:

$$\int d^3\mathbf{k_1}...d^3\mathbf{k_m}e^{-i(\mathbf{k_1}+...+\mathbf{k_m})\cdot\mathbf{b}}\prod_{i=1}^{m}\frac{1}{\mathbf{k_i^2}}\prod_{i=1}^{m-1}\frac{1}{k_i^z+i\epsilon}$$
$$=\frac{1}{m}\int d^3\mathbf{k_1}...d^3\mathbf{k_m}d^3\mathbf{\Delta}\delta^3(\mathbf{k_1}+...+\mathbf{k_m}+\mathbf{\Delta})e^{i\mathbf{b}\cdot\mathbf{\Delta}}\prod_{i=1}^{m}\frac{1}{\mathbf{k_i^2}}\sum_{\text{Perms}}\prod_{i=1}^{n-1}\frac{1}{K_i^z+i\epsilon} \tag{F.15}$$

Now let us note that this is simply the integral we had for the leading eikonal case. In the exact same way, we can work in the frame where $\Delta^z = 0$ and apply the identity (7.9), which reduces the problem to two spatial dimensions. Going through this procedure, we have:

$$\int d^3\mathbf{k_1}...d^3\mathbf{k_m}e^{-i(\mathbf{k_1}+...+\mathbf{k_m})\cdot\mathbf{b}}\prod_{i=1}^{m}\frac{1}{\mathbf{k_i^2}}\prod_{i=1}^{m-1}\frac{1}{k_i^z+i\epsilon}$$
$$=\frac{1}{m}(-2\pi i)^{m-1}[\int\frac{d^2\mathbf{k}^\perp}{(k^\perp)^2}e^{-i\mathbf{b}^\perp\cdot\mathbf{k}^\perp}]^m \tag{F.16}$$

As we will show in the next section, applying (F.16) casts the next-to-eikonal amplitude in a form that makes it much easier to see exponentiation at this order.

F.4 Results

Here we present the final results that are used in the main text. If we apply the identity (F.16) to (F.7) we have:

$$
\begin{aligned}
i\mathcal{M}^1_{n,\,k_i^2} &= \frac{2i}{(n-1)!}\frac{M_\sigma}{(2\pi)^2}(i\frac{\kappa^2 M_\sigma E_\phi}{4(2\pi)^2})^n[\int \frac{d^2\mathbf{k}^\perp}{(k^\perp)^2}e^{-i\mathbf{b}^\perp\cdot\mathbf{k}^\perp}]^{n-1}\int\frac{d^3\mathbf{k}}{\mathbf{k^2}}e^{-i\mathbf{k}\cdot\mathbf{b}}\frac{(\mathbf{k}^\perp)^2-(k^z)^2}{(k^z+i\epsilon)^2} \\
&= \frac{2}{(n-1)!}(s-M_\sigma^2)(i\chi_0)^{n-1}\chi_1
\end{aligned}
\tag{F.17}
$$

where:

$$
\chi_1 = -\frac{\kappa^2 M_\sigma}{8(2\pi)^4}\int\frac{d^3\mathbf{k}}{\mathbf{k^2}}e^{-i\mathbf{k}\cdot\mathbf{b}}\frac{(\mathbf{k}^\perp)^2-(k^z)^2}{(k^z+i\epsilon)^2}
\tag{F.18}
$$

If we apply the identity (F.16) to (F.11) we have:

$$
\begin{aligned}
i\mathcal{M}^1_{n\,k_\alpha\cdot k_\beta} &= -\frac{2}{(n-2)!}\frac{M_\sigma}{(2\pi)^3}(i\frac{\kappa^2 M_\sigma E_\phi}{4(2\pi)^2})^n[\int\frac{d^2\mathbf{k}^\perp}{(k^\perp)^2}e^{-i\mathbf{b}^\perp\cdot\mathbf{k}^\perp}]^{n-2} \\
&\quad\times\int\frac{d^3\mathbf{k}_\alpha}{\mathbf{k}_\alpha^\mathbf{2}}\frac{d^3\mathbf{k}_\beta}{\mathbf{k}_\beta^\mathbf{2}}e^{-i(\mathbf{k}_\alpha+\mathbf{k}_\beta)\cdot\mathbf{b}}(\frac{1}{k_\alpha^z+i\epsilon}\frac{1}{k_\beta^z+i\epsilon}\frac{\mathbf{k}_\alpha^\perp\cdot\mathbf{k}_\beta^\perp-k_\alpha^z k_\beta^z}{k_\alpha^z+k_\beta^z+i\epsilon}) \\
&= \frac{2}{(n-2)!}(s-M_\sigma^2)(i\chi_0)^{n-2}(i\chi_2)
\end{aligned}
\tag{F.19}
$$

where:

$$
\chi_2 = i\frac{\kappa^4 M_\sigma^2 E_\phi}{32(2\pi)^7}\int\frac{d^3\mathbf{k}_\alpha}{\mathbf{k}_\alpha^\mathbf{2}}\frac{d^3\mathbf{k}_\beta}{\mathbf{k}_\beta^\mathbf{2}}e^{-i(\mathbf{k}_\alpha+\mathbf{k}_\beta)\cdot\mathbf{b}}(\frac{1}{k_\alpha^z+i\epsilon}\frac{1}{k_\beta^z+i\epsilon}\frac{\mathbf{k}_\alpha^\perp\cdot\mathbf{k}_\beta^\perp-k_\alpha^z k_\beta^z}{k_\alpha^z+k_\beta^z+i\epsilon})
\tag{F.20}
$$

Appendix G

Useful Integrals

In this appendix we evaluate the integrals used in the main text.

G.1 I_0 Integral

Here we evaluate the integral that is needed in (7.19):

$$I_0 = \int \frac{d^2\mathbf{k}^\perp}{(\mathbf{k}^\perp)^2} e^{-i\mathbf{b}^\perp\cdot\mathbf{k}^\perp} = \int dk_\perp d\theta e^{-ik_\perp b\cos\theta} k_\perp^{d-5} \tag{G.1}$$

where in the last line we make the number of dimensions d general. In terms of Bessel functions we can write this as:

$$\begin{aligned} I_0 &= 2\pi \int dk_\perp k_\perp^{d-5} J_0(k_\perp b) \\ &= 2\pi b^{4-d} \int dy y^{d-5} J_0(y) \end{aligned} \tag{G.2}$$

Note that since:

$$\int_0^\infty dy y^m J_0(y) = 2^m \frac{\Gamma[(1+m)/2]}{\Gamma[(1-m)/2]} \tag{G.3}$$

for $-1 < m < \frac{1}{2}$, we have:

$$I_0 = 2\pi b^{4-d} 2^{d-5} \frac{\Gamma[(n-4)/2]}{\Gamma[(6-n)/2]} \tag{G.4}$$

If we expand: $\Gamma[(n-4)/2]$ about $n = 4$, we get:

$$I_0 = 2\pi b^{4-d} 2^{d-5} \frac{1}{\Gamma[(6-d)/2]} [\frac{2}{d-4} + \gamma + ...] \tag{G.5}$$

Taylor expanding the non pole part and only keeping the finite part dependent on b, we get:

$$I_0 \approx 2\pi[\frac{1}{d-4} - \log b] \tag{G.6}$$

G.2 I_1 Integral

Now let us work on evaluating the integral:

$$I_1 = \int \frac{d^3\mathbf{k}}{\mathbf{k^2}} e^{-i\mathbf{k}\cdot\mathbf{b}} \frac{(\mathbf{k}^\perp)^2 - (k^z)^2}{(k^z + i\epsilon)^2} \tag{G.7}$$

We will have to consider two cases, $z \geq 0$, and $z \leq 0$, since the sign of z will determine how we can close the contour. Note that for the $z = 0$ case, we can close in either direction. Let us first consider the $z \leq 0$ case. In this case we have:

$$I_1^{z\leq 0} = -\Theta(-z)2\pi \int \frac{d^2\mathbf{k}^\perp}{k^\perp} e^{-i\mathbf{k}^\perp\cdot\mathbf{b}^\perp} e^{k^\perp z} \tag{G.8}$$

where we have integrated over the only pole in the upper half plane ($k^z = ik^\perp$). If we integrate over the rest of the components, we arrive at:

$$\begin{aligned} I_1^{z\leq 0} &= -\Theta(-z)2\pi \int dk^\perp d\theta e^{-ik^\perp b^\perp \cos\theta} e^{k^\perp z} \\ &= -\Theta(-z)(2\pi)^2 \int dk^\perp J_0(k^\perp b^\perp) e^{k^\perp z} \\ &= -\Theta(-z)(2\pi)^2 \frac{1}{|\mathbf{b}|} \end{aligned} \tag{G.9}$$

Let us now work with the $z \geq 0$ case. In this case we have two poles in the lower half plane ($k^z = -ik^\perp$, $k^z = -i\epsilon$) so we have:

$$I_1^{z\geq 0} = -\Theta(z)2\pi[\int \frac{d^2\mathbf{k}^\perp}{k^\perp} e^{-i\mathbf{k}^\perp\cdot\mathbf{b}^\perp} e^{-k^\perp z} + z\int d^2\mathbf{k}^\perp e^{-i\mathbf{k}^\perp\cdot\mathbf{b}^\perp}] \tag{G.10}$$

The integral on the first line (corresponding to the pole $k^z = -ik^\perp$) can be evaluated in an identical method as we did for the $z \leq 0$ case, and the integral on the second line (corresponding to the pole $k^z = -i\epsilon$) simply gives a delta function so we have:

$$I_1^{z\geq 0} = -\Theta(z)2\pi[(2\pi)\frac{1}{|\mathbf{b}|} + z(2\pi)^2\delta^2(\mathbf{b}^\perp)] \tag{G.11}$$

Thus we have that:

$$\begin{aligned} I_1 &= I_1^{z\leq 0} + I_1^{z\geq 0} \\ &= -(2\pi)^2[\frac{1}{|\mathbf{b}|} + \Theta(z)z(2\pi)\delta^2(\mathbf{b}^\perp)] \end{aligned} \tag{G.12}$$

G.3 I_2 Integral

Here we evaluate the integrals needed in the evaluation of χ_2.

$$I_2 = \int \frac{d^3\mathbf{k}_\alpha}{\mathbf{k}_\alpha^2}\frac{d^3\mathbf{k}_\beta}{\mathbf{k}_\beta^2} e^{-i(\mathbf{k}_\alpha+\mathbf{k}_\beta)\cdot\mathbf{b}}(\frac{1}{k_\alpha^z+i\epsilon}\frac{1}{k_\beta^z+i\epsilon}\frac{\mathbf{k}_\alpha^\perp\cdot\mathbf{k}_\beta^\perp - k_\alpha^z k_\beta^z}{k_\alpha^z+k_\beta^z+i\epsilon}) \tag{G.13}$$

Note that the poles in (G.13) are not pinched (except in the small $k_{\alpha/\beta}^\perp$ region where the integral is explicitly IR finite via power counting) and do not result in infrared singularities. Thus the pole structure serves an important role in the above integral, which we will take advantage of later in this calculation. We can simplify this expression using the identity:

$$\int \frac{d^2\mathbf{k}^\perp}{\mathbf{k}^2} e^{-i\mathbf{b}^\perp\cdot\mathbf{k}^\perp} = 2\pi K_0\left(b^\perp|k^z|\right) \tag{G.14}$$

for the case where k_z is real. We then see that for $i = x, y$ we have:

$$\begin{aligned} \int d^2\mathbf{k}^\perp \frac{k^i}{\mathbf{k}^2} e^{-i\mathbf{b}^\perp\cdot\mathbf{k}^\perp} &= 2\pi i\frac{\partial}{\partial b^i}K_0\left(b^\perp|k^z|\right) \\ &= 2\pi i\frac{b^i}{b^\perp}\frac{\partial}{\partial b^\perp}K_0\left(b^\perp|k^z|\right) \\ &= 2\pi i\frac{b^i}{b^\perp}|k^z|K_0'\left(b^\perp|k^z|\right) \end{aligned} \tag{G.15}$$

Thus we have that:

$$\begin{aligned} I_2 = -(2\pi)^2 &\int dk_\alpha^z dk_\beta^z e^{-iz(k_\alpha^z+k_\beta^z)}\frac{1}{k_\alpha^z+k_\beta^z+i\epsilon} \\ &\times [K_0'\left(b^\perp|k_\alpha^z|\right)K_0'\left(b^\perp|k_\beta^z|\right)\sigma(k_\alpha^z k_\beta^z) + K_0\left(b^\perp|k_z^\alpha|\right)K_0\left(b^\perp|k_z^\beta|\right)] \end{aligned} \tag{G.16}$$

where $\sigma(\pm x) = \pm 1$ for $x > 0$ arises from canceling the poles in k_z with absolute values. We can rescale the integral so that we have:

$$I_2 = -\frac{(2\pi)^2}{b^\perp} \int dy_\alpha^z dy_\beta^z e^{-i(y_\alpha^z + y_\beta^z)z/b^\perp} \frac{1}{y_\alpha^z + y_\beta^z + i\epsilon} \times \left[K_0'\left(|y_\alpha^z|\right) K_0'\left(|y_\beta^z|\right) \sigma(y_\alpha^z y_\beta^z) + K_0\left(|y_z^\alpha|\right) K_0\left(|y_z^\beta|\right)\right] \tag{G.17}$$

Let us now try evaluating this integral by using the parameterization:

$$\frac{1}{y_\alpha^z + y_\beta^z + i\epsilon} = -i \int_0^\infty da e^{i(y_\alpha^z + y_\beta^z + i\epsilon)a} \tag{G.18}$$

And considering only the zeroth order term in $\frac{z}{b^\perp}$, as this ratio should be small. In this case, we have:

$$I_2 = \frac{i(2\pi)^2}{b^\perp} \int da dy_\alpha^z dy_\beta^z e^{i(y_\alpha^z + y_\beta^z + i\epsilon)a} \times \left[K_0'\left(|y_\alpha^z|\right) K_0'\left(|y_\beta^z|\right) \sigma(y_\alpha^z y_\beta^z) + K_0\left(|y_z^\alpha|\right) K_0\left(|y_z^\beta|\right)\right] \tag{G.19}$$

Let us break this integral up into two pieces, one with the primed terms and one with the unprimed terms. In this case for the primed portion we have:

$$\begin{aligned} I_{2A} &= \frac{i(2\pi)^2}{b^\perp} \int da dy_\alpha^z dy_\beta^z e^{i(y_\alpha^z + y_\beta^z + i\epsilon)a} K_0'\left(|y_\alpha^z|\right) K_0'\left(|y_\beta^z|\right) \sigma(y_\alpha^z y_\beta^z) \\ &= \frac{i(2\pi)^2}{b^\perp} \int da dy_\alpha^z dy_\beta^z e^{iy_\alpha^z a} K_0'\left(|y_\alpha^z|\right) \sigma(y_\alpha^z) e^{iy_\beta^z a} K_0'\left(|y_\beta^z|\right) \sigma(y_\beta^z) \end{aligned} \tag{G.20}$$

Note that:

$$\begin{aligned} &\int_{-\infty}^\infty dy e^{iya} K_0'\left(|y|\right) \sigma(y) \\ =&\int_0^\infty dy e^{iya} K_0'\left(|y|\right) - \int_{-\infty}^0 dy e^{iya} K_0'\left(|y|\right) \\ =&2i \int_\delta^\infty dy \sin\left(ya\right) K_0'\left(y\right) + \int_{-\delta}^\delta dy K_0'(y) \end{aligned} \tag{G.21}$$

where we have split off an infinitesmal region $(-\delta, \delta)$ in the integral. This is, as discussed earlier, to take into account the pole structure of (G.13) to guarantee there are no infrared divergences. We will preserve the pole structure by using the fact that in the small y region,

$K_0'(y) \approx -\frac{1}{y} \to -\frac{1}{y+i\epsilon}$. Thus we have using the principal value prescription that:

$$\int_{-\infty}^{\infty} dy e^{iya} K_0' \left(|y|\right) \sigma(y) = i\pi(1 - \frac{a}{\sqrt{a^2+1}}) \tag{G.22}$$

So we have that:

$$\begin{aligned} I_{2A} &= -\frac{i(2\pi)^4}{4b^\perp} \int da(1 - \frac{a}{\sqrt{a^2+1}})^2 \\ &= \frac{i(2\pi)^4}{4b^\perp}(\frac{\pi}{2} - 2) \end{aligned} \tag{G.23}$$

Note that the above integral would have been infrared divergent if not for the additional term in (G.21) included to account for the pole structure.

For the unprimed portion, we have that:

$$\begin{aligned} I_{2B} &= \frac{i(2\pi)^2}{b^\perp} \int da dy_\alpha^z dy_\beta^z e^{i(y_\alpha^z + y_\beta^z + i\epsilon)a} K_0 \left(|y_z^\alpha|\right) K_0 \left(|y_z^\beta|\right) \\ &= \frac{i(2\pi)^2}{b^\perp} \int da [\int dy e^{iya} K_0 \left(|y|\right)]^2 \\ &= \frac{i(2\pi)^4}{4b^\perp} \int da \frac{1}{a^2+1} \\ &= \frac{i(2\pi)^4}{4b^\perp}(\frac{\pi}{2}) \end{aligned} \tag{G.24}$$

So, we have that:

$$I_2 = \frac{i(2\pi)^4}{4b^\perp}(\pi - 2) \tag{G.25}$$

Bibliography

[1] S. Weinberg, *The Cosmological Constant Problem*, *Rev. Mod. Phys.* **61** (1989) 1.

[2] C. Armendariz-Picon, V. Mukhanov, and P. Steinhardt *Essentials of k-essence*, *Phys. Rev.* **D 61** (2001) 103510.

[3] C. Bonvin, C. Caprini, and R. Durrer, *No-Go Theorem for k-essence Dark Energy*, *Phys. Rev. Lett.* **97**, (2006) 081303

[4] E. Babichev, V. Mukhanov, and A. Vikman, *k-essence, Superluminal Propagation, Causality and Emergent Geometry*, *JHEP* **02** (2008) 101

[5] M. Veltman,"Quantum Theory of Gravitation", in R. Bailan and J. Zinn-Justin, eds., *Methods in Field Theory*, North-Holland, Amsterdam (1976) 265.

[6] S. Giddings, D. Gross and A. Maharana, *Gravitational Effects in Ultrahigh-Energy String Scattering*, *Phys. Rev.* **D 77** (2008) 046001.

[7] Z. Bern, J. J. M. Carrasco and H. Johansson, *New Relations for Gauge-Theory Amplitudes*, *Phys. Rev.* **D 78** (2008) 085011.

[8] R. Saotome, R. Akhoury, and D. Garfinkle, *Examining Gravitational Collapse with Test Scalar Fields*, *Class. Quant. Grav.* **27** (2010) 165019.

[9] R. Akhoury, D. Garfinkle, and R. Saotome, *Gravitational Collapse of k-essence*, *JHEP* **1104** (2011) 096.

[10] R. Akhoury, D. Garfinkle, R. Saotome, and A. Vikman *Non-Stationary Dark Energy Around a Black Hole*, *Phys. Rev.* **D 83** (2011) 084034.

[11] R. Akhoury, R. Saotome, and G. Sterman *Collinear and Soft Divergences in Perturbative Quantum Gravity*, *Phys. Rev.* **D 84** (2011) 104040.

[12] R. Saotome and R. Akhoury, *Relationship Between Gravity and Gauge Scattering in the High Energy Limit*, *JHEP* **1301** (2013) 123.

[13] R. Akhoury, S. Mukohyama, and R. Saotome, *No Classicalization Beyond Spherical Symmetry*, (2011) `arXiv:1109.3820 [hep-th]`.

[14] C. Gauthier, R. Saotome, and R. Akhoury, *Interaction of Neutrinos with a Cosmological k-essence Scalar*, *JHEP* **1007** (2010) 062.

[15] M. Choptuik, *Universality and Scaling in Gravitational Collapse of a Massless Scalar Field*, *Phys. Rev. Lett.* **70** (1993) 9

[16] B. Berger, D. Garfinkle, J. Isenberg, V. Moncrief, and M. Weaver, *The Singularity in Generic Gravitational Collapse is Space-like, Local, and Oscillatory*, *Mod. Phys. Lett. A* **13** (1998) 1565

[17] D. Garfinkle, *Numerical Simulations of Generic Singularities*, *Phys. Rev. Lett.* **93** (2004) 161101

[18] P. Csizmadia and I. Racz, *Gravitational Collapse and Topology Change in Spherically Symmetric Dynamical Systems*, *Class. Quantum Grav.* **27** (2010) 015001

[19] M. Choptuik, E. Hirschmann, and R. Marsa, *New Critical Behavior in Einstein-Yang-Mills Collapse*, *Phys. Rev.* **D60** (1999) 124011

[20] V. Belinskii, I. Khalatnikov, and E. Lifschitz, *Oscillatory Approach to the Singular Point in Relativistic Cosmology*, *Sov. Phys. Usp.* **13** (1971) 745

[21] E. Poisson and W. Israel, *Internal Structure of Black Holes*, *Phys. Rev.* **D41** (1990) 1796

[22] J. Oppenheimer and H. Snyder, *On Continued Gravitational Contraction*, *Phys. Rev.* **56** (1939) 455

[23] R. Adler, J. Bjorken, P. Chen, and J. Liu, *Simple Analytical Models of Gravitational Collapse*, *Am. J. Phys.* **73** (2005)1148

[24] P. Painleve and C. Hebd, *La Mecanique Classique et la Theorie de la Relativite*, *Acad. Sci., Paris. C. R.* **173** (1921) 677

[25] A. Gullstrand, *Allgmeine Losung des Statischen Einkorperproblems in der Einsteinschen Gravitationstheorie*, *Ark. Mat. Astron. Fys.* **16** (1922) 1

[26] M. Choptuik,"Critical Behavior in Scalar Field Collapse", in D. Hobill, A. Burd and A. Coley, eds., *Deterministic Chaos in General Relativity*, Plenum, New York, (1994) 155

[27] H. Kreiss and J. Oliger, *Methods for the Approximate Solution of Time Dependent Problems*, Global Atmospheric Research Program, Publication Series No. 10 (1973)

[28] C. Armendariz-Picon, V. Mukhanov, and P. Steinhardt, *Dynamical Solution to the Problem of a Small Cosmological Constant and Late-Time Cosmic Acceleration*, *Phys. Rev. Lett.* **85** (2000) 4438

[29] J. Kang, V. Vanchurin, and S. Winitzki, *Attractor Scenarios and Superluminal Signals in k-essence Cosmology*, *Phys. Rev.* **D 76** (2007) 083511

[30] V. Mukhanov and A. Vikman, *Enhancing the Tensor-to-Scalar Ratio in Simple Inflation*, *JCAP* **0602** (2006) 004

[31] E. Babichev, V. Mukhanov, and A. Vikman, *Escaping from the Black Hole?*, *JHEP* **09** (2006) 061

[32] C. Eling and T. Jabobson, *Black Holes in Einstein-Aether Theory*, *Class. Quant. Grav.* **23** (2006) 5643

[33] D. Garfinkle, C. Eling, and T. Jacobson, *Numerical Simulations of Gravitational Collapse in Einstein-Aether Theory*, *Phys Rev.* **D 76** (2007) 024003

[34] V. Moncrief, *Stability of Stationary, Spherical Accretion onto a Schwarzschild Black Hole*, *Astrophys J.* **235** (1980) 1038

[35] J. Ziprick and G. Kunstatter, *Numerical Study of Black-Hole Formation in Painlev-Gullstrand Coordinates*, *Phys. Rev.* **D 79** (2009) 101503

[36] C. Leaonard, J. Ziprick, G. Kunstatter, and R. Mann *Gravitational Collapse of k-essence Matter in Painleve-Gullstrand Coordinates*, *JHEP* **10** (2011) 028.

[37] E. Babichev, V. Mukhanov, and A. Vikman, *Looking Beyond the Horizon*, `arXiv:0704.3301 [hep-th]`.

[38] E. Babichev, V. Dokuchaev, and Y. Eroshenko, *Black Hole Mass Decreasing due to Phantom Energy Accretion*, *Phys. Rev. Lett.* **93** (2004) 021102.

[39] A. V. Frolov, *Accretion of Ghost Condensate by Black Holes*, *Phys. Rev.* **D70** (2004) 061501.

[40] S. Mukohyama, *Black holes in the Ghost Condensate*, *Phys.Rev.* **D71** (2005) 104019.

[41] E. Babichev, S. Chernov, V. Dokuchaev, and Y. Eroshenko, *Ultra-Hard Fluid and Scalar Field in the Kerr-Newman Metric*," *Phys. Rev.* **D78** (2008) 104027.

[42] E. Babichev, *Galileon Accretion*, *Phys. Rev.* **D83** (2011) 024008.

[43] H. Bondi, *On Spherically Symmetrical Accretion*, *Mon. Not. Roy. Astron. Soc.* **112** (1952) 195.

[44] R. Akhoury, C. S. Gauthier, and A. Vikman, *Stationary Configurations Imply Shift Symmetry: No Bondi Accretion for Quintessence / k-essence*, *JHEP* **03** (2009) 082.

[45] F. Arroja and M. Sasaki, *A Note on the Equivalence of a Barotropic Perfect Fluid with a k-essence Scalar Field*, *Phys. Rev.* **D81** (2010) 107301.

[46] S. Unnikrishnan and L. Sriramkumar, *A Note on Perfect Scalar Fields*, *Phys. Rev.* **D81** (2010) 103511.

[47] R. L. Marsa and M. W. Choptuik, *Black Hole Scalar Field Interactions in Spherical Symmetry*, *Phys. Rev.* **D54** (1996) 4929–4943.

[48] A. Y. Kamenshchik, U. Moschella, and V. Pasquier, *An Alternative to Quintessence*, *Phys. Lett.* **B511** (2001) 265–268.

[49] V. F. Mukhanov and A. Vikman, *Enhancing the Tensor-to-Scalar Ratio in Simple Inflation*, *JCAP* **0602** (2006) 004.

[50] R. M. Wald, *General Relativity*, Chicago, Univ. Press (1984).

[51] N. Arkani-Hamed, H.-C. Cheng, M. A. Luty, and S. Mukohyama, *Ghost Condensation and a Consistent Infrared Modification of Gravity*, *JHEP* **05** (2004) 074.

[52] A. V. Frolov and L. Kofman, *Inflation and de Sitter Thermodynamics*, *JCAP* **0305** (2003) 009.

[53] S. Weinberg, *Infrared Photons and Gravitons*, *Phys. Rev.* **140** (1965) B516.

[54] J. F. Donoghue and T. Torma, *Infrared Behavior of Graviton-Graviton Scattering*, *Phys. Rev.* **D 60** (1999) 024003.

[55] S. G. Naculich and H. J. Schnitzer, *Absence of Subleading Infrared Divergences in Gravity*, *JHEP* **1105** (2011) 087.

[56] C. D. White, *Factorization Properties of Soft Graviton Amplitudes*, *JHEP* **1105** (2011) 060.

[57] Z. Bern, L. J. Dixon and R. Roiban, *Is $N = 8$ Supergravity Ultraviolet Finite? Phys. Lett. B* **644** (2007) 265.

[58] S. B. Giddings, *Is String Theory a Theory of Quantum Gravity*, `arXiv:1105.6359 [hep-th]`

[59] G. Sterman, *Mass Divergences in Annihilation Processes. I. Origin and Nature of Divergences in Cut Vacuum Polarization Diagrams*, *Phys. Rev.* **D 17**, (1978) 2773.

[60] R. Akhoury, *Mass Divergences of Wide-Angle Scattering Amplitudes*, Phys. Rev. D **19** (1979) 1250.

[61] A. Sen, *Asymptotic Behavior of the Wide Angle On-Shell Quark Scattering Amplitudes in Nonabelian Gauge Theories*, *Phys. Rev.* **D28** (1983) 860.

[62] S. B. Libby and G. F. Sterman, *Jet and Lepton Pair Production in High-Energy Lepton-Hadron and Hadron-Hadron Scattering*, *Phys. Rev.* **D 18** (1978) 3252.

[63] G. F. Sterman, *An Introduction to quantum field theory*, Cambridge, UK: Univ. Pr. (1993) 572 p.

[64] R. P. Feynman, *Quantum Theory of Gravitation*, *Acta Phys. Polon.* **24**, (1963) 697-722.

[65] B. S. DeWitt, *Quantum Theory of Gravity. 1, 2, and 3.*, *Phys. Rev.* **160**, (1967) 1113; 1195; 1239.

[66] L. D. Faddeev and V. N. Popov, *Feynman Diagrams for the Yang-Mills Field*, *Phys. Lett.* **B25** (1967) 29-30.

[67] G. 't Hooft and M. J. G. Veltman, *One Loop Divergencies in the Theory of Gravitation*, *Annales Poincare Phys. Theor.* **A20** (1974) 69-94.

[68] V. E. Korepin, *Cancellation of Ultra-Violet Infinities in One Loop Gravity*, `arXiv:0905.2175 [gr-qc]`.

[69] D. M. Capper, G. Leibbrandt, M. Ramon Medrano, *Calculation of the Graviton Self-Energy Using Dimensional Regularization*, *Phys. Rev.* **D8** (1973) 4320-4331.

[70] F. A. Berends and R. Gastmans, *On the High-Energy Behavior of Born Cross Sections in Quantum Gravity*, Nucl. Phys. B **88** (1975) 99.

[71] J. F. Donoghue, *General Relativity as an Effective Field Theory: The Leading Quantum Corrections*, *Phys. Rev.* **D50** (1994) 3874-3888.

[72] L. D. Landau, *On Analytic Properties of Vertex Parts in Quantum Field Theory*, *Nucl. Phys.* **13** (1959) 181-192.

[73] J. D. Bjorken, Doctoral Dissertation, Stanford University (1959).

[74] R. J. Eden, P. V. Landshooff, D. I. Olive and J. C. Polkinghorne, *The Analytic S-Matrix*, Cambridge, UK: Univ. Pr. (1966) 287 p.

[75] J. Collins, *Foundations of Perturbative QC*, Cambridge, UK: Univ. Pr. (2011) 636 p.

[76] C. W. Bauer, S. Fleming, D. Pirjol and I. W. Stewart, *An Effective Field Theory for Collinear and Soft Gluons: Heavy to Light Decays*, *Phys. Rev.* **D63** (2001) 114020.

[77] J. Goldberg, *Conservation Laws in General Relativity*, *Phys. Rev.* **111** (1958) 315.

[78] J. C. Collins, D. E. Soper and G. F. Sterman, "Factorization of Hard Processes in QCD", in A.H. Mueller, ed.,*Perturbative QCD*, *Adv. Ser. Direct. High Energy Phys.* **5** (1988) 1, arXiv:hep-ph/0409313.

[79] J. C. Collins, D. E. Soper and G. F. Sterman, *Factorization for One-Loop Corrections in the Drell-Yan Process Nucl. Phys.* **B 223** (1983) 381.

[80] S. Weinberg, *Photons and Gravitons in S-Matrix Theory: Derivation of Charge Conservation and Equality of Gravitational and Inertial Mass*, *Phys. Rev.* **135** (1964) B1049.

[81] P. van Nieuwenhuizen, *Radiation of Massive Gravitation*, *Phys. Rev.* **D 7** (1973) 2300.

[82] S. B. Giddings, M. Schmidt-Sommerfeld and J. R. Andersen, *High Energy Scattering in Gravity and Supergravity*, *Phys. Rev.* **D82** (2010) 104022.

[83] P. Lodone and V. S. Rychkov, *Radiation Problem in Transplanckian Scattering*, JHEP **0912** (2009) 036.

[84] H. J. Schnitzer, *Reggeization of N=8 supergravity and N=4 Yang-Mills Theory*, arXiv:hep-th/0701217.

[85] Z. Bern, J. J. M. Carrasco and H. Johansson, *Perturbative Quantum Gravity as a Double Copy of Gauge Theory*, *Phys. Rev. Lett.* **105** (2010) 061602.

[86] G. 't Hooft, *Graviton Dominance in Ultra-High-Energy Scattering*, *Phys. Lett.* **B 198** (1987) 61.

[87] D. Amati, M. Ciafaloni and G. Veneziano, *Superstring Collisions at Planckian Energies*, *Phys. Lett.* **B 197** (1987) 81.

[88] D. Amati, M. Ciafaloni and G. Veneziano, *Classical and Quantum Gravity Effects from Planckian Energy Superstring Collisions*, *Int. J. Mod. Phys.* **A 3**, (1988) 1615.

[89] D. Amati, M. Ciafaloni and G. Veneziano, *Higher-Order Gravitational Deflection and Soft Bremsstrahlung in Planckian Energy Superstring Collisions*, *Nucl. Phys.* **B 347** (1990) 550.

[90] D. Amati, M. Ciafaloni and G. Veneziano, *Planckian Scattering Beyond the Semi-classical Approximation*, *Phys. Lett.* **B 289** (1992) 87.

[91] D. Amati, M. Ciafaloni and G. Veneziano, *Effective Action and All-Order Gravitational Eikonal at Planckian Energies*, *Nucl. Phys.* **B 403** (1993) 707.

[92] S. Giddings, *The Gravitational S-matrix: Erice lectures*, (2011) arXiv:1105.2036 [hep-th].

[93] M. Beneke and G. Kirilin, *Soft-Collinear Gravity*, *JHEP* **1209** (2012) 066.

[94] S. Oxburgh and C. D. White, *BCJ Duality and the Double Copy in the Soft Limit*, (2012) arXiv:1210.1110 [hep-th].

[95] P. C. Aichelburg and R. U. Sexl, *On the Gravitational Field of a Massless Particle*, *Gen. Rel. Grav.* **2**, (1970) 303.

[96] T. Dray and G. 't Hooft, *The Gravitational Shock Wave of a Massless Particle*, *Nucl. Phys.* **B 253** (1985) 173

[97] R. Jackiw, D. Kabat and M. Ortiz, *Electromagnetic Fields of a Massless Particle and the Eikonal*, *Phys. Lett.* **B 277** (1992) 148.

[98] H. Cheng and T. T. Wu, *Expanding Protons: Scattering at High Energies*, M.I.T. Press, Cambridge, MA (1987)

[99] H. Verlinde and E. Verlinde, *QCD at High Energies and Two-Dimensional Field Theory*, (1993) arXiv:hep-th/9302104

[100] Y. J. Feng, O. Hamidi-Ravari and C. S. Lam, *Cut Diagrams for High Energy Scatterings*, *Phys. Rev.* **D 54** (1996) 3114

[101] C. Boucher-Veronneau and L. J. Dixon, *$N \geq 4$ Supergravity Amplitudes from Gauge Theory at Two Loops*, *JHEP* **1112** (2011) 046.

[102] W. Siegel, *Fields*, (1999) arXiv:hep-th/9912205

[103] E. Laenen, G. Stavenga, and C. D. White, *Next-to-Eikonal Corrections to Soft Gluon Radiation: A Diagrammatic Approach*, *JHEP* **0903** (2011) 054.

[104] E. Laenen, L. Magnea, and C. D. White, *Path Integral Approach to Eikonal and Next-to-Eikonal Exponentiation*, *JHEP* **1101** (2011) 141.

[105] D. Kabat and M. Ortiz, *Eikonal Quantum Gravity and Planckian Scattering, Nucl. Phys.* **B 388** (1992) 570.

[106] N. Kaloper and J. Terning, *How Black Holes Form in High Energy Collisions, Gen. Relativ. Gravit.* **39** (2007) 1525

[107] R. Basu, J. Ramalho and G. Sterman, *Factorization at Higher Twist in Hadron-Hadron Scattering*, *Nucl.Phys.* **B 244** (1984) 22.

[108] G. Sterman, Acta Phys. Polon. B **39**, 2151 (2008).

[109] G. Dvali, G. F. Giudice, C. Gomez, and A. Kehagias, *UV-Completion by Classicalization*, (2010). arXiv:1010.1415 [hep-ph].

[110] G. Dvali and D. Pirtskhalava, *Dynamics of Unitarization by Classicalization*, *Phys. Lett.* **B 699**, 78-86 (2011).

[111] G. Dvali, *Classicalize or not to Classicalize?*, (2011), arXiv:1101.2661 [hep-th].

[112] G. Dvali, C. Gomez and A. Kehagias, *Classicalization of Gravitons and Goldstones*, *JHEP* **1111** (2011) 070.

[113] G. Dvali and C. Gomez, *Self-Completeness of Einstein Gravity*, (2010) arXiv:1005.3497 [hep-th].

[114] B. Bajc, A. Momen and G. Senjanovic, *Classicalization via Path Integral*, (2011). arXiv:1102.3679 [hep-ph].

[115] F. Berkhahn, D. D. Dietrich and S. Hofmann, *Cosmological Classicalization: Maintaining Unitarity under Relevant Deformations of the Einstein-Hilbert Action*, *Phys. Rev. Lett.* **106** (2011) 191102.

[116] D. M. Eardley and L. Smarr, *Time Function in Numerical Relativity. Marginally Bound Dust Collapse*, *Phys. Rev.* **D 19** (1979) 2239.

[117] D. Christodoulou, *Violation of Cosmic Censorship in the Gravitational Collapse of a Dust Cloud*, *Commun. Math. Phys.* **93** (1984) 171 .

[118] P. S. Joshi and I. H. Dwivedi, *Naked Singularities in Spherically Symmetric Inhomogeneous Tolman-Bondi Dust Cloud Collapse, Phys. Rev.* **D 47** (1993) 5357